
Fuelling the central engine in nearby disc galaxies

Simulating the evolution of central gas reservoirs



Pierrick Verwilghen

Munich, 2024

Fuelling the central engine in nearby disc galaxies

Simulating the evolution of central gas reservoirs

Pierrick Verwilghen

Dissertation
at the
Faculty of Physics
of the
Ludwig-Maximilians-Universität
München

submitted by
Pierrick Verwilghen
born in Verviers, Belgium

Munich, 18th December 2024

Zufuhrprozesse des zentralen Antriebs in nahegelegenen Scheibengalaxien

Simulation der Evolution zentraler Gasreservoirs

Pierrick Verwilghen

Dissertation
an der
Fakultät für Physik
der
Ludwig-Maximilians-Universität
München

vorgelegt von
Pierrick Verwilghen
aus Verviers, Belgien

München, den 18. Dezember 2024

Erstgutachter: Prof. Dr. Klaus Dolag
Zweitgutachter: Prof. Dr. Eric Emsellem
Tag der mündlichen Prüfung: 13. Februar 2025

Contents

List of Figures	xv
List of Tables	xvii
Acronyms	xx
Zusammenfassung	xxiii
Abstract	xxvii
1 Introduction	1
1.1 Evolution of galaxies from the early Universe until now	2
1.1.1 The cosmological context	2
1.1.2 Galaxy assembly and evolution from high z	4
1.1.3 The role of the central supermassive black hole	6
1.2 Structure of disc galaxies at redshift zero	8
1.2.1 Main ingredients of disc galaxies	9
1.2.2 A few words about three current observation surveys	10
1.2.3 Characteristics of the bar and spiral arms	11
1.2.4 Secular processes and their impact on the disc	13
1.3 The central structures of disc galaxies and their connection with the central black hole	14
1.3.1 A non-trivial connection	15
1.3.2 The inner molecular gas ring (central molecular zone)	15
1.3.3 The inner stellar disc	16
1.3.4 The molecular ring as a ‘gas reservoir’ for the central supermassive black hole	17
1.4 Open questions	17
1.4.1 Motivations and plan of this work	18
2 Numerical techniques and description of RAMSES	21
2.1 Fundamental equations, methods, and overview of the different astrophysical codes	22
2.1.1 Direct N-body solver, Tree code and fast multipole method (FMM)	24

2.1.2	Particle mesh method	25
2.1.3	Adaptive mesh refinement method	26
2.1.4	Methods to solve the Euler equations	26
2.1.5	Codes in Astrophysics	27
2.2	Cosmological and Astrophysical simulations	27
2.2.1	Something about the IllustrisTNG simulations	28
2.2.2	Something about the Horizon simulations	29
2.2.3	Something about the Vintergatan simulations	29
2.3	The RAMSES code	29
2.3.1	Solving the Euler equations	30
2.3.2	The Godunov method	33
2.3.3	The Riemann problem	36
2.3.4	The various Riemann solvers	41
2.3.5	Overview of the 3D Riemann problem	43
2.4	RAMSES to model the evolution of nearby disc galaxies	44
3	Methods and simulations	55
3.1	The PHANGS-ALMA sample as a basis for a grid of galactic models	56
3.1.1	Five galactic parameters	56
3.1.2	Surface density fitting to model the stellar and gas distribution	57
3.1.3	The grid of models	57
3.1.4	The choice of the Dark Matter halo profile and black hole - stellar mass relation	59
3.2	Generating the initial conditions	62
3.2.1	The Multi Gaussian Expansion method	63
3.2.2	The Jeans equations	64
3.2.3	Building dynamical models with the MGE method to generate the IC	66
3.3	Numerical recipes used in RAMSES	68
3.3.1	The Jeans refinement strategy	69
3.3.2	Gas cooling, star formation, and stellar feedback	72
4	Bar formation and the building of the central gas reservoir	77
4.1	Introduction	80
4.2	Methods	82
4.2.1	The PHANGS-ALMA sample	82
4.2.2	The control parameters	82
4.2.3	The grid of models	84
4.3	Numerical simulations	87
4.3.1	Initial conditions	87
4.3.2	Refinement strategy	89
4.3.3	Numerical recipes	89
4.4	Results	91
4.4.1	General properties and time evolution	91

4.4.2	Typical bar formation time	95
4.4.3	Evolutionary phases of isolated barred discs	100
4.4.4	Gas structure in the central 1 kpc	102
4.4.5	The conditional onset of inner stellar discs	102
4.5	Summary and conclusion	103
5	The gas structure transition in low- and high-stellar mass discs	109
5.1	Introduction	111
5.2	First evidence in simulations for a change of regime	113
5.2.1	The set of simulations	113
5.2.2	Gas surface density distribution	115
5.2.3	The radial gas density re-distribution	116
5.2.4	The redistribution of star formation across the disc	118
5.3	Physical tracers	118
5.3.1	Emergence of the ILR	118
5.3.2	The central PDF	120
5.3.3	Dynamical tracers	120
5.4	The balance between stellar feedback and gravity	123
5.4.1	Feedback versus gravity	123
5.4.2	The crucial role of supernovae in preventing the formation of an inner gas disc	125
5.5	Discussion and Conclusion	127
5.5.1	A gas reservoir chronicle	127
5.5.2	The importance of timescales	128
5.5.3	Summary	131
5.6	Mass loading factor and toy model	132
5.6.1	The mass loading factor	132
5.6.2	Toy model for the seed formation	132
6	Characterising the gas reservoir and its connection with the black hole	137
6.1	The characteristics of the gas reservoir	138
6.1.1	From the seed to the disc	138
6.1.2	The 3D structure of the underlying stellar disc	139
6.1.3	Orientation of the gas reservoir with the bar angle	139
6.2	Motion of the central black hole	142
7	Conclusion and perspectives	149
7.1	Summary	150
7.1.1	The grid of models	150
7.1.2	The phases of the bar-driven fuelling	150
7.1.3	The low- and high-mass regime	151
7.1.4	The growth and shape of the gas reservoir	152
7.2	Limitations of this work	153

7.3 Outlook	154
A Paper 1	157
A.1 Evolution of the models as a function of the parameter τ	157
B Paper 2	163
B.1 The gas and star formation distribution in non-barred systems	163
B.2 Interaction with a massive stellar cluster	163
Bibliography	178
Acknowledgements	180

List of Figures

1.1	Wilkinson Microwave Anisotropy Probe heat map of the cosmic microwave background (CMB) with temperature fluctuations ranging from -300 to 300 micro-Kelvin. Credits: https://wmap.gsfc.nasa.gov	4
1.2	Evolution over time of the scale factor in the Friedmann–Lemaître–Robertson–Walker (FLRW) metric for different values of the density parameters Ω_M (matter) and Ω_Λ (dark energy). Credits: https://jila.colorado.edu	5
1.3	Evolution of the stellar mass function (SMF) as a function of redshift for the total (left panel), star-forming (middle panel), and quiescent (right panel) galaxies of the COSMOS2020 sample (from Weaver et al., 2023).	6
1.4	Evolution of the stellar mass function (SMF) (grey dots and coloured curves) and halo mass function (HMF) (lower bound of the grey shaded area) as a function of redshift from $z = 1.5$ to $z = 7.5$. The coloured curves are the inferred stellar mass function (SMF) fitted to the data (grey dots). The different colours refer to the redshift of Fig.1.3. The grey curves are the halo mass function (HMF) scaled by a factor 0.018, corresponding to the stellar-to-halo mass function at $z = 0$. The data are stemming from the COSMOS2020 sample (from Weaver et al., 2023).	7
1.5	Evolution of the star formation rate (SFR) density (black line) and massive black hole (BH) accretion rate density (red line (Shankar et al., 2009), green shaded area (Aird et al., 2010), and blue shaded area (Delvecchio et al., 2014)) as a function of redshift (from Madau & Dickinson, 2014)	9
1.6	Image of the barred spiral galaxy NGC1300 taken with the Hubble Space Telescope (HST). We see the prominent stellar bar structure and the two ‘grand design’ spiral arms.	11
1.7	specific star formation rate as a function of the stellar mass for the GALEX+WISE sample. The dark red curve is a fit of the data and represents the galaxy’s main sequence at $z=0$ (from Leroy et al., 2019)	14
1.8	James Webb Space Telescope (JWST) image of NGC1300. We see the same spiral structure as in Fig. 1.6 but here, the central region is highlighted and shows the central gas disc/ring.	16
1.9	The black-hole to total-stellar mass relation for local active galactic nuclei (AGN)s (see Reines & Volonteri, 2015, for more details)	18

2.1	Time and spatial discretisation for the centred and upwind schemes.	32
2.2	Time and spatial discretisation scheme for the Godunov method.	33
2.3	Piecewise solution of the Godunov scheme	34
2.4	Discretisation scheme for the Godunov method.	35
2.5	Illustration of the characteristic curves of Eq. 2.41. The red curves represent the Left state (everything on the left of the interface), and the blue curves represent the right state (everything on the right of the interface). The propagation of waves shows a right-going left state and a left-going right state crossing the interface and creating a mixed state (violet curves).	39
2.6	Illustration of the characteristic curves of Eq. 2.54. The red curve represents the Left state, and the blue curves represent the right states. From left to right the waves propagate with velocity $u_0 - a$, u_0 , and $u_0 + a$, respectively. The two mixed states appear between each wave.	41
2.7	Initial condition of the Sod tube test. The initial density, velocity, and pressure profiles are illustrated by the circles with a discontinuity at a distance of 5 cm. We have used a uniform mesh size with a total number of cells of 128, corresponding to a constant level of refinement fixed to 7.	46
2.8	Solution of the EXACT Riemann solver for the Sod tube test. The final state of the density, velocity, and pressure profiles are shown by the circles. The analytical solution is shown by the purple curve. From left to right, we see the rarefaction wave ($\sim 0.2-0.5$ cm), then the contact discontinuity wave (~ 0.75 cm), and finally the shock wave (~ 0.95 cm). The mesh size (dashed blue curve) is uniform with a total number of 128 cells, corresponding to a constant level of refinement fixed to 7.	47
2.9	Same as in Fig. 2.8, but for the LLF Riemann solver.	48
2.10	Same as in Fig. 2.8, but with the HLLC Riemann solver.	49
2.11	Same as in Fig. 2.8, but with the AMR-HLLC Riemann solver. The level of refinement (dashed blue curve) varies depending on the constraint from 3 to 10 and converges with a total number of 142 cells.	50
2.12	Gas surface density map of one of our simulation snapshots (model G105, see Chap. 4) performed in this work. The more yellow, the denser the gas region is.	51
2.13	adaptive mesh refinement (AMR) grid of the simulation snapshot shown in Fig. 2.12. There are 7 levels of refinement shown by the coloured dots corresponding approximately to 780 (black), 390 (purple), 195 (orange), 98 (red), 49 (green), 25 (blue), and 12 (yellow) pc.	52
2.14	Superimposition of the adaptive mesh refinement (AMR) grid shown in Fig. 2.13 on the gas surface density map illustrated in Fig. 2.12.	53
3.1	Stellar and gas surface density profile of the galaxy NGC5134 (black dots) with their corresponding fit=1 for their discs (blue curves) and bulge (red curve).	58

3.2	Gas surface density profiles of the galaxies NGC7496 and 3239 (black dots) with their corresponding fit=0,-1 on the left and right panels, respectively for their discs (blue curves) and bulge (red curve).	59
3.3	Results of the fits for the different galactic parameters (see text). The ICs are illustrated by the stars. The purple stars represent the ICs we use in priority.	60
3.4	Three dark matter halo profiles represented by the Einasto, NFW, and Burkert profiles in the top, middle, and bottom panel, respectively.	61
3.5	Initial circular velocity curves of our 54 models. The colour of the curve illustrates the stellar mass range of the model. The shaded coloured areas show the envelopes of the PHANGS velocity curves for the different stellar mass bins.	62
3.6	Illustration of a stellar density profile reconstruction (red curve) via the MGE method with a set of 23 Gaussian functions	64
3.7	Content of one of our IC files. The left panel shows a face-on view of the model and the right panel shows an edge-on view. The colours represent the different dynamical components of the galaxy with the DM, gas, and stars in black, blue, yellow and red, respectively. The gas component is shown for a comprehensive overview of our models, but it is not given to the code as ICs. The galactic model corresponds to a galaxy having a stellar mass of $10^{10.5} M_{\odot}$ and a gas fraction of 10 %.	68
3.8	Rotation curve of the model shown in Fig. 3.7. The total rotation curve is given by the black dashed curve. The black, yellow, red, and blue curves represent the different dynamical components of the model: the DM, stars (disc and bulge), and gas, respectively.	69
3.9	Jeans mass (m_{sphn}) of the ℓ^{th} level of refinement going from the 7^{th} to the 14^{th} for a box length of 100 kpc. We also show on the top x-axis the corresponding cell size. The red dots are the Jeans mass threshold required to refine the grid from the previous to the corresponding level.	73
3.10	Equation of state (EOS) presented in Renaud et al. (2013a) and used in older versions of RAMSES.	74
3.11	Cooling function used in Agertz et al. (2013) and implemented in RAMSES.	75
4.1	Gas fraction (α) as a function of the stellar mass of the galaxies in the PHANGS sample and the corresponding histograms for the stellar mass (top panel) and gas fraction (right panel) distribution (see Sect. 4.2.2).	84
4.2	Illustrations of the fitted radial gas and stellar density profiles. The plots show the original data points (in black, see Sun et al. (2022), mega-tables version 3), i.e. the azimuthal-averaged surface density profiles for the stellar (top panel) and gas (bottom panel) components of the galaxy NGC 5134. The corresponding fits are superimposed and colour-coded accordingly (blue for the disc component, red for the total disc and ellipsoid (or bulge) component).	85

- 4.3 Results of the fit for different parameters of the models as a function of the stellar mass. Top panels: gas fraction (left) and stellar scale length (right). Middle panels: scale length ratio between the gas and stars (left) and scale length of the stellar bulge (right). Bottom panels: bulge index (left) and bulge mass fraction (right). Colour circles show the actual fits (see the text in Sec. 4.2.2 for details) to the PHANGS-ALMA sample, while the selected values for our used initial conditions (IC(models)) are shown with purple stars. 86
- 4.4 Comparison between the observed gas velocity curves of the PHANGS sample (shaded areas) and the circular velocity profiles from our models (solid curves). The vertical lines near $R=0$ illustrate the contribution of the central SMBH. The dotted curves represent the circular velocities extracted from the first snapshot (INI_SIM) of each simulation and are consistent with the analytic derivation associated with the initial conditions. The dashed curves represent the circular velocities at $\tau = 2$ (see Sect. 4.4.3, which corresponds to twice the bar formation time of our simulated galaxies). As mentioned in the text, the PHANGS rotation curves are meant as guidelines to build the initial mass models. 90
- 4.5 Comparison of the SFR stemming from the PHANGS data sample (grey crosses) and the SFR computed from the simulated galaxies (coloured squared). The colour of the squares corresponds to the different stellar masses. The red dashed line represents the star formation main sequence at $z = 0$ from Leroy et al. (2019). 92
- 4.6 Evolution over time (in millions of years) of the gas and stars of the model labelled G053M100F20L2B00 (one of the sixteen simulations presented in this paper). The two big panels illustrate four main stages, chronologically ordered from top left (0-400 Myr), to top right (500-900 Myr), bottom left (1000-1800 Myr) and bottom right (2000-2800 Myr). **Top left:** first spiral structures, cooling of the gas, onset of star formation, initial bar structure emerging. **Top right:** bar strengthening and active local star formation. **Bottom left:** building of a central concentration of gas (and new stars). **Bottom right:** growth of the gas reservoir. In each big panel, from top to bottom, we present maps for the gas mass density (GAS), the mass of young stars (≤ 50 Myr, NS), of old stars (OS) and finally the cumulative mass of new stars (formed since the beginning of the simulation, CNS). Each panel shows a 10×10 kpc² region and the colour scaling is adapted for each panel. 93
- 4.7 Evolution of the bar strength (measured through the A_2 Fourier coefficient) for the model G053. 94

- 4.8 Evolution of the maximum of the A_2 coefficient (top panels), the mass of gas within 1 kpc (middle panels), and the SFR (bottom panels) over time for the 16 simulations (evolved until max 3 Gyr). The colour gradient represents the four stellar masses (9.5, 10, 10.5 and 11 [$\log(M_\odot)$]) from the lightest to the most massive. The left column represents the less massive galaxies (9.5 and 10, in green and cyan, respectively) and the right column shows the most massive ones (10.5 and 11, in blue and dark blue, respectively). The solid and dashed curves illustrate the models without and with a bulge, respectively and the thickness of the lines accounts for the gas fraction (10 and 20% for the thinnest and thickest, respectively). The typical bar formation time t_{bar} is also shown (red diamonds) within a time interval of 200 Myr (red part of the curves). 96
- 4.9 Typical bar formation time t_{bar} as a function of the stellar mass for all 16 simulations. The colour of the squares corresponds to the different stellar masses. The size of each square represents 200 Myr (i.e. ± 100 Myr), hence illustrating the uncertainty in t_{bar} (see Sect. 4.4.2). 97
- 4.10 Typical bar formation time t_{bar} as a function of f_{disc} as defined in Bland-Hawthorn et al. (2023). The dashed lines show the relation given by (Fujii et al., 2019). f_{disc} is derived using the sole stellar disc (right panel) or the total baryonic content (i.e. stars and gas; left panel). In the right panel, f_{disc} (stars only) decreases when the gas fraction increases as expected (the relative contribution of the stellar disc gets smaller), while in the left panel, f_{disc} (total) increases with the gas fraction (as the total baryonic contribution increases). As in Figure 4.9, the size of each square represents 200 Myr (i.e. ± 100 Myr), hence illustrating the uncertainty in t_{bar} (see Sect. 4.4.2). . . . 98
- 4.11 Evolution of the maximum of the A_2 coefficient (top panels), the mass of gas within the central 1 kpc normalised by the initial mass of gas within the same radius (middle panels), and the SFR (bottom panels). The evolution is shown through the dimensionless parameter τ , which is the ratio between the time of the simulations and the corresponding time when A_2 reaches the value of 0.2. The dashed vertical lines and shaded coloured areas show peculiar values of τ we use to describe the phases of the fuelling (i.e. $\tau \in 0-1$ (blue area); $\tau \in 1-1.5$ (purple area); $\tau \in 1.5-2$ (orange area)). The colour code and the meaning of the different lines are the same as in Fig. 4.8. . . 104
- 4.12 Density map of gas for the 16 simulations at the corresponding time for which $\tau = 2$. The first three rows show a box of 10 kpc side while the last row shows a box of 20 kpc side. The model numbers are colour-encoded according to the corresponding stellar mass (from the lightest to the most massive from the top to the bottom, i.e. 9.5, 10, 10.5, and 11 in $\log_{10}(M_\odot)$). The two left columns illustrate the model with a gas fraction of 10% while the two right columns illustrate the models with a gas fraction of 20%. The odd (even) reference number accounts for models without (with) a bulge. . 105

5.1	JWST MIRI 7.7 μm images of two nearby barred main-sequence star-forming galaxies (GO 3707; PI Leroy) NGC 1087 and NGC 3507 (stellar masses of $\sim 10^{9.95}$ and $\sim 10^{10.4} M_{\odot}$, respectively) emphasising the difference in morphology. Both images have been deprojected, and the bar is set horizontally. The field of view is 7 kpc \times 7 kpc, thus showing the central ± 3.5 kpc. Those data have previously appeared in Chown et al. (2024) with data reduction following Williams et al. (2024).	112
5.2	Surface density map of gas and newly-formed stars (≤ 100 Myr) of four models in two stellar mass bins (G013, G025, with an initial stellar mass of $10^{9.5} M_{\odot}$; G037, and G053 with an initial stellar mass of $10^{10} M_{\odot}$) from our set of simulations. Each panel shows one model at different values of the parameter τ , with $\tau = 1$ corresponding to the bar formation timescale. G013 and G053 have the same 20% gas mass fraction, while G025 and G037 have 40 and 10% gas mass fraction, respectively (the latter two following the averaged properties of star-forming main sequence galaxies at their respective stellar masses).	116
5.3	Normalised surface density profile of gas for our set of simulations at $\tau = 0.5, 1,$ and 2 (see text). The faint blue curves represent low-stellar mass models ($< 10^{10} M_{\odot}$) and the faint red curves show higher-stellar mass models ($\geq 10^{10} M_{\odot}$). The strong blue and red lines are the median of the faint blue and red curves, respectively. The top panels show models that have formed a bar, sustained until the end of the simulation. The bottom panels illustrate the unbarred models.	117
5.4	Evolution over time (from left to right, $\tau = 0.5, 1$ and 2) of the normalised angular frequency Ω and $\Omega - \kappa/2$ radial profiles of the barred low-stellar mass (blue curves, top row) and high-stellar mass (red curves, bottom row) models. The quantity we use in the normalisation is the bar pattern speed Ω_b . The black dashed curve represents $\Omega = \Omega_b$	119
5.5	Evolution of the Gas density Probability Distribution Functions (PDF) of four of our simulated galaxies (i.e., models G013, G025, G037, and G053, see Fig. 5.2) as a function of τ (main panels). The normalised PDF by the PDF at $\tau = 0.5$ (NPDF) is shown at the bottom of each main panel. . . .	121
5.6	Normalised distribution of the virial parameter (top left) and Mach number (bottom left) and their components (i.e., kinetic energy E_{kin} and potential energy E_{grav} for the virial parameter and the one-dimensional velocity dispersion σ_{1D} and the sound speed v_s for the Mach number) as a function of time for the low-stellar mass model G025. The distributions are computed inside a box of $2 l_*$ in side length and a height of $1 l_*$ around the centre. . .	122
5.7	Same distributions as in Fig. 5.6 for the high-stellar mass model G037. . .	123

5.8	Evolution (from left to right) of the vertical velocity dispersion normalised by the local escape velocity (top row), the vertical velocity dispersion (solid curves), and the escape velocity (dot-dashed curves, bottom row) profiles as a function of τ . The blue curves represent low-stellar mass models and the red curve the higher-stellar mass models. The grey curves are models that do not display a bar at the end of the simulation.	124
5.9	Surface density map of gas of model G001 (left panel) and G001-NOSN (right panel) at four characteristic times. The ‘NOSN’ stands for the run without feedback from supernovae and only includes feedback from stellar winds. Each subpanel shows one model at different values of the parameter τ	126
5.10	Same as bottom panels of Fig.5.8 but for model G001 (blue curve) and G001-NOSN (orange curve).	126
5.11	Same as in Fig. 5.4 but for model G001 (blue curve) and G001-NOSN (orange curve).	127
5.12	Time evolution of simulations G025 and G053, respectively a low and intermediate stellar mass system ($10^{9.5}$ and 10^{10} M_{\odot}). Four running times are presented (from left to right, first six panels from top), with steps of 200 Myr, with a seed gas reservoir forming in G053 around $t = 1400$ Myr (in between the two middle panels). Maps with a field of view of $2 \text{ kpc} \times 1 \text{ kpc}$ of the total gas surface density, the mass of new stars (and old stars, as orange contours) and molecular gas density are shown as maps in the first to third rows for G025, and fourth to sixth row for G053. In all maps, the bar is aligned with the x-axis. The two bottom rows show the radial profiles, averaged over the y-axis ($\pm 1 \text{ kpc}$), first with the gas profiles (total and molecular), and then the stellar density profiles (bottom row; old and new stars).	129
5.13	Illustration of the phase transition using models G001 (top panel), G000M975F10L2B00 (middle panel), and G037 (bottom panel), corresponding to a low- intermediate, and high-stellar mass model, respectively. In each panel, we show the evolution of the surface density map of gas at 6 different values of τ (0.5,1,2,4,5, and 5.5).	130
5.14	Evolution of the mass loading factor as a function of time for three values of the parameter τ (1, 2, 5) for all models. Each square has a pattern corresponding to its gas fraction, and a thickness that follows the stellar mass bin as indicated in the top corner of the first panel.	133
5.15	Evolution over time of the ratio SSFR/B evaluated at $R=l_*$ for four of our models: G013 (solid blue curve), G025 (blue dashed curve), G037 (solid red curve), and G053 (red dashed curve). The green diamonds illustrate four reference times: 1150.0, 1350.0, 1550.0, and 1750.0 Myr. The green shaded area is the time interval for which we observe the formation of a gas reservoir in model G053.	135

5.16	Comparison between our toy model and Mapping Nearby Galaxies at APO (MaNGA) data. The top panel shows the specific star formation rate (orange line) and the B function (black line) with their errors illustrated by the shaded areas. The bottom panel shows the same curves and the Mapping Nearby Galaxies at APO (MaNGA) data split into different morphological types as a function of the star formation (SF) (H_α) distribution: along the bar (blue diamonds), centre (red dots), ring (red circles), and centre-bar ends (purple lemniscate (∞) symbols).	136
6.1	Evolution of the semi-major (blue curves) and semi-minor (orange curves) axes lengths of the gas reservoir for 4 of our non-bulged models. The two first top panels show models with a stellar mass of $10^{10} M_\odot$, and a gas fraction of 10 and 20% for G037 and G053, respectively. The two bottom panels show models with a stellar mass of $10^{10.5} M_\odot$, and a gas fraction of 10 and 20% for G105 and G137, respectively. The ellipticity is illustrated by the grey curve.	140
6.2	Same as in Fig. 6.1 but with the equivalent (in mass and gas fraction) bulged models.	141
6.3	Formation and evolution of the disc of newly-formed stars for model G025, G037, and G105. For each model, the five top and bottom panels show the face-on (x-y) and edge-on (x-z) view of the disc, respectively.	144
6.4	Evolution of the bar (red curve) and gas reservoir (green curve) angle as a function of the parameter τ for models G037, G053, G105, and G137. The grey curve illustrates the absolute difference between those two angles.	145
6.5	Evolution of the black hole (BH) position over time for 4 low-mass models ($10^{9.5} M_\odot$). For each model, the top panel illustrates the relative position (X-Y in kpc) of the black hole (BH) with respect to the centre of mass of the newly-formed stars. The bottom panel shows the evolution of the normalised radius (r/l_*) of the relative position observed in the top panel.	146
6.6	Same as in Fig. 6.5 but with two higher stellar-mass bins. The top panels show two models with a mass of $10^{10} M_\odot$, and the bottom panels show two models with a stellar mass of $10^{10.5} M_\odot$	147
6.7	Same as in Fig. 6.5 but with the two test cases G001-NOSN and G000M975, having a stellar mass of $10^{9.5}$ and $10^{9.75}$, respectively.	148
A.1	Time evolution as a function of τ of the gas surface density (top row, GAS), formed stars' surface density (second row, NS), old stars' surface density (third row, OS), and cumulative formed stars' surface density (bottom row, CNS) of the four lowest stellar mass models ($10^{9.5} M_\odot$). Each panel shows a box with a side length of 10 kpc.	158
A.2	Same as Fig. A.1 for the four $10^{10} M_\odot$ stellar mass models.	159
A.3	Same as Fig. A.1 for the four $10^{10.5} M_\odot$ stellar mass models.	160

A.4	Same as Fig. A.1 for the four $10^{11} M_{\odot}$ stellar mass models. The box size has been extended to 20 kpc for this most massive stellar bin.	161
B.1	Same as in Fig. 5.2 but for four non-barred models: G015, G032, G045, and G069.	165
B.2	Density map of the newly-formed stars of model G069 showing the interaction of the in situ formed stellar cluster and the bar region.	166

List of Tables

2.1	Table illustrating the different codes and their specifications (see text for more details).	27
3.1	Grid of models with the different values for the control parameters based on the PHANGS sample. The grid is built on 4 galaxy stellar mass values, then covering a broad range of characteristic properties which cover the observed sample.	59
3.2	Grid of values for the parameters describing the dark matter profiles (i.e. $\rho_{0,h}$, the halo density; l_h , the typical halo scale length; and m , the halo index) as a function of the stellar mass M_* . Those values have been inspired by the work of Kun et al. (2017), but their final values have been chosen to match the PHANGS rotation curves. The central black hole (BH) masses M_{BH} we use in the initial conditions are also shown in the last column. . .	62
4.1	Grid containing the parameters for the initial conditions of the models of this paper. From left to right columns: label, total stellar mass, mass gas fraction, stellar scale length, scale length ratio (gas over stars) and bulge mass fraction.	87
4.2	Grid of values for the parameters describing the dark matter profiles (i.e. $\rho_{h,0}$, the halo density; $l_{h,0}$, the typical halo scale length; and m , the halo index) as a function of the stellar mass M_* . Those values have been inspired by the work of Kun et al. (2017), but their final values have been chosen to match the PHANGS rotation curves. The central black hole (BH) masses M_{BH} we use in the initial conditions are also shown in the last column. . .	89
5.1	List of all models in the extended simulation set and the parameters used to set up their initial conditions. Columns from left to right are: name or label encapsulating those parameters, total stellar mass (M_* , here in \log_{10}), gas mass fraction F (in %), stellar scale length l_* (in kpc), scale length ratio l_g/l_* (gas over stellar scale lengths) and bulge mass fraction B (in %). The last column shows models developing a bar (Y) and never developing a bar (N) by the end of the run.	114

Acronyms

Λ CDM lambda cold dark matter

AGN active galactic nuclei

ALMA Atacama Large Millimeter/submillimeter Array

AMR adaptive mesh refinement

BH black hole

CIC cloud-in-cell

CMB cosmic microwave background

CMZ central molecular zone

CPU central processing unit

DM dark matter

EHT Event Horizon Telescope

EOS equation of state

FFT fast Fourier transform

FLRW Friedmann–Lemaître–Robertson–Walker

FMM fast multipole method

GECKOS Generalising Edge-on galaxies and their Chemical bimodalities and Kinematics
and Outflows out to Solar environments

GMC giant molecular cloud

GPU graphical processing unit

GS Gauss-Siedel

HMF halo mass function

HST Hubble Space Telescope

ILR inner Lindblad resonance

ISM interstellar medium

JWST James Webb Space Telescope

MaNGA Mapping Nearby Galaxies at APO

MGE Multi Gaussian Expansion

MHD magneto-hydro-dynamics

MPI message passing interface

MUSE Multi Unit Spectroscopic Explorer

MW Milky Way

NFW Navarro-Frenk-White

OLR outer Lindblad resonance

PAH polycyclic aromatic hydrocarbonate

PDE partial differential equations

PHANGS Physics at High Angular resolution in Nearby Galaxies

PM particle mesh

SF star formation

SFH star formation history

SFR star formation rate

SMBH supermassive black hole

SMF stellar mass function

SNe Supernovae

SPH smooth particle hydrodynamics

TIMER Time Inference with MUSE in Extragalactic Rings

VLT Very Large Telescope

Zusammenfassung

Die Zentralregionen naher Scheibengalaxien weisen eine große Vielfalt an Strukturen in ihren Stern- und Gasscheibe auf, die das Ergebnis einer komplexen und dynamischen Entwicklung darstellen. Die sichtbarste zentrale Struktur innerhalb der Balkenregion ist die innere molekulare Scheibe (die so genannte zentrale molekulare Zone (CMZ) in der Milchstraße). Jüngste Beobachtungskampagnen haben gezeigt, dass diese inneren molekularen Scheiben eine typische Größe von einigen hundert Parsec bis zu einem Kiloparsec haben und dazu neigen, im Zentrum von Balkenscheiben zu erscheinen. Die physikalischen Phänomene, die an der Entstehung, dem Verbrauch (z. B. Sternentstehung) und der langfristigen Entwicklung dieser inneren Gasstrukturen beteiligt sind, werden noch immer diskutiert. Es wird allgemein angenommen, dass der Balken eine Rolle bei der Zufuhr von Gas aus dem großen Bereich von einigen Kiloparsec in die innere Molekularscheibenregion spielt. Die genauen physikalischen Prozesse, die am Verlust des Gasdrehimpulses (z. B. Gravitationsmomente, Scherung, Rückkopplung) und dessen Transport zum Zentrum beteiligt sind, sind jedoch nicht vollständig geklärt. Darüber hinaus sind innere Gasscheiben intermediäre Strukturen, die die große Kiloparsec-Skala mit der Subparsec-Skala verbinden (z.B. stellar-getriebene Rückkopplung, magnetische Drehmomente), die an der Entstehung des zentralen supermassiven Schwarzen Lochs (SMBH) beteiligt sind. Daher können diese inneren Scheiben als „Gasreservoirs“ betrachtet werden und sind möglicherweise effiziente Materiallieferanten für das Flackern des zentralen Schwarzen Lochs, dem sogenannten Aktiven Galaktischen Kern (AGN).

Um die Physik und die dynamischen Prozesse, die an der Bildung dieser Gasreservoirs beteiligt sind, zu untersuchen und zu charakterisieren, haben wir eine Reihe hochauflösender hydrodynamischer Simulationen isolierter Galaxien mit dem Adaptive Mesh Refinement (AMR) Code RAMSES durchgeführt. Diese Simulationsreihe verwendet ein Gitter von Modellen, die auf einem Satz galaktischer Parameter basieren, die aus der PHANGS (Physics at High Angular Resolution in Nearby GalaxieS)-ALMA-Durchmusterung stammen. Wir haben vier Kontrollparameter ausgewählt, die typische Eigenschaften der PHANGS-Galaxienprobe abdecken: die stellare Masse (M_{\star} : $10^{9.5}$, 10^{10} , $10^{10.5}$ und $10^{11} M_{\odot}$), der Gasanteil (α : 10, 20 und 40%), die typische stellare Skalenlänge (l_{\star} : 2-5 kpc) und der Bulge-Massenanteil (β : 0, 10 und 30%), um deren Einfluss auf die Bildung und Entwicklung zentraler Gasreservoirs zu untersuchen und zu analysieren. Alle Simulationen beginnen mit achsensymmetrischen Anfangsbedingungen, die mit der Multi Gaussian Expansion (MGE) Methode erzeugt wurden.

Wir haben zunächst eine erste Stichprobe von 16 Simulationen erstellt, die sich auf die vier stellaren Massenbereiche mit Gasanteilen von 10 und 20% und Bulge-Massenanteilen von 0 und 10% konzentrieren. Wir haben diese Untergruppe verwendet, um die Auswirkungen der Kontrollparameter auf die Bildung und Entwicklung großräumiger dynamischer Strukturen (d.h. des stellaren Balkens und der Spiralarme) und ihre Rolle bei der Versorgung der zentralen 1 Kiloparsec-Region zu untersuchen. Wir haben die Sternentstehungsrate (SFR) unserer Modelle berechnet und festgestellt, dass sie mit der sternbildenden Hauptreihe oberhalb von $M_{\star} \geq 10^{10} M_{\odot}$ übereinstimmen. Wir haben festgestellt, dass das Vorhandensein einer zentralen Ausbuchtung die typische Entstehungszeit des Balkens (t_{bar}) verzögert, was die Ergebnisse früherer Studien bestätigt. Wir haben diese Balkenbildungszeit benutzt, um einen dimensionslosen Parameter $\tau = t/t_{bar}$ einzuführen, der ein ähnliches Evolutionsschema für alle unsere Balkenmodelle mit $M_{\star} \geq 10^{10} M_{\odot}$ aufzeigt. Dieses Schema beschreibt die Entwicklung der Gasmasse innerhalb der zentralen 1 Kiloparsec-Region mit vier Phasen. Wir haben beobachtet, dass sich Gasreservoirs in allen gesperrten Modellen gebildet haben, aber nur in den Modellen, die zum Bereich mit der geringsten stellaren Masse ($10^{9.5} M_{\odot}$) gehören. Dies gibt Aufschluss über auf einen Regimewechsel für die Bildung von Gasreservoirs oberhalb einer stellaren Massenschwelle um $10^{10} M_{\odot}$.

Wir haben dann eine erweiterte Untergruppe von 35 Modellen verwendet, um diesen Regimewechsel zu untersuchen, einschließlich Modellen mit einem höheren Gasanteil (40%) und Bulge-Massenanteil (30%). Wir haben beobachtet, dass Modelle mit höherer stellarer Masse ($M_{\star} \geq 10^{10} M_{\odot}$) eine charakteristische Senke im zentralen Bereich ihres Gasoberflächendichteprofiles nach der Bildung des Balkens aufweisen, was auf das Vorhandensein eines Gasreservoirs hinweist. Wir haben die Entwicklung zwischen physikalischen Indikatoren wie der inneren Lindblad-Resonanz (ILR), der Wahrscheinlichkeitsverteilungsfunktion (PDF) und der Verteilung des Virialparameters und der Machzahl für Regime mit niedriger und hoher Sternmasse verglichen und unterschiedliche Verhaltensweisen vor und nach der Bildung des Balkens festgestellt. Wir haben gezeigt, dass das Gleichgewicht zwischen der Rückkopplung durch Supernovae und der Schwerkraft der Schlüssel zum Verständnis dieses Unterschieds bei der Bildung der zentralen Massenkonzentration und der Entstehung oder Nichtentstehung des zentralen Gasreservoirs ist, was zu zwei verschiedenen stellaren Massenregimen führt.

Wir haben schließlich ein analytisches Spielzeugmodell entworfen, das die Physik des Regimewechsels beschreiben soll und dessen theoretische stellare Massenschwelle um $10^{9.75} M_{\odot}$ vorhersagt. Wir beschreiben kurz die zeitliche Entwicklung der Größe des Gasreservoirs und zeigen, dass seine Wachstumsrate nach einem kurzen, abrupten Anstieg in der Anfangsphase weitgehend konstant ist, was das von der Gemeinschaft bereits vorgeschlagene Szenario der Inside-out-Bildung bestätigt. Wir zeigen, dass unsere Reservoirs eine elliptische Form mit einer konstanten Elliptizität haben. Deren vertikale Struktur besteht aus einer darunter liegenden Kernscheibe, die die dünnere Struktur der zentralen Sternscheibe offenbart, umgeben von einer „boxy peanut“ Ausbuchtung, die aus neu gebildeten Sternen besteht. Wir zeigen, dass die Ausrichtung der Reservoirs in Bezug auf den Balken einen erwarteten Winkel von etwa 90 Grad bilden, wenn man die zugrunde liegende x2-

Bahnstruktur berücksichtigt. Wir vervollständigen unsere Analyse, indem wir die Position des zentralen Schwarzen Lochs im Laufe der Zeit berechnen. Wir zeigen einige Oszillationen seiner Position über die Zeit entlang des Balkens mit großen Amplituden in Modellen mit geringerer Sternmasse ($M_{\star} \leq 10^{10} M_{\odot}$), die mit dem Gasanteil bis zum Ende des Laufs zunehmen. In Modellen mit höherer Sternmasse ($M_{\star} \geq 10^{10} M_{\odot}$) ist die Amplitude der Oszillationen kleiner und hört auf, sobald sich das Gasreservoir bildet. Das Schwarze Loch befindet sich dann im Zentrum der zentralen stellaren Scheibe und des Gasreservoirs, was auf eine günstige Konfiguration für das Anheizen des Schwarzen Lochs im Subparsec-Bereich hindeutet. Dieses letzte Ergebnis hängt von der anfänglichen Position des Schwarzen Lochs ab und könnte größtenteils auf numerische Effekte zurückzuführen sein, weshalb es mit äußerster Vorsicht betrachtet werden sollte.

Insgesamt hat diese Arbeit bestätigt, dass der Balken eine wichtige Rolle bei der Zufuhr von Gas zum Zentrum spielt, und hat seine ursprüngliche Rolle bei der Gestaltung der zentralen Regionen in nahen Scheibengalaxien gezeigt. Diese Arbeit hat das Inside-Out-Szenario bestätigt und vier verschiedene Phasen bei der Bildung des Gasreservoirs sowie einige Merkmale seines Wachstums aufgezeigt. Diese Arbeit lieferte eine physikalische Erklärung für die Unterschiede in der Gas- und Sternentstehungsverteilung in Scheibengalaxien mit geringer und hoher Sternmasse, die bereits in früheren Studien aufgezeigt und in neueren Beobachtungen (HST, JWST) bestätigt wurden. Diese Arbeit hat gezeigt, dass der physikalische Ursprung dieses Regimewechsels mit dem Gleichgewicht zwischen der stellaren Rückkopplung aufgrund von Supernovae und der Stärke des Gravitationspotentials zusammenhängt. Sie hat gezeigt, dass die Rückkopplung durch Supernovae die Bildung zentraler Gasreservoirs in Scheiben mit geringer stellarer Masse ($< 10^{10} M_{\odot}$) verhindern kann. Dieses letzte Ergebnis könnte es uns ermöglichen, die Interaktionen und Diskussionen zwischen den Beobachtungs- und Berechnungsgemeinschaften zu verbessern.

Abstract

Central regions of nearby disc galaxies display a large variety of structures in their stellar and gas disc that illustrates the outcome of a complex and dynamic evolution. The most visible central structure inside the bar region is the inner molecular disc (the so-called Central Molecular Zone (CMZ) in the Milky Way). Recent observational campaigns have shown that those inner molecular discs have a typical size ranging from a few hundred parsecs to one kiloparsec and tend to appear at the centre of barred discs. The physical phenomena involved in the building, consumption (e.g., star formation) and long-term evolution of those inner gas structures are still strongly debated. It is commonly accepted that the bar plays a role in the fuelling of gas from the large few kiloparsec scale to the inner molecular disc region. However, the exact physical processes involved in the loss of gas angular momentum (e.g., gravitational torques, shear, feedback) and its transport to the centre are not fully understood. Moreover, inner gas discs are intermediate-scale structures which connect the large kiloparsec scale and the subparsec scale physics (e.g., stellar-driven feedback, magnetic torques) involved in the fuelling of the central supermassive black hole (SMBH). Therefore, those inner discs can be considered as ‘gas reservoirs’ and may be efficient suppliers of material for the flickering of the central black hole, the so-called Active Galactic Nuclei (AGN).

To investigate the physics and characterise the dynamical processes involved in the formation of those gas reservoirs, we have performed a suite of high-resolution hydrodynamical simulations of isolated galaxies with the Adaptive Mesh Refinement (AMR) code RAMSES. This suite of simulations uses a grid of models based on a set of galactic parameters stemming from the Physics at High Angular resolution in Nearby Galaxies (PHANGS)-ALMA survey. We have selected four control parameters spanning typical properties from the PHANGS galaxy sample: the stellar mass (M_* : $10^{9.5}$, 10^{10} , $10^{10.5}$, and $10^{11} M_\odot$), the gas fraction (α : 10, 20, and 40%), the typical stellar scale length (l_* : 2-5 kpc), and the bulge mass fraction (β : 0, 10, and 30%) to study and analyse their impact on the formation and evolution of central gas reservoirs. All the simulations start with axisymmetric initial conditions generated with the Multi Gaussian Expansion (MGE) method.

We have initially built a first sample of 16 simulations, focusing on the four stellar mass bins with gas fractions of 10 and 20% and bulge mass fractions of 0 and 10%. We have used this subset to investigate the impact of the control parameters on the formation and evolution of large-scale dynamical structures (i.e., the stellar bar and spiral arms), and

their role in fuelling the central 1 kiloparsec region. We have computed the star formation rate (SFR) of our models and found that they match the star-forming main sequence above $M_{\star} \geq 10^{10} M_{\odot}$. We have found that the presence of a central bulge delays the typical formation time of the bar (t_{bar}), thus confirming results from previous studies. We have used this bar formation time to introduce a dimensionless parameter $\tau = t/t_{bar}$, revealing a similar evolutionary scheme for all our barred models with $M_{\star} \geq 10^{10} M_{\odot}$. This scheme describes the evolution of the gas mass inside the central 1 kpc region with four phases. We have observed that gas reservoirs were formed inside all barred models but in models belonging to the lowest-stellar mass bin ($10^{9.5} M_{\odot}$), shedding light on a change of regime for the building of gas reservoirs above a stellar mass threshold around $10^{10} M_{\odot}$.

We have then used an extended subset composed of 35 models to investigate this change of regime, including models with a higher gas fraction (40%) and bulge mass fraction (30%). We have observed that higher-stellar mass models ($M_{\star} \geq 10^{10} M_{\odot}$) show a characteristic dip in the central region of their gas surface density profile after the formation of the bar, indicating the presence of a gas reservoir. We have compared the evolution between physical tracers such as the inner Lindblad resonance (ILR), probability distribution function (PDF), and distribution of the virial parameter and the Mach number for low- and high-stellar mass regimes and revealed different behaviours before and after the formation of the bar. We have shown that the balance between the feedback due to supernovae and gravity is the key to understanding this difference in the building of the central mass concentration and the emergence or not of the central gas reservoir, leading to two separate stellar mass regimes.

We have finally designed an analytical toy model which aims at describing the physics of the change of regime and predicts its theoretical stellar mass threshold around $10^{9.75} M_{\odot}$. We briefly describe the time evolution of the size of the gas reservoir, and we show that its growth rate is mostly constant in time after a brief abrupt early increase, confirming the inside-out formation scenario already proposed by the community. We show that our reservoirs have an elliptical shape with a constant ellipticity. Their vertical structure is made of an underlying nuclear disc, revealing the thinner structure of the central stellar disc, surrounded by a ‘boxy peanut’ bulge made of newly-formed stars. We show that the gas reservoirs’ orientation with respect to the bar forms an expected angle of around 90 degrees, considering the underlying x2 orbital structure. We complete our analysis by computing the location of the central black hole (BH) over time. We show some oscillations of its position over time along the bar with large amplitudes in lower stellar-mass models ($M_{\star} \leq 10^{10} M_{\odot}$), increasing with the gas fraction, until the end of the run. In higher-stellar mass models ($M_{\star} \geq 10^{10} M_{\odot}$), the amplitude of the oscillations is smaller and stops once the gas reservoir forms. The BH is then at the centre of the central stellar disc and the gas reservoir, suggesting a favourable configuration for the subparsec scale fuelling of the black hole. This last result depends on the initial location of the BH and could be mostly due to numerical effects, therefore it should be taken with extreme caution.

Overall, this work has confirmed that the bar plays an important role in the fuelling of gas to the centre, and has shown its primordial role in shaping the central regions in nearby disc galaxies. This thesis has confirmed the inside-out scenario, revealed four dis-

tinct phases involved in the building of the gas reservoir, and some characteristics of its growth. This work has provided a physical explanation for the differences in the gas and star-formation distribution in low- and high-stellar mass discs, already highlighted in past studies and confirmed in new recent observations (HST, JWST). This work has shown that the physical origin of this change of regime is connected with the balance between the stellar feedback due to supernovae and the strength of the gravitational potential. It has demonstrated that the supernovae feedback may prevent the formation of central gas reservoirs in low-stellar mass discs ($< 10^{10} M_{\odot}$). This last result could allow us to enhance the interactions and discussions between the observational and computational communities.

Chapter 1

Introduction

1.1 Evolution of galaxies from the early Universe until now

1.1.1 The cosmological context

Humanity has believed for a long time that our Universe has always been as we observe it and will always stay the same. Even now, galaxies we observe today in the nearby Universe at very low redshift ($z \approx 0$) seem quite static. One of the first observations showing a contradiction with this static view of the Universe goes back to the last century. In 1929, the American astronomer Edwin Hubble published his observations on the spectra of Cepheids located in distant galaxies. In these observations, he noticed a shift of their spectra toward redder wavelengths and deduced that this redshift was due to a relative motion of the galaxies hosting those stars with respect to us. He also noticed that the further the galaxy is from us, the more the spectrum is shifted toward the red wavelengths. From this observation, he deduced that the further the galaxies are, the faster they are moving away from us, resulting in the Hubble-Lemaître law (Hubble, 1929) given by:

$$V = H_0 D, \quad (1.1)$$

where V is the so-called recession velocity of a galaxy, H_0 is the Hubble constant at the time of observation, and D is the distance of a galaxy from us. We see that the above equation confirms the recession motion of galaxies as predicted by Hubble's observations. The Hubble's law was the first piece of evidence to prove the expansion of the Universe. Without going into the mathematical details, the Hubble relation can be derived from the Einstein field equations (Einstein, 1915) by using the Friedmann–Lemaître–Robertson–Walker (FLRW) metric (Friedmann, 1922). From these equations, they defined a scale factor $a(t)$ depending on time, for which the Hubble constant is given by:

$$H(t) = \frac{\dot{a}}{a}(t). \quad (1.2)$$

where $H(t)$ is the time depending Hubble's constant and $\dot{a}(t)$ is the time derivative of the scale factor. The deep meaning of this relation is that the space itself is expanding, dragging the galaxies inside its fabric and taking them away from us (and not that galaxies are moving away from us inside a static space). This shows that our Universe is not static and follows an evolutionary path, as also demonstrated theoretically by the works of Lemaître (1931). From this statement, two main questions have arisen during the last century, which are: *What is the history of our Universe?* And the second complementary and obvious question is: *How will it evolve in the future?*

The first question is answered by stating that since we see the galaxies moving away from us now, we can 'rewind the movie' and then observe the galaxies moving toward us as we go back to the past. This is possible thanks to the time reversibility of Einstein's equations. When we reverse the time in those equations, we see that galaxies are getting closer and closer to each other until all the matter is concentrated in a point, a dimensionless region of

space, corresponding to the event that we commonly call the Big Bang or the ‘origin’ of our Universe about 13.8 billion years ago. It is important to keep in mind that the question of the origins remains completely open, and the Big Bang¹ is a hypothesis, for which we have found a large number of pieces of evidence. However, our most recent physical theories remain unable to provide a detailed explanation of what happened before 10^{-42} seconds after the Big Bang, corresponding to the so-called ‘Planck wall’. To understand what happened beyond this limit, we would need a more advanced theory connecting General Relativity and quantum mechanics (i.e., a theory of everything). This would require a theory bridging the corpuscular and wave nature of particles, as we are already trying with speculative theories such as the string theory (see e.g., Schwarz, 1982) or the loop quantum gravity (see e.g., Ashtekar et al., 1991).

The most convincing piece of evidence for this scenario is the relic radiation which happened ~ 380000 years after the Big Bang, whose echo was first accidentally detected in 1965 by the radio astronomers Arno Penzias and Robert Wilson (Penzias & Wilson, 1965). The signal they detected is the so-called cosmic microwave background (CMB) and is illustrated in Fig.1.1. This figure shows the fossil radiation of our Universe, relating to an event corresponding to the time at which the matter density was low enough to let the photons escape and diffuse their first light everywhere in the young Universe. In this figure, we observe that the amplitude of the temperature inhomogeneities is very low ($< 200 \mu K$) leading to the fact that we can consider our Universe homogeneous and isotropic at large scales (> 100 Mpc). It is worth already mentioning that we use the observed fluctuations inferred from the CMB as the starting point for initial conditions in state-of-the-art cosmological simulations such as HORIZON, ILLUSTRIS-TNG, and EAGLE (see Ocvirk et al., 2008; Vogelsberger et al., 2014b; Schaye et al., 2015, respectively).

The second question is much more difficult to answer because it strongly depends on the composition of the Universe. In the lambda cold dark matter (Λ CDM) paradigm, we assume a Universe composed of baryonic matter, cold dark matter (DM), and dark energy. The DM is the non-baryonic matter, which does not directly interact with light and constitutes $\sim 25\%$ of the Universe in terms of mass (energy) density. The dark energy (or vacuum energy) given by Λ is the unknown energy opposing gravity, which is responsible for the expansion and constituting $\sim 70\%$ of the Universe. The rest is the baryonic matter and radiation composing everything we can observe around us through interactions with light and constituting only $\sim 5\%$ of our Universe. In other words, we still ignore the physical nature of 95% of our Universe. Usually, when we want to model the future evolution of our Universe, we use Einstein’s equations with the FLRW metric to derive the time evolution of the scale factor as a function of the values of the different density parameters Ω_M , Ω_R , and Ω_Λ stating for the matter (baryonic and DM), radiation, and vacuum energy. Figure 1.2 illustrates the evolution of the scale factor as a function of time (or redshift) for the different values of the density parameters. In this figure, we see that the curvature of the Universe is determined by its content. Our Universe can be

¹This ironic name was used for the first time by the British Physicist Fred Hoyle in the BBC show *Nature of Things*.

flat (curvature=0) and dominated by Matter and Vacuum (purple curve) or just matter (cyan curve). It can be open (curvature > 0 , blue curve) or closed (curvature < 0 , orange curve). We observe that a flat or open Universe will expand indefinitely, tearing it apart or making it cooler and cooler (Big Rip or Big Freeze), but a closed Universe will reach a maximum of its expansion before collapsing with a decreasing scale factor (Big Crunch). This last scenario has given rise to the theory of a bouncing Universe, oscillating between a Big Bang phase followed by an expansion and collapsing phase before restarting a new Big Bang and keeping this cycle indefinitely. We have currently no evidence for this bouncing Universe theory, and the most recent observations suggest that we live in a flat Universe, with $\Omega_{total} \equiv \Omega_M + \Omega_\Lambda = 1 \pm 0.02$.

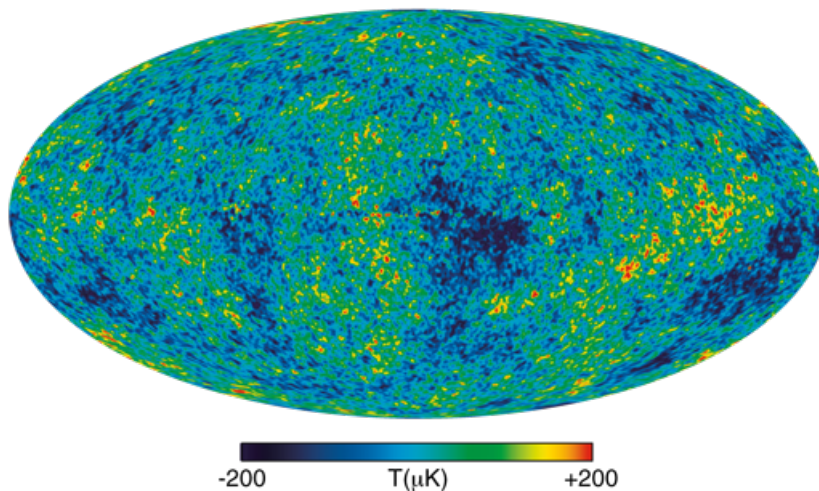


Figure 1.1: Wilkinson Microwave Anisotropy Probe heat map of the CMB with temperature fluctuations ranging from -300 to 300 micro-Kelvin. Credits: <https://wmap.gsfc.nasa.gov>

1.1.2 Galaxy assembly and evolution from high z

Astronomy aims to study, understand, and model the physical mechanisms involved in the formation and evolution of structures in our Universe. Those mechanisms include the gravitational structuring of large-scale structures (e.g., DM halos and filaments) and the following gas redistribution, star formation (SF) and its associated stellar feedback, galaxy interaction and mergers, formation and growth of supermassive black hole (SMBH)s and their impact on their host (e.g., active galactic nuclei (AGN)). The farther we observe, the more we see the structure of the primordial Universe, which is important to understand and model the evolution of galaxies until today. The furthest echo of the primordial Universe we have ever detected is the CMB. From this epoch, the matter has cooled down and condensed into cosmic webs, thus forming the very first DM halos while gas started to fall into them and form the very first stars, building the very first galaxies. The most

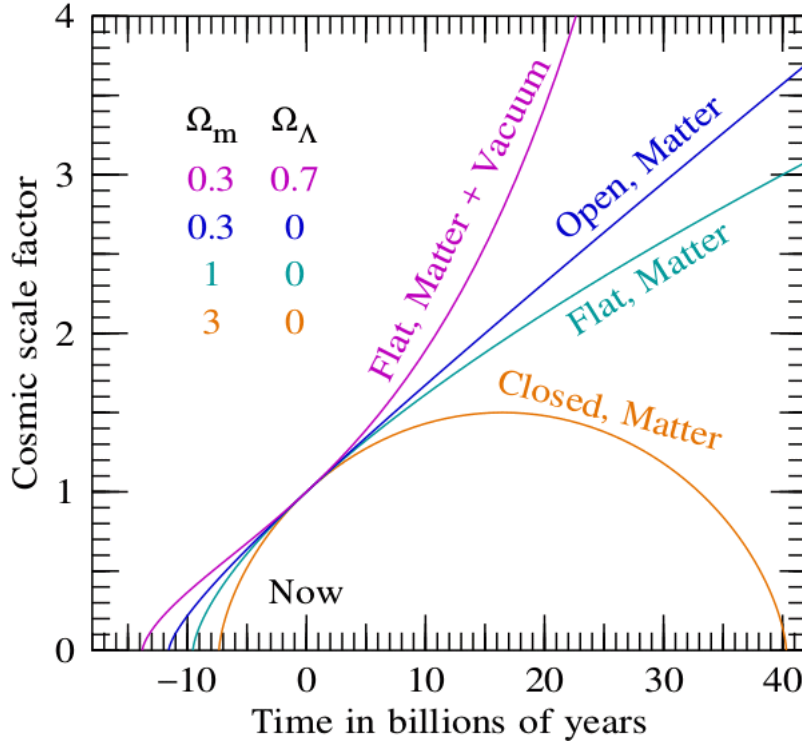


Figure 1.2: Evolution over time of the scale factor in the FLRW metric for different values of the density parameters Ω_M (matter) and Ω_Λ (dark energy). Credits: <https://jila.colorado.edu>

distant galaxy (JADES-GS-z14-0) we have detected with the James Webb Space Telescope (JWST) so far, is located 13.5 billion years away at redshift $z \approx 14$, corresponding to 300 million years after the Big Bang (Carniani et al., 2024). The epoch following the CMB is a time during which there were no stars to illuminate the Universe. This period is thus sometimes called the ‘Dark Age’ and our most recent models predict the formation of the very first stars (Population III) about a few hundred million years after the Big Bang (Weiss et al., 2000; Abel et al., 2002; O’Shea & Norman, 2007; Klessen, 2019). Since the Universe was completely dark, we cannot observe events or structures occurring between the CMB epoch ($z \approx 1100$) and the formation of the first galaxies. We can still use cosmological simulations to provide constraints on the structure of the Universe during this epoch (i.e., from the CMB to the formation of the first galaxies) and study the evolution of those structures and galaxies until $z = 0$.

We have already probed and constrained fundamental properties of the structures shaping our Universe by connecting the evolution of objects at high and low redshift. Observations and simulations of the population of nearby and distant galaxy clusters have allowed us to derive the evolution over redshift of the halo mass function (HMF) and galactic stellar mass function (SMF) (Fontana et al., 2006; Mortlock et al., 2015; Somerville et al., 2015; Lovell et al., 2021; Santini et al., 2022), as shown in Fig 1.3 and 1.4 from Weaver

et al. (2023). The SMF illustrates the stellar mass distribution of galaxies for a given redshift. Fig. 1.3 illustrates the evolution of the SMF across redshift for the COSMOS2020 sample (see Weaver et al., 2023). Those are well approximated by a Schechter function (Schechter, 1976) for the full sample (left panel) with the two slopes and the ‘knee’ around $10^{11} M_{\odot}$. We see that star-forming galaxies (middle panel) dominate the total distribution, especially at higher redshift, where the number of quiescent galaxies (right panel) tends to decrease. We note that the total distribution goes away from a pure Schechter profile when redshift increases. The evolution with redshift of the HMF is shown in Fig. 1.4. In this figure, we see the comparison between the SMF (coloured curves) and HMF (lower bound of the grey-shaded region, derived from Tinker et al. (2008)) across redshift, witnessing the potential connection between those two distributions. The evolution of the star formation rate (SFR) with redshift (i.e., star formation history (SFH)) is also a key factor in modelling the evolution of the SMF (Gruppioni et al., 2013; Lapi et al., 2017), as illustrated by the black curve in Fig. 1.5. In that figure, we observe a SFR density having a bell shape and peaking around $z = 2$.

Probing the behaviour and the connection between those three distributions and the ratio of HMF and SMF as a function of redshift is of paramount importance to better understand, constrain, and model the gas accretion and merging events that have built the galaxies of the nearby Universe we observe today.

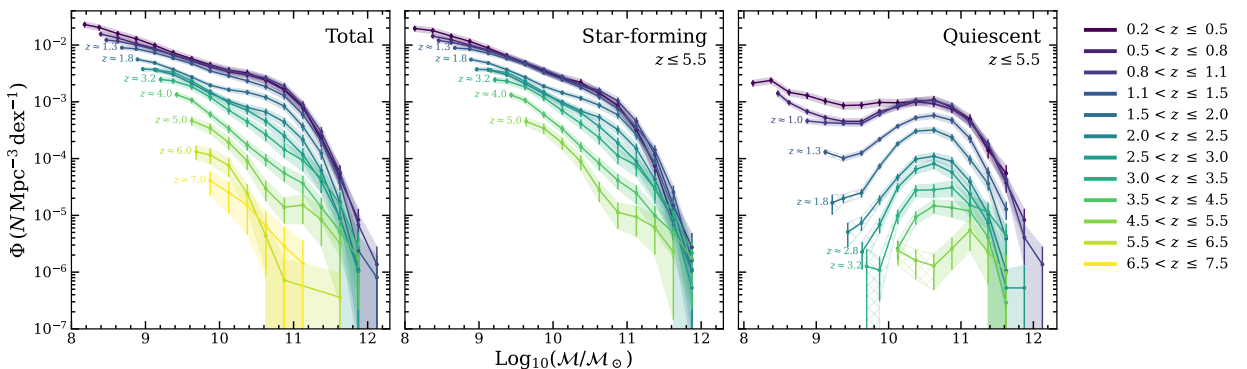


Figure 1.3: Evolution of the stellar mass function (SMF) as a function of redshift for the total (left panel), star-forming (middle panel), and quiescent (right panel) galaxies of the COSMOS2020 sample (from Weaver et al., 2023).

1.1.3 The role of the central supermassive black hole

One of the key factors that we believe influences the high mass end distribution of the SMF is the presence and role of SMBHs at the centre of galaxies. SMBHs are celestial objects that can play an important role in the formation and evolution of galaxies. Black Holes were first theoretically discovered as an implication of Einstein’s theory of General Relativity and SMBHs were further used in the modelling of active galaxies. black hole (BH)s do not directly emit light, but we can still detect them through their interaction

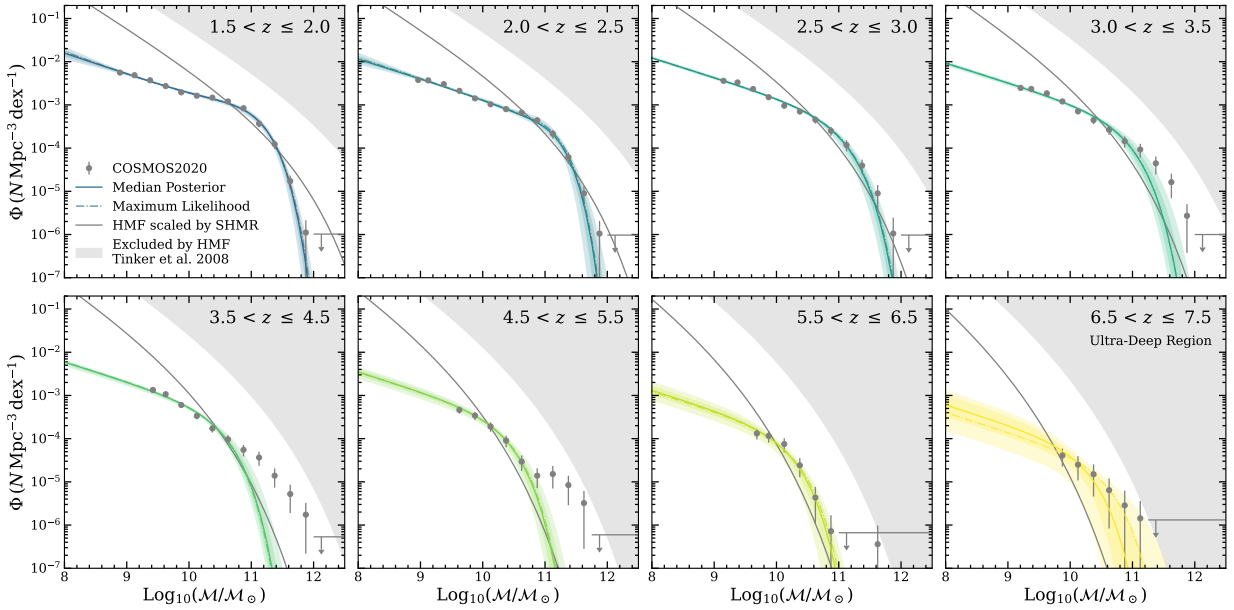


Figure 1.4: Evolution of the SMF (grey dots and coloured curves) and HMF (lower bound of the grey shaded area) as a function of redshift from $z = 1.5$ to $z = 7.5$. The coloured curves are the inferred SMF fitted to the data (grey dots). The different colours refer to the redshift of Fig.1.3. The grey curves are the HMF scaled by a factor 0.018, corresponding to the stellar-to-halo mass function at $z = 0$. The data are stemming from the COSMOS2020 sample (from [Weaver et al., 2023](#)).

with the baryonic matter. When material (e.g., cloud of gas, star) approaches close enough to the BH, it can get gravitationally captured and tidally disrupted, which may lead to the formation of an accretion disc of gas surrounding the BH. The physics of accretion discs is a complex topic, but dynamical friction and shear may help transport the gas very close to the event horizon and eventually, the material may fall inside the BH. As the material gets closer to the event horizon, it accelerates until it reaches a velocity close to the speed of light, leading to the emission of high-energy photons (e.g., X-rays, gamma rays) detectable by our telescopes. In the case of SMBHs observed at the centre of galaxies, the accretion of material can lead to central activity (i.e., AGN) (see [Krolik, 1999](#)). This picture was recently confirmed by the very first image of the SMBH at the centre of M87 taken with the Event Horizon Telescope (EHT) (see [Event Horizon Telescope Collaboration et al., 2019](#)). The complex structure of those objects (i.e., the orientation of the BH spin with respect to the accretion disc and torus of dust), coupled with their orientation to us, was considered as a key to explain the spectral classification of active galaxies we know today: quasars, radio-quiet and loud, liners, Seyfert 1 and 2 (see [Lawrence, 1987](#); [Krolik, 1999](#); [Kewley et al., 2006](#)).

The formation and evolution of SMBHs is not an easy problem to solve. There are several orders of magnitude between the mass of stellar BHs (a few to a few hundred M_{\odot}) and the mass of galactic SMBHs detected in the central region of galaxies ($\sim 10^5$

- $10^{10} M_{\odot}$, see [Reines & Volonteri, 2015](#)). We understand the basics of the mechanism leading to the formation of stellar-mass BHs during the core collapse and the explosion of a giant star into supernovae, and we have detected the presence of such BHs in X-ray binaries ([Tauris & van den Heuvel, 2006](#); [Dunn et al., 2010](#)). Concerning the SMBHs, we still lack a global picture of the exact mechanisms responsible for their formation and growth. Once the mass of the SMBH reaches a few $10^5 M_{\odot}$, theory and simulations have shown that super Eddington accretion events coupled with BH coalescence during galaxy mergers can allow a sufficient mass growth to explain the emergence of the most massive BHs we observe today. Theoretical works suggest the formation of an intermediate-mass seed ($\sim 10^2 - 10^4 M_{\odot}$) to sustain accretion events over several billion years, but we do not have a solid detection of such intermediate-mass BH so far (see the review of [Greene et al., 2020](#)). Those intermediate-mass BHs could, for example, have been formed from the runaway collisions of stars in nuclear star clusters ([Portegies Zwart et al., 2006](#); [Giersz et al., 2015](#); [Fujii et al., 2024](#)).

The evolution of the accretion rate of SMBHs (red curve) and SFH (black line) across redshift ([Madau & Dickinson, 2014](#)) is illustrated in [Fig. 1.5](#). In this figure, we see a similarity between those two profiles, suggesting that the accretion events experienced by SMBHs could be closely connected to SF of the host galaxy. We observe that the maximum of the SF (i.e., Cosmic Noon) occurs about redshift 2 and corresponds to the maximum of the SMBH mass growth. This highlights the importance of investigating the potential link between SF and the fuelling of central SMBHs. Another important aspect of SMBHs in galaxy evolution is the impact of the AGN on the galaxy gas content and thus, their role in recovering the shape of the high-mass end of the SMF as shown in [Bower et al. \(2012\)](#); [Puchwein & Springel \(2013\)](#).

1.2 Structure of disc galaxies at redshift zero

The story we have sketched until now, starting with the early stages of the Universe, the formation and the distribution of galaxies across redshift, and the potential role played by SMBHs, has designed the galaxies of our nearby Universe. When we observe the Universe around us, we see that most of those objects have a discy nature and a spiral structure (late-type galaxies) and show a higher SFR compared with elliptical galaxies (early-type, see [Bamford et al., 2009](#); [Calvi et al., 2018](#)). Our own Galaxy, the Milky Way (MW), is itself classified as a barred spiral one (SBb or SBc type in the Hubble sequence), located on the main sequence of star-forming galaxy (see [Fig. 1.7](#)), and is the only galaxy where we know that ‘life’ has emerged so far². Another feature of the MW is the presence of its central SMBH (Sagittarius A*), whose first image of the close environment was released in 2022. Sagittarius A* is a quiescent SMBH but some active periods might have occurred in the past or could happen in the future. Some characteristics of active disc galaxies indicate that all of them host a SMBH at their centre (see [Kormendy & Ho, 2013](#)). Understanding

²The concept of ‘life’ is tedious to define and is one of the hot topics in sciences. Here, I refer to intelligent life (like us) as we know it on Earth.

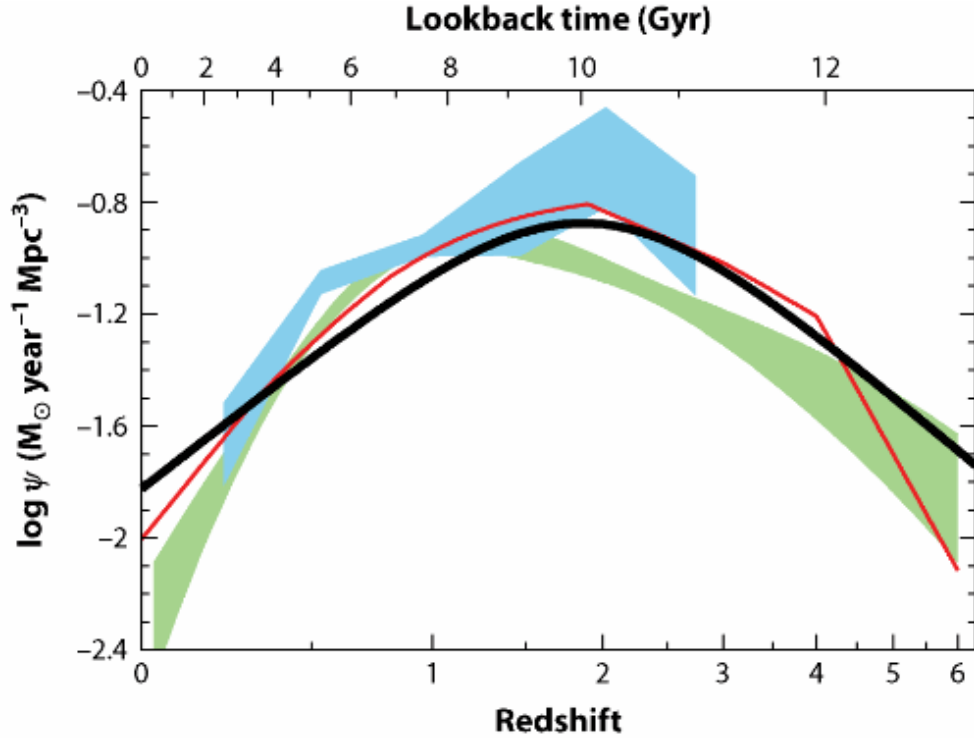


Figure 1.5: Evolution of the SFR density (black line) and massive BH accretion rate density (red line (Shankar et al., 2009), green shaded area (Aird et al., 2010), and blue shaded area (Delvecchio et al., 2014)) as a function of redshift (from Madau & Dickinson, 2014)

and characterising the connection between the large-scale structures (i.e., bar, spiral arms) of those galaxies and the AGN activity cycle is a hot topic in this field. In this section, I will describe the basic ingredients to design a disc galaxy and their properties, the different secular processes, and what we know about their central SMBH.

1.2.1 Main ingredients of disc galaxies

Observations of nearby galaxies revealed that some of them display features in their disc of stars (e.g., stellar bar, spiral arms) and their disc of gas (e.g., bar lanes, central gas structure inside the bar region). Nowadays, the current generation of ground-based instruments such as the radio telescope Atacama Large Millimeter/submillimeter Array (ALMA) and the optical Very Large Telescope (VLT) and its Multi Unit Spectroscopic Explorer (MUSE) spectrograph have recently allowed us to probe and trace specific components of the gas disc at high angular resolution. Space telescopes such as the Hubble Space Telescope (HST) and JWST are also of paramount importance since they allow us to probe star-forming regions of the disc by tracing the ionised gas and dust (e.g., via emission from polycyclic aromatic hydrocarbonate (PAH)s). The JWST has further revolutionised our view on the gas discs, showing their fine structure at the giant molecular cloud (GMC) scale ($\sim 10-100$

pc) and exhibiting the impact of complex phenomena (i.e., shear, stellar feedback, bubbles) occurring inside them.

Quantitative studies of the stellar and gas distributions suggest a picture where disc galaxies are basically composed of an exponential disc of stars inside which we find another thinner exponential disc of gas embedded in a large spherical DM halo. The disc of gas usually extends further than the stellar one with a radius going up to 50 kpc for the most massive galactic systems. It is commonly suggested that the halo is responsible for the flat, non-Keplerian behaviour of the rotation curve, even extending beyond the stellar disc with a radius going up to ten times the typical radius of the stellar component. Since the DM halo cannot be directly measured, we usually constrain the halo mass in such a way that the combination of its profile and the rest of the baryonic matter matches the observed total rotation curve. To this end, we can use various profiles such as the Einasto (Einasto, 1965), Burkert (Burkert, 1995), Navarro-Frenk-White (NFW) (Navarro et al., 1997), generalised Di Cintio profile (Di Cintio et al., 2014), coreNFW (Read et al., 2016), or Dekel-Zhao (Freundlich et al., 2020). The choice of these profiles has been motivated by results from cosmological pure DM simulations and sometimes from tensions with observed galaxies and galaxy clusters.

Those three components (i.e., the stellar, gas disc, and DM halo) participate in structuring the global gravitational potential, ruling the dynamical evolution of the stars and gas. In the case of an undisturbed and idealised two-dimensional stellar disc, the stars can all be simply assumed to be on circular orbits with an angular frequency Ω that depends on the galactic radius. In real galaxies, stars on three-dimensional orbits. Those orbits are often described via a linear approximation introducing a radial (κ), azimuthal (ν_ϕ), and vertical (ν_z) oscillation frequency describing the deviation from the idealised circular orbits (i.e., the epicycle approximation).

1.2.2 A few words about three current observation surveys

The understanding of the complex structure and formation of those disc galaxies is a current challenge that many observational campaigns are still trying to tackle. Among all the current surveys, the Mapping Nearby Galaxies at APO (MaNGA) with its impressive sample of about 10,000 galaxies, offers an exceptional opportunity to probe their SF and merger history (see Bundy et al., 2015; Stark et al., 2018; Fraser-McKelvie et al., 2020). The recent Generalising Edge-on galaxies and their Chemical bimodalities and Kinematics and Outflows out to Solar environments (GECKOS) survey, with its 35 edge-on disc galaxies, reveals their complex vertical structure and tries to better constrain the phenomena involved in the building of their central bulge (see van de Sande et al., 2024). Among all those surveys, the multi-wavelength Physics at High Angular resolution in Nearby Galaxies (PHANGS) survey that involves the use of various facilities (HST, ALMA, MUSE, JWST) is particularly relevant to studying and understanding the connection between the large-scale structures of the stellar disc such as the bar and spiral arms and the smaller gas structures we observe inside the bar region (i.e., bar lanes and inner molecular disc). The PHANGS sample aims at observing low-inclination star-forming disc galaxies with a

high angular resolution to highlight and understand their complex baryon cycle (see e.g., [Turner et al., 2021](#); [Leroy et al., 2021](#); [Emsellem et al., 2022](#); [Sandstrom et al., 2023](#)). In the rest of this chapter, we will use the PHANGS sample to illustrate the properties of nearby galaxies.



Figure 1.6: Image of the barred spiral galaxy NGC1300 taken with the HST. We see the prominent stellar bar structure and the two ‘grand design’ spiral arms.

1.2.3 Characteristics of the bar and spiral arms

Bars and spiral arms are the two main large-scale structures we can observe in the stellar disc of galaxies (see [Eskridge et al., 2000](#); [Nair & Abraham, 2010](#); [Kruk et al., 2017](#)), as illustrated with NGC1300 in Fig. 1.6. In this figure, we see a central stellar bar and two spiral arms attached to the bar ends. One arm is going upward while the other one is going downward. This type of object with a prominent stellar bar and spiral arms is called a ‘grand design’ galaxy.

Galaxy bars

Bars are non-axisymmetric structures built around a specific set of elongated orbits (i.e., the family of x1 orbits, see [Athanasoula, 1992a](#)). This family of x1 orbits can be mathematically described by solving the motion equations in an analytical rotating potential (see e.g., [Binney et al., 2009](#)). Stellar bars have three properties that we commonly use to

characterise them. Those properties are their rotation pattern Ω_p , strength, and scaling radius (or extend).

The rotation pattern, also called ‘pattern speed’ is a bar property that can be interesting to measure because it provides a reference time scale for the secular evolution time of a galactic system. Measuring the pattern speed of a stellar bar is not straightforward because those objects are dynamic structures evolving on long timescales (~ 100 Myr) that cannot be captured by observations. The community has developed many methods over the past decades to try to measure the bar pattern speed. One of them was proposed by [Tremaine & Weinberg \(1984\)](#), who theoretically derived a pattern speed based on the continuity equation of the stellar component. They tested their method on simulated barred disc galaxies and found coherent results. In the nearby Universe, we have measured bar pattern speeds ranging from 10 to 40 with a median value around 25 km/s/kpc ([Guo et al., 2019](#); [Garma-Oehmichen et al., 2022](#), from MaNGA data). Barred galactic systems thus involve an angular frequency Ω_p associated with the bar. It adds on the natural frequencies of the system, which include Ω the circular frequency (associated with circular orbits in a disc) and the epicycle frequencies κ and ν (radial and vertical frequencies, resp.) that describe linear deviations from the circular orbits. Disc galaxies can therefore exhibit frequencies that can interact with each other, opening the possibility of orbital resonances. One of those resonances occurs when $\Omega_p = \Omega$ and defines the co-rotation radius of the bar. Another resonance may also happen when the bar angular frequency interacts with the epicycle frequencies and leads to the emergence of e.g., the so-called inner Lindblad resonance (ILR) and outer Lindblad resonance (OLR) (i.e., $\Omega_p = \Omega \pm \kappa/2$). The pattern speed is therefore a key factor in defining orbital resonances in the stellar disc such as the Lindblad Resonances and the co-rotation radius. Those resonances have been suggested to be closely connected with the formation of dynamical gas structures such as the central molecular gas and stellar disc ([Athanasoula, 1992b](#)).

The amplitude of the perturbation associated with the presence of a bar is often named the ‘strength’ of the bar. This has been estimated in various ways, including the method computing the maximum of the second-order A_2 Fourier coefficient ([Efstathiou et al., 1982a](#); [Athanasoula, 2002, 2003](#)). This coefficient indicates the amplitude of the second moment $m = 2$ of the Fourier decomposition of the stellar disc. The value of its amplitude shows the degree of asymmetry of the disc as a function of the galactic radius. In the nearby Universe, the typical values of A_2 are between 0.3 and 0.8 as reported by [Stuber et al. \(2023\)](#) for the PHANGS sample.

The last parameter used to characterise a stellar bar is its typical semi-major axis length (or bar radius). It is not simple to determine the radius of a bar as bars do not have a clear edge. Bars contain stellar populations with various edges, SF sights and dust making the size measurements very dependent on wavelength and on the method used. Among the techniques to measure one consists of using the A_2 profile and taking the radius at which A_2 reaches a fraction (e.g., 100 to 70 %) of its maximum value (see [Ghosh & Di Matteo, 2024](#)). A second method uses ellipses to fit the iso-density contours of the stellar surface brightness ([Michel-Dansac & Wozniak, 2006](#)) and use the variation of position angle to detect the edge of the bar. The value of the bar radius in nearby disc galaxies is typically

between 2 and 5 kpc, with larger bars observed in massive disc galaxies (i.e., ≥ 10 kpc, see [Marinova & Jogee, 2007](#); [Aguerri et al., 2009](#)).

Spiral structures

As already mentioned above, large-scale spiral arms are another main non-axisymmetric dynamic structure in disc galaxies and they usually extend much farther than the stellar bar. Spiral arms are dense regions with sometimes a high rate of SF and are thus believed to be connected to the large 10 kpc scale molecular gas redistribution in the disc ([Colombo et al., 2022](#)). Spiral arms are characterised in various ways, including their type (e.g., grand design, flocculent), pitch angle, rotation pattern, and spatial extent (see the review of [Dobbs & Baba, 2014](#), and references therein).

The physical origin and nature of spiral arms is still a debated topic. Those structures are generally considered as density waves emerging from disc instabilities and built around a special arrangement of stellar orbits as demonstrated by the pioneering work of [Toomre \(1964\)](#); [Lin & Shu \(1964\)](#). Nowadays this picture has changed and all spiral structures in the stellar disc cannot be always associated with density waves (e.g., flocculent-type arms like in M51 as shown by [Meidt et al., 2013](#)).

Simulations have shown that spiral arms evolve on shorter time scales than the stellar bar and can experience multiple phases in their growth via, for instance, swing amplification and damping phenomena ([Toomre, 1981](#); [Sellwood, 2000](#); [Baba, 2015](#)). Due to their shorter lifetime, it is not a straightforward task to measure their pattern speed, but some methods exist (see e.g., [Pfenniger et al., 2023](#)).

1.2.4 Secular processes and their impact on the disc

Stellar bars and spiral arms are the main drivers of the secular processes happening inside the disc. An intriguing characteristic about SF in our Universe is that most stars form in discs, at nearly all redshift. Nearby disc galaxies actively form stars and constitute the so-called star-forming main sequence (see [Leroy et al., 2019](#)), as shown in Fig. 1.7. Among those disc galaxies, the ones displaying a stellar bar have a higher SF rate at a fixed stellar mass ([Carles et al., 2016](#)). It is commonly accepted that bars enhance the formation of new stars in the central regions because they fuel gas efficiently to the centre where gas accumulates and is efficiently converted into stars. This central gas concentration due to the bar tends to increase the SFR.

Spiral arms also have an important role to play in forming new stars because of their high-density gas regions. The SF regions inside the disc affect the structure of the interstellar medium (ISM) because they form massive stars ($> 8 M_{\odot}$) that will explode into type II Supernovae (SNe), releasing a large amount of energy and momentum into the ISM. Other sources of stellar feedback can release energy such as stellar winds and SNe of types Ia and Ib which increase turbulence in the ISM. Depending on the physical conditions of the medium in which new stars form (ie., density, temperature, and pressure), their feedback can induce the propagation of shock waves and the formation of bubbles ([Dale et al., 2012](#);

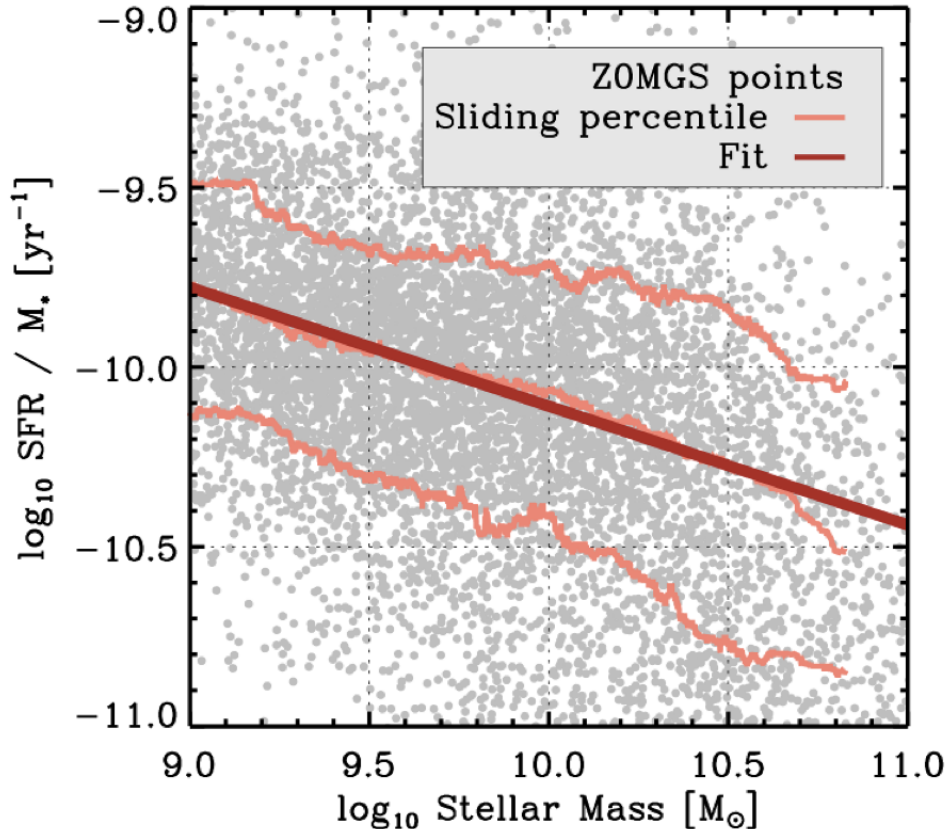


Figure 1.7: specific star formation rate as a function of the stellar mass for the GALEX+WISE sample. The dark red curve is a fit of the data and represents the galaxy’s main sequence at $z=0$ (from [Leroy et al., 2019](#))

[Raskutti et al., 2016](#); [Barnes et al., 2022](#)). In some cases, stellar feedback can even trigger the gravitational collapse of GMCs, leading to the emergence of new star-forming regions, thus restarting a new cycle.

1.3 The central structures of disc galaxies and their connection with the central black hole

In this section, we describe in more detail the disc-like structure of gas we observe in the central inner bar region of disc galaxies and the peculiar case of the inner gas ring of the Milky Way (central molecular zone (CMZ)). We present their physical characteristics and their associated physical process of gas consumption. We also connect this gas ring with the inner stellar disc and its underlying orbital structure and mention some results from the most recent studies leading to various formation scenarios. We also highlight the non-trivial link between those two structures and the sub-parsec fuelling of the central SMBH.

We finish this section by showing the challenges we have to tackle to understand the role of the inner gas ring as a ‘gas reservoir’ in fuelling the central BH and triggering the AGN activity.

1.3.1 A non-trivial connection

One challenge we need to tackle if we want to understand the physics involved in the fuelling of central SMBHs and triggering the AGN, is to connect the transport of gas from the large 10 kpc scale of the galactic disc down to the event horizon (i.e., Schwarzschild radius) of the central BH itself with a typical size of about $10^{-6} - 10^{-7}$ pc. This huge range of spatial scales (10 orders of magnitude) implies that the physics and the typical time scales of the different processes responsible for the loss of the gas angular momentum can vary widely (Hopkins & Quataert, 2010; Cheung et al., 2015). At the large 10 kpc scale, gas experiences dynamical processes such as gravitational torques due to the bar and spiral arms, shear, stellar feedback, transporting gas inside the bar region (Fukuda et al., 1998; Shlosman et al., 1989; Ho et al., 1997). Once gas crosses the bar region, it may accumulate in a central ring (or disc) at a typical distance of a few 100 pc from the centre. This gas ring located at an intermediate scale seems to be a crucial step before the sub-parsec-scale transport of gas to the vicinity of the central BH. The exact physical phenomena involved in the gas transport from the ~ 100 pc scale gas ring to the sub-parsec scales are still not fully understood. Recent studies have shown the role of stellar feedback and magnetic field in removing angular momentum from the gas at those scales (Shlosman et al., 1990; Emsellem et al., 2015; Anglés-Alcázar et al., 2021), but we still lack a comprehensive view of the interconnection between inner rings and the central SMBH activity.

1.3.2 The inner molecular gas ring (central molecular zone)

The inner molecular ring is a high-density gas structure we observe in the central region of a large number of barred disc galaxies. Those gas structures have a typical radius of a few hundred parsecs to one kiloparsec (Comerón et al., 2010), as shown in Fig. 1.8, illustrating a JWST picture of the ring in NGC1300. In the Milky Way, the inner molecular ring is called the CMZ and has a radius of about 200 pc with a gas mass of $\sim 1 - 7 \times 10^7 M_{\odot}$ (Ferrière et al., 2007; Longmore et al., 2013; Henshaw et al., 2023). Both observations and simulations have shown that a connection exists between the gas fuelling at large-kiloparsec-scale by the stellar bar and those central hundred-parsec-scale gas structures (Combes et al., 2004; García-Burillo et al., 2005; Boone et al., 2007; Comerón et al., 2010; Sormani & Barnes, 2019).

Those gas rings exhibit active SF associated with intense stellar feedback. Past and recent hydro-dynamical simulations have suggested that the building of those central rings is triggered by the emergence of an ILR (Athanasoula, 1992b; Sormani et al., 2023a) with a growth following an inside-out scenario. This seems to be confirmed by observations of the stellar age gradient inside those rings. In this scenario, the bar forms and starts to funnel gas towards the central region, increasing the gas density at the centre and triggering a

central starburst, with a high SF rate. Once the stellar density has increased enough in the centre, the galaxy forms an ILR able to capture gas efficiently. The ring is then able to grow thanks to the fuelling by the bar and reach the typical size of a few hundred parsecs corresponding to the typical size we observe for those objects.

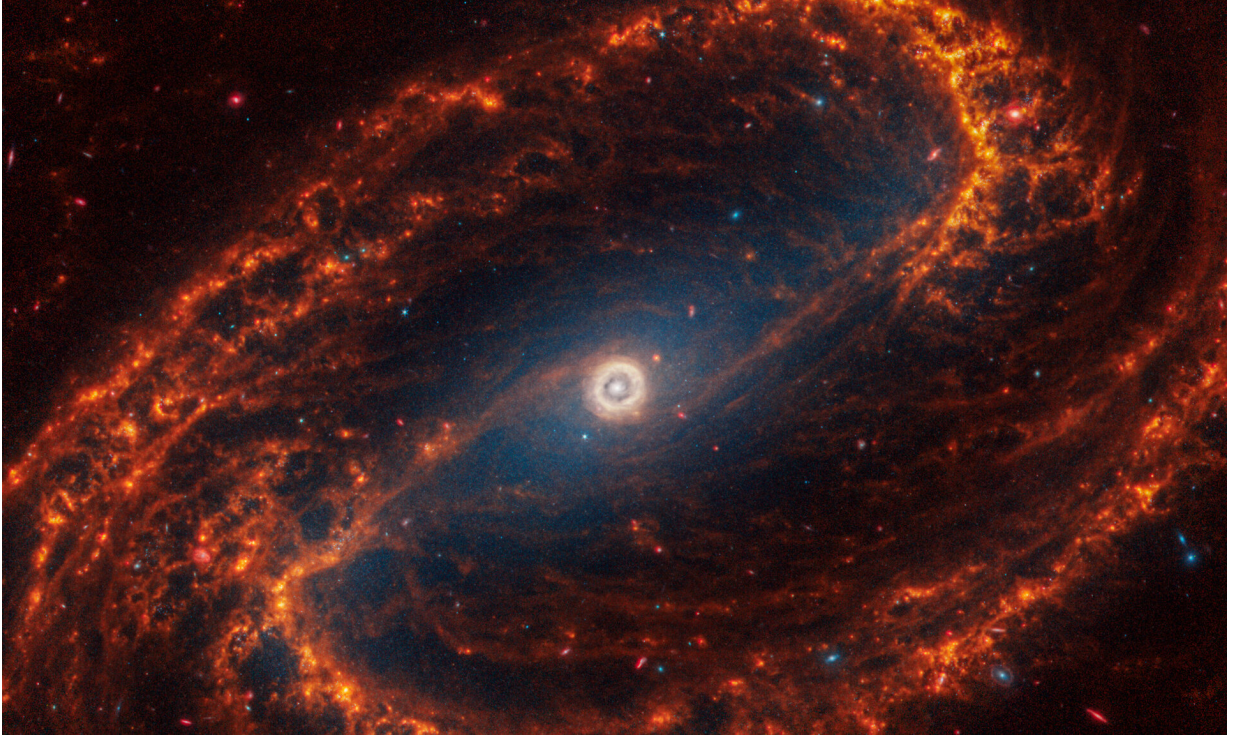


Figure 1.8: JWST image of NGC1300. We see the same spiral structure as in Fig. 1.6 but here, the central region is highlighted and shows the central gas disc/ring.

1.3.3 The inner stellar disc

The inner stellar disc is a central stellar structure with a typical radius of a few hundred parsecs and coincides with the inner gas ring. As mentioned above, this structure is thought to be formed while the gas ring grows and is often considered as its underlying stellar counterpart (Bittner et al., 2020). In the Milky Way, the inner stellar disc is called the ‘nuclear stellar disc’ and has the same radius as the molecular ring. Studies of its stellar kinematics have shown that it is dynamically cool with a vertical thickness of about 50 pc. The backbone structure of those stellar discs is explained by the stellar dynamics in a barred potential thanks to the family of x2 orbits which are less elongated than the orbits of the bar (x1) and oriented almost perpendicular to them (Athanasoula, 1992a). The peculiar configuration of the x2 orbits shapes the structure of the gas ring and explains their disc-like structure. Inner stellar discs are important because they can inform us about the history of the gas ring growth and give us some indications on the typical age of the

stellar bar as shown, for example, by the Time Inference with MUSE in Extragalactic Rings (TIMER) survey (Gadotti et al., 2019; de Sá-Freitas et al., 2023).

1.3.4 The molecular ring as a ‘gas reservoir’ for the central supermassive black hole

Observations of the centre of nearby disc galaxies have revealed the presence of central SMBHs through their activity. The typical masses of SMBHs we observe at the centre of nearby disc galaxies have a mass range between a few 10^5 and a few $10^8 M_{\odot}$. Their mass is correlated with the total mass of the galaxy, but also with the mass of the central bulge as shown in Fig. 1.9 from Reines & Volonteri (2015). The mass of the SMBH at the centre of the Milky Way is about $4.3 \times 10^6 M_{\odot}$ and is not presently active. To fuel and trigger the activity of the central SMBH, only a small fraction of gas contained inside the inner ring needs to be transported even further to the sub-parsec scale, down to the vicinity of the central BH. To better understand it, one challenge is the typical time and spatial scale we need to take into account to transport the gas from the gas ring (~ 100 pc) down to the AGN (i.e., dust torus and accretion disc). In this picture, gas rings can be seen as ‘gas reservoirs’ for the central SMBH and we will use this term to refer to the gas ring in the rest of this work.

1.4 Open questions

The different stellar structures such as the bar and spiral arms we introduce above should play an important role in funnelling gas from the large 10 kpc scale to the central 100 pc region. Many studies have already investigated the effect of a barred potential on the flow characteristics and the transport of gas to the inner bar region. We know that gas loses a large part of its angular momentum by interacting with the stellar bar via gravitational torques, inducing hydrodynamic shocks. However, we still lack a clear understanding and a quantitative description of the exact physical processes experienced by gas while it interacts with the bar. The first question that motivated this work is then: **What are the characteristics of the fuelling of gas by the bar?**

In the previous section, we have described the stellar and gas structures we observe inside the bar region, at an intermediate scale of ~ 100 pc. We have shown the presence of an inner gas ring and stellar disc in barred galactic systems, but we still ignore the physical processes involved in their formation (i.e., the fuelling and connection with the bar) and evolution (i.e., building, growing rate, and consumption via SF). Moreover, we do not know whether a gas reservoir forms in every barred galactic system and we still need to investigate the conditions for the formation of such inner gas structures with more depth. The second question coming with the formation and evolution of the gas reservoir is thus: **What are the characteristics of the building of the gas reservoir by the bar and its consumption by star formation?**

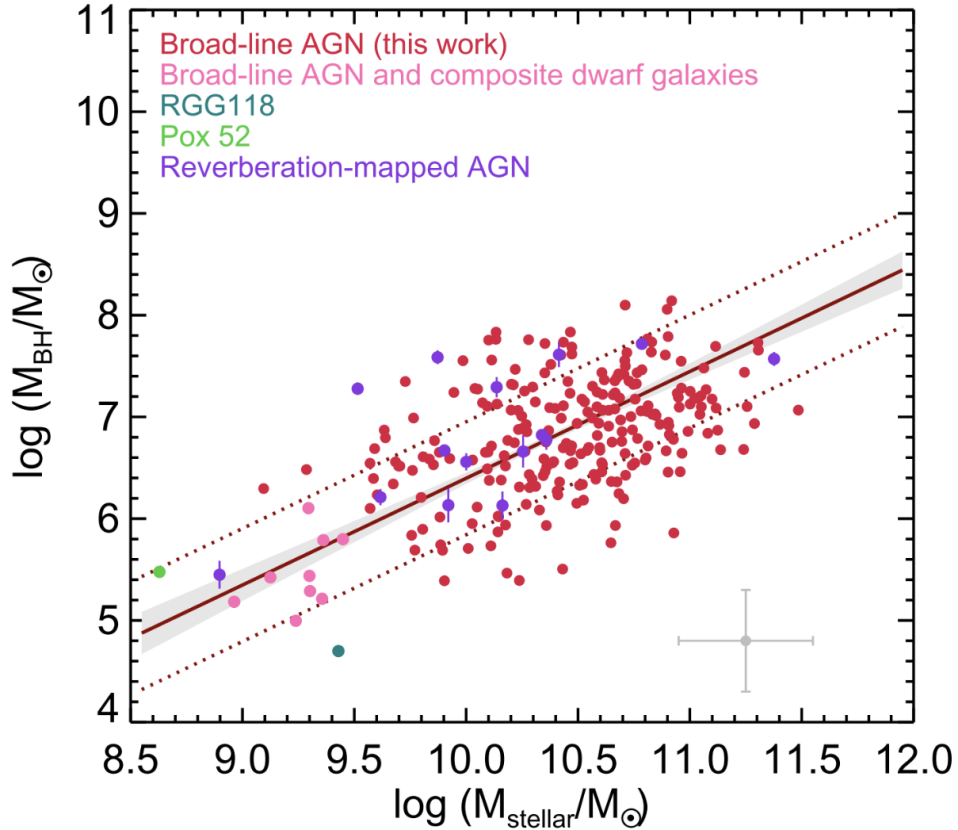


Figure 1.9: The black-hole to total-stellar mass relation for local AGNs (see [Reines & Volonteri, 2015](#), for more details)

Once we have those two first questions in mind with the gas ring seen as a gas reservoir for the central BH, we naturally think about the potential connection that exists between the formation and evolution of those gas reservoirs and the duty cycle of the central AGN. The third and last question, which is one of the hot topics in this field, is then: **What is the connection between the gas reservoir and the activity of the central black hole?** We have seen in the previous section that this connection is not trivial because of the orders of magnitude in spatial and time scales between the gas reservoir (~ 100 pc) and the AGN ($< \text{sub-pc}$).

1.4.1 Motivations and plan of this work

The goal of this work is to try to answer the first two questions and take a step forward toward a better understanding of the fuelling and duty cycle of the central SMBH in nearby disc galaxies. As mentioned, we have accumulated a large body of observational evidence illustrating the richness of structures in barred galaxies. While those addressed well-resolved samples of 10's (PHANGS) or 1000's (MaNGA) of galaxies, they provide a rather static

picture of the evolution of discs. To further investigate this problem. To further investigate and try to answer these two first questions, we have performed hydro-dynamical N-body simulations of isolated galaxies based on a grid of galactic models inspired by the PHANGS-ALMA sample. We give a detailed description of the RAMSES code, as well as various numerical techniques in Chap. 2. In Chap. 3 we describe the grid of models, the PHANGS-ALMA sample, and the numerical recipes we used in this work. In Chap. 4, 5, and Chap. 6 we show the work carried out during this thesis to answer the two first questions. We conclude and give some perspective offered by this work in Chap. 7.

Chapter 2

Numerical techniques and description of RAMSES

This chapter aims to introduce the concept of astrophysical codes we use to model the mechanisms involved in the formation (e.g., assembling of the first DM halos and galaxies) and evolution (e.g., expansion, interaction between galaxies) of our observable Universe. Those codes are of paramount importance to improve our understanding of the evolution of our Universe and the formation of nearby galaxies we observe today. The work of this thesis specifically focuses on the physical processes responsible for the fuelling and formation of central gas structures in isolated disc galaxies. Therefore, we particularly focus this chapter on the description of the equations we use to model isolated galactic systems, evolving away from any cosmological context, in a non-expanding (static) Universe. We first present the set of fundamental equations the most simple hydro-N-body code has to account for, and we review the main astrophysical codes using different numerical techniques to solve (or approximate the solution of) those equations. Then, we look in more detail at the modelling of isolated nearby disc galaxies and justify the decision to use RAMSES to simulate them. Then, we further describe the RAMSES code itself with a brief explanation of the different numerical methods used to solve the set of fundamental equations. We conclude this chapter by demonstrating the relevance of RAMSES to modelling such galactic systems with a brief review of the works already carried out using this code in the frame of isolated galactic systems.

2.1 Fundamental equations, methods, and overview of the different astrophysical codes

Having a comprehensive model of the Universe has always been one of the biggest challenges in numerical Astrophysics because we need to include a large variety of physical phenomena occurring and acting on different time and spatial scales. Indeed, we need to properly include the expansion, the interaction of the matter (i.e., DM, stars, and gas) through gravity, and the physics we know about baryons (e.g., radiation and its interaction with dust, magnetic field, plasmas). The complexity of our Universe is reflected by the variety and interconnected nature of the processes (e.g., gravity, star formation, stellar feedback) and the large range of involved spatial and time scales. Moreover, since we can not reach a spatial and time resolution arbitrarily small, we need to complement our set of fundamental equations with some sub-grid recipes or post-processing techniques to take into account all the physics which is not directly included in the equations.

Whether it is to perform cosmological or isolated galaxy simulations, the first aspect we want a code to include is a set of equations modelling the motion of astrophysical systems and objects. Real galaxies are made of DM and stars interacting with each other through gravity. An accurate modelling of the evolution of such systems often requires describing them with a large number of particles. For each of those particles, the first set of equations

a code has to solve is the motion and the Poisson equations given by:

$$\frac{d\vec{r}}{dt} = \vec{v}, \quad (2.1a)$$

$$\frac{d\vec{v}}{dt} = \vec{F}_g = -\vec{\nabla}\Phi, \quad (2.1b)$$

$$\vec{\nabla}^2\Phi = 4\pi G\rho, \quad (2.1c)$$

where \vec{r} , \vec{v} are the position and velocity vectors of each particle. Equations 2.1a and 2.1b are the so-called equations of motion and need to be solved for each particle. The gravitational potential Φ is given by Eq. 2.1c, the so-called Poisson's equation where G is the gravitational constant and ρ is the density distribution of the particles. This potential needs to be computed to be injected in Eq. 2.1b and give rise to the gravitational force \vec{F}_g . The above set of Eq. 2.1 describes the motion of each particle such as the DM and stars, for example.

For the gas component, we need to use statistical tools given by macroscopic variables to jointly address the thermodynamics and motion, which are generally treated via a full set of hydrodynamic equations whose conservative forms are given by:

$$\partial_t\rho + \vec{\nabla}\cdot(\rho\vec{v}) = 0, \quad (2.2a)$$

$$\partial_t(\rho\vec{v}) + \vec{\nabla}\cdot(\rho\vec{v} \otimes \vec{v}) = -\vec{\nabla}P - \rho\vec{\nabla}\Phi, \quad (2.2b)$$

$$\partial_t(\rho E) + \vec{\nabla}\cdot(\rho E\vec{v}) = -\vec{\nabla}\cdot(P\vec{v}) - \rho\vec{v}\cdot\vec{\nabla}\Phi, \quad (2.2c)$$

$$P = P(\rho, T), \quad (2.2d)$$

where ρ , \vec{v} , P and E are the gas density, velocity field, pressure, and energy density, respectively. Equation. 2.2a is the so-called continuity equation, Eq. 2.1b is the impulsion conservation equation (i.e., the Euler equation for non-viscous fluids), and Eq. 2.2c is the energy conservation equation. The set of equations 2.2 is called Euler's equations and must be complemented by an equation of state (EOS) (Eq. 2.2d) linking the pressure to the gas temperature T and density. We note here that the above set of equations is in general incomplete to describe accurately the behaviour of gas since astrophysical environments are more complex and other processes may be important to include (such as magnetic fields). In that case, the set of Eq. 2.2 needs to be modified by adding the magnetic field \vec{B} resulting in a set of magneto-hydro-dynamics (MHD) equations. In the rest of the thesis, we will assume that magnetic fields do not significantly affect the gas fuelling and will therefore ignore them.

In the following, we will briefly cover various methods and numerical implementations used to solve the gravitational interaction between the particles given by the set of Eq. 2.1 and the above set of hydro-dynamical equations (Eqs 2.2). We distinguish two main classes of methods to solve Eq. 2.1: 1) computing directly the force (gravitational potential) between the particles, 2) defining a grid and distributing the mass of the particles over this grid to generate the mass density distribution and then, solving the Poisson's equation on that grid. Methods of the first class are for example the direct N-body, Tree code,

or the fast multipole method (FMM) and the methods belonging to the second class are the particle mesh (PM) and adaptive mesh refinement (AMR) methods. We also classify the methods to solve Eq. 2.2 into two categories: 1) solving the hydro-dynamical equation using a spatial and time discretisation (grid), 2) mimicking the properties of gas using kernel functions. We classify the methods of the first class as grid-based (e.g., AMR) or moving mesh and the method of the second class as smooth particle hydrodynamics (SPH).

2.1.1 Direct N-body solver, Tree code and FMM

In the case of a direct N-body solver, we need to directly compute the gravitational potential between each particle. The total gravitational force, as defined in the Newton theory, acting on a particle i having a mass m_i and a position vector \vec{r}_i for a system of N particles is given by:

$$\vec{F}_{g,i} = \sum_{j=1}^N G \frac{m_i m_j}{|\vec{r}_i - \vec{r}_j|^3} (\vec{r}_i - \vec{r}_j), \quad (2.3a)$$

$$\Rightarrow \Phi_i = \sum_{j=1}^N -G \frac{m_i m_j}{|\vec{r}_i - \vec{r}_j|} \quad (2.3b)$$

We see that computing the gravitational potential for each particle increases the number of operations to something proportional to N^2 , which has thus a high computational cost for a large number of particles. Such a type of algorithm for a large number of particles (i.e., > 1 million) is not really tractable on one single central processing unit (CPU) and requires efficient parallel programming, usually achieved using the message passing interface (MPI) or OpenMP library. The other method is to use graphical processing unit (GPU) instead. The reference code in the field is the well-known NBODY6 code (see [Aarseth, 1999](#)) which was first designed to run on CPUs, and has been optimized over the past decades to be now able to run on GPUs.

People elaborated various ways to address this computing cost problem but one of the early ideas of solving Eq. 2.1 by directly computing the gravitational potential in Eq. 2.3b with a different method than the direct N-body solver was first proposed by [Barnes & Hut \(1986a\)](#); [Bouchet & Hernquist \(1988\)](#) with a Tree code method. There are other methods than the Tree code to bypass the direct N-body solver, such as the particle mesh method that we develop further in the next subsection. The idea of Tree codes is to divide the domain into chunks with different sizes forming a hierarchical octree structure in which the particles are distributed. To compute the force on each individual particle, we need to compute the centre of mass of each group of cells and, according to a distance criterion (depending on an opening angle), calculate the corresponding gravitational force as if it were generated by the centre of mass of the cell. This transforms the number of iterations from something proportional to N^2 to something proportional to $N \log(N)$, which is more convenient and tractable on CPUs.

A different algorithm based on an improvement of the Tree code by using a multipole expansion of the gravitational potential and called FMM (see [Dehnen, 2000](#)) is able to

scale the number of iterations to something proportional to N , which is the best we can obtain for such N -body problem.

2.1.2 Particle mesh method

The PM method was first introduced and developed by [Hockney & Eastwood \(1988\)](#). The idea is to generate a uniform grid covering the entire domain and distribute the mass of each particle on the mesh of the grid following some criteria. With this method, the particle is no longer considered as a physical object having a well-defined position, but rather as a diffuse massive cloud spread over a part of the cell. The most popular technique for mass deposition is the so-called cloud-in-cell (CIC) method, consisting of distributing the mass of the particle to the neighbouring cells to ensure a smooth and continuous mass distribution. The 1D shape function S in the case of a mesh spacing Δx for the CIC method is given by:

$$S(x) = \frac{1}{\Delta x} \Pi\left(\frac{x}{\Delta x}\right), \quad (2.4)$$

where the function Π is the selection function of the CIC method corresponding to a gate function. The resulting mass distribution of particle i is written as follows:

$$\rho_i = \frac{1}{\Delta x^3} \sum_p m_p \int_{V_i} S(\vec{x}_p - \vec{x}_i) d^3\vec{x}. \quad (2.5)$$

Equation. 2.5 is valid for any function 2.4: we can easily use other selection functions such as the delta function or some with more complex shapes (e.g., triangular). The complexity of the shape may increase the smoothness of the mass distribution, but also the numerical cost. The CIC method is a good compromise between those two aspects, assuring a fast computation for a smooth mass distribution.

The potential is computed thanks to Poisson equation 2.1c by solving the linear problem $A\Phi = B$, where A is the matrix representing the Laplacian operator ∇^2 , Φ the potential we want to compute on the grid, and B , the matrix representing the density distribution. It is easy to show that in a 2D grid with a mesh size $\Delta x = \Delta y = 1$, the component $\phi_{i,j}$ of the potential generated by a density ρ (assuming the constant $4\pi G = 1$) is given by:

$$\phi_{i,j} = \frac{1}{4} (\phi_{i+1,j} + \phi_{i-1,j} + \phi_{i,j+1} + \phi_{i,j-1}) - \frac{1}{4} \rho_{i,j}, \quad (2.6)$$

and with appropriate boundary conditions, it is then trivial to compute all the components of the potential on the grid. The main issue with this technique is that we need a large number of cells to have a good estimation of the gravitational potential and the force-softening effect becomes important when the cell size becomes smaller and smaller. This results in a propagating error, making the above scheme unstable. Therefore, the PM method is not well suited to high resolutions and the number of iterations is scaled as $N \log(N)$.

2.1.3 Adaptive mesh refinement method

The AMR method uses the same principle as the PM technique but with a set of multi-grids having different mesh sizes. The AMR method allows to reach high resolutions without softening the force too much and propagating a too-big numerical error. One hurdle is that the computation of the gravitational potential is not as straightforward as in Eq. 2.6 since the multi-grid levels must be taken into account. There are many different solvers of Poisson's equation for the AMR method and they come in two different flavours: the relaxation and convolutions solvers. Relaxation solvers guess a solution at the coarse level, relax the initial guess until they find the correct potential, and interpolate the solution to the fine grid where appropriate Dirichlet boundary conditions have been imposed (i.e., Jacobi and Gauss-Siedel (GS) method, conjugate gradient, multigrid). Convolution solvers convolve directly the mass distribution with a Green function (i.e., Hierarchical fast Fourier transform (FFT), and FMM).

To give the reader an idea of the complexity of an AMR grid compared with just a uniform grid as in the PM method, we mention here below the GS method for computing the gravitational potential. The idea is to first compute the gravitational potential at level n by inverting the matrix of the linear problem. Then, by using the appropriate Dirichlet boundary conditions, we use the expression of the potential at level n (coarse level) to find the potential at level $n+1$ (fine level). This results in the following form for the component i, j of the potential on a multi-grid at level $n + 1$:

$$\phi_{i,j}^{n+1} = \frac{1}{4} \left(\phi_{i+1,j}^n + \phi_{i-1,j}^n + \phi_{i,j+1}^n + \phi_{i,j-1}^n \right) - \frac{1}{4} \rho_{i,j}, \quad (2.7)$$

The advantage of the AMR method is that it is fast and the number of iterations scales as N .

2.1.4 Methods to solve the Euler equations

The set of Eq. 2.2 dealing with the hydrodynamic part of the simulation can be solved in many ways. The easiest way is to consider a spatial and time discretization of the equations by adopting the so-called finite difference (leapfrog) approach and discretizing the time and spatial derivatives using an upwind scheme. We will see in the next section 2.3 why the upwind scheme is stable but still diffuses a bit the solution. In RAMSES, the approach used is the Godunov technique, also called the finite volume scheme, allowing writing the set of Euler equations as a conservation law and solving it via a Riemann solver. We will also develop this method and the attached concepts in sect. 2.3.

The second method is the so-called SPH one and consists of replacing the gas component with fluid particles ruled by an EOS. Then, we attribute a smoothing kernel to all of them, allowing interactions with each other and mimicking the physical properties of the gas component.

Code	Finite Volume	SPH	N-body	Eulerian	Lagrangian	AMR
ART			✓			✓
FLASH	✓			✓		✓
RAMSES	✓		✓	✓		✓
PLUTO	✓			✓		✓
ENZO	✓			✓		✓
ATHENA++	✓			✓		✓
GADGET-4		✓	✓		✓	
PHANTOM		✓	✓		✓	
SWIFT		✓	✓		✓	
AREPO	✓		✓		✓	

Table 2.1: Table illustrating the different codes and their specifications (see text for more details).

2.1.5 Codes in Astrophysics

Many astrophysical codes have been developed and optimised over the past decades to study and learn about our Universe through numerical simulations. Table 2.1 illustrates the different astrophysical codes with their properties and the methods they use to solve motion, Poisson, and Euler equations. The main codes using the AMR methods are ART (Kravtsov et al., 1997), FLASH (Fryxell et al., 2000), RAMSES (Teyssier, 2002a), PLUTO (Mignone et al., 2007), ENZO (Bryan et al., 2014), and ATHENA++ (Stone et al., 2020). Those codes use different Poisson solvers: ART and ENZO use an FFT method, RAMSES a GS algorithm, but FLASH, PLUTO, and ATHENA only include a hydro solver. All those codes belong to the category of Eulerian codes since we can only access the gas physical quantities of each cell for every time step without following the gas flow over time. The other category of codes is called Lagrangian code and allows the tracking of gas particles over time via an SPH method. The main codes using the latter method are OpenGadget-3 (Groth et al., 2023), GADGET-4 (Springel et al., 2022), PHANTOM (Price et al., 2018), and SWIFT (Schaller et al., 2024). Some grid-based codes do not use the AMR method with the most famous one being the AREPO code (see Springel et al., 2019) using a moving-mesh (unstructured Voronoi tessellation of the simulation volume) method. This code is considered as a semi-Lagrangian code since it is designed to track the particle flow over time.

2.2 Cosmological and Astrophysical simulations

All the codes introduced and cited above are the key ingredients at the basis of a large number of state-of-the-art cosmological simulations. The large-scale aspect of those simulations, in terms of computational resources, suits perfectly the design of astrophysical codes. Those codes were designed to be parallelised and allow us to simulate the evolution

of our observable Universe. The main motivation for such big cosmological simulations is to understand better and constrain the formation and evolution of large-scale DM structures, and the distribution and properties of galaxies, starting from the epoch of the CMB. The formation and evolution of galaxies is a complex topic because it involves many different physical phenomena occurring over a large range of spatial and time scales, such as the formation of DM halos, gas accretion from filaments, star formation, stellar feedback, AGN, etc. Due to their characteristics, we can also use those astrophysical codes to model isolated galactic systems or perform zoom-in simulations. This allows us to focus on high-resolution simulations to study and characterise the physical phenomena occurring at small scales (i.e., parsec or sub-parsec) and study their impact on the secular evolution of galaxies without any external interactions. In this work, we have performed such a type of isolated galaxy simulation using the RAMSES code that we will develop in more detail in Sect. 2.3. To illustrate the more ambitious simulations performed in a cosmological context, I will only briefly review three simulations performed with state-of-the-art hydrodynamical codes: IllustrisTNG, Horizon, and Vintergatan. The IllustrisTNG project is a set of recent cosmological simulations including a comprehensive set of physical phenomena, as developed below. The Horizon and Vintergatan simulations used the RAMSES code.

2.2.1 Something about the IllustrisTNG simulations

The IllustrisTNG project (see [Springel et al., 2018](#); [Pillepich et al., 2018](#); [Nelson et al., 2018](#); [Naiman et al., 2018](#); [Marinacci et al., 2018](#)) is composed of a series of 18 cosmological magneto-hydro-dynamical simulations performed inside three different boxes: TNG50, TNG100, and TNG300, having a box side-length of 50, 100, and 300 cMpc, respectively. Those simulations are the new generation simulations of the initial Illustris project (see e.g., [Vogelsberger et al., 2014b,a](#); [Genel et al., 2014](#)), which was carried out using the moving-mesh code AREPO. The IllustrisTNG project is an upgraded version of the original Illustris project, focusing on the implementation of key physical processes involved in the formation and evolution of galaxies. The main processes implemented in the TNG galaxy formation model are¹: 1 - Microphysical gas radiative mechanisms, including primordial and metal-line cooling and heating with an evolving background radiation field. 2 - Star formation in the dense interstellar medium. 3 - Stellar population evolution and chemical enrichment following supernovae Ia, II, and AGB stars, individually tracking elements: H, He, C, N, O, Ne, Mg, Si, and Fe. 4 - Stellar feedback-driven galactic-scale outflows. 5 - The formation, merging, and accretion of nearby gas by SMBHs. 6 - Multi-mode BH feedback operating in a thermal 'quasar' mode at high accretion states, and a kinetic 'wind' mode at low accretion states. 7 - The amplification of cosmic magnetic fields from a minute primordial seed field at early times. This suite of simulations has shed light on the different processes involved in the formation and evolution of galaxies and galaxy clusters, and has helped constrain the nature of DM and dark energy.

¹This list is taken from <https://www.tng-project.org/about/>

2.2.2 Something about the Horizon simulations

The Horizon simulations are a suite of cosmological simulations based on the initial Horizon project. The goal of this project is to deal with the multi-scale problem involved in galaxy formation by simulating a cosmological volume corresponding to our ‘Horizon’. The first simulation of this suite is the Horizon-MareNostrum simulation (Ocvirk et al., 2008) and comes from the consortium between the Horizon Project in France and the MareNostrum cosmological project in Spain. This first Horizon simulation has opened the door to several other projects. One of those projects is the Horizon-AGN simulation (Dubois et al., 2014) using a 100 Mpc/h comoving volume with 1024^3 dark matter particles with the Planck cosmology. This simulation has a maximum resolution of 1 kpc and includes a large panel of numerical recipes for the stellar feedback, evolution of metals, and AGN feedback. The NewHorizon (Dubois et al., 2021) project is a high-resolution version of the Horizon-AGN simulation inside a zoom-in region of $(16 \text{ Mpc})^3$ around a single DM halo, and reaching a maximum resolution of 34 pc.

2.2.3 Something about the Vintergatan simulations

The VINTERGATAN project (see Agertz et al., 2021a; Renaud et al., 2021a,b; Segovia Otero et al., 2022) consists in a zoom-in simulation of a Milky Way-like galaxy identified at redshift zero in a DM-only cosmological simulation performed with RAMSES. This galaxy experienced its last major merger ~ 9 Gyr ago, which is the same as what was suggested for the Milky Way. This Milky Way-like galaxy was traced back until redshift 100 to restart a zoom-in run of this galaxy by increasing the number of DM particles and including hydrodynamics. This zoom-in simulation has also been used to study the merger history of the Milky Way as discussed in Renaud et al. (2022). A more recent offspring made of a complementary suite of simulations of Milky Way-like galaxies was carried out by Rey et al. (2023); Joshi et al. (2024).

2.3 The RAMSES code

RAMSES (Teyssier, 2002a) is a hydro-dynamical N-body code including an AMR grid that is parallelised on CPUs by using the MPI library. The domain decomposition is made via a Peano-Hilbert space decomposition algorithm to ensure optimised communications between the CPUs. In this section, we will focus on the main modules the authors implemented when they wrote RAMSES. Many other modules and patches have been implemented with time, such as the cooling function of gas, SF, and stellar feedback (developed in more detail in Chap. 3), but we will not be mentioning them in the following description. The code includes four main modules which are the AMR, GRAV, HYDRO, and PART modules dealing with the AMR grid, Poisson solver, Euler equations, and the mass, position, and velocity of each particle, respectively. We also mention a fifth MHD module that we will not consider further since it is an extension of the hydro module including the magnetic field and it requires a higher computational cost. This choice is also motivated by the fact

that we have only used the hydro module for all the research that we have carried out in this work. In the previous sections, we have already described the method implemented in the code to solve Poisson's equation 2.1c on the AMR grid by using a GS algorithm. In this section, we will focus on the description of the methods used to solve the Euler equations 2.2 including the Godunov discretization scheme implemented in RAMSES, the Riemann problem, and the various Riemann solvers.

Note to the reader

The following section is quite heavy in terms of mathematical developments and has been inspired by one of the lectures given by Romain Teyssier that I found on the internet². The main motivation for such an effort is the intense and profound desire to understand the numerical techniques of the code and unveil the secrets of the black box hiding the heart of RAMSES. I have used the code for the last three years and this is my personal contribution to this thesis manuscript to try to explain the numerical methods used for the HYDRO solver. I do not pretend that it is a comprehensive description of the solver since there are many aspects that I did not develop (e.g., the higher-order schemes and slope limiters) but it is enough to consider that this part of RAMSES is no longer a total black box, with the detailed description of the Godunov scheme and the Riemann problem. This part of this thesis manuscript is not essential for the work carried out during my PhD. Therefore, I invite the non-interested reader to skip the rest of this section and resume the reading of this manuscript in Sect. 2.4

2.3.1 Solving the Euler equations

The set of Euler equations 2.2 is a system of partial differential equations (PDE) with a set of conservative variables given by:

$$\vec{U} = (\rho, \rho\vec{v}, \rho E), \quad (2.8)$$

depending on the three spatial variables (x, y, z) and the time variable t . We can show that Eq. 2.2, without the source term coming from the gravitational potential, can always be written as:

$$\partial_t \vec{U} + \vec{\nabla} \mathbf{F} = 0, \quad (2.9)$$

where \mathbf{F} are the corresponding fluxes given by:

$$\mathbf{F} = (\rho\vec{v}, \rho(\vec{v} \otimes \vec{v}) + P, \vec{v}(\rho E + P)). \quad (2.10)$$

We note that the flux given by Eq. 2.10 is not a vector and the nabla operator in Eq. 2.9 must apply as a divergent or gradient on the different components of \mathbf{F} depending on their nature (i.e., scalar (ρ, p) , vector (\vec{v}) , or tensor $(\vec{v} \otimes \vec{v})$).

²The lecture can be found here: <https://www.youtube.com/watch?v=530nHbpa6NQ>

It is straightforward to show that using only the primitive variables

$$\vec{W} = (\rho, \vec{v}, P), \quad (2.11)$$

Eq. 2.2, without the source term, can be rewritten as:

$$\partial_t \rho + \rho \vec{\nabla} \cdot \vec{v} + \vec{v} \cdot \vec{\nabla} \rho = 0, \quad (2.12a)$$

$$\partial_t \vec{v} + (\vec{v} \cdot \vec{\nabla}) \vec{v} = -\frac{1}{\rho} \vec{\nabla} P, \quad (2.12b)$$

$$\partial_t P + \vec{v} \cdot \vec{\nabla} P + \gamma P \vec{\nabla} \cdot \vec{v} = 0, \quad (2.12c)$$

$$P = (\gamma - 1) \rho \epsilon, \quad (2.12d)$$

where we consider Eq. 2.12d as the EOS of an ideal gas where $E = \epsilon + v^2/2$, with ϵ the internal energy per unit mass of the gas. In the following, we only consider the first equation from the above set of PDE with only one dimension in the x direction, where we assume a constant velocity a and a density ρ noted $u(x, t)$. We discretise the equations with a uniform time step Δt and a spatial step Δx .

We first need to choose the appropriate scheme for the resolution of the simplest case which is the advection equation (i.e., Eq. 2.12a with a constant speed a) given by:

$$\partial_t u + a \partial_x u = 0, \quad (2.13)$$

and using appropriate boundary and initial conditions with:

$$u(x, 0) = u_0(x), \quad u(0, t) = U(t) \quad (2.14)$$

Unstable centered scheme

To discretise Eq. 2.13, we can visualise the scheme in Fig. 2.1, where we show the spatial discretisation around the point x_i for the time steps t^n and t^{n+1} . The most natural scheme we can choose to discretise the partial derivatives of Eq. 2.13 is given by the following expressions:

$$\partial_t \approx \frac{u(x, t + \Delta t) - u(x, t)}{\Delta t} = \frac{u_i^{n+1} - u_i^n}{\Delta t}, \quad (2.15a)$$

$$\partial_x \approx \frac{u(x + \Delta x, t) - u(x - \Delta x, t)}{2\Delta x} = \frac{u_{i+1}^n - u_{i-1}^n}{2\Delta x}, \quad (2.15b)$$

and replacing them in Eq. 2.13, we obtain:

$$\frac{u_i^{n+1} - u_i^n}{\Delta t} + a \frac{u_{i+1}^n - u_{i-1}^n}{2\Delta x} \approx 0, \quad (2.16)$$

where n and i stand for the time and spatial steps, respectively. When we try to solve Eq. 2.16 with the above scheme, we see that the solution does not converge and is unstable

because we are trying to numerically solve an unstable diffusion equation. Indeed, using the Taylor expansion of the velocity

$$u(x, t + \Delta t) = u(x, t) + \Delta t \left(\frac{\partial u}{\partial t} \right) + \frac{\Delta t^2}{2} \left(\frac{\partial^2 u}{\partial t^2} \right) + O(\Delta t^3), \quad (2.17a)$$

$$u(x + \Delta x, t) = u(x, t) + \Delta x \left(\frac{\partial u}{\partial x} \right) + \frac{\Delta x^2}{2} \left(\frac{\partial^2 u}{\partial x^2} \right) + O(\Delta x^3), \quad (2.17b)$$

$$u(x - \Delta x, t) = u(x, t) - \Delta x \left(\frac{\partial u}{\partial x} \right) + \frac{\Delta x^2}{2} \left(\frac{\partial^2 u}{\partial x^2} \right) + O(\Delta x^3), \quad (2.17c)$$

and replacing Eq. 2.17 in Eq. 2.16 and only keeping the first order terms, we can show that it is equivalent to solving the following equation:

$$\left(\frac{\partial u}{\partial t} \right) + a \left(\frac{\partial u}{\partial x} \right) \approx -a^2 \frac{\Delta t}{2} \left(\frac{\partial^2 u}{\partial x^2} \right), \quad (2.18)$$

which is completely unstable due to the negative factor in front of the second partial derivative with respect to x in the right-hand side of Eq. 2.18. Therefore, the centred scheme is not appropriate and we need to define a more stable scheme.

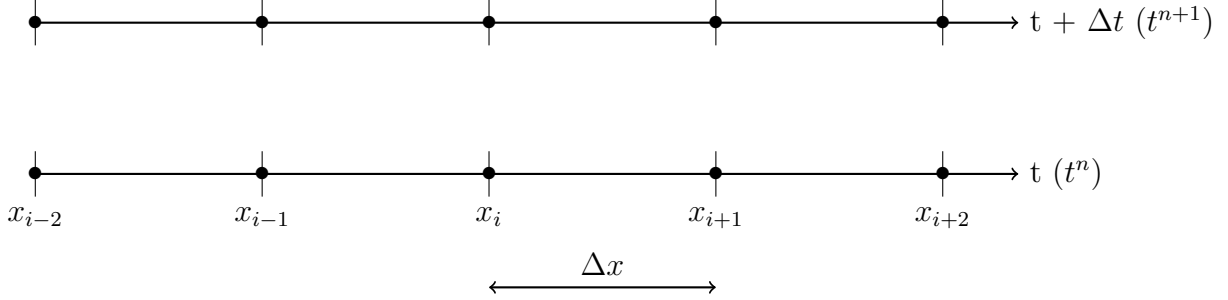


Figure 2.1: Time and spatial discretisation for the centred and upwind schemes.

Upwind scheme

The idea remains the same for this scheme (see again Fig. 2.1), but this time we will use the following expressions for the partial derivatives given by:

$$\partial_t \approx \frac{u(x, t + \Delta t) - u(x, t)}{\Delta t} = \frac{u_i^{n+1} - u_i^n}{\Delta t}, \quad (2.19a)$$

$$\partial_x \approx \frac{u(x, t) - u(x - \Delta x, t)}{\Delta x} = \frac{u_i^n - u_{i-1}^n}{\Delta x}, \quad (2.19b)$$

leading to the following expression for Eq. 2.13:

$$\frac{u_i^{n+1} - u_i^n}{\Delta t} + a \frac{u_i^n - u_{i-1}^n}{\Delta x} \approx 0. \quad (2.20)$$

This time, we can show by using the Taylor expansion (Eq. 2.17) in Eq. 2.20 that the numerical equation we are trying to solve is given by:

$$\left(\frac{\partial u}{\partial t}\right) + a \left(\frac{\partial u}{\partial x}\right) \approx a \frac{\Delta x}{2} (1 - C) \left(\frac{\partial^2 u}{\partial x^2}\right), \quad (2.21)$$

where $C = a\Delta t/\Delta x$ is the courant factor. We see that as long as C remains smaller than 1, Eq. 2.21 is stable, but the solution is diffused over time. To conclude, when we try to solve the most simple PDE equation, such as the advection equation, we see that we cannot avoid numerical diffusion at the first order in Δx .

2.3.2 The Godunov method

The Godunov strategy (Godunov, 1959) consists of considering the volumes rather than the positions. Fig. 2.2 illustrates the Godunov scheme with the volumes inside which the positions (points) are located. The Godunov scheme is also called the finite volume method and this is the exact solution for the discretisation of Eq. 2.12. The main constraint with this method is that it is very expensive in terms of numerical cost as we will see in the next sections. The Godunov scheme of the advection equation is obtained by integrating

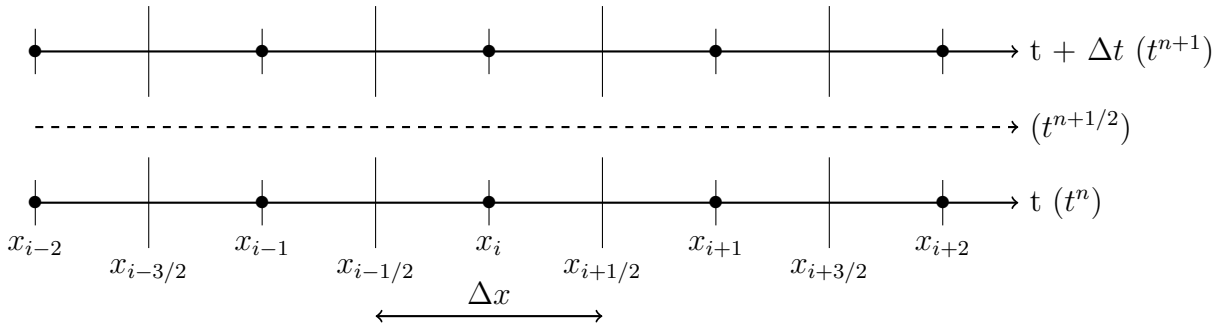


Figure 2.2: Time and spatial discretisation scheme for the Godunov method.

Eq. 2.13 over the full space-time domain which is given by:

$$\begin{aligned} & \int_{t^n}^{t^{n+1}} \int_{x_{n-1/2}}^{x_{n+1/2}} (\partial_t u + a \partial_x u) dx dt = 0 \\ & \Leftrightarrow \int_{x_{n-1/2}}^{x_{n+1/2}} [u(x, t)]_{t^n}^{t^{n+1}} dx + a \int_{t^n}^{t^{n+1}} [u(x, t)]_{x_{i-1/2}}^{x_{i+1/2}} dt = 0 \\ & \Leftrightarrow \int_{x_{n-1/2}}^{x_{n+1/2}} [u(x, t^{n+1}) - u(x, t^n)] dx + a \int_{t^n}^{t^{n+1}} [u(x_{i+1/2}, t) - u(x_{i-1/2}, t)] dt = 0 \\ & \Leftrightarrow \frac{u_i^{n+1} - u_i^n}{\Delta t} + a \frac{u_{i+1/2}^{n+1/2} - u_{i-1/2}^{n+1/2}}{\Delta x} = 0, \end{aligned} \quad (2.22)$$

where we have defined

$$u_i^n = \frac{1}{\Delta x} \int_{x_{n-1/2}}^{x_{n+1/2}} u(x, t^n) dx, \quad u_{i+1/2}^{n+1/2} = \frac{1}{\Delta t} \int_{t^n}^{t^{n+1}} u(x_{i+1/2}, t) dt. \quad (2.23)$$

The challenge here is to determine the expression of $u_{i+1/2}^{n+1/2}$ and $u_{i-1/2}^{n+1/2}$. To this end, we consider the piecewise constant profiles as shown in Fig. 2.3. We see that the solution is given by:

$$\begin{aligned} u(x_{i+1/2}, t) &= u_i^n & \text{if } a > 0, \\ u(x_{i+1/2}, t) &= u_{i+1}^n & \text{if } a < 0, \\ u(x_{i-1/2}, t) &= u_{i-1}^n & \text{if } a > 0, \\ u(x_{i-1/2}, t) &= u_i^n & \text{if } a < 0, \end{aligned} \quad (2.24)$$

and Eq. 2.22 can be rewritten as:

$$\frac{u_i^{n+1} - u_i^n}{\Delta t} + a \frac{u_i^n - u_{i-1}^n}{\Delta x} = 0, \quad (2.25)$$

which is completely equivalent to the result we obtained with the upwind scheme in Eq. 2.20. We see that the Godunov method is a much better justification since we only consider the problem through volumes.

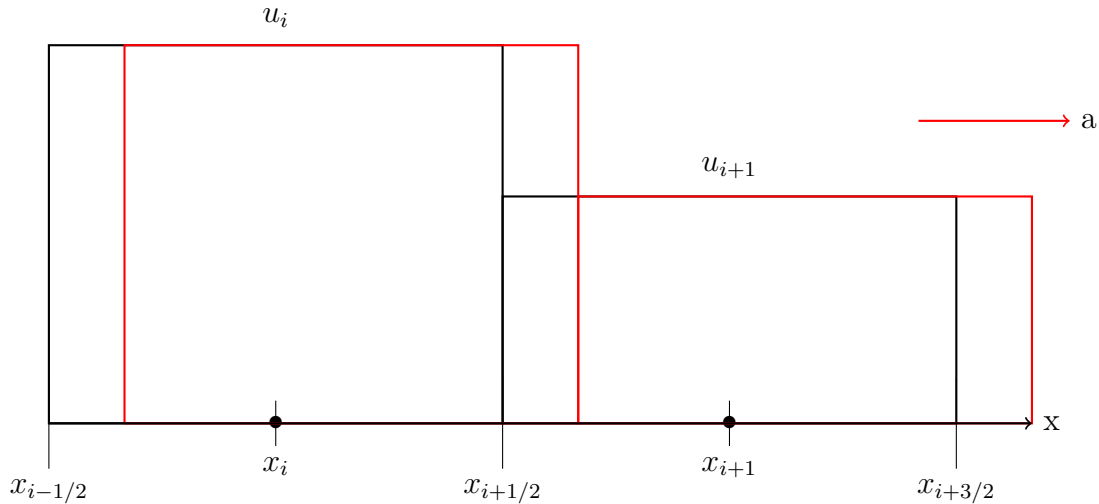


Figure 2.3: Piecewise solution of the Godunov scheme

Non-uniform mesh (toward the AMR method)

The Godunov and upwind schemes only consider a uniform spatial mesh size. However, RAMSES is designed with an AMR grid which complicates the simple scheme of Eq. 2.25. To see how the implementation of a non-uniform mesh impacts the scheme and the modified equation we need to develop the term of the spatial discretisation in Eq. 2.22 following the mesh configuration shown in Fig. 2.4. We introduce a mesh centred on a point labelled $x_{i-\alpha}$ located at a distance $\alpha\Delta x$ of the point with the label x_i . The two flux terms are

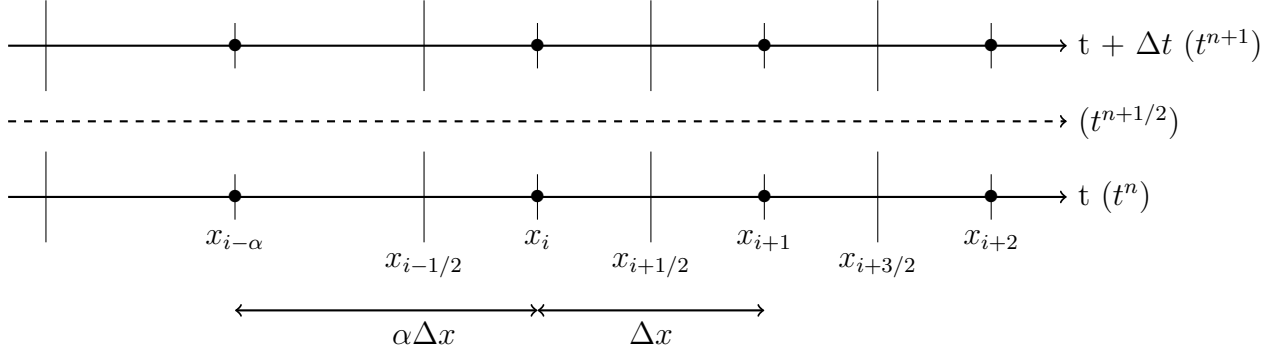


Figure 2.4: Discretisation scheme for the Godunov method.

written as follows:

$$\begin{aligned}
 u_{i+1/2}^{n+1/2} &= u(x_i + \Delta x/2, t^n + \Delta t/2) \\
 &= u(x_i, t^n) + \frac{\Delta x}{2} \left(\frac{\partial u}{\partial x} \right)_i + \frac{\Delta t}{2} \left(\frac{\partial u}{\partial t} \right)_i + O(\Delta x^2, \Delta t^2) \\
 &= u_i^n + (1 - C) \frac{\Delta x}{2} \left(\frac{\partial u}{\partial x} \right)_i + O(\Delta x^2, \Delta t^2)
 \end{aligned} \tag{2.26a}$$

$$\begin{aligned}
 u_{i-1/2}^{n+1/2} &= u(x_i - \Delta x/2, t^n + \Delta t/2) \\
 &= u(x_{i-\alpha} + (\alpha - 1/2)\Delta x, t^n + \Delta t/2) \\
 &= u_{i-\alpha}^n + (2\alpha - 1 - C) \frac{\Delta x}{2} \left(\frac{\partial u}{\partial x} \right)_{i-\alpha} + O(\Delta x^2, \Delta t^2) \\
 &= u_{i-\alpha}^n + (2\alpha - 1 - C) \frac{\Delta x}{2} \left(\frac{\partial u}{\partial x} \right)_{i-1} + O(\Delta x^2, \Delta t^2)
 \end{aligned} \tag{2.26b}$$

where we have used the following Taylor expansion up to the second order of the partial derivative of u with respect to x to find the final expression of Eq. 2.26b given by:

$$\left(\frac{\partial u}{\partial x} \right)_{i-\alpha} = \left(\frac{\partial u}{\partial x} \right) (x_{i-1} + (1 - \alpha)\Delta x, t^n) = \left(\frac{\partial u}{\partial x} \right)_{i-1} + O(\Delta x) \tag{2.27}$$

The following developments aim to show the issue arising when we use the Godunov scheme in Eq. 2.22 by only keeping the zeroth order terms. Using the following Taylor expansion:

$$\begin{aligned}
 u_{i-\alpha}^n &= u(x_{i-\alpha}, t^n) = u(x_i - \alpha\Delta x, t^n) \\
 &= u_i^n - \alpha\Delta x \left(\frac{\partial u}{\partial x} \right)_i + \frac{\alpha^2\Delta x^2}{2} \left(\frac{\partial^2 u}{\partial x^2} \right)_i + O(\Delta x^3)
 \end{aligned} \tag{2.28}$$

We successively write:

$$\begin{aligned}
& \frac{u_i^{n+1} - u_i^n}{\Delta t} + a \frac{u_{i+1/2}^{n+1/2} - u_{i-1/2}^{n+1/2}}{\Delta x} = 0 \\
& \Leftrightarrow \frac{u_i^{n+1} - u_i^n}{\Delta t} + a \frac{u_i^n - u_{i-\alpha}^n}{\Delta x} = 0 \\
& \Leftrightarrow \left(\frac{\partial u}{\partial t} \right)_i + \frac{a\Delta x}{2} C \left(\frac{\partial^2 u}{\partial x^2} \right)_i + \frac{a}{\Delta x} \left(\alpha \Delta x \left(\frac{\partial u}{\partial x} \right)_i - \frac{\alpha^2 \Delta x^2}{2} \left(\frac{\partial^2 u}{\partial x^2} \right)_i \right) = O(\Delta x^2, \Delta t^2) \\
& \Leftrightarrow \boxed{\left(\frac{\partial u}{\partial t} \right) + \alpha a \left(\frac{\partial u}{\partial x} \right) = \frac{a\Delta x}{2} (\alpha^2 - C) \left(\frac{\partial^2 u}{\partial x^2} \right) + O(\Delta x^2, \Delta t^2)}
\end{aligned} \tag{2.29}$$

We see in Eq. 2.29 that our leading order error is now in the first derivative of u with respect to x , which is a big issue if $\alpha \gg 1$ because that means we are not solving the advection-diffusion equation with a velocity a but with a velocity αa , which will lead to a completely different result. To get rid of this term proportional to α , we need to consider the first-order terms of Eq. 2.26 in Eq. 2.22. With those additional terms, we can show that Eq. 2.22 is now given by:

$$\boxed{\left(\frac{\partial u}{\partial t} \right) + a \left(\frac{\partial u}{\partial x} \right) = \frac{a\Delta x}{2} (\alpha - C)(1 - \alpha) \left(\frac{\partial^2 u}{\partial x^2} \right) + O(\Delta x^2, \Delta t^2),} \tag{2.30}$$

and we see that the α factor does not appear anymore in front of the partial derivative mentioned above. Eq. 2.30 represents the modified advection equation with a non-uniform mesh size. We note that we have lost one order of accuracy at the level boundary, which can induce non-linear effects and make the Godunov scheme unstable for some values of α . In particular, for $\alpha = 1.5$, AMR is unstable at the level boundary and some artificial diffusion is required to counterbalance this effect.

2.3.3 The Riemann problem

The Riemann problem is the determination of the solution of a conservation law system (i.e., Eq. 2.12) with piecewise initial conditions made of a constant left state and a constant right state with an interface between the two. The Godunov scheme introduced above with a piecewise constant left and right states and the interface between each volume (cell) is a Riemann problem. From these initial conditions, we want to determine the result of the new left and right states for the next time step. Solving the Riemann problem requires an accurate description of the phenomena occurring at the interface between two cells. We understand that the discontinuity between the left and right states generated by the interface is responsible for the propagation of waves from one edge to another inside the two cells. In other words, the information contained in the left cell must be communicated through the interface to the right cell and inversely. Using the notation introduced in

Eq. 2.11 we can consider that our primitive variables can be written like the sum of a constant state and a small perturbation given by:

$$\vec{W} = \vec{W}_0 + \Delta\vec{W}. \quad (2.31)$$

It is straightforward to show that we can always write the 1D Euler equation as follows:

$$\partial_t \Delta\vec{W} + A_0 \partial_x \Delta\vec{W} = 0, \quad (2.32)$$

where A_0 is a matrix with constant coefficients. The key idea here is to diagonalise this matrix and rewrite the above equations as follows:

$$\partial_t \Delta\vec{\alpha} + D \partial_x \Delta\vec{\alpha} = 0, \quad (2.33)$$

where D is a diagonal matrix containing the eigenvalues of A_0 on its diagonal. Eq. 2.33 is a system of decoupled equations for which each equation is just a simple advection equation. The components of the $\Delta\vec{\alpha}$ vector are Riemann invariant along the characteristic curves moving at velocities corresponding to the eigenvalues of A_0 . Then, we use the general expression of the conservation law 2.9 in 1D given by:

$$\partial_t \vec{U} + \partial_x \vec{F} = 0, \quad (2.34)$$

where the fluxes \vec{F} are expressed as a function of the $\Delta\vec{\alpha}$ vector. Once we determine the fluxes, we can use the Godunov scheme given by:

$$\frac{U_i^{n+1} - U_i^n}{\Delta t} + \frac{F_{i+1/2}^{n+1/2} - F_{i-1/2}^{n+1/2}}{\Delta x} = 0, \quad (2.35)$$

and solve the problem by computing the value of U_i^{n+1} for every time step. In the following, we illustrate the decomposition of the set of Eq. 2.32 into the decoupled set of Eq. 2.33 in the case of the 1D isothermal and adiabatic Euler equations. The first case illustrates the Riemann problem and the solution provided via the Godunov scheme. The second case shows a simpler representation of the challenge arising when we implement a HYDRO module using the Godunov method to solve the Riemann problem.

The isothermal wave equations

The simplest model to illustrate the Riemann problem is obtained when we apply the Godunov scheme to the so-called linearised 1D isothermal wave equations. To this end, we first need to use the set of variables of Eq. 2.31 given by:

$$\vec{W} \equiv \begin{pmatrix} \rho \\ u \end{pmatrix} = \begin{pmatrix} \rho_0 \\ u_0 \end{pmatrix} + \begin{pmatrix} \Delta\rho \\ \Delta u \end{pmatrix}, \quad (2.36)$$

and replace them into the set of Eq. 2.12 for a fixed temperature ($P = a^2\rho$), with a the sound speed, given by:

$$\partial_t \Delta\rho + u_0 \partial_x \Delta\rho + \rho_0 \partial_x \Delta u = 0 \quad (2.37a)$$

$$\partial_t \Delta u + u_0 \partial_x \Delta u + \frac{a^2}{\rho_0} \partial_x \Delta\rho = 0 \quad (2.37b)$$

The above system can be written as Eq. 2.32 with the matrix A_0 given by:

$$A_0 = \begin{pmatrix} u_0 & \rho_0 \\ \frac{a^2}{\rho_0} & u_0 \end{pmatrix}. \quad (2.38)$$

As mentioned above, the key idea here is to diagonalise the matrix A_0 and rewrite Eq. 2.37 under a decoupled form given by Eq. 2.33. Without going into the mathematical developments, we find that the eigenvalues of A_0 are given by:

$$\begin{aligned} \lambda^+ &= u_0 + a \\ \lambda^- &= u_0 - a, \end{aligned} \quad (2.39)$$

and their corresponding eigenvectors by:

$$\vec{X}^+ \propto \begin{pmatrix} \rho_0 \\ a \end{pmatrix}, \quad \vec{X}^- \propto \begin{pmatrix} \rho_0 \\ -a \end{pmatrix}, \quad (2.40)$$

and the system of equations 2.37 can be rewritten as follows:

$$\partial_t \Delta \alpha^+ + (u_0 + a) \partial_x \Delta \alpha^+ = 0 \quad (2.41a)$$

$$\partial_t \Delta \alpha^- + (u_0 - a) \partial_x \Delta \alpha^- = 0, \quad (2.41b)$$

where:

$$\Delta \vec{\alpha} \equiv \begin{pmatrix} \Delta \alpha^+ \\ \Delta \alpha^- \end{pmatrix} = \frac{1}{2} \begin{pmatrix} \Delta \rho + \frac{\rho_0}{a} \Delta u \\ \Delta \rho - \frac{\rho_0}{a} \Delta u \end{pmatrix}. \quad (2.42)$$

We highlight again that the system of Eq. 2.41 is simply two decoupled advection equations 2.13. To interpret those two equations, Fig. 2.5 shows the characteristic curves and the propagation of waves coming from the left and going to the right ($\Delta \alpha^+$) and the waves coming from the right and going to the left ($\Delta \alpha^-$). We also show the interface separating the left and right states (ρ_L, u_L and ρ_R, u_R), as well as the resulting mixed states, given by:

$$\Delta \rho^* = \Delta \alpha_L^+ + \Delta \alpha_R^- \quad (2.43a)$$

$$\Delta u^* = \frac{a}{\rho_0} (\Delta \alpha_L^+ - \Delta \alpha_R^-) \quad (2.43b)$$

To give the reader the keys for the rest of the method to solve the Riemann problem, we will only develop here the mathematical expression of one flux for the continuity equation with the notation ($L, R \equiv i, i + 1$). When we apply the Godunov scheme 2.35 to that equation, we see that the flux $F_{1+1/2}^{n+1/2}$ writes:

$$F_{1+1/2}^{n+1/2} = u_0 \Delta \rho_{i+1/2}^{n+1/2} + \rho_0 \Delta u_{i+1/2}^{n+1/2}, \quad (2.44)$$

with the following expressions for the perturbations:

$$\begin{aligned} \Delta \rho_{i+1/2}^{n+1/2} &= \Delta \alpha_i^+ + \Delta \alpha_{i+1}^- = \frac{\Delta \rho_i + \Delta \rho_{i+1}}{2} - \frac{\rho_0}{2a} (\Delta u_{i+1} - \Delta u_i) \\ \Delta u_{i+1/2}^{n+1/2} &= \frac{a}{\rho_0} (\Delta \alpha_i^+ - \Delta \alpha_{i+1}^-) = \frac{\Delta u_i + \Delta u_{i+1}}{2} - \frac{a}{2\rho_0} (\Delta \rho_{i+1} - \Delta \rho_i), \end{aligned} \quad (2.45)$$

and using Eq. 2.45 in 2.44, the flux is then given by:

$$\begin{aligned}
 F_{1+1/2}^{n+1/2} &= u_0 \frac{\Delta\rho_i + \Delta\rho_{i+1}}{2} + \rho_0 \frac{\Delta u_i + \Delta u_{i+1}}{2} - u_0 \frac{\rho_0}{2a} (\Delta u_{i+1} - \Delta u_i) - \rho_0 \frac{a}{2\rho_0} (\Delta\rho_{i+1} - \Delta\rho_i) \\
 &\approx u_0 \frac{\Delta\rho_i + \Delta\rho_{i+1}}{2} + \rho_0 \frac{\Delta u_i + \Delta u_{i+1}}{2} - \frac{a}{2} \Delta x \left(\frac{\partial\rho}{\partial x} \right) - \frac{u_0\rho_0}{2a} \Delta x \left(\frac{\partial u}{\partial x} \right).
 \end{aligned}
 \tag{2.46}$$

We note that Eq. 2.46 is composed of a 'true' flux given by the averaged in the two first terms and a diffusive flux given by the two last terms. We can thus write the flux as follows:

$$\vec{F} = \vec{F}_{true} - \nu \vec{\nabla} q,
 \tag{2.47}$$

which leads to the final modified equation given by:

$$\frac{\partial\rho}{\partial t} + \vec{\nabla} \cdot \vec{F}_{true} = \nu \vec{\nabla}^2 q.
 \tag{2.48}$$

We highlight here that Eq. 2.48 has exactly the same expression as Eq. 2.21 with the positive term $\nu \vec{\nabla}^2 q$, which diffuses the solution and makes the Godunov scheme stable.

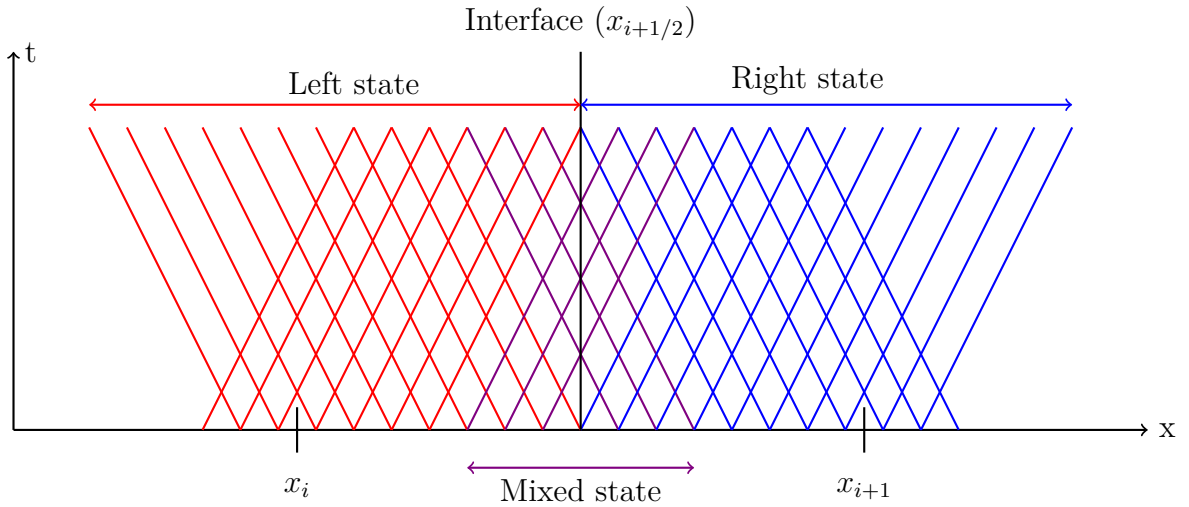


Figure 2.5: Illustration of the characteristic curves of Eq. 2.41. The red curves represent the Left state (everything on the left of the interface), and the blue curves represent the right state (everything on the right of the interface). The propagation of waves shows a right-going left state and a left-going right state crossing the interface and creating a mixed state (violet curves).

The adiabatic wave equations

The adiabatic Euler equations are given by Eq. 2.12. We see that we already have a third equation and the vector of primitive variables is this time given by:

$$\vec{W} \equiv \begin{pmatrix} \rho \\ u \\ P \end{pmatrix} = \begin{pmatrix} \rho_0 \\ u_0 \\ P_0 \end{pmatrix} + \begin{pmatrix} \Delta\rho \\ \Delta u \\ \Delta P \end{pmatrix}, \quad (2.49)$$

where the pressure p also depends on the temperature through Eq. 2.12d. The perturbed adiabatic Euler equations are thus written as:

$$\partial_t \Delta\rho + u_0 \partial_x \Delta\rho + \rho_0 \partial_x \Delta u = 0, \quad (2.50a)$$

$$\partial_t \Delta u + u_0 \partial_x \Delta u + \frac{1}{\rho_0} \partial_x \Delta P = 0, \quad (2.50b)$$

$$\partial_t \Delta P + u_0 \partial_x \Delta P + \gamma P_0 \partial_x \Delta u = 0, \quad (2.50c)$$

Once again, the above system can be written under the shape of Eq. 2.32 with a matrix A_0 given by:

$$A_0 = \begin{pmatrix} u_0 & \rho_0 & 0 \\ 0 & u_0 & \frac{1}{\rho_0} \\ 0 & \gamma P_0 & u_0 \end{pmatrix}. \quad (2.51)$$

The eigenvalues of the matrix A_0 are given by:

$$\begin{aligned} \lambda^+ &= u_0 + a, \\ \lambda^0 &= u_0, \\ \lambda^- &= u_0 - a, \end{aligned} \quad (2.52)$$

with their corresponding eigenvectors expressed as follows:

$$\vec{X}^+ \propto \begin{pmatrix} 1 \\ a/\rho_0 \\ a^2 \end{pmatrix}, \quad \vec{X}^0 \propto \begin{pmatrix} 1 \\ 0 \\ 0 \end{pmatrix}, \quad \vec{X}^- \propto \begin{pmatrix} 1 \\ -a/\rho_0 \\ a^2 \end{pmatrix}, \quad (2.53)$$

Hence, the above system of equations 2.50 can be rewritten as follows:

$$\partial_t \Delta\alpha^+ + (u_0 + a) \partial_x \Delta\alpha^+ = 0, \quad (2.54a)$$

$$\partial_t \Delta\alpha^0 + u_0 \partial_x \Delta\alpha^0 = 0, \quad (2.54b)$$

$$\partial_t \Delta\alpha^- + (u_0 - a) \partial_x \Delta\alpha^- = 0, \quad (2.54c)$$

where the eigenstate vector $\Delta\vec{\alpha}$ has the following shape:

$$\Delta\vec{\alpha} \equiv \begin{pmatrix} \Delta\alpha^+ \\ \Delta\alpha^0 \\ \Delta\alpha^- \end{pmatrix} = \frac{1}{2} \begin{pmatrix} \frac{\Delta P}{a^2} + \frac{\rho_0}{a} \Delta u \\ 2 \left(\Delta\rho - \frac{\Delta P}{a^2} \right) \\ \frac{\Delta P}{a^2} - \frac{\rho_0}{a} \Delta u \end{pmatrix}. \quad (2.55)$$

We immediately see that the above system of decoupled equations is much more complicated than the equivalent isothermal one given by Eq. 2.41. This is due to the additional pressure variable and we note that the above system represents the propagation of three waves at velocity $u_0 + a$, u_0 , and $u_0 - a$. The Riemann problem we need to solve in this case is composed of three waves propagating in both directions through the interface and interacting with each other as shown in Fig. 2.6. There are two mixed states labelled ‘Left’ and ‘Right’ (L, R), and the mixed-state perturbations write:

$$\Delta u_{L,R}^* = \frac{a}{\rho_0} (\Delta \alpha_L^+ - \Delta \alpha_R^-), \quad (2.56a)$$

$$\Delta P_{L,R}^* = a^2 (\Delta \alpha_L^+ + \Delta \alpha_R^-), \quad (2.56b)$$

$$\Delta \rho_L^* = (\Delta \alpha_L^+ + \Delta \alpha_L^0 + \Delta \alpha_R^-), \quad (2.56c)$$

$$\Delta \rho_R^* = (\Delta \alpha_L^+ + \Delta \alpha_R^0 + \Delta \alpha_R^-). \quad (2.56d)$$

From this step, if we use the Godunov scheme and compute the fluxes, we can show that even in the adiabatic wave case, the modified equation has the same mathematical expression as the advection-diffusion equation 2.48, which is once again a stable scheme.

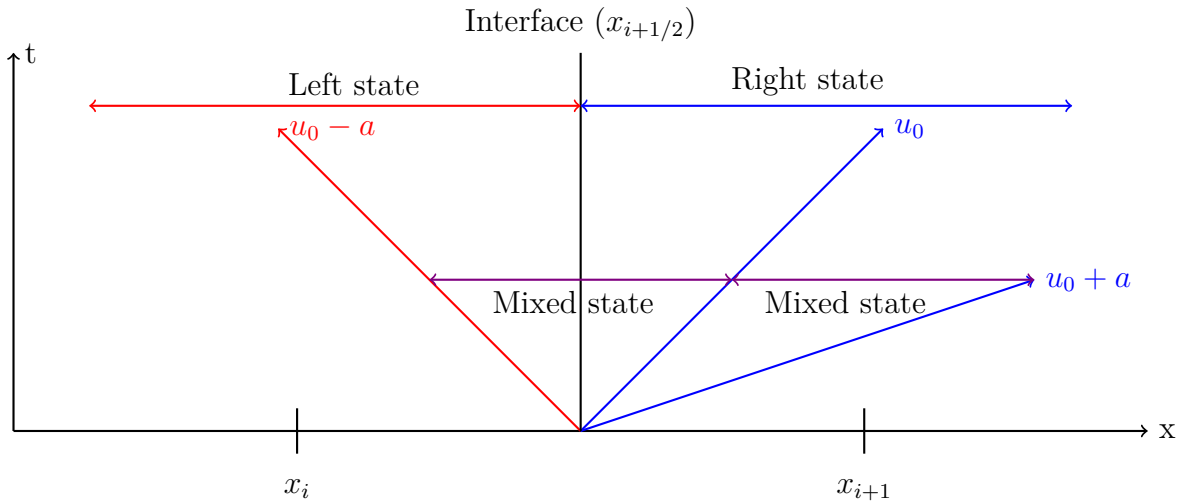


Figure 2.6: Illustration of the characteristic curves of Eq. 2.54. The red curve represents the Left state, and the blue curves represent the right states. From left to right the waves propagate with velocity $u_0 - a$, u_0 , and $u_0 + a$, respectively. The two mixed states appear between each wave.

2.3.4 The various Riemann solvers

The Godunov scheme of the Euler conservative equations is always written as in Eq. 2.35. At the edge of each cell, we need to solve a Riemann problem (noted *RP*) for which we

need to determine the mixed states \vec{U}^* and where the fluxes are given by:

$$\begin{aligned}\vec{F}_{i+1/2}^{n+1/2} &= \vec{F}(\vec{U}_{i+1/2}^*(0)), \\ \vec{U}_{i+1/2}^* &= RP(\vec{U}_i^n, \vec{U}_{i+1}^n),\end{aligned}\tag{2.57}$$

with the corresponding Godunov flux:

$$\vec{F}_{i+1/2}^{n+1/2} = \vec{F}^*(\vec{U}_i^n, \vec{U}_{i+1}^n).\tag{2.58}$$

The two examples we have introduced above (i.e., isothermal and adiabatic Euler equations) are straightforward cases. In reality, the equations are not linear, especially in the presence of shocks, leading to a shock wave, contact discontinuity, and rarefaction wave (i.e., a decompression wave which often follows the shock wave). In this case, the exact solution to the Riemann problem using the Godunov scheme of Eq. 2.35 requires exact Riemann solvers. Those solvers need to determine the roots of non-linear functions coming from Eq. 2.58 by using the Newton-Raphson method, which is costly in terms of computing resources, especially with the full MHD equations and a large grid. To speed up the process, approximate Riemann solvers were introduced to simplify Eq. 2.35 and 2.58 and make it more tractable for a large number of cells.

The two main families of approximate Riemann solvers are the Linear and the so-called HLL (Harten, Lax, and van Leer) Riemann solvers. The linear solvers are designed to simplify the expression of the Godunov flux by averaging the right and left states and introducing a linear diffusive term. HLL Riemann solvers are designed to reduce the number of waves to only two (even in the MHD case, which contains seven waves). Among the HLL Riemann solvers, we mention here the Lax-Friedrich (LLF) and the HLLC solver. LLF solvers have a robust scheme leading to a closed form for the flux. HLLC solvers add a third contact (entropy) wave which reduces the complexity of the problem. The LLF solver is the most diffusive one and the HLLC is the closest to the exact Riemann solver (see Toro, 2009).

To illustrate the behaviours of those various solvers, we show the well-known 1D shock sod tube test with the initial problem represented in Fig. 2.7. In this figure, we see a discontinuity of the density and pressure at 0.5 cm, which is responsible for the formation of shock waves propagating in the tube. We see that this problem is particularly relevant to illustrate what we developed in the previous section since we observe two constant states for the initial conditions. The Riemann problem of the initial condition occurs at the interface between the two cells located on the left and right to the interface at 0.5 cm. From what we have developed above, we know that we will observe the propagation of three waves. The first shock wave will propagate to the right, followed by the second contact discontinuity wave. A third rarefaction wave will propagate to the left, connecting the two initial states. Figure 2.8, 2.9, and 2.10 illustrate the result of the EXACT, LLF, and HLLC Riemann solver, respectively. The main difference between these solvers is visible in the density profile (top panel) for which we see the diffusive term acting close to the contact discontinuity shock (~ 0.75 cm). We observe the EXACT and HLLC Riemann solvers give quite the same result, but the LLF solver is more diffusive than the others.

To illustrate the power of the AMR method, we show in Fig. 2.11 the same experience with the shock sod tube but this time, we use an AMR-HLLC Riemann solver to compute the solution. We see that the mesh is refined close to the flow discontinuity (see the blue dashed line), which strongly reduces the diffusion of the HLLC solver. Moreover, the solution is almost identical to the analytical one with a full capture of the shock discontinuities.

2.3.5 Overview of the 3D Riemann problem

All the mathematical developments we did above are considered only in one dimension. The flux is just given by the vector \vec{F} and the decoupling by diagonalisation of Eq. 2.32 is straightforward. In 3D, Eq. 2.9 writes:

$$\partial_t \vec{U} + \partial_x \vec{F} + \partial_y \vec{G} + \partial_z \vec{H} = 0, \quad (2.59)$$

where the conservative variable vector \vec{U} and the fluxes \vec{F} , \vec{G} , and \vec{H} are given by:

$$\vec{U} = (\rho, \rho u, \rho v, \rho w, \rho E) \quad (2.60)$$

$$\vec{F} = \begin{pmatrix} \rho u \\ \rho u u + P \\ \rho u v \\ \rho u w \\ u(\rho E + P) \end{pmatrix}, \vec{G} = \begin{pmatrix} \rho v \\ \rho v u \\ \rho v v + P \\ \rho v w \\ v(\rho E + P) \end{pmatrix}, \vec{H} = \begin{pmatrix} \rho w \\ \rho w u \\ \rho w v \\ \rho w w + P \\ w(\rho E + P) \end{pmatrix}. \quad (2.61)$$

The primitive form of Eq. 2.59 is again obtained by using the primitive vector variable given by:

$$\vec{W} = (\rho, u, v, w, P), \quad (2.62)$$

and the following Jacobian matrices for the change of variables between the fluxes \vec{F} , \vec{G} , \vec{H} with the conservative (primitive) variable vector \vec{U} (\vec{W}) given by:

$$J = \frac{\partial \vec{F}}{\partial \vec{U}}, \quad K = \frac{\partial \vec{G}}{\partial \vec{U}}, \quad L = \frac{\partial \vec{H}}{\partial \vec{U}}, \quad (2.63)$$

$$M^{-1} = \frac{\partial \vec{U}}{\partial \vec{W}}.$$

Using Eq. 2.63 in 2.59, we obtain the following equation depending only on the primitive variable vector \vec{W} :

$$\partial_t \vec{W} + M J M^{-1} \partial_x \vec{W} + M K M^{-1} \partial_y \vec{W} + M L M^{-1} \partial_z \vec{W} = 0, \quad (2.64)$$

which is simply written as:

$$\partial_t \vec{W} + A \partial_x \vec{W} + B \partial_y \vec{W} + C \partial_z \vec{W} = 0. \quad (2.65)$$

where A, B , and C are matrices. We see that Eq. 2.65 is much more complex than its equivalent in 1D because we have now a partial derivative in each direction of space. We also note that the decoupling of this system in the case of small perturbations is no longer possible because of the three matrices we need to diagonalise at the same time.

The 3D Godunov scheme is then given by:

$$\begin{aligned} U_i^{n+1} = U_i^n &+ \frac{\Delta t}{\Delta x} \left(F_{i+1/2,j,k}^{n+1/2} - F_{i-1/2,j,k}^{n+1/2} \right) \\ &+ \frac{\Delta t}{\Delta y} \left(G_{i,j+1/2,k}^{n+1/2} - G_{i,j-1/2,k}^{n+1/2} \right) \\ &+ \frac{\Delta t}{\Delta z} \left(H_{i,j,k+1/2}^{n+1/2} - H_{i,j,k-1/2}^{n+1/2} \right) = 0. \end{aligned} \quad (2.66)$$

In this case, the Riemann problem becomes tedious, but we can approximate its solution by splitting Eq. 2.66 into three different 1D Riemann problems in each direction of space. This method is called dimensional splitting and the three 1D Godunov schemes are just given by:

$$U_i^{n+1} = U_i^n + \frac{\Delta t}{\Delta x} \left(F_{i+1/2,j,k}^{n+1/2} - F_{i-1/2,j,k}^{n+1/2} \right), \quad (2.67a)$$

$$U_i^{n+2} = U_i^{n+1} + \frac{\Delta t}{\Delta y} \left(G_{i,j+1/2,k}^{n+3/2} - G_{i,j-1/2,k}^{n+3/2} \right), \quad (2.67b)$$

$$U_i^{n+3} = U_i^{n+2} + \frac{\Delta t}{\Delta z} \left(H_{i,j,k+1/2}^{n+5/2} - H_{i,j,k-1/2}^{n+5/2} \right), \quad (2.67c)$$

which is much more convenient for the computation of the fluxes because the diagonalisation of Eq. 2.65 is again possible since Eq. 2.59 can be split following the three directions of space. The advantage of the directional splitting method is that the problem is again reduced to the well-known 1D Riemann problem. The disadvantage is that we need to solve three Riemann problems instead of a single one.

2.4 RAMSES to model the evolution of nearby disc galaxies

Before we justify the choice of RAMSES to model nearby disc galaxies, it is important to keep in mind that the N-body and HYDRO solvers of RAMSES are coupled through gravity. In this section, we have developed with more depth the hydro solver by only considering the Euler equations given by the system of PDE 2.9. This system is quite simple as the fluid (gas) it describes is completely decoupled from the gravitational potential generated by the gas itself and the particles. The full Euler equations we need to solve to have comprehensive modelling of isolated galactic systems is the set of Eq. 2.2 with the source term stemming from the total gravitational potential. In this case, the Godunov scheme still works, but we need to add a source term with the gradient of the gravitational potential. We note that the addition of this source term in Eq. 2.9 does not change its conservative nature, and we just need to modify the flux by adding the potential into

it. In RAMSES, the gas is composed of different components: atomic hydrogen, helium, and metals such as iron and oxygen. Those elements can be seen as different fluids (gas components) and we need to solve the Euler equations for each of those chemical species.

We motivate the modelling and study of nearby disc galaxies with RAMSES because the code offers a comprehensive approach with its N-body and HYDRO solvers. With RAMSES, we are able to describe the evolution of the star and DM system, as well as the formation of spiral arms, stellar bars, and other features. We can also describe the full evolution of the gas dynamics and the formation and evolution of intermediate- and small-scale structures of the gas such as dust lane and central molecular discs. Moreover, the AMR method allows us to focus our study on the very central dense regions of nearby disc galaxies, with a high resolution going up to 12 pc while adopting a low resolution in the outer part of the galaxy. The power of the AMR method has already been shown in Fig. 2.11 for the 1D case. A more complex structure of the 3D AMR grid is shown in Fig. 2.12, 2.13 and 2.14 where we illustrate the AMR grid on one of the snapshots of one of our models. This clearly illustrates the resolution we can reach (12 pc) in the central regions of simulations, which is a crucial factor if we want to study the evolution of central gas structures.

In addition to the first version of RAMSES, many patches have been written over the past two decades to implement a gas cooling function, formation of new stars, and stellar feedback. Those patches, especially the one written and used in [Agertz et al. \(2013\)](#) and [Renaud et al. \(2013a\)](#) are the key to increasing the realism of galaxy simulations and starting to compare our results with observations of nearby disc galaxies.

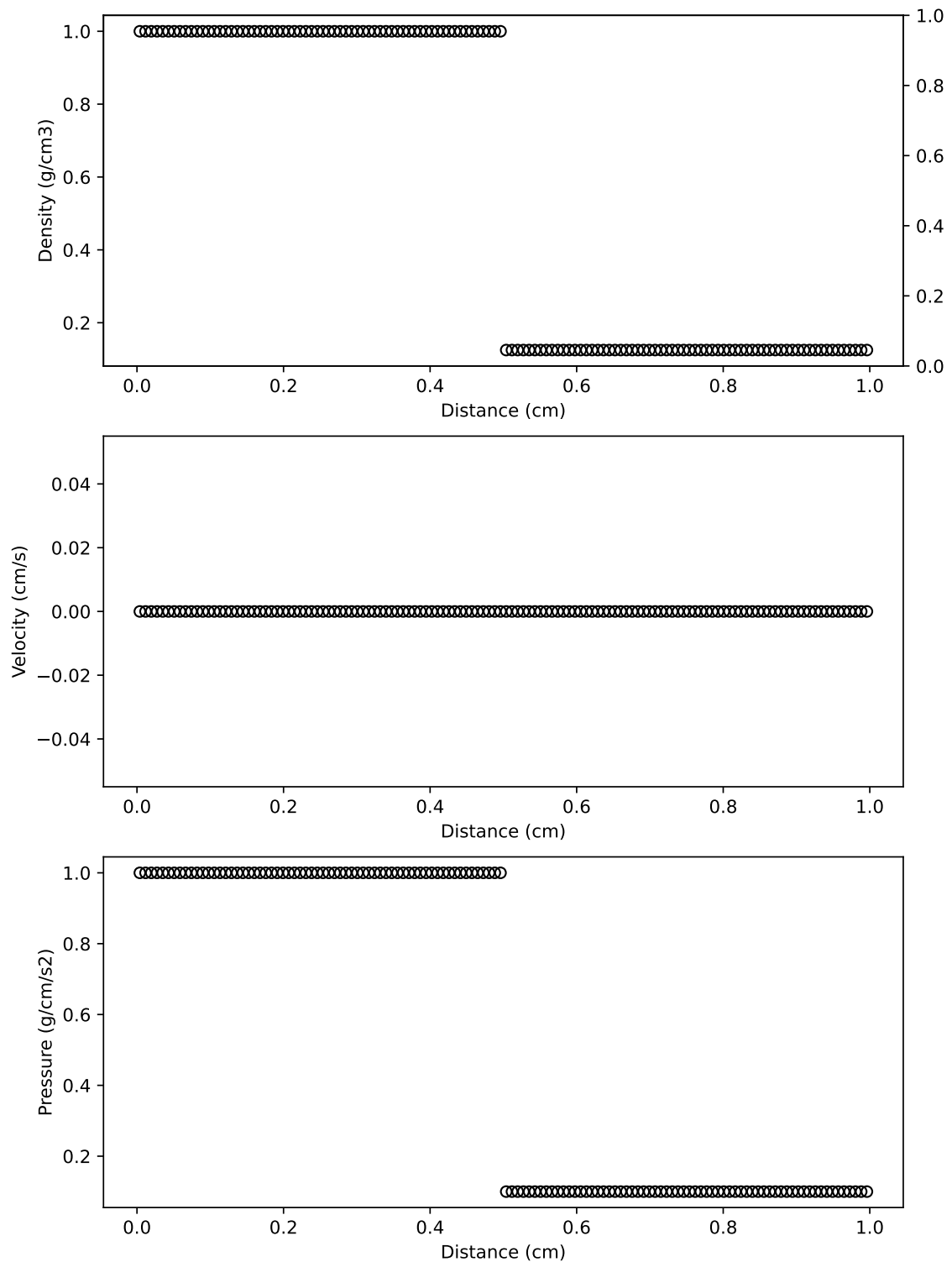


Figure 2.7: Initial condition of the Sod tube test. The initial density, velocity, and pressure profiles are illustrated by the circles with a discontinuity at a distance of 5 cm. We have used a uniform mesh size with a total number of cells of 128, corresponding to a constant level of refinement fixed to 7.

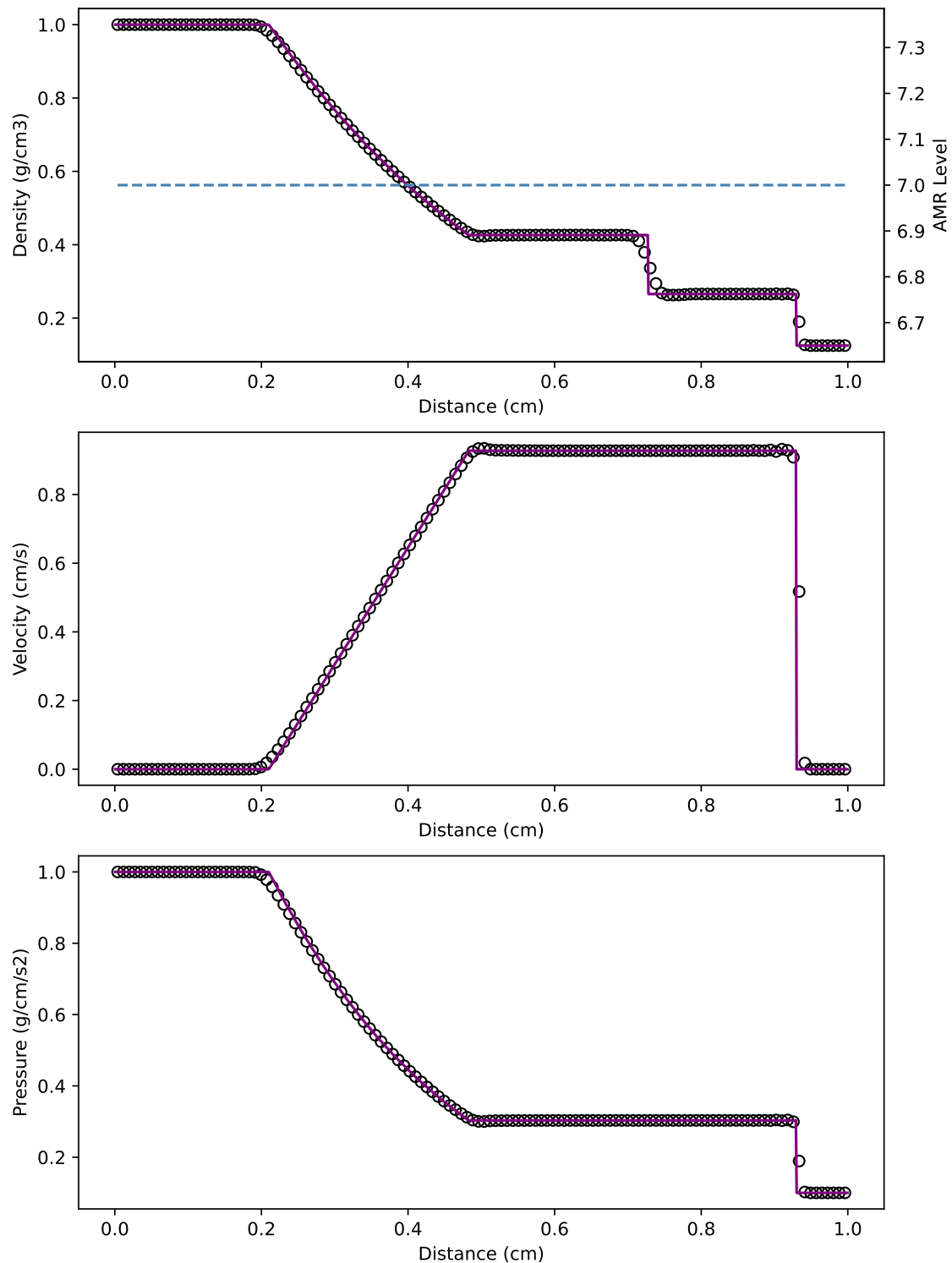


Figure 2.8: Solution of the EXACT Riemann solver for the Sod tube test. The final state of the density, velocity, and pressure profiles are shown by the circles. The analytical solution is shown by the purple curve. From left to right, we see the rarefaction wave (~ 0.2 - 0.5 cm), then the contact discontinuity wave (~ 0.75 cm), and finally the shock wave (~ 0.95 cm). The mesh size (dashed blue curve) is uniform with a total number of 128 cells, corresponding to a constant level of refinement fixed to 7.

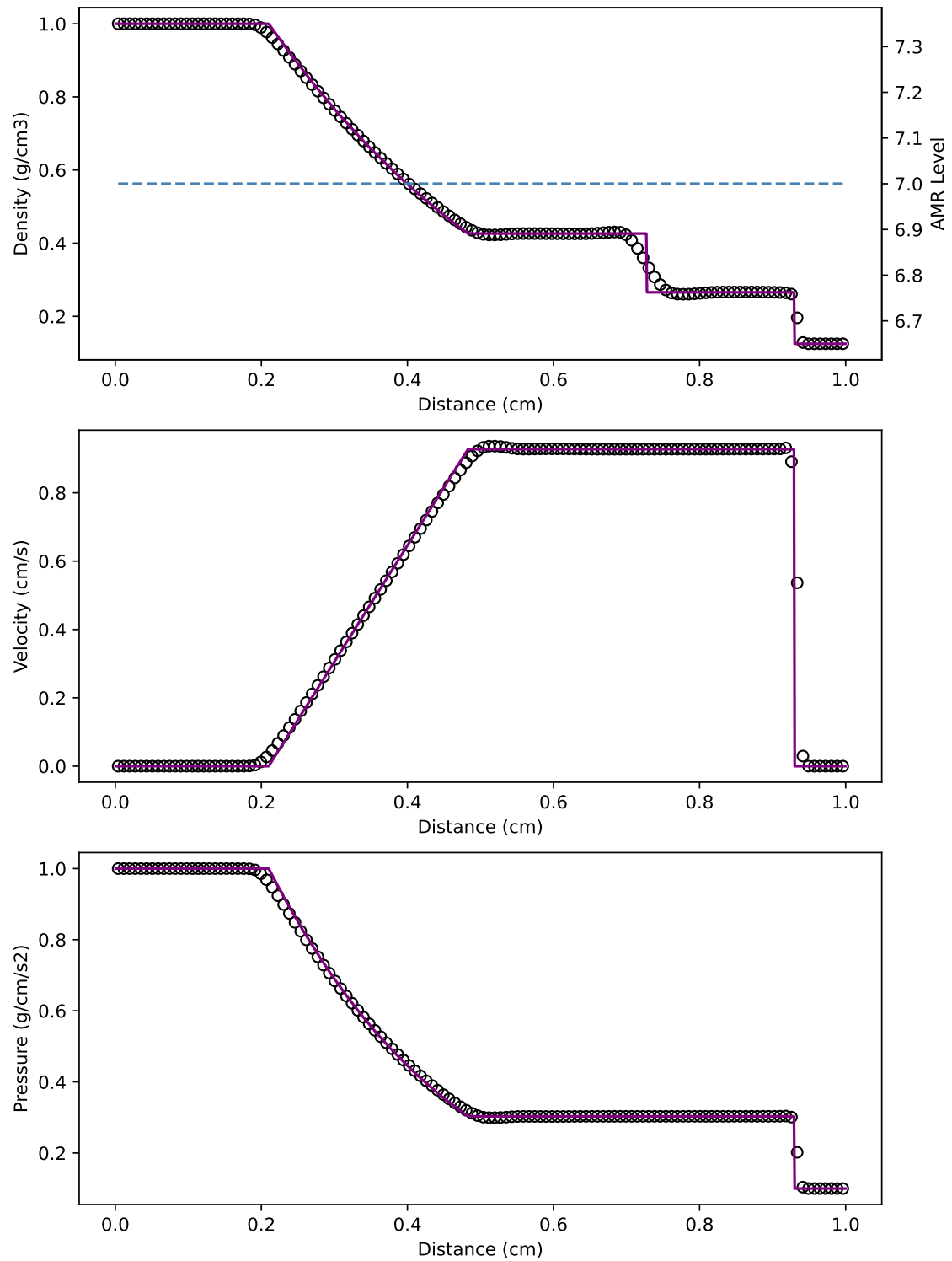


Figure 2.9: Same as in Fig. 2.8, but for the LLF Riemann solver.

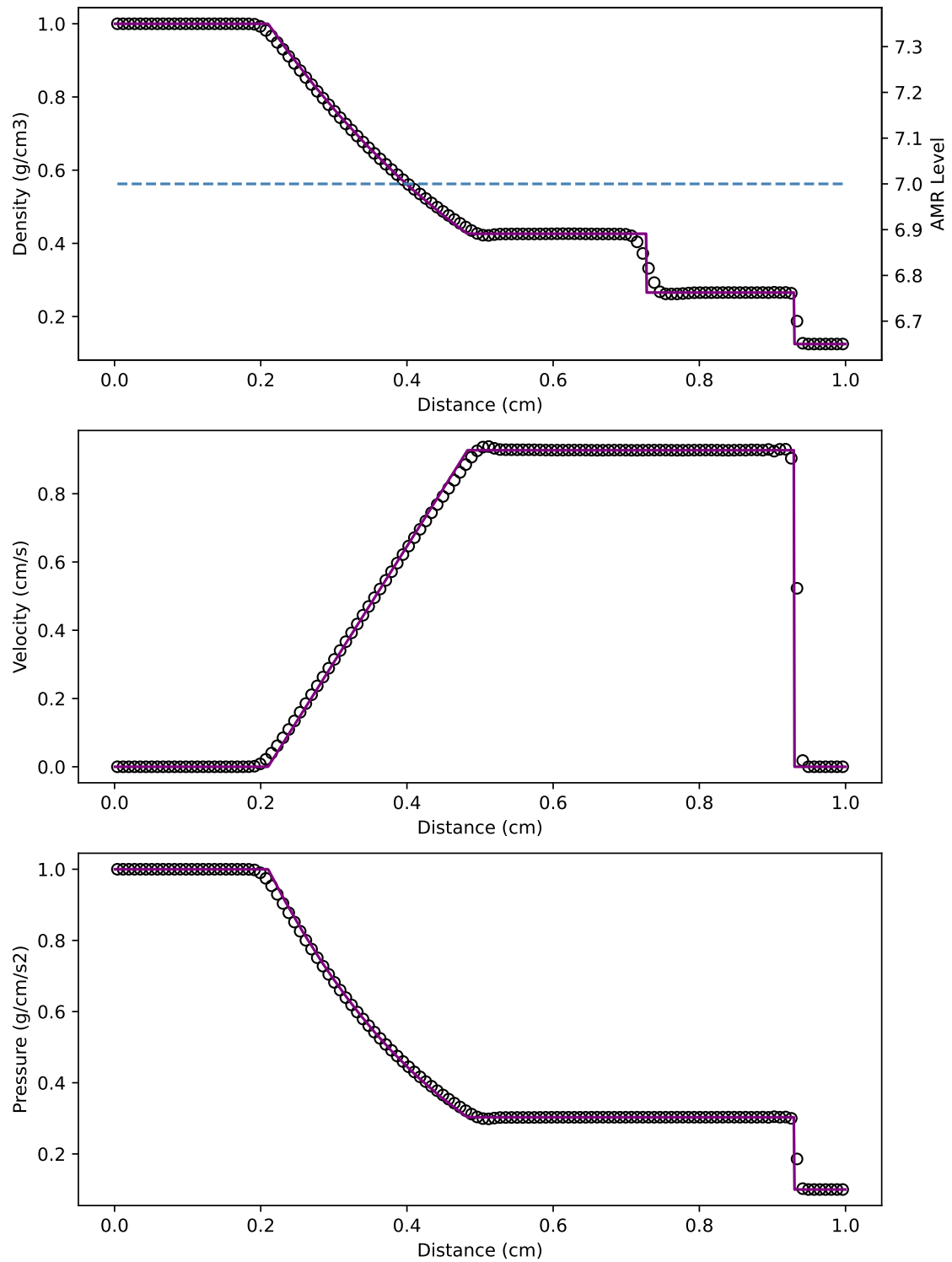


Figure 2.10: Same as in Fig. 2.8, but with the HLLC Riemann solver.

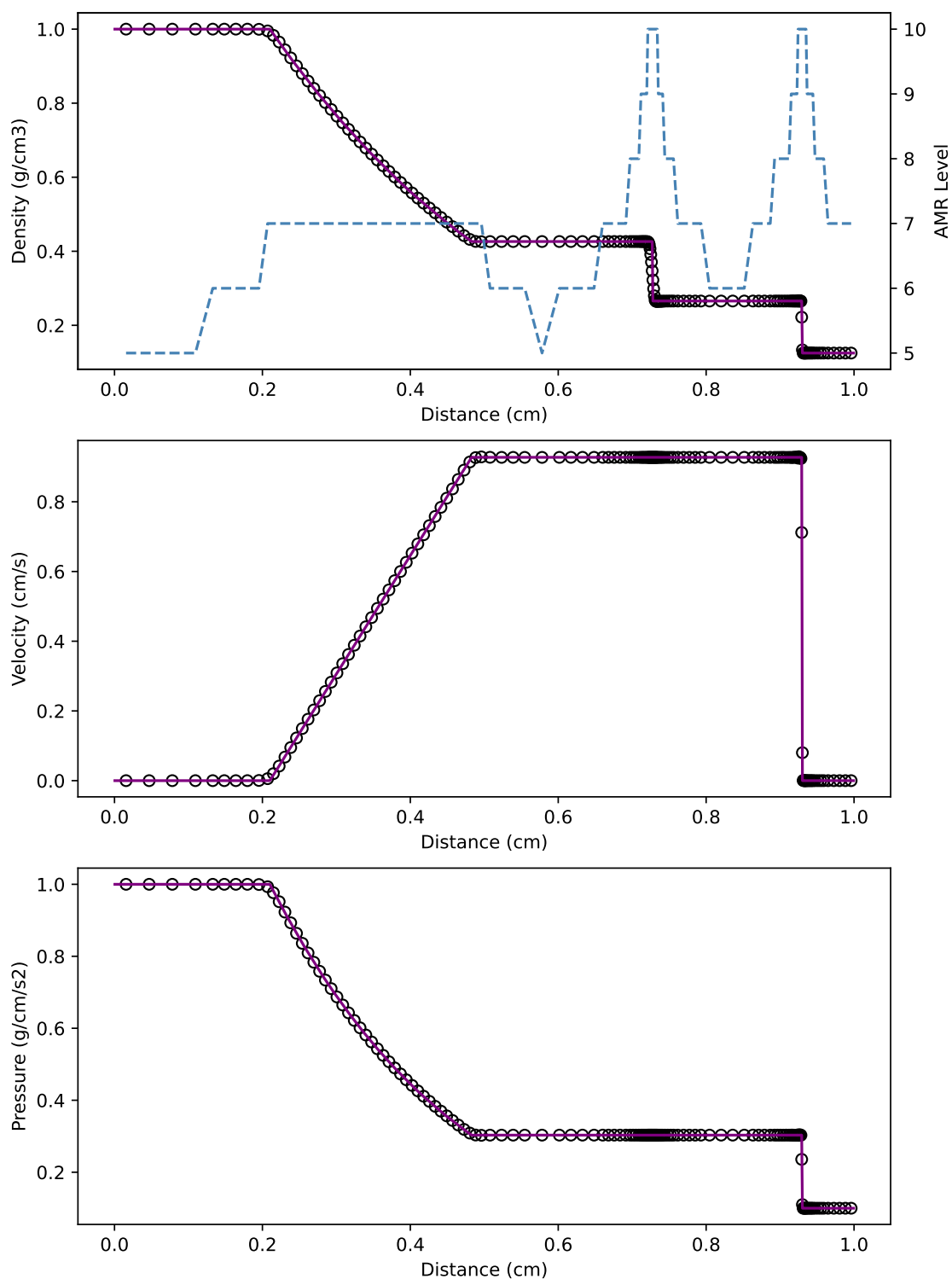


Figure 2.11: Same as in Fig. 2.8, but with the AMR-HLLC Riemann solver. The level of refinement (dashed blue curve) varies depending on the constraint from 3 to 10 and converges with a total number of 142 cells.

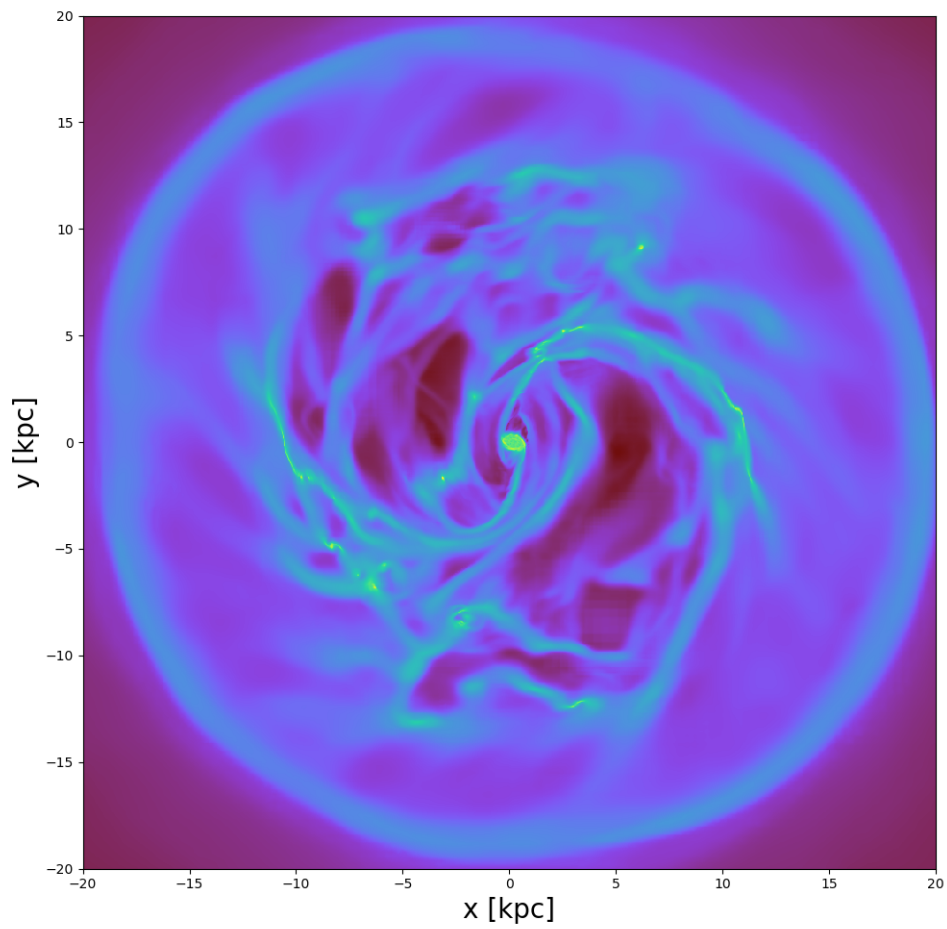


Figure 2.12: Gas surface density map of one of our simulation snapshots (model G105, see Chap. 4) performed in this work. The more yellow, the denser the gas region is.

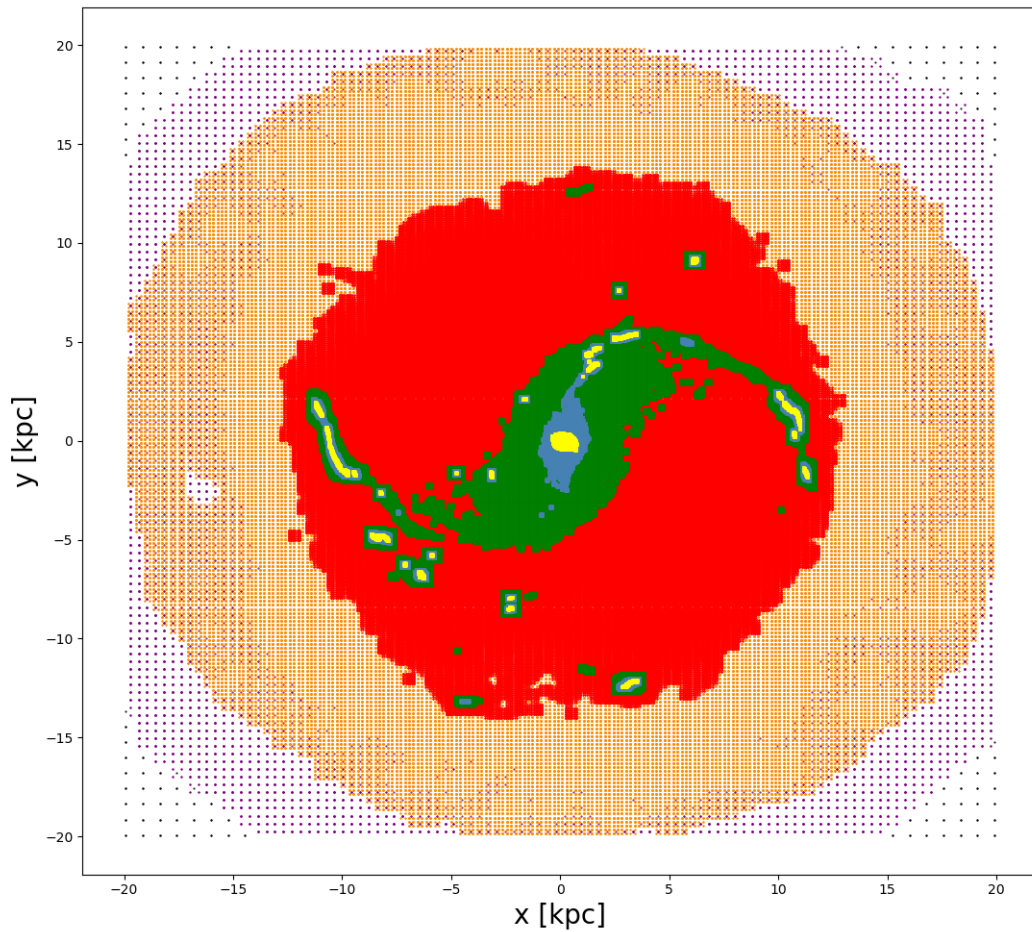


Figure 2.13: AMR grid of the simulation snapshot shown in Fig. 2.12. There are 7 levels of refinement shown by the coloured dots corresponding approximately to 780 (black), 390 (purple), 195 (orange), 98 (red), 49 (green), 25 (blue), and 12 (yellow) pc.

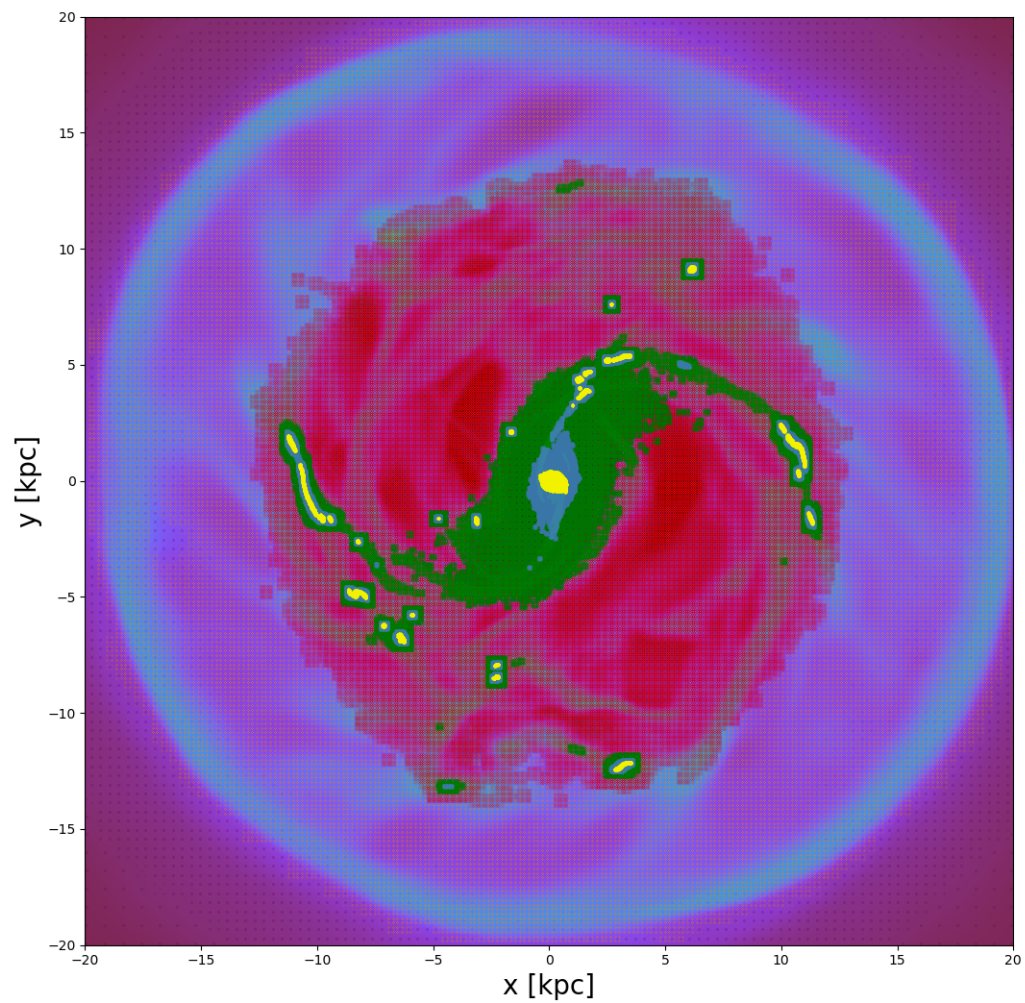


Figure 2.14: Superimposition of the AMR grid shown in Fig. 2.13 on the gas surface density map illustrated in Fig. 2.12.

Chapter 3

Methods and simulations

This chapter aims to describe and explain in detail the analysis of the PHANGS-ALMA sample (see Leroy et al., 2021) we performed to design the grid of models based on five galactic parameters (i.e., the stellar mass, the gas fraction, the scale length of the star and gas distribution, and the bulge mass fraction). This grid is the basis of the initial condition (IC) files containing the positions and velocities of the star and DM particles and the total rotation curve for the gas component. We will also describe the technique we used to generate the particle file by solving the Jeans equation. We will conclude with an insight into the various numerical recipes implemented in the code.

3.1 The PHANGS-ALMA sample as a basis for a grid of galactic models

The PHANGS-ALMA survey (Leroy et al., 2021) is a robust set of data that we can use to explore the morphology and dynamics of a hundred nearby main sequence low-inclined disc galaxies. This specific configuration ‘almost face on’ of those galaxies allows us to probe their central region and study the gas properties of their inner molecular disc (Sormani & Barnes, 2019). It also allows us to extract more robust values of their stellar and gas mass contents and their azimuthally-averaged radial surface density profiles. The grid of galactic models we present in this chapter is based on control parameters derived from those quantities. It aims to cover the full sample without modelling each galaxy composing it.

3.1.1 Five galactic parameters

The galactic properties we want to extract from the PHANGS-ALMA sample must contain a comprehensive description of the galaxies we want to model. We need at least two parameters for the global properties of the star and gas components: the total stellar mass M_\star and gas mass M_g (atomic, molecular, and ionised hydrogen). We also need to know the distribution of those components and in the following, we will assume a simple exponential distribution that leads us to use two additional parameters: the stellar scale length l_\star and the gas scale length l_g . The last parameter is related to the morphological properties of the central few kiloparsec region of disc galaxies that can display the presence of a stellar bulge for which we can use its mass M_b as the main indicator. We can summarise those five galactic properties with the following set of parameters:

1. the stellar mass $M_\star = M_d + M_b$,
2. the gas fraction $\alpha = M_g / (M_\star + M_g)$,
3. the typical stellar scale length l_\star ,
4. the ratio between the stellar and gas scale length l_\star / l_g ,
5. the bulge mass fraction $\beta = M_b / M_\star$,

where M_d stands for the mass of the stellar disc. We can directly obtain the first two parameters (i.e., M_* and M_g) from the sample, but we need further analysis to obtain the values of the last three parameters.

3.1.2 Surface density fitting to model the stellar and gas distribution

The analysis of the stellar and gas surface density profiles reveals that the stellar and gas components show an exponential behaviour for their disc but necessitate an additional non-exponential component in the central region in the stellar profile. The exponential surface density profile for the star and gas disc is written as follows:

$$\Sigma_{d,*/g}(r) = \Sigma_{0,d,*/g} \exp\left(-\frac{r}{l_{*,g}}\right), \quad (3.1)$$

where $\Sigma_{*,g,0}$ is the surface density profile at $r = 0$. The non-exponential component in the central region of the stellar profile can be interpreted as a 3D bulge or central disc¹ and can be modelled thanks to a Sersic profile (Sérsic, 1963) written as follows:

$$\Sigma_b(r) = \Sigma_{0,b} \exp\left(-b_n \left[\left(\frac{r}{R_{e,b}}\right)^{1/n_b} - 1\right]\right), \quad (3.2)$$

where $\Sigma_{0,b}$ is the surface density profile at $R_{e,b}$ corresponding to the typical bulge scale length, n_b the bulge index, and b_n is a coefficient depending on the value of n_b . Assuming that the stellar density profile is the sum of both, the disc and bulge components, we can apply a fitting method to the PHANGS stellar and gas surface density profiles and obtain a range of values for l_* , l_g , and β through $R_{e,b}$ and n_b .

Depending on their quality, we classify the results of the fit by ranking them with three different values: 1 when the fit is good, 0 when the fit is good enough, and -1 when the fit is bad and the results cannot be trusted. Figure 3.1 shows an example of a good fit of the stellar (top panel) and gas (bottom panel) surface density profile. The blue curves represent the exponential fit of the disc and the red curve in the top panels shows the total fit with the bulge taken into account. Figure 3.2 shows the result of a good enough fit (left panel) and a bad fit (right panel). The fit becomes worse when the profile shows some peculiar features and cannot be modelled with a simple exponential disc and a bulge component.

3.1.3 The grid of models

The results of the fits of the entire set of PHANGS surface density profiles and the chosen values of the IC are shown in Fig. 3.3. In this figure, the attributed rank 1, 0, and -1

¹The degeneracy between a real 3D bulge and a central disc can be only raised thanks to a more advanced analysis of the kinematics and has not been performed in this work.

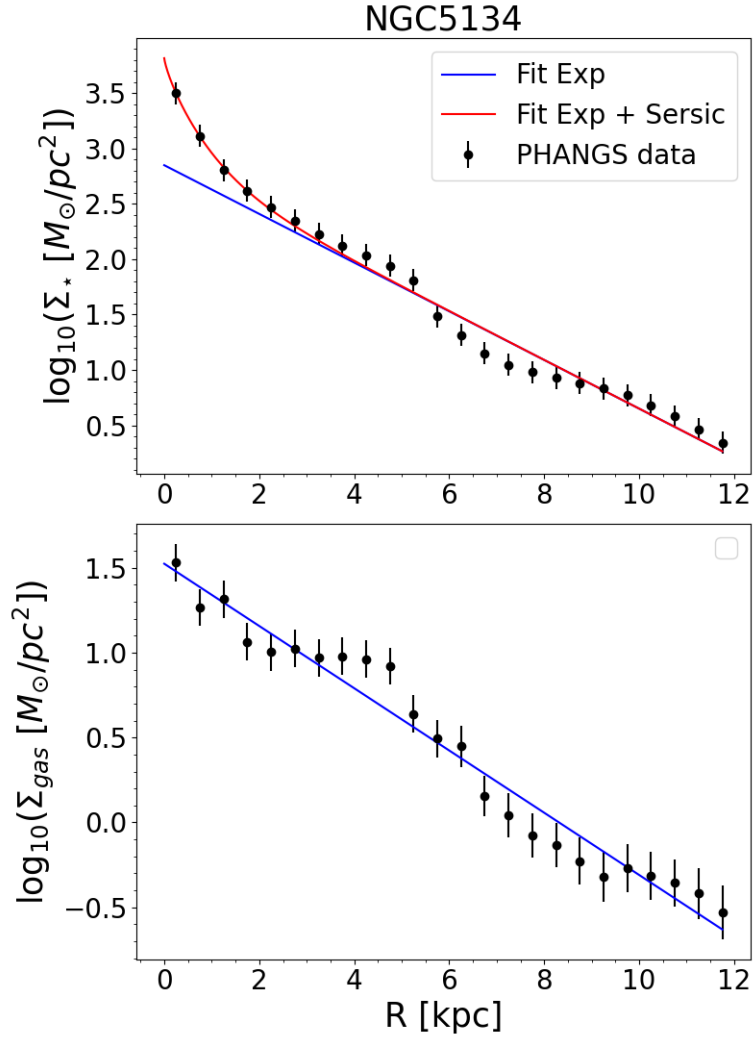


Figure 3.1: Stellar and gas surface density profile of the galaxy NGC5134 (black dots) with their corresponding fit=1 for their discs (blue curves) and bulge (red curve).

of the fits are represented by the green, yellow, and brown circles, respectively. The stars represent the values we chose for the IC and the purple stars indicate the first-priority set of models we decided to simulate. This first-priority set represents most of the parameter values covered by the PHANGS sample and is the basis for our first publication (Verwilghen et al., 2024) presented and detailed further in Chap. 4. The ICs are based on five different values of the stellar mass (i.e., $10^{9.5}$, 10^{10} , $10^{10.5}$, and $10^{11} M_{\odot}$) as illustrated by our grid of models as shown in Tab. 3.1.

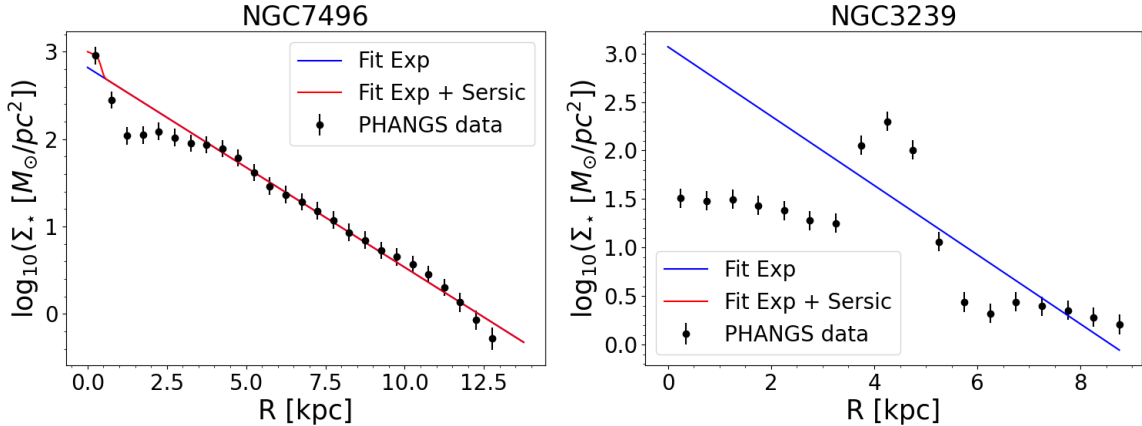


Figure 3.2: Gas surface density profiles of the galaxies NGC7496 and 3239 (black dots) with their corresponding fit=0,-1 on the left and right panels, respectively for their discs (blue curves) and bulge (red curve).

$\log_{10}(M_\star [M_\odot])$	α [%]	l_\star [kpc]	l_g/l_\star	β [%]
9.5	10, 20, 40	2, 3	2	0, 10, 30
10	10, 20, 40	2, 3	2	0, 10, 30
10.5	10, 20	3, 4	2	0, 10, 30
11	10, 20	5	2	0, 10, 30

Table 3.1: Grid of models with the different values for the control parameters based on the PHANGS sample. The grid is built on 4 galaxy stellar mass values, then covering a broad range of characteristic properties which cover the observed sample.

3.1.4 The choice of the Dark Matter halo profile and black hole - stellar mass relation

In addition to the stellar and gas components, we also need to include a proper DM halo in our models. The choice of the DM halo can be done in different ways, but in this work, we used an approach reproducing as much as possible the global trend of the PHANGS rotation curves, knowing already the rotation curves obtained with the gas and stellar components. Since the determination of the DM halo can be only done via indirect measurements, it is fairly difficult to determine which DM halo profile, such as Einasto, NFW, or Burkert (Einasto, 1965; Burkert, 1995; Navarro et al., 1997) reproduces as best as possible the DM halo of PHANGS galaxies. A brief representation of those three profiles is shown in Fig. 3.4. In our galactic models, we use the Einasto profile because it is quite similar to the Sersic one and does not go to infinity at the centre. Moreover, we see that the choice of the halo index leads to behaviours similar to the NFW and Burkert profiles. The Einasto profile is given by:

$$\rho_h(r) = \rho_{0,h} \exp\left(-2m \left[\left(\frac{r}{l_h}\right)^{1/m} - 1\right]\right), \quad (3.3)$$

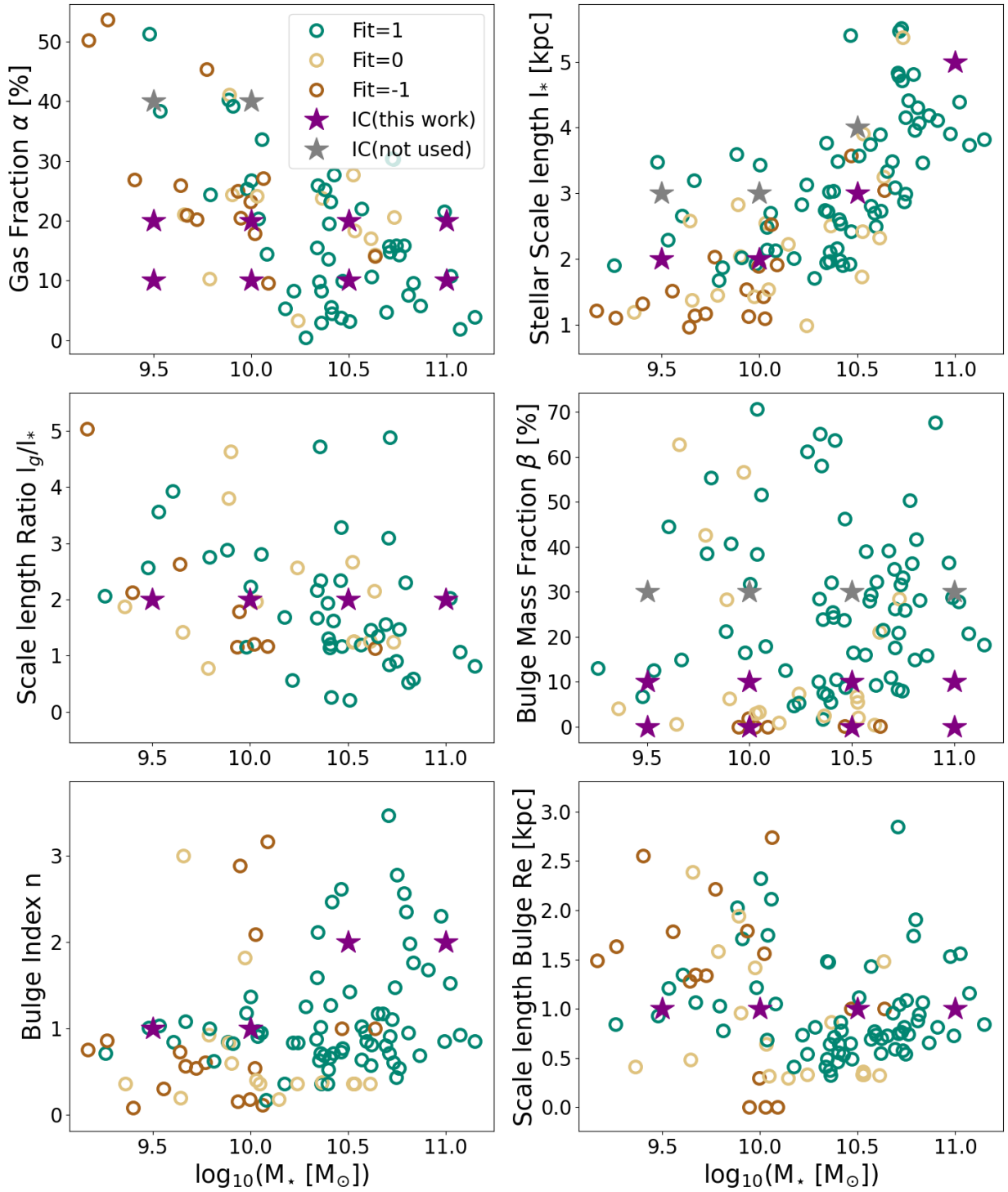


Figure 3.3: Results of the fits for the different galactic parameters (see text). The ICs are illustrated by the stars. The purple stars represent the ICs we use in priority.

where $\rho_{0,h}$, l_h , and, m are the halo density at $r = l_h$, scale length, and index, respectively. The values of those parameters and the central BH mass (see Reines & Volonteri, 2015, in Fig. 1.9) are computed as a function of the stellar mass of our models and are shown in Tab. 3.2.

Figure 3.5 shows a comparison between the rotation curves obtained from our galactic models (coloured solid curves) and the PHANGS rotation curves (coloured shaded areas) for the four different stellar masses. We observe that our models reproduce quite well the global trend of the PHANGS ones. It is important to note here that those curves are our initial conditions and will evolve over time, leading to various features (e.g., peak in the central kpc region) in the rotation curves.

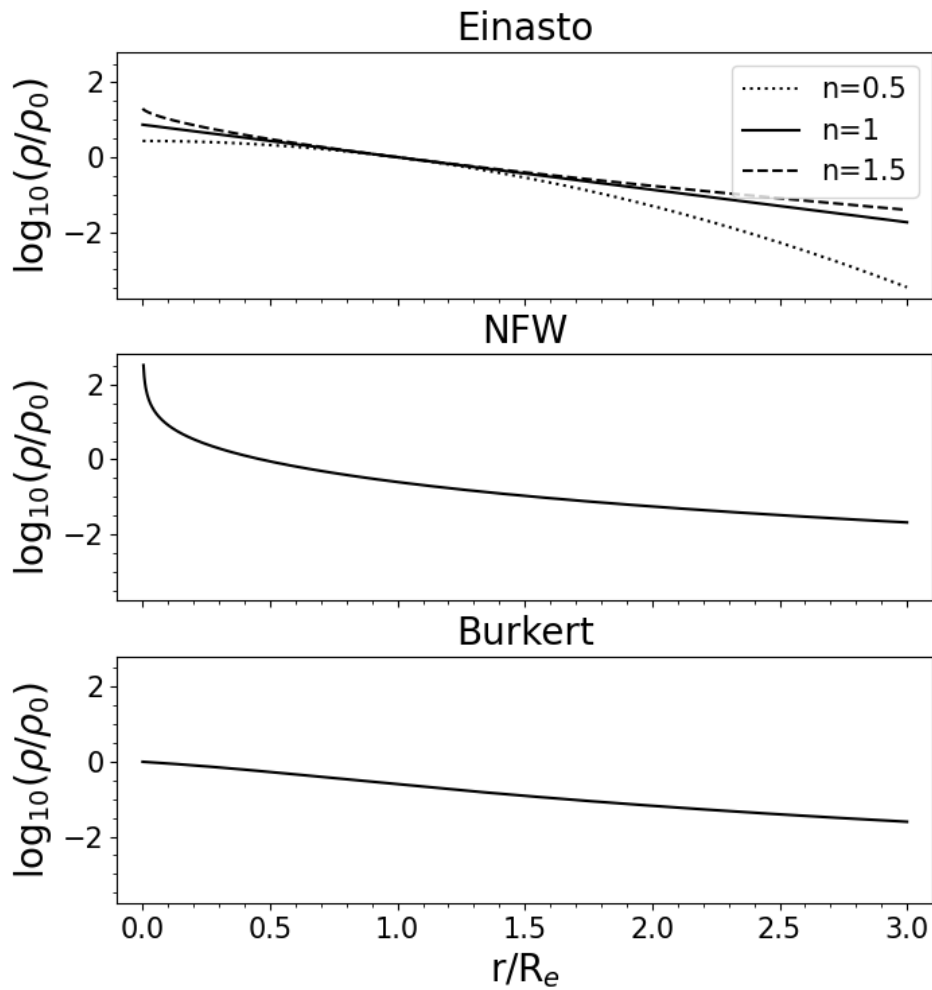


Figure 3.4: Three dark matter halo profiles represented by the Einasto, NFW, and Burkert profiles in the top, middle, and bottom panel, respectively.

M_\star $\log_{10}([M_\odot])$	$\rho_{0,h}$ $[M_\odot/\text{pc}^3]$	l_h [kpc]	m	M_{BH} $\log_{10}([M_\odot])$
9.5	3×10^{-4}	20	3	5.5
10	6×10^{-4}	25	3.5	6
10.5	7×10^{-4}	30	1.5	6.5
11	8.5×10^{-4}	35	2	7

Table 3.2: Grid of values for the parameters describing the dark matter profiles (i.e. $\rho_{0,h}$, the halo density; l_h , the typical halo scale length; and m , the halo index) as a function of the stellar mass M_\star . Those values have been inspired by the work of [Kun et al. \(2017\)](#), but their final values have been chosen to match the PHANGS rotation curves. The central BH masses M_{BH} we use in the initial conditions are also shown in the last column.

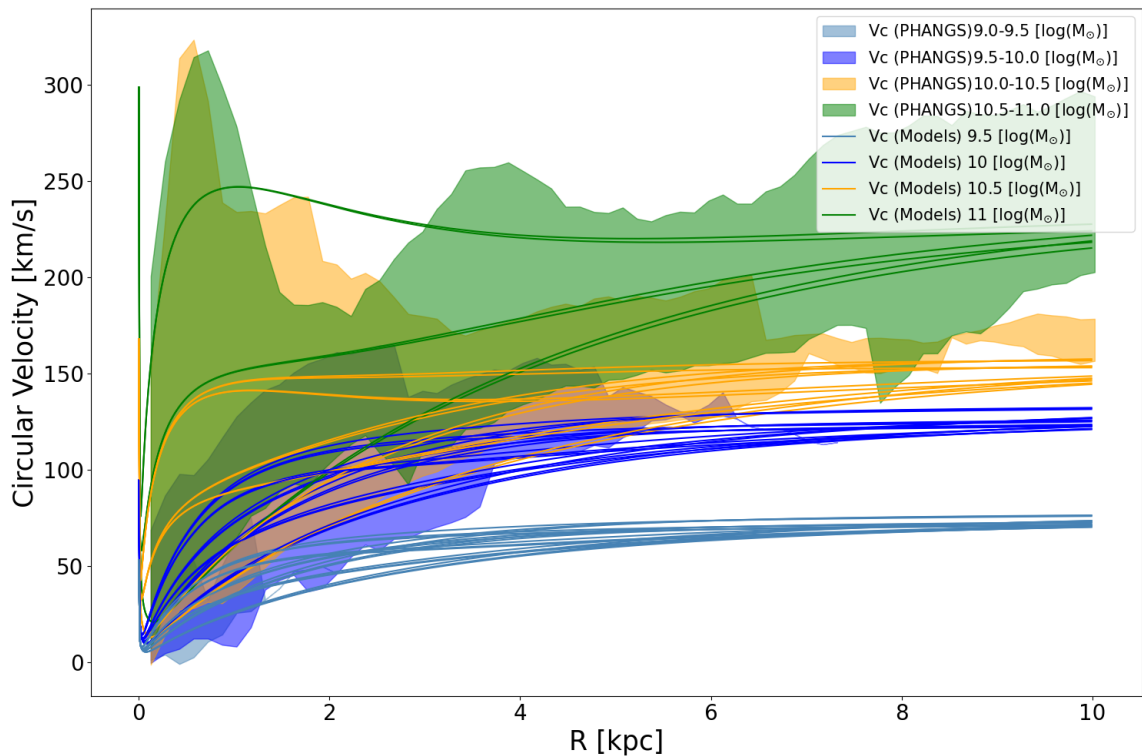


Figure 3.5: Initial circular velocity curves of our 54 models. The colour of the curve illustrates the stellar mass range of the model. The shaded coloured areas show the envelopes of the PHANGS velocity curves for the different stellar mass bins.

3.2 Generating the initial conditions

This section aims to describe the tools we used to generate the IC of our galactic models. We briefly show the basics of the MGE method in a very simple case where we assume the galaxies are face-on with a simple axis ratio in the z direction for the different dynamical

components. Then, we explain how to use the Jeans equations to build our dynamical models at equilibrium and create a file containing all the positions and velocities of each particle.

3.2.1 The Multi Gaussian Expansion method

Our models have three or four dynamical components: the disc and bulge of stars (stellar component), the gas disc, and the DM halo. As mentioned in the previous section, we have fitted the azimuthally-averaged surface density profiles of the stellar and gas components of the full sample of PHANGS galaxies and extracted the general properties of those profiles with the values of the galactic parameters in Tab. 3.1. The goal of the Multi Gaussian expansion (MGE, see Monnet et al., 1992; Emsellem et al., 1994a) method here is to fit those individual profiles with different sets of 1D Gaussian functions and deproject them in the 3D space to obtain a 3D density profile.

The general 2D form of the observed surface density profile $\Sigma_{*,g,h}$ (stars, gas, and DM halo) is then approximated as follows:

$$\Sigma_{*,g,h}(x', y') = \sum_{n=1}^N I_n \exp\left(-\frac{x_n'^2 + \frac{y_n'^2}{q_n^2}}{2\sigma_n^2}\right), \quad (3.4)$$

with

$$\begin{cases} x'_n = (x' - x'_{0n}) \cos(\alpha_n) + (y' - y'_{0n}) \sin(\alpha_n), \\ y'_n = -(x' - x'_{0n}) \sin(\alpha_n) + (y' - y'_{0n}) \cos(\alpha_n), \end{cases} \quad (3.5)$$

where (x'_{0n}, y'_{0n}) is the position of the maximum of the intensity in the sky plane coordinates (x', y') , and α_n the position angle of the major axis. I_n , q'_n , and σ_n are the amplitude, the axis ratio, and the standard deviation of the nth Gaussian. In the following, we consider that our galactic models are already centred (i.e., $(x'_{0n}, y'_{0n}) = (0,0)$) and face-on with all $q'_n = 1$ and $\alpha_n = 0$. Hence, the sky plane parameter $s_n^2 = x_n'^2 + y_n'^2/q_n'^2$ corresponds with the squared galactic radius $r^2 = x^2 + y^2$ written as a function of the galactic coordinates (x, y) and the observed surface density profile given by Eq. 3.4 can be rewritten as:

$$\Sigma_{*,g,h}(r) = \sum_{n=1}^N I_n \exp\left(-\frac{r^2}{2\sigma_n^2}\right). \quad (3.6)$$

Now, we just need to find a set of N Gaussian functions with the appropriate intensities I_n and standard deviations σ_n to fit the PHANGS surface density profiles of stars and gas. Figure. 3.6 illustrates the decomposition of a stellar density profile with a set of 23 Gaussian functions (bulge and disc). The deprojection requires an axis ratio q_n in the z direction, thus leading to the general expression for a three-dimensional density profile given by:

$$\rho_{*,g,h}(x, y, z) = \sum_{n=1}^N P_n \exp\left(-\frac{x^2 + y^2 + \frac{z^2}{q_n^2}}{2\sigma_n^2}\right), \quad (3.7)$$

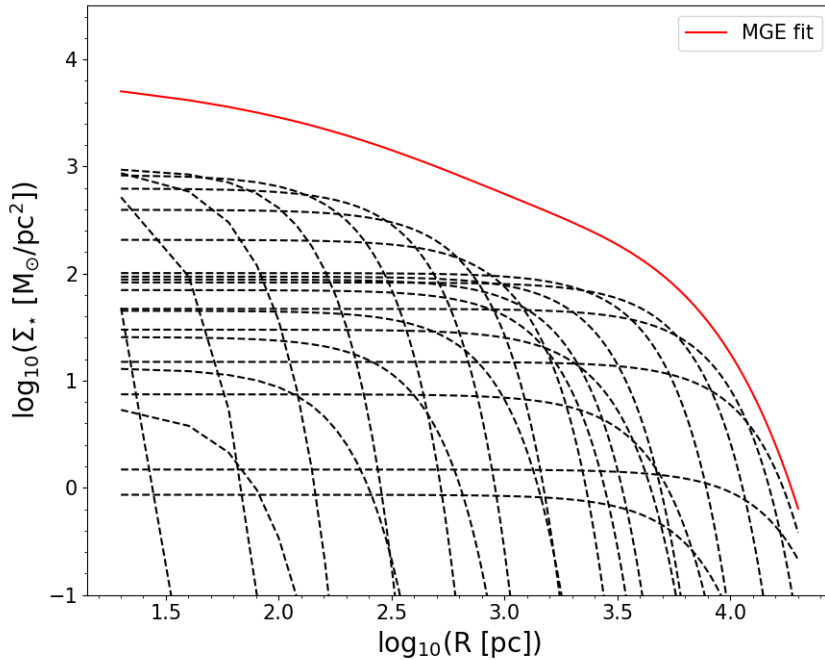


Figure 3.6: Illustration of a stellar density profile reconstruction (red curve) via the MGE method with a set of 23 Gaussian functions

where $P_n = I_n/(\sqrt{2\pi}\sigma_n)$. We have now all the ingredients to model the different dynamical components of our models, but we still need one last thing to generate the initial conditions that we will develop in the next section.

3.2.2 The Jeans equations

The galaxies we want to simulate are initially in equilibrium and we need a set of equations to model such systems. Since our galactic systems are composed of a large number of particles, we can consider them as a fluid of stars and DM and we introduce the distribution function $f(\vec{r}, \vec{v}, t)$, which is defined in a phase space of $6-N$ parameters (3 position components and 3 velocity components), with N being the number of particles. If we knew the form of this function at any time, then we would be able to fully describe the system. However, this function cannot be analytically written with millions of parameters and has to be treated from a statistical point of view.

If we assume that the collision term vanishes, we can write that:

$$\frac{df}{dt} = 0 \quad (3.8)$$

because the phase-space density f of the fluid around a given star remains the same if we

do not take the collisions between stars into account (i.e., the flow through phase space of the probability fluid is incompressible). Developing the total derivative with respect to time, we get:

$$\frac{\partial f}{\partial t} + \vec{v} \cdot (\vec{\nabla}_{\vec{r}} f) - \vec{\nabla}_{\vec{r}} \Phi \cdot (\vec{\nabla}_{\vec{v}} f) = 0, \quad (3.9)$$

where the operator $\vec{\nabla}_{\vec{r}, \vec{v}}$ stands for the partial derivative with respect to the positions ($\vec{r} = (x, y, z)$) and velocities ($\vec{v} = (v_x, v_y, v_z)$). The gravitational potential Φ is the total gravitational potential and only depends on the positions. Equation. 3.9 is known as the collisionless Boltzmann (or Vlasov) equation and is used to derive the so-called Jeans equations.

The first Jeans equation corresponds to the integral over the velocity space of Eq. 3.9 and is given by:

$$\begin{aligned} \int \frac{\partial f}{\partial t} d^3 \vec{v} + \int \vec{v} \cdot (\vec{\nabla}_{\vec{r}} f) d^3 \vec{v} - \int \vec{\nabla}_{\vec{r}} \Phi \cdot (\vec{\nabla}_{\vec{v}} f) d^3 \vec{v} &= 0 \\ \Leftrightarrow \frac{\partial \nu}{\partial t} + \vec{\nabla} \cdot (\nu \vec{v}) &= 0 \end{aligned} \quad (3.10)$$

which corresponds to the continuity equation with

$$\begin{aligned} \nu &= \int f d^3 \vec{v} \\ \vec{v} &= \frac{1}{\nu} \int \vec{v} f d^3 \vec{v}, \end{aligned} \quad (3.11)$$

where ν and \vec{v} are the normalised density distribution and mean velocity field, respectively.

The second Jeans equation is obtained with a second moment integration over the velocities. Using the component notation and the Einstein convention for the sum over repeated index, the j th component is written as:

$$\begin{aligned} \int v_j \frac{\partial f}{\partial t} d^3 \vec{v} + \int v_j v_i \frac{\partial f}{\partial x_i} d^3 \vec{v} - \int v_j \frac{\partial \Phi}{\partial x_i} \frac{\partial f}{\partial v_i} d^3 \vec{v} &= 0 \\ \Leftrightarrow \frac{\partial}{\partial t} (\nu \bar{v}_j) + \frac{\partial}{\partial x_i} (\nu \bar{v}_i \bar{v}_j) &= -\nu \frac{\partial \Phi}{\partial x_j} \end{aligned} \quad (3.12)$$

with

$$\bar{v}_i \bar{v}_j = \frac{1}{\nu} \int v_i v_j f d^3 \vec{v} \quad (3.13)$$

using Eq. 3.10 and assuming the following form for the stress tensor

$$\sigma_{ij}^2 = \bar{v}_i \bar{v}_j - \bar{v}_i \bar{v}_j \quad (3.14)$$

we can show that Eq. 3.12 can be rewritten:

$$\frac{\partial \bar{v}_j}{\partial t} + \bar{v}_i \frac{\partial \bar{v}_j}{\partial x_i} = -\frac{1}{\nu} \frac{\partial}{\partial x_i} (\nu \sigma_{ij}^2) - \frac{\partial \Phi}{\partial x_j} \quad (3.15)$$

which corresponds to the equivalent of the equations of hydrodynamics or the so-called Navier-Stokes equations.

3.2.3 Building dynamical models with the MGE method to generate the IC

The unknowns we need to extract to generate our IC are the positions and velocities of each particle, including the mean and dispersion velocities. The calculation of the positions is straightforward and is determined thanks to a Gaussian random draw after generating our dynamical model. The velocities are computed in two steps.

The first ingredient we need to build our dynamical model is to find a form for the mean velocities, to this end, we need to solve Eq. 3.12 for the three components of the mean velocity field $\vec{v} = (\bar{v}_x, \bar{v}_y, \bar{v}_z)$ in the stationary case ($\partial(\rho\bar{v}_j)/\partial t = 0$) for each dynamical component of the system. We also replace ν by the actual physical density $\rho_{*,g,h} \equiv \rho$ that we have obtained in the previous section. We then get:

$$\frac{\partial}{\partial x}(\rho\bar{v}_x^2) + \frac{\partial}{\partial y}(\rho\bar{v}_y\bar{v}_x) + \frac{\partial}{\partial z}(\rho\bar{v}_z\bar{v}_x) = -\rho\frac{\partial\Phi}{\partial x} \quad (3.16a)$$

$$\frac{\partial}{\partial y}(\rho\bar{v}_y^2) + \frac{\partial}{\partial x}(\rho\bar{v}_x\bar{v}_y) + \frac{\partial}{\partial z}(\rho\bar{v}_z\bar{v}_y) = -\rho\frac{\partial\Phi}{\partial y} \quad (3.16b)$$

$$\frac{\partial}{\partial z}(\rho\bar{v}_z^2) + \frac{\partial}{\partial x}(\rho\bar{v}_x\bar{v}_z) + \frac{\partial}{\partial y}(\rho\bar{v}_y\bar{v}_z) = -\rho\frac{\partial\Phi}{\partial z} \quad (3.16c)$$

It is important to note that Φ in Eq. 3.16 represents the total gravitational potential of the galactic system (i.e., stars, gas and DM halo), but the density ρ can just be the density of any component. To solve this equation for the three squared mean velocity components $(\bar{v}_x^2, \bar{v}_y^2, \bar{v}_z^2)$, we need to integrate this equation with respect to the corresponding spatial variable (x, y, z) . Taking into account the fact that $(\bar{v}_x^2, \bar{v}_y^2, \bar{v}_z^2) \rightarrow 0$ when $(x, y, z) \rightarrow \infty$, we have:

$$\bar{v}_x^2 = \int_x^\infty \left(\rho\frac{\partial\Phi}{\partial x} + \frac{\partial}{\partial y}(\rho\bar{v}_y\bar{v}_x) + \frac{\partial}{\partial z}(\rho\bar{v}_z\bar{v}_x) \right) dx, \quad (3.17a)$$

$$\bar{v}_y^2 = \int_y^\infty \left(\rho\frac{\partial\Phi}{\partial y} + \frac{\partial}{\partial x}(\rho\bar{v}_x\bar{v}_y) + \frac{\partial}{\partial z}(\rho\bar{v}_z\bar{v}_y) \right) dy, \quad (3.17b)$$

$$\bar{v}_z^2 = \int_z^\infty \left(\rho\frac{\partial\Phi}{\partial z} + \frac{\partial}{\partial x}(\rho\bar{v}_x\bar{v}_z) + \frac{\partial}{\partial y}(\rho\bar{v}_y\bar{v}_z) \right) dz. \quad (3.17c)$$

In the general case, we can always write a relation between the first and second moment of the mean velocity given by:

$$\bar{v}_x\bar{v}_y = (1 + \mu)\bar{v}_x\bar{v}_y, \quad (3.18a)$$

$$\bar{v}_x\bar{v}_z = \mu'\bar{v}_x\bar{v}_y, \quad (3.18b)$$

$$\bar{v}_y\bar{v}_z = \mu''\bar{v}_x\bar{v}_y, \quad (3.18c)$$

where the function μ, μ' , and μ'' are called the anisotropy functions. To solve the system of Eq. 3.17, we need to compute the gravitational potential Φ and find a relation for the

second-order terms of the velocity components $\overline{v_i v_j}$. In the following, we will consider an oblate ellipsoid described in a cylindrical coordinate system. Given the form of Eq. 3.7, the gravitational potential is written as (see Binney et al., 2009; Emsellem et al., 1994a):

$$\Phi(R, z) = -4\pi G \sum_{i=1}^N q_n \sigma_n^2 P_n \int_0^1 \frac{\exp\left(-\frac{T^2}{2\sigma_n^2} \left(R^2 + \frac{z^2}{1-(1-q_n^2)T^2}\right)\right)}{\sqrt{1-(1-q_n^2)T^2}} dT \quad (3.19)$$

The second ingredient is the determination of the form of the dispersion velocity tensor given in Eq. 3.14 assuming cylindrical symmetry about the z-axis for an oblate ellipsoid. We will then need to use the cylindrical coordinates (R, ϕ, z) to compute the respective velocities (v_r, v_ϕ) , and v_z . In such a case, the different components of the stress tensor are given by:

$$\sigma_R^2 = \overline{v_R^2}, \quad (3.20a)$$

$$\sigma_\phi^2 = \overline{v_\phi^2} - \overline{\Theta}^2, \quad (3.20b)$$

$$\sigma_z^2 = \overline{v_z^2}, \quad (3.20c)$$

and the corresponding Jeans equations are written:

$$\frac{\partial(\rho\sigma_R^2)}{\partial R} + \rho \left(\frac{\sigma_R^2 - (\sigma_\phi^2 + \overline{\Theta}^2)}{R} + \frac{\partial\Phi}{\partial R} \right) = 0, \quad (3.21a)$$

$$\frac{\partial(\rho\sigma_z^2)}{\partial z} + \rho \frac{\partial\Phi}{\partial z} = 0. \quad (3.21b)$$

We know that in the oblate case:

$$\mu = \frac{\sigma_R^2 - \sigma_\phi^2}{\overline{\Theta}^2}, \quad (3.22a)$$

$$\mu' = \mu'' = 0, \quad (3.22b)$$

$$k_\phi(R, z) = \frac{\sigma_\phi^2}{\sigma_z^2}, \quad (3.22c)$$

and if we assume that $\sigma_R^2 = \sigma_z^2$ we can write:

$$\rho\sigma_z^2 = \int_z^\infty \rho \frac{\partial\Phi}{\partial z} dz, \quad (3.23a)$$

$$\rho(\sigma_\phi^2 + \overline{\Theta}^2) = R \frac{\partial(\rho\sigma_z^2)}{\partial R} + \rho\sigma_z^2 + \rho R \frac{\partial\Phi}{\partial R}, \quad (3.23b)$$

and we have now all the ingredients for our dynamical models. We just need to compute the velocity dispersions and then inject the result in Eq. 3.17 to compute the mean velocities. Once the dynamical model is built, we can use a Gaussian random draw to create the particles with their respective position (x, y, z) and velocities (v_x, v_y, v_z) in an ASCII file.

The content of one of our IC files is shown in Fig. 3.7 with a face-on (edge-on) view of the galaxy in the left (right) panel. This figure illustrates the position of the DM, gas, and stellar components with the black, blue, and yellow particles, respectively. A bulge component (red) is also present in the central region of the model. It is important to note that the gas particles are shown in both panels for comprehension purposes, but they are not given to RAMSES in the IC file since the code generates the gas component on the AMR grid with an initial tangential velocity given by the rotation curve (i.e., circular velocity) presented in Fig. 3.8. In this figure, the total rotation curve is shown by the black dashed curve and is split into its individual dynamical components given by the DM, stars, and gas illustrated by the black, yellow, red, and blue curves. The 54 rotation curves are shown in Fig. 3.5. More details on the numerical recipes of the gas component are developed in the following section.

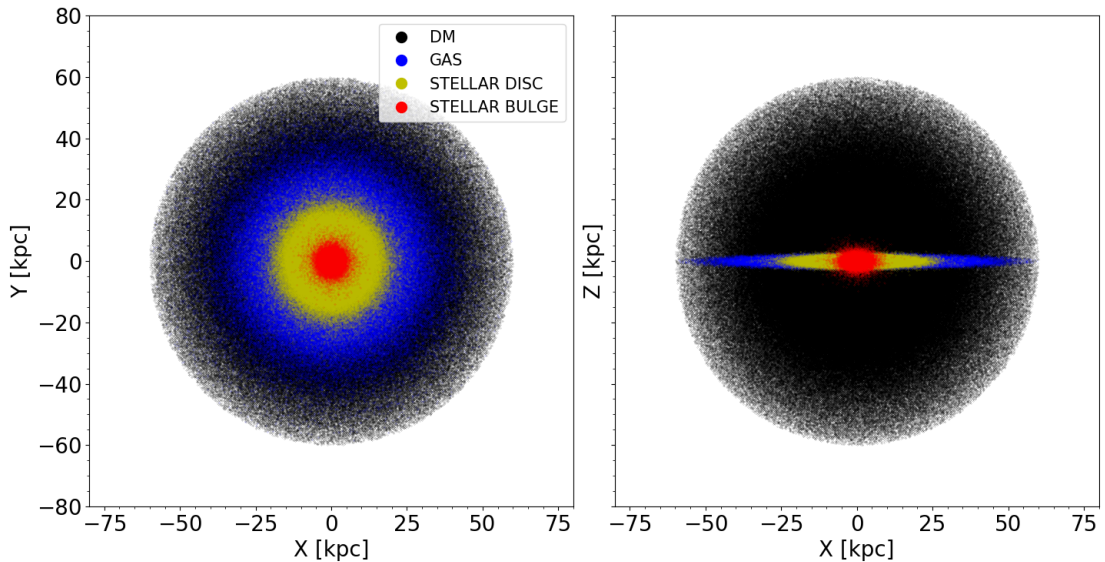


Figure 3.7: Content of one of our IC files. The left panel shows a face-on view of the model and the right panel shows an edge-on view. The colours represent the different dynamical components of the galaxy with the DM, gas, and stars in black, blue, yellow and red, respectively. The gas component is shown for a comprehensive overview of our models, but it is not given to the code as ICs. The galactic model corresponds to a galaxy having a stellar mass of $10^{10.5} M_{\odot}$ and a gas fraction of 10 %.

3.3 Numerical recipes used in RAMSES

In this section, we describe the three main aspects of the code we used to model the sub-grid physical phenomena in our simulations. We first present and detail the Jeans refinement strategy we applied to set the constraints on the AMR grid and reach a maximum resolution of 12 pc for our grid of models. Then, we briefly show the main characteristics

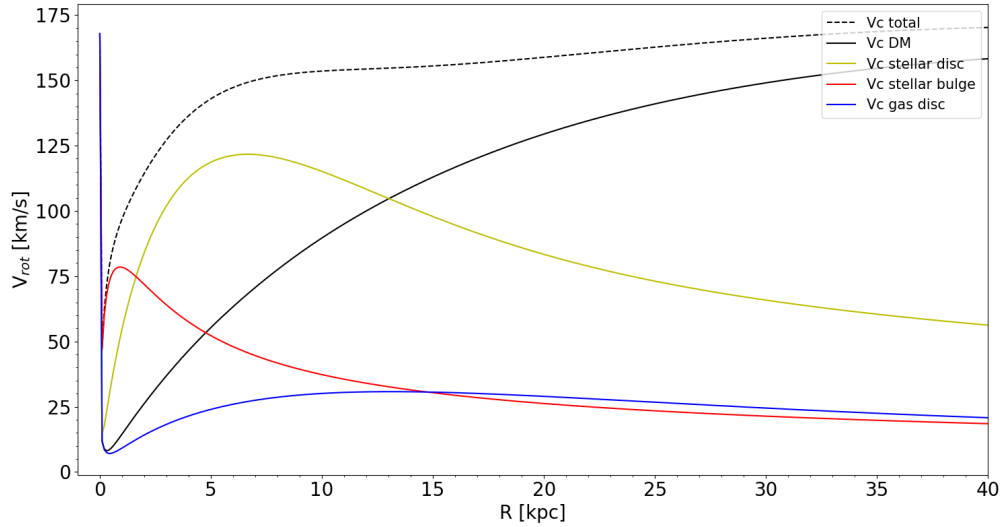


Figure 3.8: Rotation curve of the model shown in Fig. 3.7. The total rotation curve is given by the black dashed curve. The black, yellow, red, and blue curves represent the different dynamical components of the model: the DM, stars (disc and bulge), and gas, respectively.

of the EOS and the cooling function we used to model the thermodynamics of the gas component. Finally, we will illustrate the star formation method and detail the numerical recipes implemented in RAMSES for the stellar feedback.

3.3.1 The Jeans refinement strategy

The Jeans mass

The code deals with the hydrodynamics of the simulation by distributing the gas component on the AMR grid. The refinement of the grid (i.e., the creation of new cells smaller than the ones on the lower refinement levels) is determined by a constraint on the mass of the cell based on the Jeans criterion. The Jeans mass of a molecular cloud is the critical mass above which the cloud will start to collapse by fragmenting and creating new stars. The Jeans mass of a molecular cloud of radius R_J is simply given by:

$$M_J = \frac{4\pi}{3} R_J^3 \rho, \quad (3.24)$$

where ρ is the density of the sphere. Here, $R_J = \lambda_J/2$ with λ_J is the Jeans scale length given by:

$$\lambda_J = \frac{c_s}{1/t_{ff}}, \quad (3.25)$$

where c_s is the sound speed and t_{ff} the so-called free-fall time. This characteristic time is obtained by computing the time it would take for a sphere of radius R to collapse and

reach its centre by only considering the gravity and without any pressure force acting on it and pushing the material outward. This free-fall time is written as:

$$t_{ff} = \frac{1}{(G\rho)^{1/2}}, \quad (3.26)$$

where G is the gravitational constant. Using Eq. 3.25 and 3.26 in 3.24, we obtain:

$$M_J = \frac{\pi}{6} \frac{c_s^3}{G^{3/2}\rho^{1/2}}. \quad (3.27)$$

We see that the Jeans mass is inversely proportional to the square root of the gas density, which means that M_J decreases with increasing density. The main problem with the above reasoning is that it does not take into account the thermodynamics of the molecular cloud. Indeed, it is important to keep in mind that the sound speed c_s also depends on the temperature.

To determine the relation between the Jeans mass and the temperature, we present a very simple model of a self-gravitating sphere of radius R made of an ideal gas which experiences a contraction of its radius from R to $R - dR$. The work done by gas is given by:

$$dW = pdV = \frac{\rho k_B T}{m_\mu} 4\pi R^2 dR \quad (3.28)$$

where k_B is the Boltzmann constant and m_μ is the mean molecular weight of the gas. The gravitational energy released during this contraction is written as:

$$dU = \frac{3G}{5} \frac{M^2}{R^2} dR. \quad (3.29)$$

The critical mass is reached when the work is equal to the gravitational energy. Replacing R by $(M/(\frac{4}{3}\pi\rho))^{1/3}$ and after a bit of algebra one can write:

$$M_J = \left(\frac{375k_B^3}{4\pi G^3 m_\mu^3} \right)^{1/2} \left(\frac{T^3}{\rho} \right)^{1/2}. \quad (3.30)$$

By comparing Eq. 3.30 with 3.27, we see that the sound speed is then proportional to the square root of the temperature. We need to express the gas temperature as a function of the gas density to obtain an expression for the Jeans mass which only depends on the thermodynamic variable ρ . We assume that the collapse is, as a first approximation, an adiabatic process and we can thus write:

$$\begin{aligned} PV^\gamma &= \text{constant}, \\ \Rightarrow V &\propto P^{(1/\gamma)} \Rightarrow P \propto T^{\frac{\gamma}{\gamma-1}}, \end{aligned} \quad (3.31)$$

where γ is the adiabatic exponent. If we consider a polytrope having an EOS given by $P \propto \rho^\gamma$, with the same adiabatic exponent, we find the following relation:

$$T \propto \rho^{\gamma-1}, \quad (3.32)$$

and using Eq. 3.30, we can write that the final relation between the Jeans mass and the density is given by:

$$M_J \propto \rho^{\frac{3}{2}(\gamma - \frac{4}{3})} \quad (3.33)$$

where we can see different regimes for the Jeans mass depending on the value of γ . When $\gamma < 4/3$, the Jeans mass decreases with increasing density. In particular, $\gamma = 1$ corresponds to Eq. 3.27 and 3.30 in the case of an isothermal sphere. When $\gamma > 4/3$ then we have a regime for which the Jeans mass increases with increasing density. In the case of an ideal monoatomic gas ($\gamma = 5/3$) the Jeans mass is proportional to the square root of the density.

The refinement strategy

To derive a law for the refinement scheme, we need to express the Jeans mass as a function of the cell size. The Jeans mass can be written without loss of any generality as follows:

$$\begin{aligned} M_{J,l} &= K \rho^\alpha = K \left(\frac{M_{J,l}}{V_l} \right)^\alpha \\ \Leftrightarrow M_{J,l} &= K \left(\frac{M_{J,l}}{\left(\frac{L_{box}}{2^l} \right)^3} \right)^\alpha \\ \Leftrightarrow M_{J,l} &= K \left(\frac{L_{box}}{2^l} \right)^{\frac{3\alpha}{\alpha-1}} \end{aligned} \quad (3.34)$$

where K is just a coefficient related to the geometry of the cloud, L_{box} the size of the box we use in the simulations, and l the level of refinement. We will see in the next section that the gas can be approximated by a polytrope of index $\gamma = 1/2$ (see, Fig. 3.10 from Renaud et al., 2013a, only for the part where $\gamma = 1/2$), which corresponds to an index $\alpha = -5/4$ and a Jeans mass given by:

$$M_{J,l} = K \left(\frac{L_{box}}{2^l} \right)^{5/3}. \quad (3.35)$$

In practice, to determine the Jeans mass of the cell at level l , we introduce the following notation: $l = l_{min} + lev_i$, assuming a minimum level l_{min} for which every cell has reached this minimum level of refinement. In the following, lev_i is simply the i^{th} level from which we start to apply the Jeans refinement strategy. We can then write:

$$M_{J,i} = K \left(\frac{L_{box}}{2^{l_{min}}} \right)^{5/3} \frac{1}{(2^{lev_i})^{5/3}} = K \left(\frac{cl_{min}}{2^{lev_i}} \right)^{5/3}, \quad (3.36)$$

where cl_{min} is the length of the cell corresponding to l_{min} . Introducing some arbitrary level lev_0 , we can write:

$$M_{J,0} = K \left(\frac{cl_{min}}{2^{lev_0}} \right)^{5/3} = K (cl_0)^{5/3}, \quad (3.37)$$

and dividing Eq. 3.36 by 3.37, we find:

$$\frac{M_{J,i}}{M_{J,0}} = \left(\frac{cl_{min}}{cl_0} \right)^{5/3} \frac{1}{(2^{lev_i})^{5/3}}. \quad (3.38)$$

Now, we consider that we can write $M_{J,i} \equiv m_{sphn,i} = m_{sph,i} m_{ref,i}$, where $m_{sph,i}$ is the mass scale length for cells at level i , and $m_{ref,i}$ is a number we set corresponding also to the number of particles (stars and DM) inside a cell we use as a threshold for the refinement to the next level. In the end, the expression for the jeans mass of the cell at level i is given by:

$$m_{sphn,i} = m_{sph,0} m_{ref,0} \left(\frac{cl_{min}}{cl_0} \right)^{5/3} \frac{1}{(2^{lev_i})^{5/3}}. \quad (3.39)$$

We have used a box scale length L_{box} of 100 kpc with $l_{min} = 7$ for the majority of our set of simulations (we have used a box length of 200 kpc for the most massive model and just needed to shift the refinement levels). This corresponds to a minimum cell size cl_{min} of 781.25 pc. The arbitrary level $lev_0 = 9$ corresponds to a cell size cl_0 of 195.3125 pc and a Jeans mass $m_{sph,0}$ of $1.77 \times 10^5 M_\odot$, with $m_{ref,0} = 8$ particles. Fig. 3.9 shows the law of Eq. 3.39 for an AMR grid going from the 7th to the 14th level of refinement for a box of 100 kpc. In this figure, the red dots correspond to the jeans mass threshold required to refine the cell from the previous to the indicated level. In our simulations, we refine the grid up to the 13th level, corresponding to a cell size of ~ 12 pc.

3.3.2 Gas cooling, star formation, and stellar feedback

Energy equation and cooling function

The hydro-dynamical equations RAMSES needs to solve are coupled to an energy equation with a cooling term. This cooling term is a function of the gas temperature as shown in Fig. 3.11 (from Agertz et al., 2013) for different values of the metallicity Z . In our simulations, we have used the same value as for the Sun ($Z = 1Z_\odot$ shown by the solid black curve). The physical processes implemented in the cooling function include (see Rey et al., 2020, for more details) photoionisation, collisional ionisation and excitation, recombination, bremsstrahlung, Compton cooling and heating, and dielectronic recombination. The contribution of metal lines to the total cooling is extracted from tabulated models generated with CLOUDY (see Ferland et al., 1998). The heating is modelled from reionization through a spatially uniform, time-dependent UV background. This implementation is based on an updated version of Haardt & Madau (1996).

Star formation and stellar feedback

When one of the smallest cells of the AMR grid reaches a certain threshold of atom density n_\star , the cell starts to create new stars following the law:

$$\frac{d\rho_\star}{dt} = \frac{\rho_g}{t_{SF}} \text{ for } \rho_g \geq m_h n_\star, \quad (3.40)$$

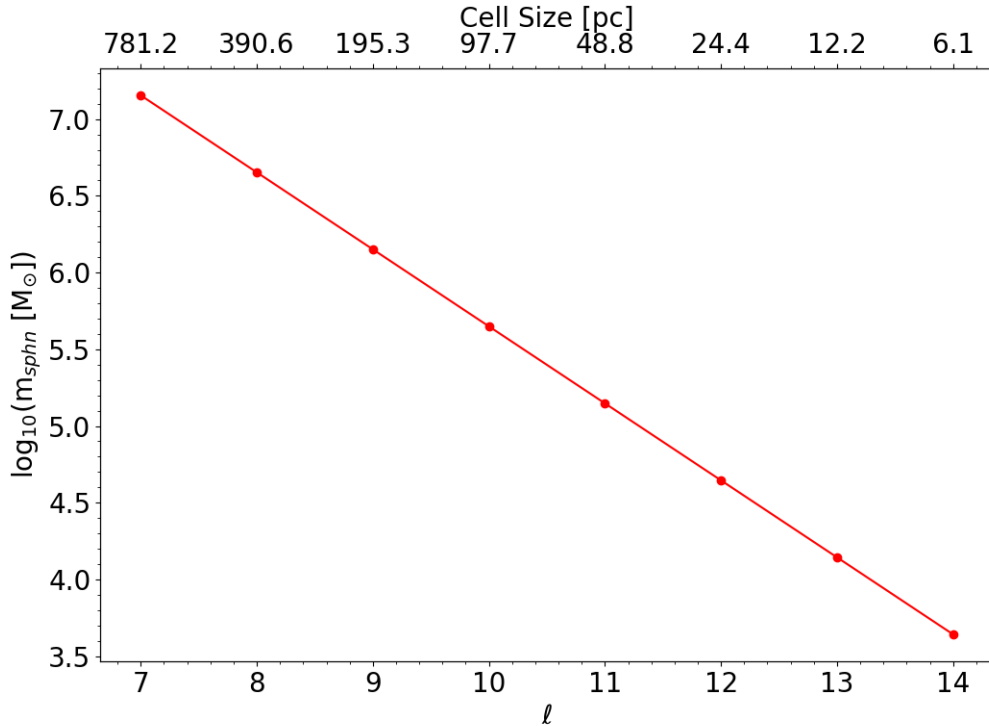


Figure 3.9: Jeans mass (m_{sphn}) of the ℓ^{th} level of refinement going from the 7th to the 14th for a box length of 100 kpc. We also show on the top x-axis the corresponding cell size. The red dots are the Jeans mass threshold required to refine the grid from the previous to the corresponding level.

with

$$t_{SF} = \frac{t_{ff}}{\epsilon_{ff}}, \quad (3.41)$$

where ρ_{\star} and ρ_g , t_{SF} , t_{ff} , ϵ_{ff} , and m_h are the density of newly-formed stars, the gas density, the typical gas depletion time, the free-fall time, the star-forming efficiency per free-fall time, and the mass of the hydrogen atom. The value of the parameter n_{\star} is determined thanks to Eq. 3.39 by computing the density we would need to refine the last level of refinement from the 13th (12 pc) to the 14th (6 pc) and use that Jeans mass as a threshold for star formation. We find as a result a density corresponding to $\sim 100 \text{ cm}^{-3}$, which corresponds to a stellar mass density of $\sim 2.42 M_{\odot}/\text{pc}^3$ and a free-fall time t_{ff} of ~ 9.59 Myr. We chose a star-forming efficiency per free-fall time ϵ_{ff} of 2%, corresponding to a typical gas depletion time of ~ 479 Myr. In our simulation, we set the stellar mass of the newly-formed stars to $2000 M_{\odot}$.

The following numerical recipe for stellar feedback is described with more detail in Agertz et al. (2021a). Once a new star forms, it is treated as a single-age stellar population with an initial mass function (Chabrier, 2003). The code accounts for the injection of energy, momentum, mass, and heavy elements over time from core-collapse SN and SNIa,

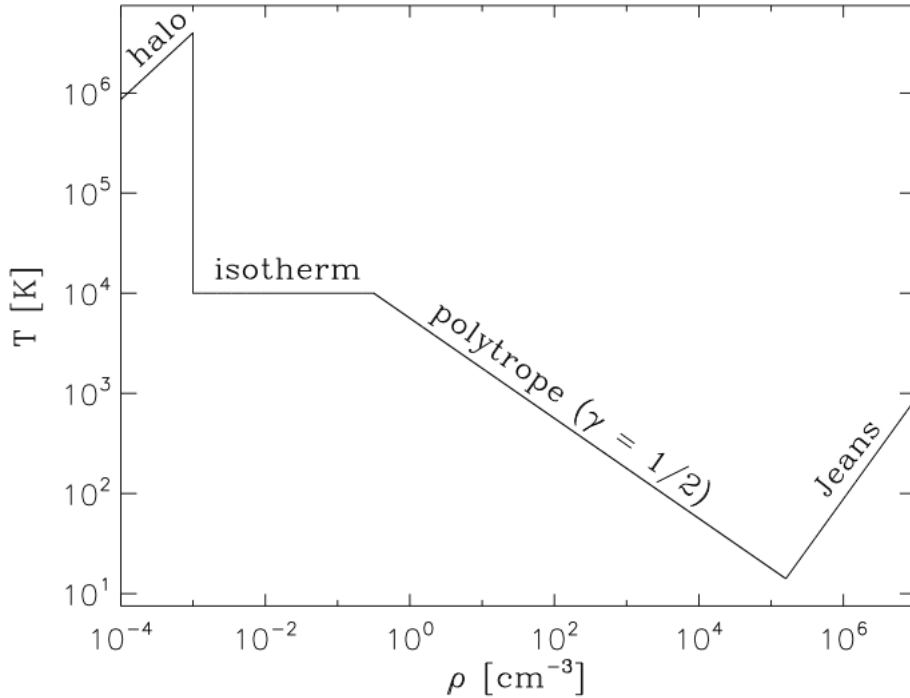


Figure 3.10: Equation of state (EOS) presented in [Renaud et al. \(2013a\)](#) and used in older versions of RAMSES.

stellar winds, and radiation pressure on the surrounding gas. Each mechanism depends on stellar age, mass, and gas/stellar metallicity (through the metallicity-dependent age–mass relation ([Raiteri et al., 1996](#)), calibrated on the stellar evolution code STARBURST99 (see [Leitherer et al., 1999](#)). More details on the specifics of how it is implemented are described in ([Agertz et al., 2013](#)). To account for the effect of SN feedback, we adopt the model suggested by [Kim & Ostriker \(2015\)](#). They demonstrated that to capture the momentum injection from individual SNe, the cooling radius must be captured by at least three grid cells to avoid numerical overcooling. In this thesis, we adopt six grid cells per cooling radius as a minimum requirement for SNe to be considered as resolved. If this criterion is fulfilled, we initialize the explosion in the ‘energy conserving’ phase by injecting 10^{51} erg per SN into the nearest grid cell. When insufficient resolution is available, the explosion is instead initialized in its ‘momentum conserving’ phase, with the momentum built up during the Sedov–Taylor phase injected into cells surrounding the star particle.

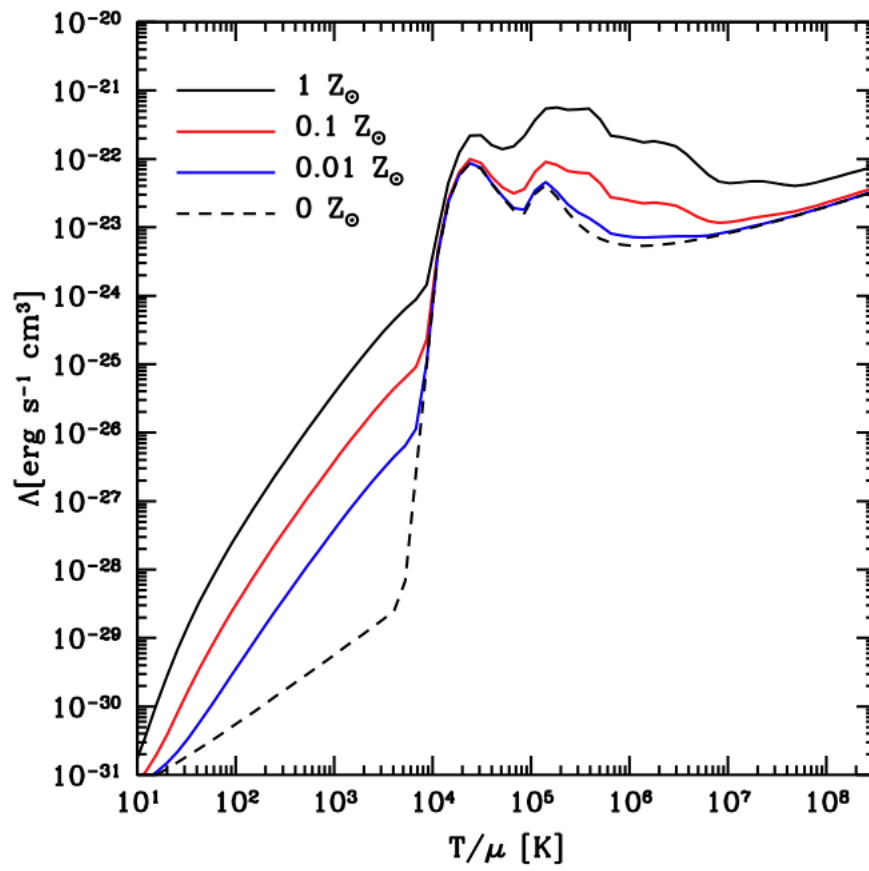


Figure 3.11: Cooling function used in [Agertz et al. \(2013\)](#) and implemented in RAMSES.

Chapter 4

Bar formation and the building of the central gas reservoir

This chapter and the following one are a slight rearrangement of the first (Verwilghen et al., 2024) and the second (Verwilghen et al., submitted) publication. Those two papers are to be published in the *A&A* Journal and we had to make minor modifications to make them fit and keep coherence with the present thesis manuscript. Note that we provided an extended part of the method section (from the present chapter) to build a more detailed and coherent flow in the previous chapter of the thesis manuscript, leading to some limited repetitions (text, figure).

Abstract

Past studies have long emphasised the key role played by galactic stellar bars in the context of disc secular evolution, via the redistribution of gas and stars, the triggering of star formation, and the formation of prominent structures such as rings and central mass concentrations. However, the exact physical processes acting on those structures, as well as the timescales associated with the building and consumption of central gas reservoirs are still not well understood. We are building a suite of hydro-dynamical RAMSES simulations of isolated, low-redshift galaxies that mimic the properties of the PHANGS sample. The initial conditions of the models reproduce the observed stellar mass, disc scale length, or gas fraction, and this paper presents a first subset of these models. Most of our simulated galaxies develop a prominent bar structure, which itself triggers central gas fuelling and the building of an over-density with a typical scale of 100-1000 pc. We confirm that if the host galaxy features an ellipsoidal component, the formation of the bar and gas fuelling are delayed. We show that most of our simulations follow a common time evolution, when accounting for mass scaling and the bar formation time. In our simulations, the stellar mass of $10^{10} M_{\odot}$ seems to mark a change in the phases describing the time evolution of the bar and its impact on the interstellar medium. In massive discs ($M_{\star} \geq 10^{10} M_{\odot}$), we observe the formation of a central gas reservoir with star formation mostly occurring within a restricted starburst region, leading to a gas depletion phase. Lower-mass systems ($M_{\star} < 10^{10} M_{\odot}$) do not exhibit such a depletion phase, and show a more homogeneous spread of star-forming regions along the bar structure, and do not appear to host inner bar-driven discs or rings. Our results seem to be supported by observations, and we briefly discuss how this new suite of simulations can help our understanding of the secular evolution of main sequence disc galaxies.

4.1 Introduction

Bars and spiral arms both form naturally in galaxy disc-like systems (see [Eskridge et al., 2000](#); [Buta et al., 2015](#); [Sellwood & Masters, 2022](#), and references therein). They have a significant impact on the internal disc structures, induce specific torques and resonant regions, and impose, via the tumbling and varying gravitational potential, constraints on the galactic orbital skeleton. Bars have been specifically and extensively studied and modelled ([Combes & Sanders, 1981](#); [Kaufmann & Contopoulos, 1996](#); [Athanasoula, 1992a](#); [Kormendy & Kennicutt, 2004](#); [Barazza et al., 2008](#); [Gadotti, 2008](#); [Kraljic et al., 2012](#); [Goz et al., 2015](#); [Fragkoudi et al., 2017](#)) and have a direct influence on the short- and long-term evolution of the system. We know that bars funnel the gas to the central regions (~ 100 pc) of galaxies, and have been suggested to play a role in the large-scale fuelling of the central SMBH (SMBH; [Fukuda et al., 1998](#); [Shlosman et al., 1989](#); [Ho et al., 1997](#)).

Similarly to our own Milky Way, most nearby disc galaxies are also believed to host central SMBHs, with masses between $10^6 - 10^9 M_{\odot}$, at their centres ([Magorrian et al., 1998](#); [Reines & Volonteri, 2016](#)). When gas builds into a surrounding accretion disc, those SMBHs can drive nuclear activity ([Krolik, 1999](#); [Padovani et al., 2017](#)), releasing a large amount of energy in its environment in the form of mainly radiative (quasar mode) or mechanical (radio mode) feedback ([Sanders et al., 1988](#); [Fabian, 2012](#)). Such active galactic nuclei (AGNs) may impact the dynamical evolution of their host galaxy, their chemical composition, and even modulate the central gas accretion itself (see e.g. [Combes, 2017](#), and references therein).

The exact physical mechanisms and timelines associated with the fuelling of central SMBHs are still heavily debated (see e.g. [Hopkins & Quataert, 2010](#); [Cheung et al., 2015](#)), both due to the range of spatial and timescales involved and to the complexity and non-linear nature of the physical processes involved. The duty cycle of an accretion disc more directly depends on small-scale physics and the close environment of the BH (10^{-6} to 10^{-2} pc), while the larger-scale kiloparsec dynamics and structures may influence its long-term evolution. Two main avenues are generally called upon for the global transport of gas in disc galaxies. An external channel or origin is when low angular momentum gas is falling from, for example, the circum-galactic medium (CGM) towards the galaxy centre ([Lacey & Fall, 1985](#); [Bilitewski & Schönrich, 2012](#)). An internal channel is connected to the secular evolution and processes, such as gravitational torques and stellar-driven feedback, acting as a way to extract angular momentum from the gas ([Porciani et al., 2002](#); [Stewart et al., 2013](#); [Übler et al., 2014](#); [Genel et al., 2015](#); [Pezzulli & Fraternali, 2016](#); [Schmidt et al., 2016](#); [Valentini et al., 2017](#)). The required amount of gas to trigger the AGN is relatively small compared with the total mass of gas available in the galaxy ([Hickox et al., 2012](#); [Padovani, 2017](#)). This means that only a very small fraction of the gas funnelled within the central few hundreds of parsecs is needed to account for the nuclear black-hole-related activity. Further considering the several orders of magnitude in spatial scale that are spanned from the galactic bar (kiloparsecs) to an accreting BH ($\sim 10^{-4} - 0.1$ pc, see e.g. [Guo et al., 2023](#); [Izumi et al., 2023](#), and references therein), it is not yet clear how the bar relates to the processes that are most relevant to drive the duty cycle of AGNs.

Progress may come from the realisation that many disc galaxies host a central overdensity of gas at a scale of a few hundreds of parsec from the centre (Comerón et al., 2010). While such structures may not directly relate with the ongoing nuclear activity itself, they can play the role of a ‘gas reservoir’ and represent an intermediate milestone that we need to understand if we wish to draw a full picture of central gas accretion and its time evolution. Those gas reservoirs are often interpreted in the context of bars as coinciding with a change in the sign of the torques (Sanders, 1977; Wada, 1994), that is, the location of the so-called inner Lindblad resonance (ILR). However, these models fail to reproduce the results of hydro-dynamical simulations (Sormani et al., 2015), thus calling for a new framework that can explain the full picture (see Sormani et al., 2023a)). In the Milky Way, a ~ 200 pc central molecular zone (CMZ) with a gas mass of $\sim 1 - 7 \times 10^7 M_{\odot}$ has been identified and extensively studied (Ferrière et al., 2007; Longmore et al., 2013; Henshaw et al., 2023). In other galaxies, such gas reservoirs (or CMZs) have also been observed and again, often interpreted in the context of the gas fuelling by bars, while details of its building and life cycle (consumption via e.g. star formation) are not well constrained.

Some pioneering work was carried out by Athanassoula (1992b), who studied the response of gas to an idealised two-dimensional barred potential and observed the building of a central gas concentration within the central 1 kpc region. This study raised questions about the building, consumption, and overall evolution of central gas reservoirs, as well as their related physical phenomena, such as gravitational torques, shear, feedback, and the exact role of bars and spiral arms in fuelling the central regions. Those questions further triggered observational surveys and numerical works to study the fuelling rate and the size of those gas reservoirs (Combes et al., 2004; García-Burillo et al., 2005; Boone et al., 2007; Comerón et al., 2010; Sormani & Barnes, 2019; Sormani et al., 2023b). We still need a systematic approach to investigate numerically and characterise the different scenarios of the building and evolution of such gas reservoirs in a three-dimensional live potential (including stars, gas, and dark matter) for a set of models tailored to nearby disc galaxies.

In this paper, we focus on the design, running, and exploitation of a suite of numerical hydro-dynamical simulations of isolated disc galaxies to study the formation and evolution of bars, and the associated building of the central gas reservoirs. We motivated such a grid of simulations using the PHANGS¹-ALMA galaxy sample as a guiding baseline, which provides high-resolution, high-sensitivity, and short-spacing CO spectral cubes of nearby disc galaxies and they are ideal for comparison with the models.

In Sect. 4.2 we introduce the grid of models. In Sect. 4.3 we provide details regarding the code and numerical recipes we used to perform the simulations, and in Sect. 4.4 we present the first results extracted from that grid of simulations. We conclude in Sect. 4.5 with a brief summary.

¹Physics at High Angular resolution in Nearby GalaxieS: <https://sites.google.com/view/phangs/home>

4.2 Methods

4.2.1 The PHANGS-ALMA sample

As a basis to build our simulation sample, we used the PHANGS-ALMA survey (Leroy et al., 2021) which consists of 118 low inclination nearby main sequence star-forming disc galaxies (in a distance range of $\sim 3\text{-}30$ Mpc) with varying properties, including stellar mass, gas fraction, surface density and rotation curve (Lang et al., 2020). Those input parameters can be used to extract relevant control parameters to design a grid of initial conditions for our simulations. The most directly relevant galactic properties to build such a grid of simulations relate to the gravitational potential and associated baryonic mass distribution, hence including the stellar mass, the gas fraction and the presence of a stellar bar or not (Querejeta et al., 2021). The top panel of Fig. 4.1 shows the distribution of the stellar masses in the PHANGS sample, emphasising the distribution of barred and non-barred galaxies. The stellar masses range from $\sim 10^{9.25}$ up to $\sim 10^{11}$ M_{\odot} and the vast majority (~ 75 %) of that sample shows the presence of a central bar (Stuber et al., 2023).

4.2.2 The control parameters

The main objective of our grid of hydro-dynamical models is to study the impact of galaxy properties on the building and evolution of the central (few 100 pc) gas reservoirs. We thus focus primarily on the properties of galaxies that we expect would more directly impact the structure of bars and spiral arms (i.e. size, strength and pattern speed). Based on the observed properties of the PHANGS sample, we focus on five galactic parameters for our models, namely:

1. the stellar mass M_{\star} ;
2. the gas fraction $\alpha = M_g / (M_g + M_{\star})$ where $M_g = M_{\text{HI}} + M_{\text{H}_2}$;
3. the typical scale length of the stellar distribution l_{\star} ;
4. the typical scale length of the gas (HI and H2) distribution l_g ;
5. and the central bulge mass fraction $\beta = M_b / M_{\star}$.

In this work, only four of these parameters are used as control parameters since we set the value of the gas scale length to $2 l_{\star}$. We decompose the stellar mass into a given disc and central ellipsoid as $M_{\star} = M_d + M_b$, with M_d and M_b the mass of the stellar disc and the stellar ellipsoid, respectively. In the following, we will label ‘bulge’ this central ellipsoid, emphasising the fact that such a label is often misused to describe a central excess of light above a given larger-scale disc (Gadotti et al., 2020), leading to confusion. In our semantic usage, bulge refers to a structure that bulges out of the disc and must then be both extended (with scales significantly larger than e.g. a nucleus, or the scale height of

the disc) and puffed (e.g. axis ratio significantly above 0.2). Simple relations connect the gas and stellar disc masses with the α and β parameters, namely:

$$M_g = \frac{\alpha}{1 - \alpha} \cdot M_*, \quad M_d = (1 - \beta) \cdot M_*. \quad (4.1)$$

We select four values for the stellar mass, namely $\log_{10} M_*(M_\odot) = 9.5, 10, 10.5, 11$, to cover the PHANGS range (see Fig. 4.1).

We further examine the trends of all the other four input parameters as a function of the stellar mass. The right and bottom panels of Fig. 4.1 show the distribution of the gas fraction among the PHANGS galaxies and its values as a function of the stellar mass, respectively. The gas fraction tends to increase with decreasing stellar masses below $10^{10} M_\odot$. We assume exponential radial profiles both for the initial stellar and gas surface density (Σ_d, Σ_g accordingly) profiles and fitted all azimuthally averaged observed PHANGS profiles accordingly.

$$\Sigma_{d,*/g}(r) = \Sigma_{0,*/g} \exp\left(-\frac{r}{l_{*/g}}\right), \quad (4.2)$$

where l_* and l_g are respectively the stellar and gas scale length, and $\Sigma_{0,b}$ is the initial bulge surface density. During the fitting of the stellar density profile, we allow the simultaneous presence of a central component with a surface brightness profile described as an additional Sersic profile (Sérsic, 1963):

$$\Sigma_b(r) = \Sigma_{0,b} \exp\left(-b_n \left[\left(\frac{r}{R_{e,b}}\right)^{1/n_b} - 1\right]\right), \quad (4.3)$$

where r is the bulge coordinate radius, $\Sigma_{0,i}$ is the initial surface density, $R_{e,b}$ is the scale length, n_b is the Sersic index, and b_n is a coefficient depending on n_b calibrated to reach the half of the total luminosity at $R_{e,b}$. Since we wish that the three-dimensional ellipsoidal representation based on the one-dimensional Sersic function follows averaged properties of galactic bulges (Sérsic, 1963), we forced an intrinsic ellipticity of 0.4 (axis ratio of 0.6, see Moriondo et al. (1998); Sotnikova et al. (2012)), as opposed to the standard assumptions of a spheroid (i.e. a spherical bulge). As mentioned, in the following, that component will be referred to as the ‘central bulge’.

Fig. 4.2 shows an example of the stellar (top panel) and gas (bottom panel) surface density fits for one specific PHANGS galaxy (NGC 5134). Fits to the observed surface brightness profiles were not always satisfactory when the data could not be well represented by a single exponential or a combined exponential plus Sersic components. We thus visually classified our fits into three categories: [1] good fits, [0] reasonable fits (exhibiting radial ranges with significant residuals), and [-1] failed fits when no good representation of the data could be found using the above-mentioned functions (see Chap. 3, Fig. 3.2 for more details). This classification is subjective and only meant as a guide for the values of reference parameters when building up the grid of initial conditions: it does not have a significant impact on the chosen grid of models we have selected. This analysis led us to fix a set of values for l_* , l_g , $R_{e,b}$ and n_b for each galaxy in the PHANGS-ALMA sample:

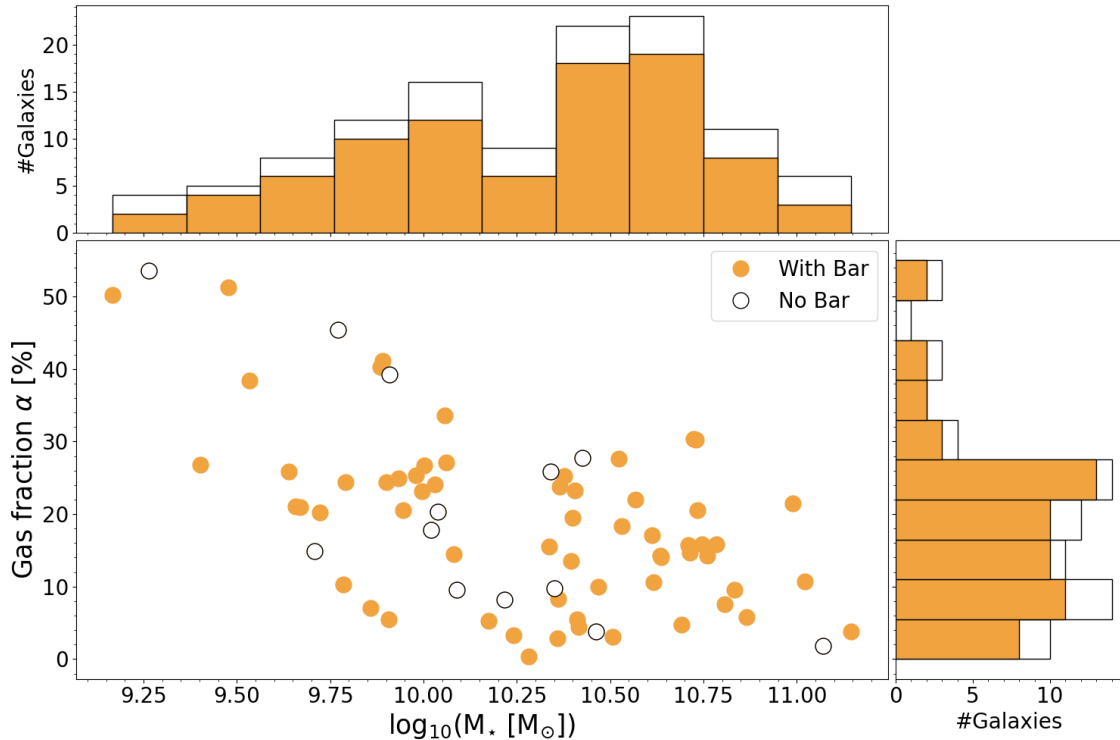


Figure 4.1: Gas fraction (α) as a function of the stellar mass of the galaxies in the PHANGS sample and the corresponding histograms for the stellar mass (top panel) and gas fraction (right panel) distribution (see Sect. 4.2.2).

those are shown in Fig. 4.3 where they are plotted as a function of the stellar mass. We also show the values of the gas fraction α and those of the bulge mass fraction as derived from the obtained scale lengths.

4.2.3 The grid of models

Our grid of models relies on a selected set of values for each of the four control parameters (see previous Section). As a first approximation, this set provides a fair representation of the global trends (e.g. with respect to the stellar mass) observed in the PHANGS sample. We sometimes constrained the value of a given parameter to stay constant at all masses, at the expense of missing the more relevant range of observed parameters². This is true, for instance, for the gas fractions (α) at the lowest stellar mass bin, where we chose to only probe 0 and 10%, thus departing from the significantly larger observed values. It is also the case for bulge mass fraction (β) for which we also kept low values (0 and 10%) while many targets exhibit values up to 40% or higher. This latter choice was motivated by the fact that we expect the central region to grow in mass during the secular evolution of the system and that most of the measured bulge indices are on the low side, hence most

²Note that an extended grid of models, better covering those missed ranges, is planned (see Sect. 4.5).

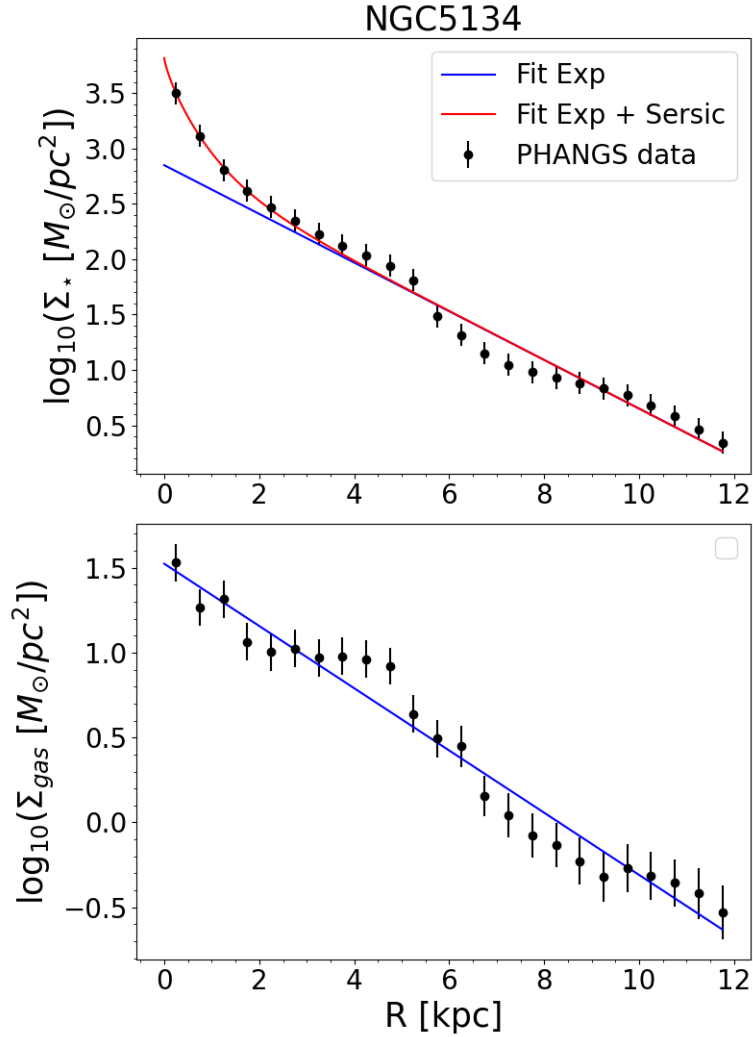


Figure 4.2: Illustrations of the fitted radial gas and stellar density profiles. The plots show the original data points (in black, see Sun et al. (2022), mega-tables version 3), i.e. the azimuthal-averaged surface density profiles for the stellar (top panel) and gas (bottom panel) components of the galaxy NGC 5134. The corresponding fits are superimposed and colour-coded accordingly (blue for the disc component, red for the total disc and ellipsoid (or bulge) component).

possibly reflecting the presence of a central (flattened) disc (not a puffed-up spheroid). In practice, those values have been used to build initial conditions for the hydro-dynamical simulations: they are illustrated by purple stars in Fig. 4.3 as mentioned before and are all tabulated in Table 4.1.

In the following, all models share a common labelling scheme, namely: each model adopts a format as GxxxMxxxFxxLxBxx, where "G (stands for Galaxy)" is followed by an integer (used as an internal reference), M by the log of the stellar mass multiplied by 10, F

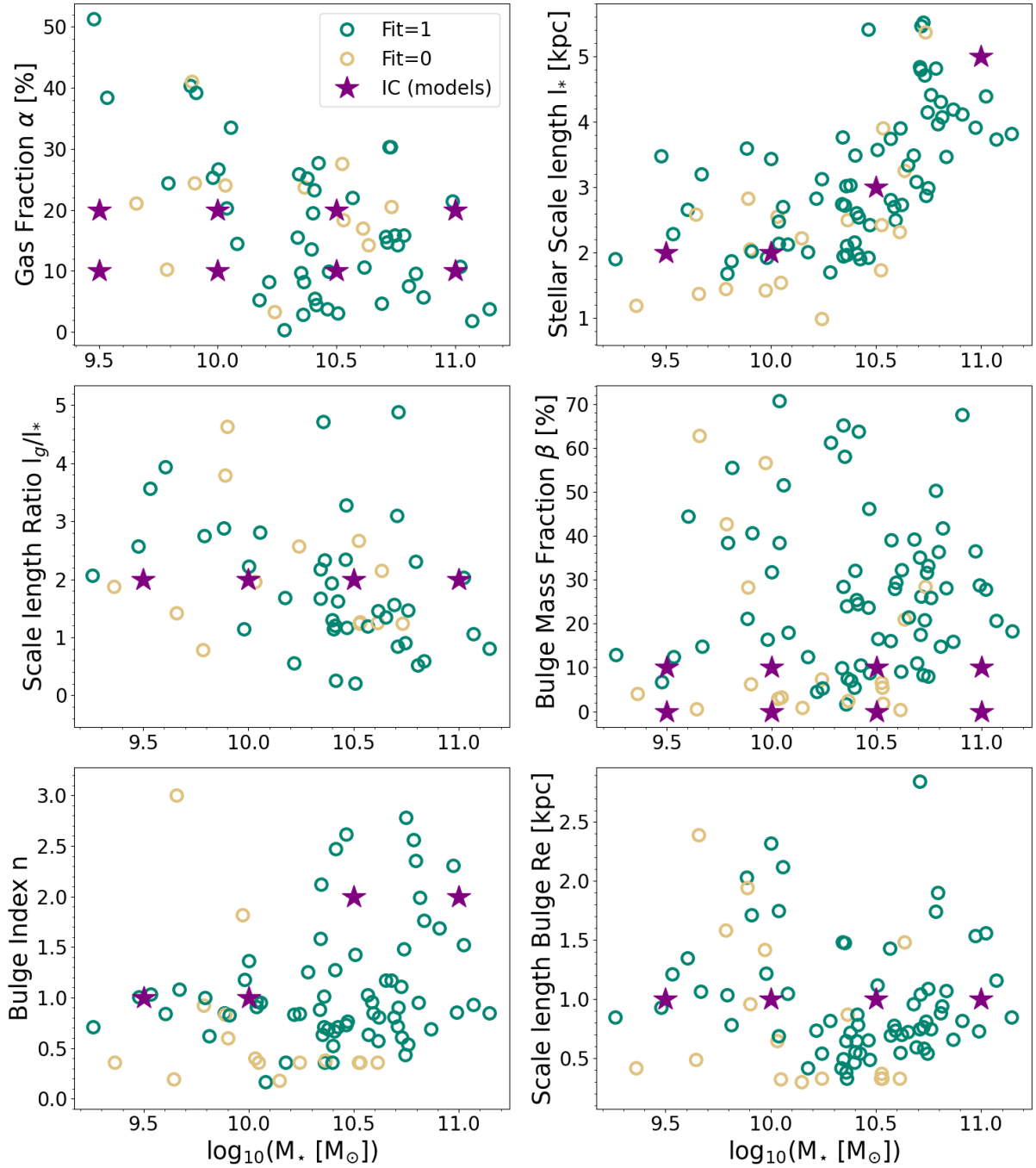


Figure 4.3: Results of the fit for different parameters of the models as a function of the stellar mass. Top panels: gas fraction (left) and stellar scale length (right). Middle panels: scale length ratio between the gas and stars (left) and scale length of the stellar bulge (right). Bottom panels: bulge index (left) and bulge mass fraction (right). Colour circles show the actual fits (see the text in Sec. 4.2.2 for details) to the PHANGS-ALMA sample, while the selected values for our used initial conditions (IC(models)) are shown with purple stars.

Model	$\log_{10}(M_{\star})$ [M_{\odot}]	α [%]	l_{\star} [kpc]	l_g/l_{\star}	β [%]
G001M095F10L2B00	9.5	10	2	2	0
G002M095F10L2B10	9.5	10	2	2	10
G013M095F20L2B00	9.5	20	2	2	0
G014M095F20L2B10	9.5	20	2	2	10
G037M100F10L2B00	10	10	2	2	0
G038M100F10L2B10	10	10	2	2	10
G053M100F20L2B00	10	20	2	2	0
G054M100F20L2B10	10	20	2	2	10
G105M105F10L3B00	10.5	10	3	2	0
G106M105F10L3B10	10.5	10	3	2	10
G137M105F20L3B00	10.5	20	3	2	0
G138M105F20L3B10	10.5	20	3	2	10
G161M110F10L5B00	11	10	5	2	0
G162M110F10L5B10	11	10	5	2	10
G177M110F20L5B00	11	20	5	2	0
G178M110F20L5B10	11	20	5	2	10

Table 4.1: Grid containing the parameters for the initial conditions of the models of this paper. From left to right columns: label, total stellar mass, mass gas fraction, stellar scale length, scale length ratio (gas over stars) and bulge mass fraction.

by the gas fraction, L by the typical scale length of stars, and B by the bulge mass fraction. This represents a set of 16 high-priority models, spanning typical PHANGS parameters, and tractable in terms of computing time. This paper focuses on this preliminary first subset of 16 initial conditions, with suitable values of control parameters for the comparison between all the stellar mass bins (see Table 4.1) that already covers a good range of properties for this sample. An extended grid of 54 models is planned but requires a significantly larger investment in computational time, and its analysis will be presented in a future paper.

4.3 Numerical simulations

4.3.1 Initial conditions

Initial conditions for the RAMSES adaptive mesh refinement (AMR) code (Teyssier, 2002b) require information both for the particles (stars, dark matter, a central SMBH), and gas

content. The grid of values gathered in Table 4.1 is used for the description of the distribution of each individual component. We use the Python library ‘pymge’ based on the Multi-Gaussian Expansion (Emsellem et al., 1994a,b, MGE) method to fit the associated two-dimensional distributions (e.g. exponential discs) and deproject them into three-dimensional density distributions. The vertical axis ratios of the ellipsoid resulting from that 3D deprojection are set to $q = 0.6, 0.1, 0.05$, respectively for the bulge, stellar disc and gas disc. The dark matter is constrained by the averaged rotation curves observed via the PHANGS sample and generated using an Einasto spherical mass distribution (Einasto, 1965; Ludlow & Angulo, 2017) as given by:

$$\rho_h(r) = \rho_{h,0} \exp \left(-2m \left[\left(\frac{r}{l_h} \right)^{1/m} - 1 \right] \right), \quad (4.4)$$

where ρ_h is the 3D density profile of the dark matter halo, r is the spherical radius, l_h is the scale length and m is the halo index. The values we chose for the parameters of Eq. 4.4 are summarised in Table 4.2. Once those three-dimensional profiles are fixed for all the components, we fix the number of particles and derive their initial positions and velocities by solving the Jeans equations. We assume a local anisotropy constrained by the flattening of the individual components, with $\delta = 1 - \sigma_z^2/\sigma_R^2 = 0.6 \times (1 - q)$ where σ_R, z is the radial and vertical stellar velocity dispersion in cylindrical coordinates (Binney et al., 2009). The more flattened the component is, the larger its (initial) velocity anisotropy. We use a constant mass resolution of $10^4 M_\odot$ for all stars present in the initial conditions (‘old’ stellar particles). This leads to an increasing number of stellar particles, that is, about $3 \times 10^5, 10^6, 3 \times 10^6$ and 10^7 , for the corresponding four stellar masses 9.5, 10, 10.5 and 11 (in $\log_{10}[M_\odot]$), respectively. The number of particles for the dark matter component was fixed to 10^6 for all models.

Fig. 4.4 shows a comparison between the PHANGS rotation curves (shaded areas, encompassing individual velocity profiles for a given stellar mass bin, Lang et al. 2020) and our 16 models (solid curves) for the different mass ranges. Our models are, by design, in good agreement with the PHANGS galaxies, reproducing the global trend of real galaxies. We note that the limited extent in the observed rotation curves for the lower mass bins is expected considering the smaller size and shorter radial extent of the (mostly CO and HI) tracers (Leroy et al., 2019). We also emphasise that those circular velocity curves represent the initial state of our hydro-dynamical simulations, and are thus meant to evolve with time (i.e. see the black curves). It is worth mentioning that the PHANGS rotation curves are the observed gas velocity profiles. Converting such velocity profiles to actual circular velocities, as measured in our simulations, would require detailed modelling, including, for example, the effect of asymmetric drift and non-circular motions. Considering the relatively low velocity dispersion of the molecular gas, we do not expect the impact of asymmetric drift to be significant. Non-circular motions may, however, dominate in the central region. This motivated us to use those PHANGS observed rotation curves only as guidelines to build our mass models.

M_\star $\log_{10}([M_\odot])$	$\rho_{h,0}$ $[M_\odot/\text{pc}^3]$	$l_{h,0}$ [kpc]	m	M_{BH} $\log_{10}([M_\odot])$
9.5	3×10^{-4}	20	3	5.5
10	6×10^{-4}	25	3.5	6
10.5	7×10^{-4}	30	1.5	6.5
11	8.5×10^{-4}	35	2	7

Table 4.2: Grid of values for the parameters describing the dark matter profiles (i.e. $\rho_{h,0}$, the halo density; $l_{h,0}$, the typical halo scale length; and m , the halo index) as a function of the stellar mass M_\star . Those values have been inspired by the work of [Kun et al. \(2017\)](#), but their final values have been chosen to match the PHANGS rotation curves. The central BH masses M_{BH} we use in the initial conditions are also shown in the last column.

4.3.2 Refinement strategy

All simulations in the three lower stellar mass bins (resp. higher mass bin) are run within a 100 kpc (resp. 200 kpc) cubic box. A refinement level l thus corresponds to a $100/2^l$ (resp. $100/2^l$) kpc cubic cell. We imposed a minimal refinement level of 7 (resp 8; ~ 780 pc) and a maximal one of 13 (resp. 14; ~ 12 pc). The refinement strategy we adopt for the gas is based on a Jeans polytropic approximation (see [Renaud et al., 2013b](#)) allowing us to set a realistic threshold for the amount of gas contained inside a cell. The maximum mass of gas contained inside a cell at the second last level ($l=12$ or 13 , 24 pc) before the triggering of the refinement to the last level ($l=13$ or 14 , 12 pc) is around $14000 M_\odot$. An additional refinement criterion is constrained by the minimum number of particles per cell (stars and dark matter) that is set to 8.

4.3.3 Numerical recipes

A number of standard physical processes were implemented including gas cooling, star formation, stellar feedback and the evolution of metals such as iron and oxygen (see [Agertz et al. 2013](#) for more detailed information). The physics of the heating follows a uniform UV background model proposed by [Haardt & Madau \(1996\)](#) and calibrated for redshift $z = 0$. The physics of the cooling is implemented and divided into two different regimes. The first regime goes down to 10^4 K and uses collisional de-excitation and atomic recombinations. The second regime, below 10^4 K, follows the table of [Sutherland & Dopita \(1993\)](#). The formation of new stars is triggered above a gas density threshold via a constant efficiency, as given by the following equation:

$$\dot{\rho}_* = \frac{\rho_g}{t_{SF}} \text{ for } \rho_g \geq m_h n_*, \quad (4.5)$$

where $\dot{\rho}_*$ is the star-formation rate (SFR), ρ_g is the gas density, m_h is the mass of the hydrogen atom and t_{SF} is the typical gas depletion time (~ 2 Gyr). The latter is given by:

$$t_{SF} = t_{ff}/\epsilon_{ff}, \quad (4.6)$$

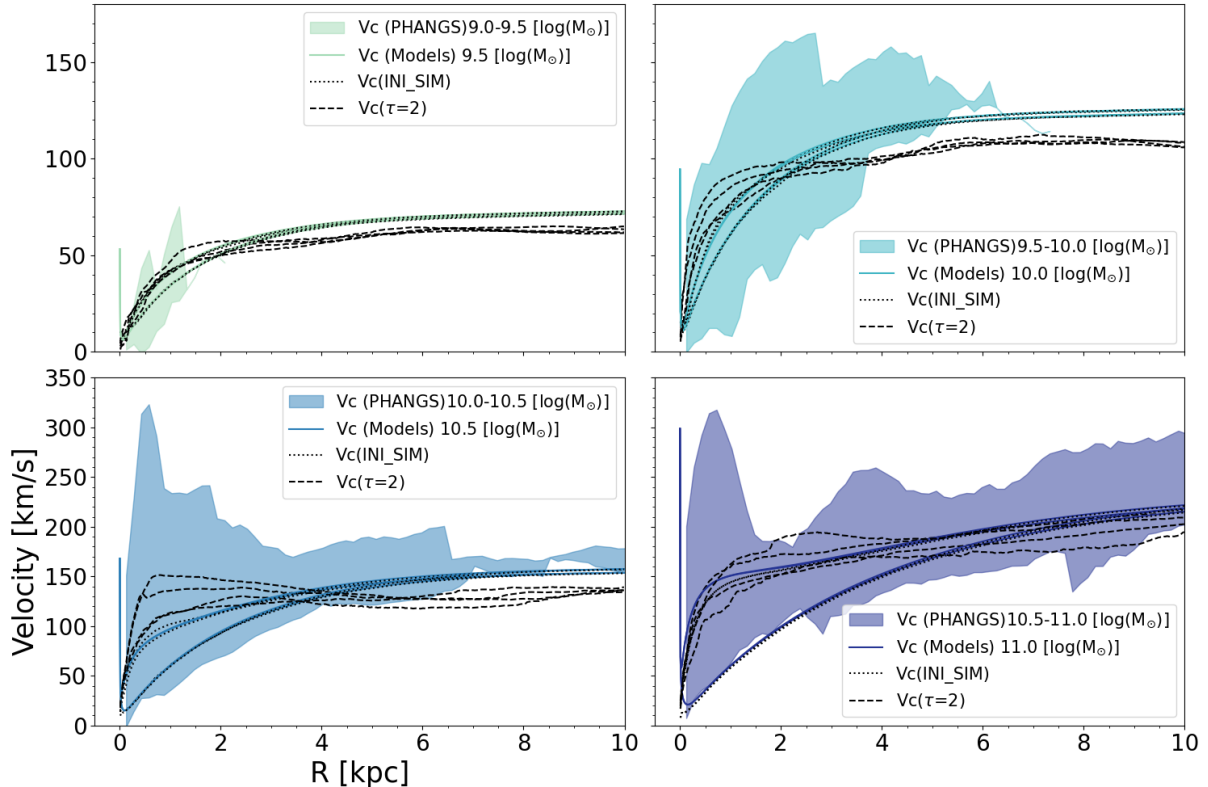


Figure 4.4: Comparison between the observed gas velocity curves of the PHANGS sample (shaded areas) and the circular velocity profiles from our models (solid curves). The vertical lines near $R=0$ illustrate the contribution of the central SMBH. The dotted curves represent the circular velocities extracted from the first snapshot (INI_SIM) of each simulation and are consistent with the analytic derivation associated with the initial conditions. The dashed curves represent the circular velocities at $\tau = 2$ (see Sect. 4.4.3, which corresponds to twice the bar formation time of our simulated galaxies). As mentioned in the text, the PHANGS rotation curves are meant as guidelines to build the initial mass models.

with t_{ff} the local free fall time and ϵ_{ff} the star formation efficiency per free-fall time. We set the efficiency to 2%, and n_* to 100 cm^{-3} , a posteriori checking that our systems follow the trend observed in the PHANGS galaxies (see Fig. 4.5). Stellar feedback, which releases energy, momentum and metals in the surrounding ISM, is implemented by taking into account the contribution from supernovae (SN) SNIa, SNIId and stellar winds. The energy released by the supernova depends on the local cooling radius (see Kim & Ostriker, 2015) Finally, we also adopt solar metallicity as initial condition ($Z = 1 Z_{\odot}$), which does not have a significant impact on the gas processes (star formation, feedback).

4.4 Results

In this section, we first describe some general properties of the evolved systems and then illustrate the global time evolution and bar formation. We briefly discuss the bar formation times in the light of past results, and consider the time evolution in terms of specific successive phases. We finally hint at a significant difference in the phases of the building of a central gas concentration impacting the way star formation proceeds in the lowest mass bin of our sample.

4.4.1 General properties and time evolution

The star-forming main sequence

We want our simulated galaxies to be representative of the star-forming main sequence of nearby disc galaxies, hence located on the Kennicutt-Schmidt relation (Schmidt, 1959; Kennicutt, 2007). Our choices for the initial properties (e.g. distribution of baryons, gas fractions, etc.) and sub-grid recipes (e.g. star formation efficiency, see Sect. 4.3.2) do not guarantee such a result, because star formation may partly regulate itself in such numerical experiments (Ostriker & Kim, 2022). We thus computed the global SFR for all 16 simulations and compared its characteristics and trends with the instantaneous SFR of the PHANGS-ALMA sample as shown in Fig. 4.5. We computed the SFR by taking the time average of the SFR, only including times between $\tau = 1$ and $\tau = 2$ (see Sect. 4.4.3, which corresponds to the starburst phase of our simulated galaxies), thus focusing on the active star formation regime.

In Fig. 4.5, we confirm that our simulations are almost all following the PHANGS main sequence, except for galaxies with the lowest stellar mass bin (i.e. 9.5 in $\log_{10}(M_{\odot})$): those have SFR lower than the observed values in this sample. This is expected since we intentionally chose to run this first subset of simulations with only two values of the gas mass fraction, those being significant underestimating the observed gas fractions ($\sim 30\text{--}40\%$) for that stellar mass bin, as shown in Fig. 4.3. Higher gas fractions (thicker squares) naturally lead to a higher SFR, and models with a bulge (hatched squares) tend to have lower resulting SFR as expected if the self-gravity of the disc is lowered. The impact of the bulge reaches its maximum for the bulged model with the highest stellar mass, and a gas fraction of 10%. We describe in more detail the characteristics of this model in the next sections.

Building of the bar

Figure 4.6 illustrates the global evolution of one galaxy over time by showing the maps of gas, new and old stars. We start with an axisymmetric distribution of gas and stars, which rapidly develops low-contrast spiral arm structures. Gas follows up by cooling and forming new stars (top left panel). After a few hundred Myr we start to observe the formation of a bar and spiral arms in the old and new stars (top right panel). Once the bar has formed, the gas concentration in the central region starts to increase, leading to the build-up of an

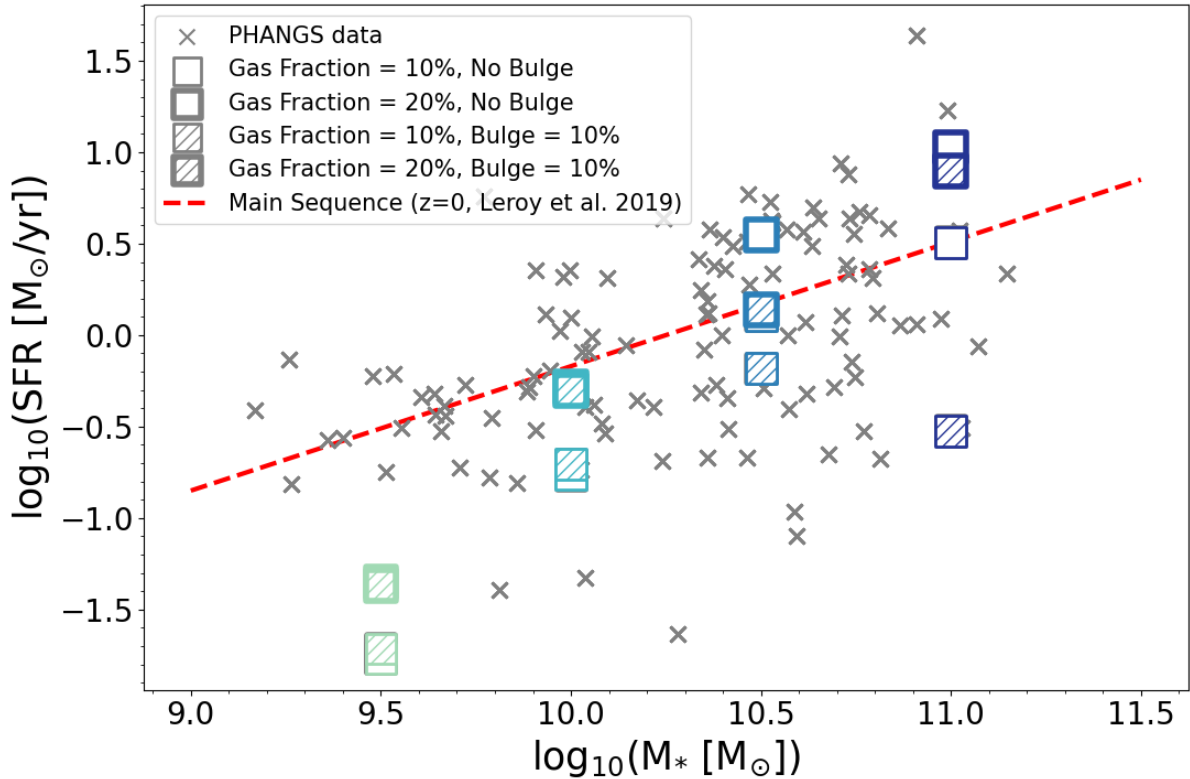


Figure 4.5: Comparison of the SFR stemming from the PHANGS data sample (grey crosses) and the SFR computed from the simulated galaxies (coloured squared). The colour of the squares corresponds to the different stellar masses. The red dashed line represents the star formation main sequence at $z = 0$ from [Leroy et al. \(2019\)](#).

early gas reservoir (bottom left panel). This could be induced by the emergence of an inner Lindblad resonance (ILR: [Lin et al., 2008](#); [Sormani et al., 2023a](#)). Finally, we observe the building and growth of a central gas reservoir (bottom right panel).

This scenario is similar for most of the 16 simulated galaxies and the evolution over time of the 16 simulations is shown in the [Appendix A.1](#) where the different times are chosen to emphasise the evolution of the building of the gas reservoir within the central 1 kpc region (see [Sect. 4.4.1](#)).

One of the main features developed by almost all our simulations is a stellar bar (except for models G162M110F10L5B10 and G178M110F20L5B10). We present model G053M100F20L2B00 in [Fig. 4.6](#) to illustrate the growth of the bar witnessed in our simulations (see third row). To more quantitatively characterise the evolution of the bar over time, we estimated the amplitude of the bar via a polar (R, θ) Fourier decomposition of the face-on surface stellar mass density, and specifically used the traditional A_2 Fourier coefficient ([Efstathiou et al., 1982b](#); [Athanasoula & Misiriotis, 2002](#); [Athanasoula et al.,](#)

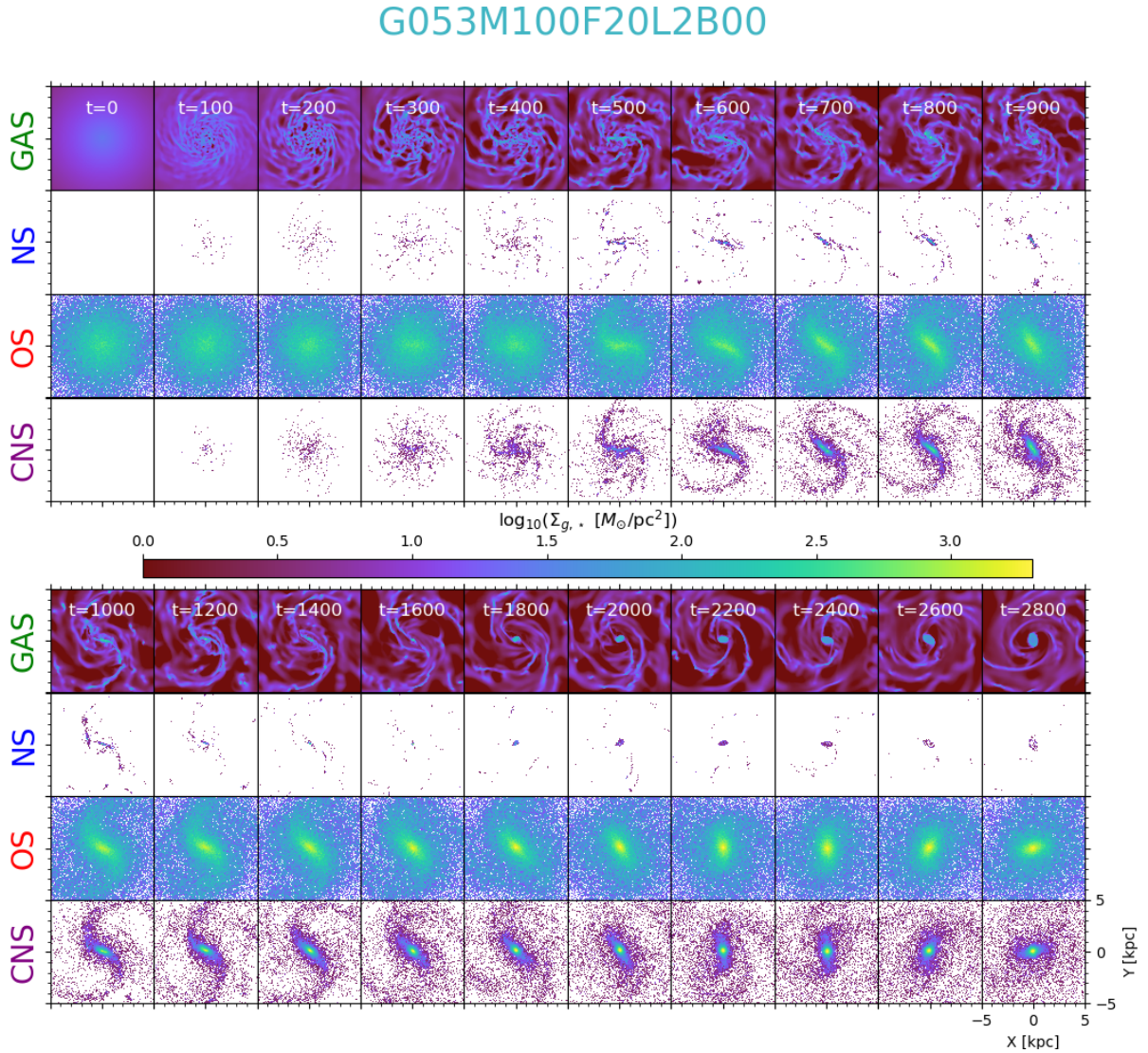


Figure 4.6: Evolution over time (in millions of years) of the gas and stars of the model labelled G053M100F20L2B00 (one of the sixteen simulations presented in this paper). The two big panels illustrate four main stages, chronologically ordered from top left (0-400 Myr), to top right (500-900 Myr), bottom left (1000-1800 Myr) and bottom right (2000-2800 Myr). **Top left:** first spiral structures, cooling of the gas, onset of star formation, initial bar structure emerging. **Top right:** bar strengthening and active local star formation. **Bottom left:** building of a central concentration of gas (and new stars). **Bottom right:** growth of the gas reservoir. In each big panel, from top to bottom, we present maps for the gas mass density (GAS), the mass of young stars (≤ 50 Myr, NS), of old stars (OS) and finally the cumulative mass of new stars (formed since the beginning of the simulation, CNS). Each panel shows a $10 \times 10 \text{ kpc}^2$ region and the colour scaling is adapted for each panel.

2013) given by

$$A_2 = \frac{\sqrt{a_2^2 + b_2^2}}{a_0}, \quad a_n = \sum_{i=1}^N m_i \cos(n\theta_i), \quad b_n = \sum_{i=1}^N m_i \sin(n\theta_i), \quad (4.7)$$

where m_i is the mass of the i -th star and θ_i its corresponding position angle. The full radial $A_2(R)$ profile is then used, for example, to track its maximum over time, giving us a quantitative assessment of the evolution of the bar strength, as shown in Fig. 4.7 for the model labelled G053M100F20L2B00. In that Figure, we see that the bar grows rapidly during the first 500-600 Myr, roughly following an exponential behaviour (Binney, 2020; Bland-Hawthorn et al., 2023). Then, it reaches a first maximum after ~ 750 Myr and a second after ~ 1000 Myr. This characteristic shape of A_2 was already reproduced by Athanassoula (2002). At later times, A_2 exhibits some oscillations until the end of the simulation. These modulations coincide with the relative cycling (and alignment) between the bar and the outer spiral arms which have different pattern speeds (Hilmi et al., 2020).

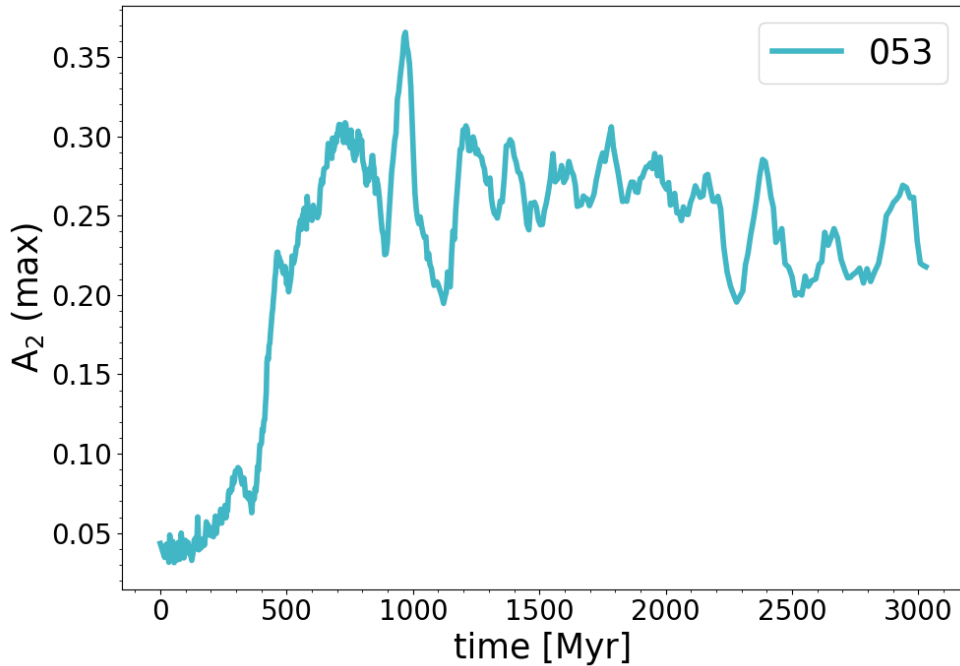


Figure 4.7: Evolution of the bar strength (measured through the A_2 Fourier coefficient) for the model G053.

We emphasise that the resulting A_2 values should depend on the tracer to compute it, for instance, using particle masses, accounting only for old or newly formed stars, or using luminosity-weighted quantities as is naturally the case for observations. It may also be influenced by the presence of dust and by additional processing stages (e.g. deprojection of observed photometry). Still, the A_2 values found in our simulations are in the range

[0.2 – 0.5], consistent with the ones observed by [Díaz-García et al. \(2016\)](#) for star-forming late-type galaxies, and also consistent with the majority of barred galaxies in the PHANGS sample. [Stuber et al. \(2023\)](#) reports significantly larger values ($A_2 > 0.4$), but those are representative of the high tail of the bar strength distribution. The fact that we do not reproduce this tail of high A_2 values may naturally arise from the early bar phase that we are probing with our simulations (i.e. up to about 3 Gyr). Some of the strong bars observed in the PHANGS sample could be at a later evolutionary stage for which the bar has experienced a second (secular) growth (see [Athanassoula, 2013](#)).

The central 1 kpc

In the PHANGS-ALMA galaxy sample, we observe inner molecular rings with typical sizes ranging from ~ 100 pc to ~ 1 kpc ([Leroy et al., 2021](#)). Our simulations suggest their size and mass evolve with time. We thus monitored the evolution of the central gas mass concentration and star formation within the central 1 kpc, and their relation with the bar using our 16 simulations. In the rest of this section, we refer to the (central 1 kpc) ‘gas reservoir’ to describe the mass of gas inside the central 1 kpc region.

In [Fig. 4.8](#), the left (resp. right) column presents time evolution profiles for models with the lower (9.5 and 10 in $\log_{10}(M_{\odot})$) (resp. higher, 10.5 and 11 in $\log_{10}(M_{\odot})$) stellar masses. The middle panels show the evolution of the total gas mass contained inside a cylindrical radius of 1 kpc and a thickness of 1 kpc. The initial gas mass within 1 kpc correlates with the initial stellar mass and gas fraction as expected. After a generic plateau lasting about 300 Myr, the gas concentration increases steadily. This increase of the gas mass inside the central 1 kpc region is coincident with an increase of the SFR: those roughly correspond to t_{bar} , the time at which the A_2 coefficient reaches the value of ~ 0.2 , whatever the stellar mass, gas fraction or the presence of a bulge. Since bulges tend to increase t_{bar} (see [Sections 4.4.1](#) and [4.4.2](#)), models with bulges also show a corresponding delay in the start of the increase of the gas mass.

G162M110F10L5B10 seems to be a peculiar case among the two models that do not form a bar: A_2 never reaches a value of 0.2. Gas is consequently not funnelled towards the centre as for other models, and there are no star formation bursts with SFR staying around $10^{-3} M_{\odot}/\text{yr}$. In that simulation, the bulge has a stabilising effect, enough in this specific case to prevent any bar to form for the duration of our simulation. This is a well-known result, and has been already studied and recently emphasised in various papers (see e.g. [Sellwood & Evans, 2001](#); [Saha & Naab, 2013](#); [Kataria & Das, 2018](#); [Fujii et al., 2019](#)). In that context, the bar in G162M110F10L5B10 possibly has a formation time t_{bar} significantly larger than a Hubble time (see also [Bland-Hawthorn et al., 2023](#)).

4.4.2 Typical bar formation time

Using simulation G053M100F20L2B00 as an example, we witness the onset of bar formation as early as $t = 300$ Myr ([Fig. 4.6](#)). However, the bar seems to more robustly emerge between $t=400$ and $t=500$ Myr and this corresponds with the time when A_2 reaches a

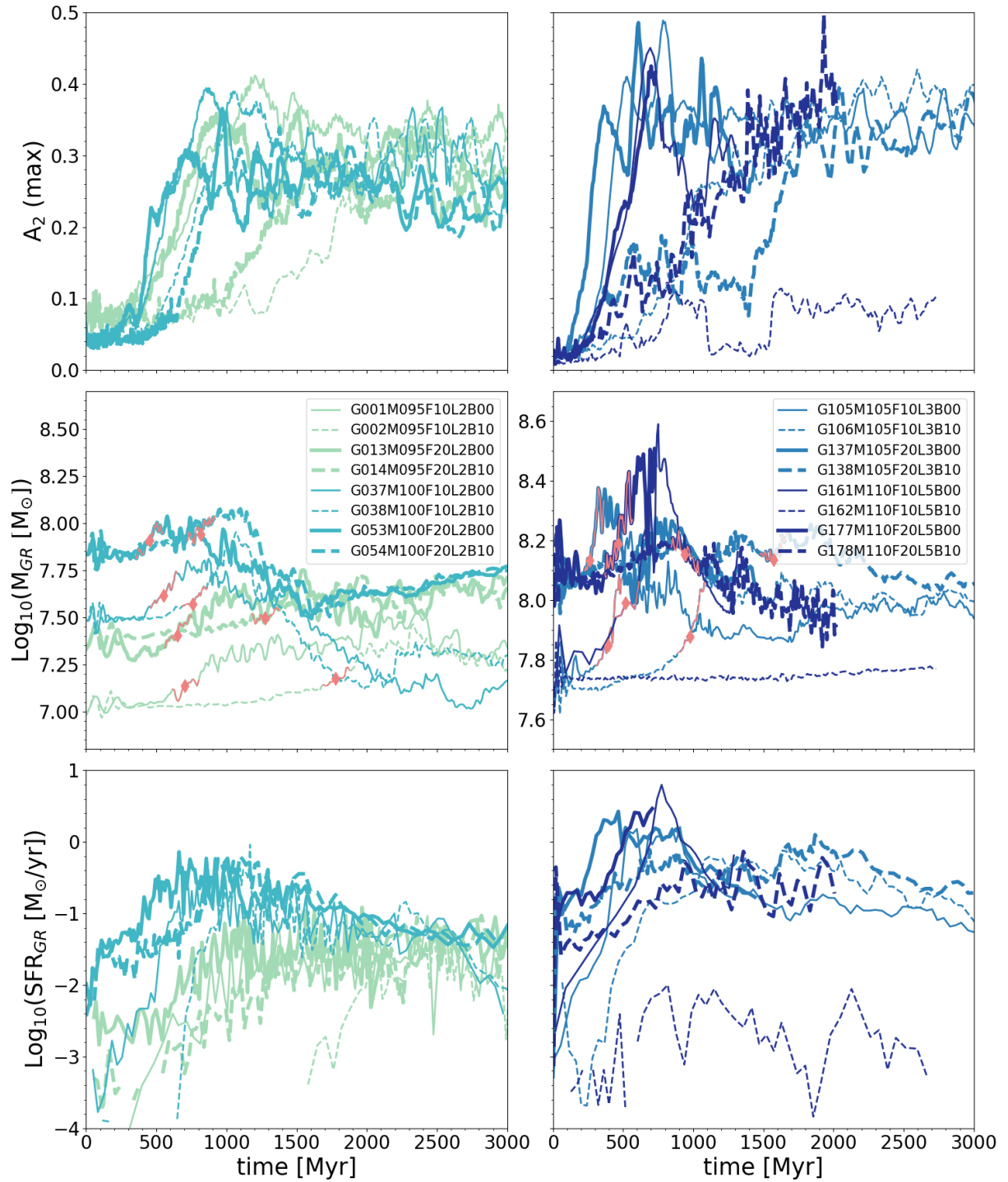


Figure 4.8: Evolution of the maximum of the A_2 coefficient (top panels), the mass of gas within 1 kpc (middle panels), and the SFR (bottom panels) over time for the 16 simulations (evolved until max 3 Gyr). The colour gradient represents the four stellar masses (9.5, 10, 10.5 and 11 [$\log(M_{\odot})$]) from the lightest to the most massive. The left column represents the less massive galaxies (9.5 and 10, in green and cyan, respectively) and the right column shows the most massive ones (10.5 and 11, in blue and dark blue, respectively). The solid and dashed curves illustrate the models without and with a bulge, respectively and the thickness of the lines accounts for the gas fraction (10 and 20% for the thinnest and thickest, respectively). The typical bar formation time t_{bar} is also shown (red diamonds) within a time interval of 200 Myr (red part of the curves).

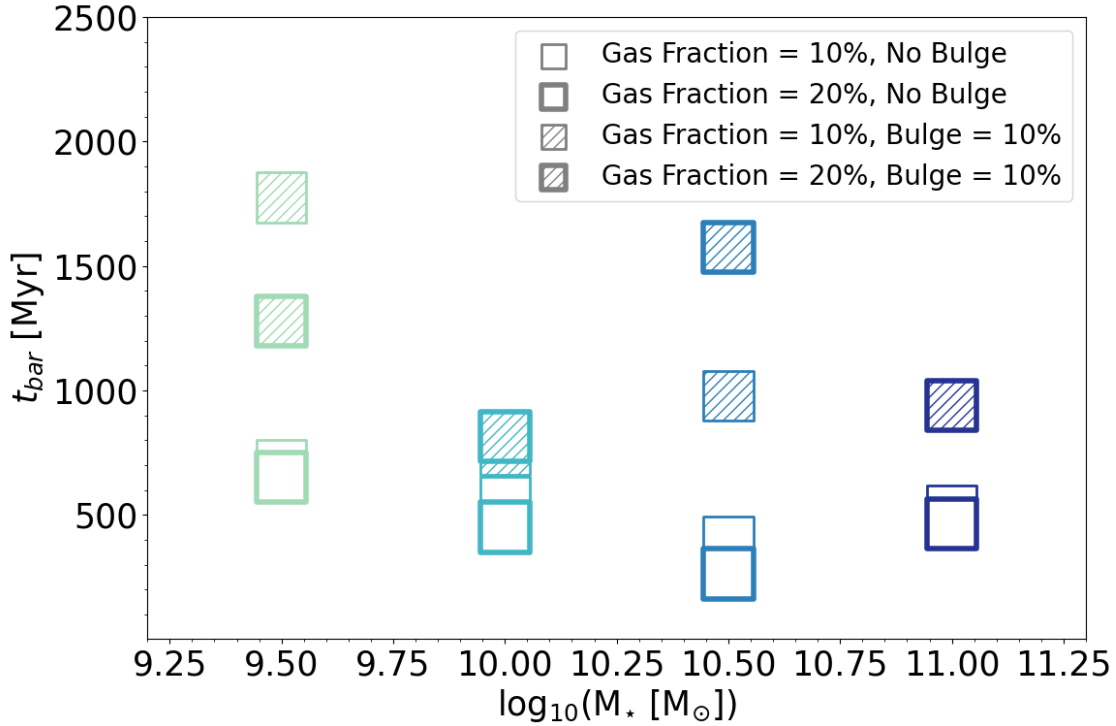


Figure 4.9: Typical bar formation time t_{bar} as a function of the stellar mass for all 16 simulations. The colour of the squares corresponds to the different stellar masses. The size of each square represents 200 Myr (i.e. ± 100 Myr), hence illustrating the uncertainty in t_{bar} (see Sect. 4.4.2).

value of ~ 0.2 . This is also true for the other simulations in our sample. In the following, we therefore use t_{bar} , the time corresponding to $A_2 = 0.2$, as the reference time for the bar formation (see Sect. 4.4.1). Such a reference measurement is commonly used in the literature (Athanasoula & Misiriotis, 2002; Fujii et al., 2018).

All simulations, except two (models G162M110F10L5B10 and G178M110F20L5B10) form bars. The values for t_{bar} are shown for the 14 simulations forming a bar in Fig. 4.9. To further probe the stability of our models against bar formation, we have applied the criterion established by Efstathiou et al. (1982a) for all 16 models. We indeed find that only the two above-mentioned models do overshoot the threshold for stability. While this is an interesting result, suggesting that we should indeed not expect the formation of a bar in models G162M110F10L5B10 and G178M110F20L5B10, we caution the reader regarding the use of that stability criterion as a robust quantitative diagnostic. As pointed out by Athanasoula (2008), this criterion does not take into account the interaction between the disc and the halo, nor the velocity dispersion, which plays a major role in disc stability. They also suggested that this parameter is not designed for the stability analysis of multi-component discs. This has also been shown in a recent work carried out by Romeo et al.

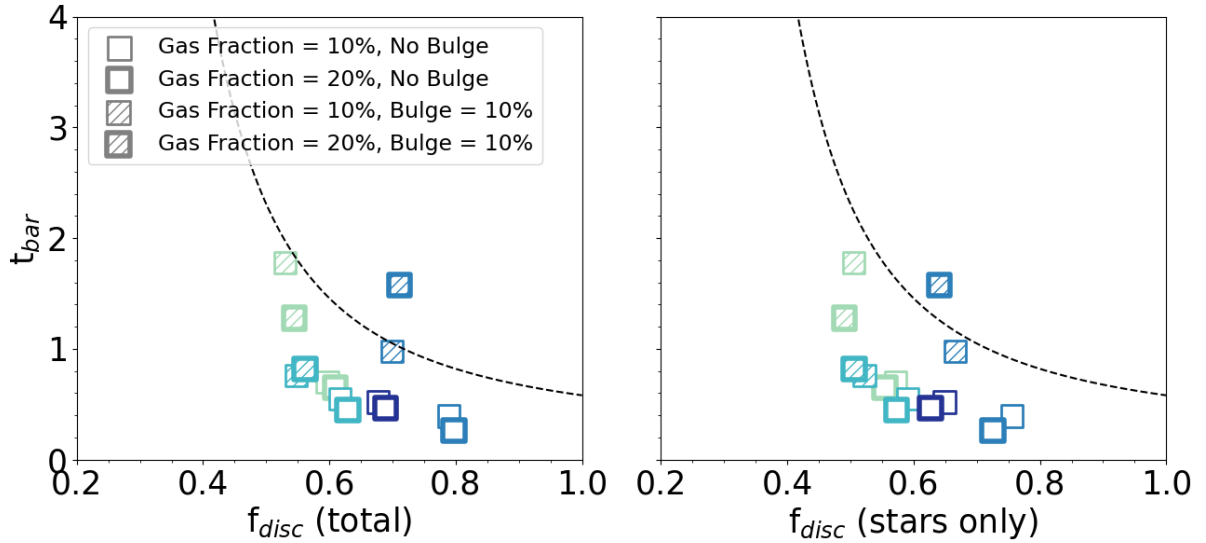


Figure 4.10: Typical bar formation time t_{bar} as a function of f_{disc} as defined in Bland-Hawthorn et al. (2023). The dashed lines show the relation given by (Fujii et al., 2019). f_{disc} is derived using the sole stellar disc (right panel) or the total baryonic content (i.e. stars and gas; left panel). In the right panel, $f_{disc} \text{ (stars only)}$ decreases when the gas fraction increases as expected (the relative contribution of the stellar disc gets smaller), while in the left panel, $f_{disc} \text{ (total)}$ increases with the gas fraction (as the total baryonic contribution increases). As in Figure 4.9, the size of each square represents 200 Myr (i.e. ± 100 Myr), hence illustrating the uncertainty in t_{bar} (see Sect. 4.4.2).

(2023), whose conclusion is that this parameter fails at separating barred and non-barred galaxies in 55 per cent of the cases.

We further emphasise the fact that t_{bar} should be considered a relative indicator that exhibits significant systematics. We have conducted a series of tests using the simulation G037M100F10L2B00 as a reference, varying the initial number of particles and the maximum level of refinement, and even shutting off the gas cooling and star formation recipes. As long as we keep the gas disc live within the simulation, we do not witness a significant change in the evolution of the A_2 profile and thus in t_{bar} . When the number of disc particles is changed (from 0.5 to 1, 2, 5 or 10 million), the time increase (i.e. increasing rate) of A_2 looks similar. However, the starting time of that initial increase, tracing the growth of $m = 2$ modes typically varies from one simulation to the next by ± 75 Myr. That timing offset does not seem to depend monotonically on the number of particles, as it is, for instance, slightly lower for 2 and 10 million disc particles, and thus higher for 1 and 5 million disc particles. We interpret it as partly due to the contribution of the spiral modes that may interfere with the bar mode, as well as variations in the initial relaxation phase. While it is beyond the scope of this study to further probe such a dependence, it does show that a significant systematic uncertainty should be included when discussing t_{bar} measured in such a way. In the rest of the paper, we added a (conservative) systematic uncertainty

of ± 100 Myr on our t_{bar} measurements and checked that it did not impact our results.

The most obvious trend associated with t_{bar} is connected with the impact of the initial ellipsoid (or bulge). When an ellipsoid or bulge (hatched squares in the figure) is added to the model, a delay of a few 100's of Myr in the bar formation is induced, leading to a delay in the building and fuelling of the central 1 kpc (see also Sect. 4.4.1). Note that the induced time delay is significant, and much larger than the above-mentioned systematic uncertainty in t_{bar} . For models without bulges (empty squares), a larger gas fraction (thick squares) tends to decrease t_{bar} confirming early results by Athanassoula et al. (2013) who found a similar outcome for systems with up to 50% of gas. For more gas-rich systems (e.g. gas fractions equal or larger than 75%) Athanassoula et al. (2013) witnessed an inverse trend considering the initial growth of the bar. They also find that such trends significantly depend on the halo triaxiality (see their Fig. 7), something we do not test with our present simulations. We note that the delay in the early bar growth due to higher gas fractions in our simulations does not simply hold for our bulged models, suggesting, together with the above-mentioned results from Athanassoula et al. (2013) that a more relevant parameter may drive the initial bar growth.

Fujii et al. (2018) recently suggested to use of f_{disc} , the ratio between the disc mass and the total galaxy mass within $2.2 R_{disc}$ as a relevant driving parameter for the bar growth timescale. This parameter f_{disc} is admittedly one way to quantify the importance of the stellar disc within the global potential (baryonic + dark matter) that may be connected with the onset of bar instabilities. Fujii et al. (2018) used a series of pure N-body simulations of systems with stellar masses of a few $10^{10} M_{\odot}$, with varying bulge to disc ratios, using 500 million particles (8 million for the baryonic disc) and 10 pc softening length to study timescales associated with bar and spiral growth (see also Valencia-Enrquez et al., 2017). They suggested a relation between f_{disc} and t_{bar} . Bland-Hawthorn et al. (2023) reviewed the Fujii et al. (2018) results by running simulations both using dry runs (stars and dark matter particles only) and a few wet runs (including gas but excluding cooling and star formation) using the AMR code RAMSES, with spatial sampling of 6 and 12 pc: they mostly confirmed the existence of a relation between f_{disc} and t_{bar} , the 'Fujii relation', albeit with a large scatter for f_{disc} larger than 0.5 (their Fig. 4). Bland-Hawthorn et al. (2023) further suggested that the addition of gas tends to decrease the value of t_{bar} , as also witnessed in our bulgeless simulations (but not in our bulged models; and see Athanassoula et al., 2013).

We take the opportunity of our sample of simulations to test further the validity range of the 'Fujii relation'. Our simulations have similar resolution and particle numbers, and use a very similar code than Bland-Hawthorn et al. (2023) but include cooling and star formation. As compared to the original Fujii et al. (2018) simulations that are pure N-body via a tree-code (Barnes & Hut, 1986b), our simulations have 8 times fewer particles in the disc (and a mass resolution for the dark matter halo about 100 times larger) and again include gas and star formation. Figure. 4.10 specifically illustrates the trend of t_{bar} as a function of f_{disc} for our set of simulations, emphasising the fact that we are so far only probing values of f_{disc} larger than 0.5 by design.

The left (resp., right) panel shows the Fujii et al. (2018) relation for f_{disc} (dashed lines)

computed with the star and gas (resp. only star) component. The inclusion of the gas as part of the disc potential (left panel) increases f_{disc} only slightly, as expected: for galaxies without a bulge, increasing the gas fraction also systematically decreases t_{bar} : that can be understood in terms of the destabilising effect of the additional disc of gas. For the more massive simulations with bulges, the trend seems the opposite, illustrating that the addition of an ellipsoid dominates the budget for t_{bar} . Finally, the simulation at the lowest stellar mass bin and with a bulge shows a smaller t_{bar} when the gas fraction is increased.

At fixed f_{disc} , our sample of simulations seems to overall lie a factor of two below the Fujii et al. (2019) relation, with differences of about 500 Myr or more, well beyond the expected uncertainty associated with the measured t_{bar} values. As emphasised, one difference with the results from Fujii et al. (2019) is that our simulations contain gas. While, as mentioned above, the bar formation time may depend on the gas fraction, this discrepancy does not change significantly if we include the gas component in the value of f_{disc} . Another significant difference between our simulations and those by Fujii et al. (2019) is that the latter used pure N-body simulations with a large number of particles (with a softening length of about 10 pc). Still, we are in a regime where we should have enough mass resolution, at least for the 3 larger mass bins (leading to a minimum of 2 million particles), and we do not detect a trend in stellar mass in the context of the t_{bar} discrepancy with Fujii et al. (2019). Even considering the added systematic error of ± 100 Myr (see the beginning of the present Section), we do not retrieve the Fujii et al. (2018) relation. We also need to emphasise the fact that simulations performed by Bland-Hawthorn et al. (2023) use a similar setup as ours (and the same AMR code, RAMSES), and do not see such a discrepancy with Fujii et al. (2019, their Fig. 4).

More fundamentally, other differences could be at the root of this discrepancy, including more concentrated discs and dark matter distributions in Bland-Hawthorn et al. (2023), different initial velocity distributions (anisotropies), or the lack of cooling, star formation and feedback in the latter experiments. As emphasised by Athanassoula et al. (2013), other parameters, including the shape of the halo and the initial dynamical set up for the disc, can strongly influence the growth of unstable modes, including the bar and spirals.

Our results confirm and extend previous studies showing that t_{bar} seems to depend on many details in the initial conditions, including the steepness of the inner potential (e.g. via the index of the Sersic bulge), the overall contribution of the disc components (w.r.t. other baryonic and non-baryonic components; see also Athanassoula, 2013). This may naively suggest that t_{bar} is not fully described by a single parameter such as f_{disc} . However, we cannot yet conclude, as we would need to probe a more extended set of simulations, including, for example, models with varying properties (e.g. anisotropies) at fixed f_{disc} , and models with value of f_{disc} below 0.5 to detect the exponential increase of t_{bar} (and where values of t_{bar} are significantly larger than about 2 Gyr).

4.4.3 Evolutionary phases of isolated barred discs

Since the characteristic bar formation time seems to play a major role in the formation of the central gas reservoir, we have normalised the time by t_{bar} and have introduced the

dimensionless parameter $\tau = t/t_{bar}$. We have also normalised the gas mass by the initial amount of gas contained within 1 kpc as shown in Fig. 4.11. In this figure, we can see that the bars and SFRs share a similar time evolution with a slight trend of increasing amplitude as a function of the stellar mass, for all simulations with initial stellar masses equal or above $10^{10} M_{\odot}$ (see Sect. 4.4.5 for a discussion on simulations in the lower stellar mass bin). These similarities between barred systems confirm the relevance of the choice of τ allowing us to naturally account for the delay caused by the presence of a bulge.

Except for the models G162M110F10L5B10 and G178M110F20L5B10, the normalised gas mass always peaks with τ between 1 and 1.5. This peak also roughly coincides with the maximum of the bar strengths and the SFRs. Those are associated with a central starburst leading to an increase in the number of new stars and a decrease in the gas mass inside the central 1 kpc. For simulations with $M_{\star} \geq 10^{10} M_{\odot}$, we can roughly decompose the time evolution of the gas mass inside 1 kpc in three main phases referenced by the bar formation timescale t_{bar} :

1. From $\tau = 0$ to ~ 1 , the bar forms and the gas mass inside the central 1 kpc region is nearly constant or increase weakly. The star formation rate slowly increases with time (by about 1 order of magnitude in 500 Myr).
2. From $\tau = 1$ to ~ 1.5 , the bar is strong (by definition, $A_2 > 0.2$) and significantly influences the redistribution of gas. Gas is being funneled towards the centre, leading to a more rapid increase of the gas mass, that triggers a starburst inside that region. The star formation evolution then reaches a plateau.
3. From $\tau = 1.5$ to ~ 2 , the bar keeps its high amplitude, and a steeper decrease in the amount of gas in the central 1 kpc region is associated with a slow decline in star formation rate. This gas depletion phase marks the emergence of a small gaseous and stellar central mass overdensity, a discy structure that is fuelled by the bar. Follow-up star formation tends to predominantly occur within this inner disc region building up further beyond $\tau = 2$.

The fact that those phases are similar for all barred models having an initial stellar mass bigger or equal to $10^{10} M_{\odot}$ suggests that the fuelling and the consumption of gas inside the central 1 kpc region is driven by the same physical phenomena and evolution, and only depends weakly on the initial gas fraction and the presence or absence of a central ellipsoid (within the range of parameters probed by our simulations). While there are clear local differences between simulations, it is still an interesting and relevant result as it sets the stage of the evolution of barred systems which could serve as an "isolated case" reference for further studies. Note that we are not here discussing the evolution beyond 3 Gyr, which could, for instance, lead to a secondary growth of the stellar bar, and to the emergence of large bars (see e.g. Schinnerer et al., 2023; Bland-Hawthorn et al., 2023).

4.4.4 Gas structure in the central 1 kpc

In Sect. 4.4.1, we briefly discussed the property and global evolution in the central kpc. In Fig. 4.12, we now present the gas distributions and reservoir by providing a gas density map for all 16 simulations at $\tau = 2$, in order to illustrate the emergence of distinct inner gas structures. In that figure, the four lines correspond to the four different stellar mass bins (colour-coded labels), the models having a lower (resp. higher) gas fraction (α) being in the two left (resp. right) columns. The models without bulges ($\beta = 0$) are given by the first and third columns, whereas the models with bulges (here $\beta = 10$) are given by the second and the fourth columns.

We observe a distinct central concentration of gas for almost all barred models having a stellar mass larger than $10^{9.5} M_{\odot}$. For these stellar mass ranges, only model G162M110F10L5B10 does not show any bar structure and central gas concentration. We see that models with a bulge have a more extended gas reservoir. While the bulge delays the bar formation, once the bar is formed, the bulge does not prevent the formation of a gas reservoir and actually allows the emergence of a prominent inner structure. We discuss the detailed properties and growth of those structures in a subsequent paper, but we can already suggest here that the extent of such an inner disc (or rings, see Fig. 4.12) closely follows the change of the inner mass concentration.

4.4.5 The conditional onset of inner stellar discs

As illustrated in Fig. 4.8, we do not witness strong differences between simulations above and below the $10^{10} M_{\odot}$ values in terms of the amplitude of the bar (A_2) or the global SFR. The main difference between those two sub-samples shows up in the evolution of the gas in the central 1 kpc. The decrease of the central gas mass leading to a long-term gas depletion mentioned as Phase 3 in the previous Section is observed for all galaxies with an initial mass of $10^{10} M_{\odot}$ and above. For the less massive galaxies (i.e. models G001M095F10L2B00, G002M095F10L2B10, G013M095F20L2B00 and G014M095F20L2B10, having an initial stellar mass of $10^{9.5} M_{\odot}$), the gas mass stays roughly constant or even increases during that phase. This means that the channelling of gas towards the central region (and subsequent star formation) is still occurring but seems to proceed in a different manner.

To understand this better, we turn to the spatial distribution of star formation (and new stars). Fig. A.1 in the Appendix shows (second row in each panel) that for the lowest stellar mass models, star formation occurs mainly along and inside the bar until the end of the simulation without showing the emergence of a central gas reservoir. For the higher stellar mass models (Fig. A.2, A.3 and A.4), star formation occurs also along and inside the bar until $\tau = 1.5 - 2$, when we start to see the emergence of a central gas overdensity. Subsequent star formation is mainly distributed inside this central gas reservoir. This result also connects with the fact that distinct inner streaming lanes, as well as disc or ring structures form and grow for the more massive end systems, while the lower mass systems exhibit more heterogeneous gas distribution within the bar region. This is quite an intriguing result as it means that star formation is either prevented or triggered in

significantly different regions for the lowest mass simulation bin.

This trend has been reported by [Fraser-McKelvie et al. \(2020\)](#) using emission-line mapping via integral-field spectroscopic observations for a large sample of nearby galaxies (but see also [Díaz-García et al., 2020](#)). The stellar mass value of $10^{10} M_{\odot}$ at which this occurs also coincides with the one in our simulation set. It is worth mentioning that most of the galaxies presented in the above survey have a much higher gas fraction compared with the PHANGS sample. Their typical gas fraction ³ in the $10^{9.5-10} M_{\odot}$ stellar mass bin is above $\sim 30\%$ and goes up to $\sim 60-70\%$. Since we tuned our initial conditions to an observed sample of star-formation main sequence galaxies, this may mean either that the change is built in our set of morphological parameters (e.g. scale lengths) or that it is related to the varying relative contributions of physical processes at play, for example, the influence of feedback versus the strength of the gravitational potential, associated with a change of stellar mass.

The physical origin of this change in the regime between the lowest and highest stellar masses is not yet fully understood. [Fraser-McKelvie et al. \(2020\)](#) extrapolated from earlier simulations ([Emsellem et al., 2015](#)) that shear may be an important ingredient in setting up such differences. While this may play a role, we note that two of our simulations, one at $10^{9.5} M_{\odot}$ and one at $10^{10} M_{\odot}$, share almost exactly the same radial mass gradient (only the mass scaling is different), and those two do present the above-mentioned change in the evolved morphology. We thus suggest that the main driver for such a difference lies with the relative contribution of the stellar-driven feedback within those scaled gravitational potential (see e.g. [Collins & Read, 2022](#), and references therein). This will be specifically discussed in a subsequent paper.

4.5 Summary and conclusion

In this work, we have performed a set of 16 three-dimensional high-resolution hydrodynamical simulations (see Table 4.1) using the RAMSES AMR code to study and characterise the building and evolution of central gas reservoir in nearby main sequence disc galaxies. We have designed this grid based on the PHANGS-ALMA sample. We made use of four control parameters (i.e. stellar mass, gas fraction, scale length for the star distribution, and bulge mass fraction), and for each model started from axisymmetric initial conditions including gas, stars and dark matter.

We have further quantified the characteristic formation time for the bar t_{bar} in our simulations using a reference value of 0.2 for A_2 , and compared them with the relation suggested by [Fujii et al. \(2019\)](#). We have found that our simulations are located significantly below the relation (have smaller t_{bar} at fixed f_{disc}). We could not conclude robustly on the origin of such a discrepancy as it may both reflect the intrinsic scatter of such a relation and the imposed variety in the initial conditions (i.e. halo concentration, anisotropy). A larger set of simulations including gas and star formation covering lower values of f_{disc} (hence larger values of t_{bar}) are needed to confirm this trend.

³Value added Catalogs (SDSS): https://data.sdss.org/sas/dr17/-env/MANGA_HI

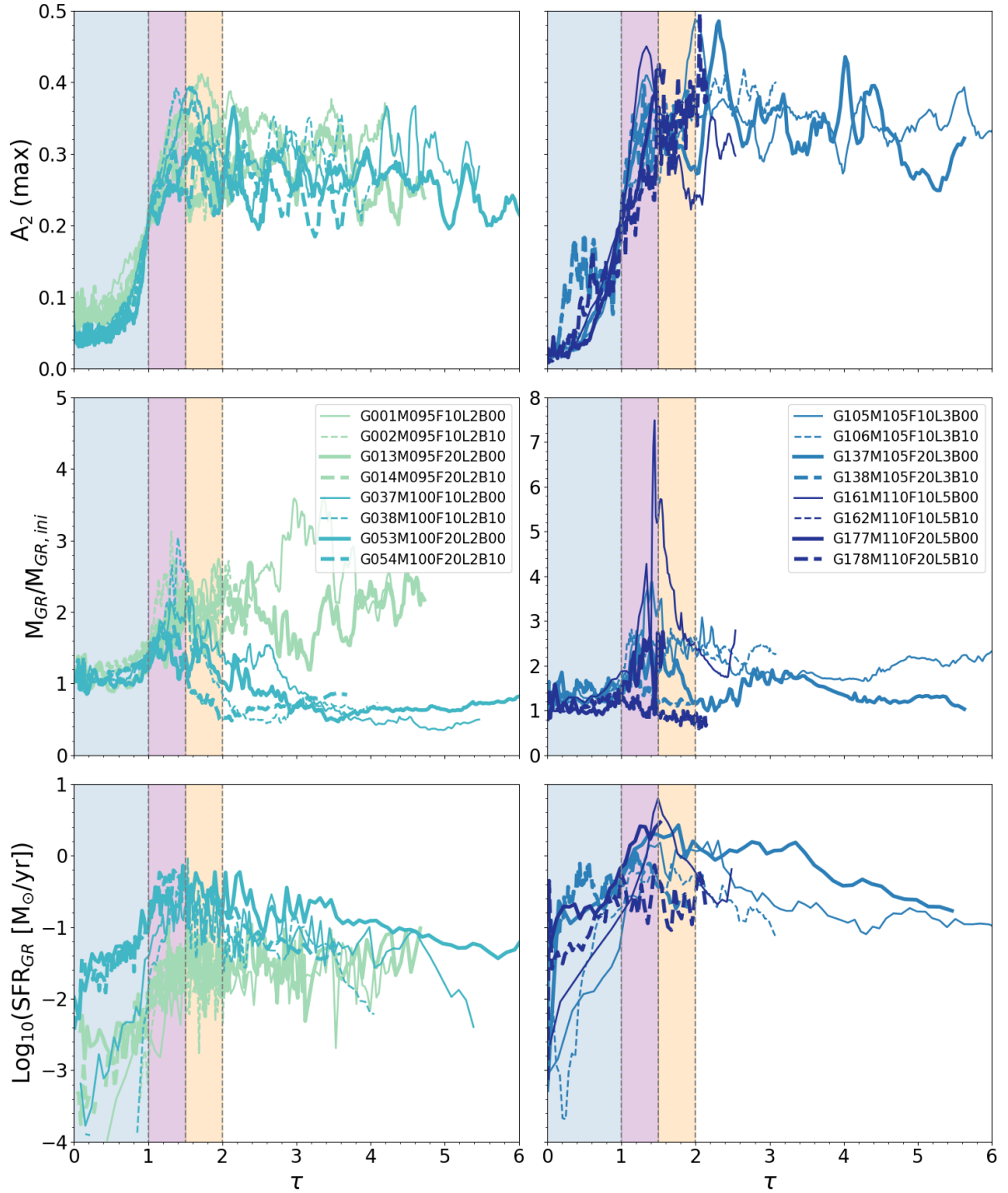


Figure 4.11: Evolution of the maximum of the A_2 coefficient (top panels), the mass of gas within the central 1 kpc normalised by the initial mass of gas within the same radius (middle panels), and the SFR (bottom panels). The evolution is shown through the dimensionless parameter τ , which is the ratio between the time of the simulations and the corresponding time when A_2 reaches the value of 0.2. The dashed vertical lines and shaded coloured areas show peculiar values of τ we use to describe the phases of the fuelling (i.e., $\tau \in 0-1$ (blue area); $\tau \in 1-1.5$ (purple area); $\tau \in 1.5-2$ (orange area)). The colour code and the meaning of the different lines are the same as in Fig. 4.8.

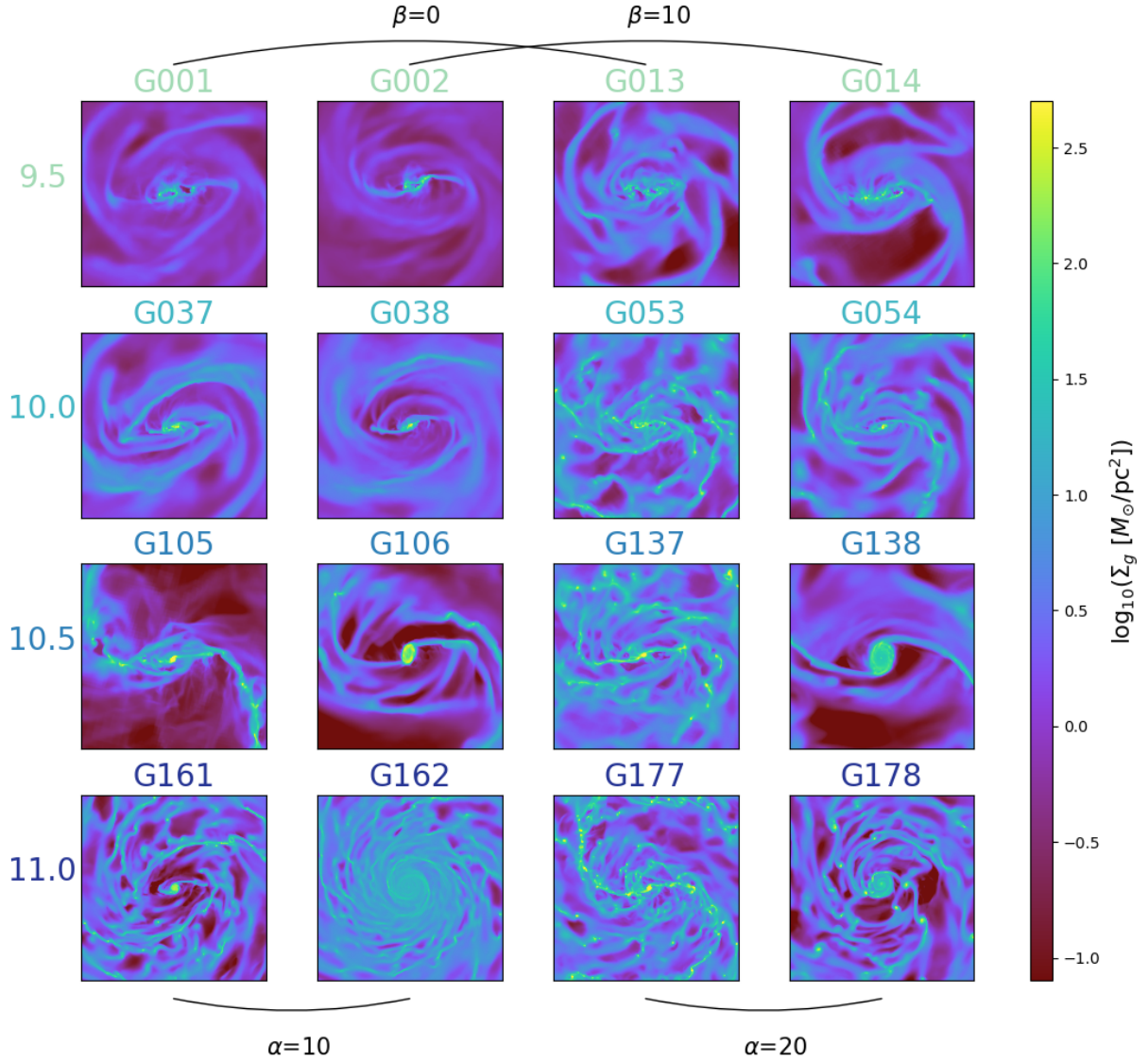


Figure 4.12: Density map of gas for the 16 simulations at the corresponding time for which $\tau = 2$. The first three rows show a box of 10 kpc side while the last row shows a box of 20 kpc side. The model numbers are colour-encoded according to the corresponding stellar mass (from the lightest to the most massive from the top to the bottom, i.e. 9.5, 10, 10.5, and 11 in $\log_{10}(M_{\odot})$). The two left columns illustrate the model with a gas fraction of 10% while the two right columns illustrate the models with a gas fraction of 20%. The odd (even) reference number accounts for models without (with) a bulge.

We have found that models G162M110F10L5B10 and G178M110F20L5B10 are expected to be significantly more stable against bar formation (according to the criterion established by [Efstathiou et al. \(1982a\)](#); but see Sect. 4.4.2). Note that the criterion we use to decide if a bar is formed or not (i.e. $A_2 = 0.2$) is met for model G178M110F20L5B10 despite the lack of an apparent proper bar structure: we interpret that case as A_2 capturing the evolution of the strong spiral arms.

We have studied the impact of three control parameters on the evolution of the central 1 kpc region. The mass inside the central gas reservoir naturally increases with the initial stellar and gas mass. The presence of a bulge delays the formation of the bar (i.e. values of t_{bar} are larger) and thus the formation of the gas reservoir, but does not prevent its formation.

The global evolution of the 12 models having a stellar mass $\geq 10^{10} M_{\odot}$ can be roughly described using a dimensionless bar formation time parameter $\tau = t/t_{bar}$, including three subsequent phases:

1. A formation phase: from $\tau = 0$ to ~ 1 , the bar forms and the gas mass inside the central 1 kpc region is nearly constant or increases weakly. The star formation rate slowly increases with time.
2. A fueling and growth phase: from $\tau = 1$ to ~ 1.5 , the bar is strong enough (i.e. $A_2 > 0.2$) and starts to transport gas towards the centre, leading to a steeper increase of the gas mass and a starburst inside that region. The star formation reaches a plateau.
3. A depletion phase: from $\tau = 1.5$ to ~ 2 , the bar stays strong, and a steep decrease in the amount of gas in the central 1 kpc region is associated with a slow decline in star formation rate. This phase witnesses the emergence of a central stellar mass seed growing into a more extended inner stellar and gas structure (discs and rings). The sizes of the inner discy structure seem to vary with e.g. the initial stellar mass and the presence or absence of an ellipsoid.

Simulated galaxies with initial stellar masses below $10^{10} M_{\odot}$ falling in the lowest mass bin, exhibit differences with respect to the more massive galaxies in the sample as for their inner gas structures, the spatial distribution of star forming regions for $\tau \geq 2$ and the gas depletion timescales in the central kpc. More specifically, the two first above-mentioned phases are also witnessed for the lower stellar mass models ($M_{\star} = 10^{9.5} M_{\odot}$), but we do not observe Phase 3, that is, a steep decrease of the gas mass inside the 1 kpc central region at $\tau > 1.5$. The gas mass in the central kpc thus stays roughly constant and is associated with a relatively constant SFR over time (until at least $\tau = 4$). We have also shown evidence for two distinct star formation distributions for $\tau \geq 2$ below and above the $10^{10} M_{\odot}$ initial stellar mass of our models. For models with $M_{\star} < 10^{10} M_{\odot}$ (hence only for the lower mass bin), we observe that the star formation mainly occurs along the bar, whereas star formation is mostly triggered inside the inner gas concentration for models with $M_{\star} \geq 10^{10} M_{\odot}$. This trend echoes the reporting made by [Fraser-McKelvie et al. \(2020\)](#) using H α two-dimensional mapping of a sample of nearby galaxies. We suggest that this relates to the

relative contribution of stellar-driven feedback within a given gravitational potential: this will be probed and discussed in detail in a subsequent paper (Verwilghen in preparation). The subset of simulations presented here only covers a restricted range of observational properties and are constrained by a fixed and limited set of initial structural parameters. We can thus already presume that stellar mass may not be the only or even the prime driver of the differences we observe in our simulations (see e.g. [Díaz-García et al., 2020](#)).

In this paper, we provide a first pilot study at the structures and time evolution of a set of simulations probing the star formation main sequence of nearby disc galaxies. Subsequent papers in this series will focus on examining in detail the advent and growth of the above-mentioned inner gas structures (and their associated stellar content), as well as study in more detail the origin of the change of regime around $10^{10} M_{\odot}$ observed in [Fraser-McKelvie et al. \(2020\)](#) and reproduced with this first subset of models. We have already planned for an extended sample of 54 models better covering the range of observed properties of the PHANGS-ALMA sample in this stellar mass range: a more full-fledged account of this "complete" set of hydro-dynamical simulations will be presented when available. Such studies can then serve as a benchmark for simulations embedded in a more comprehensive environment, including, for example, gas accretion, interactions or evolution in a cosmological context.

Chapter 5

The gas structure transition in low-
and high-stellar mass discs

Abstract

Recent hydro-dynamical simulations of isolated barred disc galaxies have suggested a structural change in the distribution of the interstellar medium around a stellar mass of $10^{10} M_{\odot}$. In the higher-mass regime, we observe the formation of a central gas and stellar disc connected through lanes to the ends of the stellar bar, with a typical size of a few hundred parsecs. In the lower-mass regime, such an inner disc is absent and the gas component is more turbulent and exhibits a more chaotic distribution. Observations of nearby star-forming galaxies support the existence of such a change. Those inner gas discs may represent an important intermediate scale connecting the large-scale (few kpc) structures with the nuclear (sub-parsec) region, transporting gas inwards to fuel the central supermassive black hole. In this work, we use an extended set of high-resolution hydro-dynamical simulations of isolated disc galaxies with initial basic properties (i.e., stellar mass, gas fraction, scale length of the disc of stars, and the bulge mass fraction) with properties covering the range of galaxies in the PHANGS sample to specifically investigate this change of regime and probe the stellar mass threshold for which the gas structure transition is observed. We study the physical properties of the star-forming interstellar medium in both stellar mass regimes and extract a few physical tracers (i.e., Inner Lindblad Resonance (ILR), probability distribution function (PDF), virial parameter, and Mach number) that shed some light on the observed PHANGS systems. The structure transition in the simulations occurs between a stellar mass of $10^{9.5}$ and $10^{10} M_{\odot}$, in line with observations. We show that the physical origin of this change of regime is driven by stellar feedback and its contribution relative to the underlying gravitational potential. With their shallower potential and typically higher gas mass fraction, lower-mass disc PHANGS galaxies combine two ingredients that significantly delay or even prevent the formation of a central gas (and stellar) disc. This result has strong implications for the star formation regimes, growth of central structures and overall secular evolution of disc galaxies.

5.1 Introduction

Recent observational campaigns (see e.g., PHANGS¹; Leroy et al., 2021; Lee et al., 2022; Emsellem et al., 2022; Lee et al., 2023) have shown that nearby disc galaxies exhibit a wide variety of structures in the distribution of the interstellar medium (ISM) such as spiral arms, dust lanes, and inner gas discs (Querejeta et al., 2021; Stuber et al., 2023). One of the most common characteristics is the presence of a well-defined gas concentration (rings or discs) within the central few hundreds of parsecs of galactic bars, often referred to as central molecular zone (CMZ) to echo the observed flattened structure in the Milky Way (see Morris & Serabyn, 1996; Henshaw et al., 2023). Those disc-like structures are sometimes believed to represent an intermediate stalling region towards a potential SMBH, and can thus be considered as "gas reservoirs" a small fraction of which could help feed the central SMBH (Emsellem et al., 2015; Yu et al., 2022).

The characteristic arrangement of the stellar bar, dust and gas lanes, and central disc reservoir seems to be preferentially observed in relatively high stellar mass barred disc galaxies. A stellar bar is an essential ingredient that drives the inward gas fuelling from kiloparsec scales to the inner region often via higher-density gas lanes that connect with the inner gas reservoirs. Those reservoirs are naturally associated with an increase in the local surface density of the ISM and may thus catalyse the formation of new stars (Sormani et al., 2020; Schinnerer et al., 2023). Star formation (SF) further leads to stellar-driven feedback, which is one of the mechanisms that may influence the gas transport further down to sub-parsec scales (e.g. Emsellem et al., 2015).

Observations suggest that these gas reservoirs only emerge in barred galaxies with a stellar mass above a given threshold (e.g. Verley et al., 2007; Fraser-McKelvie et al., 2020). Most nearby disc galaxies on the star-formation main sequence (SFMS) above a stellar mass of $\sim 10^{10} M_{\odot}$ have gas mass fractions below 25% (Catinella et al., 2012; Butcher et al., 2016) and the neutral, ionised and molecular ISM is well structured around a well-defined galactic centre (see bottom panel of Fig. 5.1). In systems with stellar mass below $10^{10} M_{\odot}$, the gas inside the bar region often appears less structured and its surface density distribution is more complex and less regular (see top panel of Fig. 5.1). The gas mass fraction is also significantly higher than in more massive discs, reaching values above 40%, and the structure of their ISM appears more clumpy and disorganised with star-forming regions located all along the stellar bar. Observations suggest that the galaxy's stellar mass is a key parameter determining whether a disc galaxy forms a central gas reservoir. While the properties of gas reservoirs in higher-mass systems have been investigated via observations (Sormani & Barnes, 2019; Neumann et al., 2019; Schinnerer et al., 2023; Choi et al., 2023; Sormani et al., 2023b) and simulations (Athanasoula, 1992b; Seo et al., 2019; Sormani et al., 2024), the large-scale galactic or small-scale local physical conditions required for the emergence of a central gas disc are still not understood.

In this work, we investigate the time evolution of main sequence star-forming discs in

¹PHANGS: Physics at High Angular resolution in Nearby Galaxies
(<https://sites.google.com/view/phangs/home>)

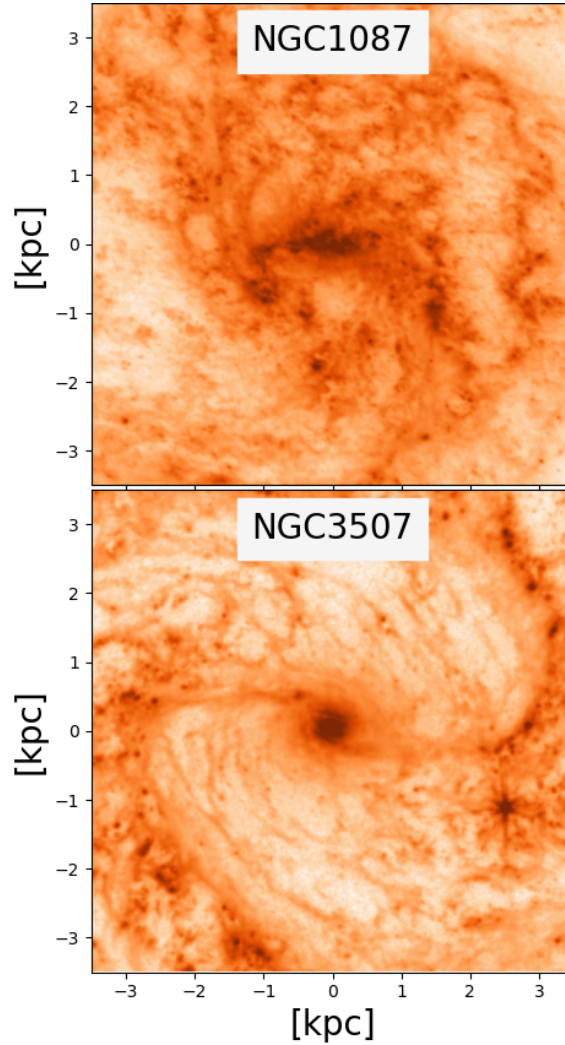


Figure 5.1: JWST MIRI $7.7 \mu\text{m}$ images of two nearby barred main-sequence star-forming galaxies (GO 3707; PI Leroy) NGC 1087 and NGC 3507 (stellar masses of $\sim 10^{9.95}$ and $\sim 10^{10.4} M_{\odot}$, respectively) emphasising the difference in morphology. Both images have been deprojected, and the bar is set horizontally. The field of view is $7 \text{ kpc} \times 7 \text{ kpc}$, thus showing the central $\pm 3.5 \text{ kpc}$. Those data have previously appeared in [Chown et al. \(2024\)](#) with data reduction following [Williams et al. \(2024\)](#).

order to better understand the underlying principles that drive the formation and growth of central structures. We address the questions of whether or not this evolution depends on e.g., stellar mass, and question the origin of this dependence, using controlled experiments, i.e., simulations mocking star-forming main sequence galaxies. We thus build an extended grid of generic disc galaxies ([Verwilghen et al., 2024](#)) based on properties of nearby disc galaxies on the star-formation main sequence ([Leroy et al., 2019](#)). We use various physical tracers (i.e., inner Lindblad resonance (ILR) PDF, virial parameter, and Mach number)

to probe a potential change of regime in the star formation distribution, focusing on the advent of bar-driven central mass concentrations.

After briefly presenting the extended set of hydro-dynamical simulations, we illustrate in Section 5.2 the overall variation in the evolutionary tracks and properties of galaxies in the low- and high-mass regimes. We focus on the properties of the gas before and after the formation of the bar in Section 5.3, using tracers such as the velocity dispersion, the Mach number or the virial parameter. In Section 5.4 we further demonstrate the role of stellar feedback in establishing such a change of regime, and its relative weight against the local gravitational potential. Section 5.5 follows with a brief discussion and a summary of the results.

5.2 First evidence in simulations for a change of regime

In this section, we emphasise the differences in evolution of the gas morphology and distribution of star-forming regions (Sect. 5.2.2) between the low- ($< 10^{10} M_{\odot}$) and high- ($\geq 10^{10} M_{\odot}$) stellar mass models within our set of simulations (briefly presented in Sect. 5.2.1). We also illustrate the variation of the surface density profiles below and above this stellar mass threshold.

5.2.1 The set of simulations

In this paper, we use an extended set of high-resolution simulations of isolated nearby disc galaxies based on the properties of the PHANGS galaxy sample (Verwilghen et al., 2024, Chapters 3 and 4). This simulation set is currently composed of a grid of 35 models having different control parameters encoded as GxxxMxxxFxxLxBxx, where the number after G stands for an internal reference, M for the stellar mass (i.e., 095, 100, 105, and 110 for the stellar mass bins $10^{9.5}$, 10^{10} , $10^{10.5}$, and $10^{11} M_{\odot}$, respectively), F for the total gas fraction (i.e., 10, 20, and 40 %), L for the scale length of the stellar disc (2-5 kpc), and B for the bulge mass fraction (i.e., 0, 10 and 30 % of the total stellar mass). A first subset of 16 simulations with a more restricted set of parameters has been presented in Verwilghen et al. (2024) and in Chapters 3 and 4 of the present manuscript, with an emphasis on the phases and timescales associated with bar formation. We list the values of the control parameters of the initial conditions for all models in the extended set in Table 5.1.

Briefly, all simulations have been performed with RAMSES (Teyssier, 2002b), an adaptive mesh refinement (AMR) hydro-dynamical code. The code treats the stars and dark matter (DM) as particles and gas via cells via the AMR grid. The code also includes numerical recipes implementing the cooling of gas, star formation and stellar feedback (supernovae and stellar winds), and the evolution of the metallicity via two tracers (see Agertz et al., 2013, 2021b, for more details). Those simulations reach a minimum spatial sampling of 12 pc, and a typical mass resolution of 10^4 and $2 \times 10^3 M_{\odot}$ for the old and new stellar particles, respectively. More details regarding the sub-grid recipes, detailed setup of the simulations and initial conditions can be found in Verwilghen et al. (2024).

Model	$\log_{10}(M_*)$ [M_\odot]	F [%]	l_* [kpc]	l_g/l_*	B [%]	BAR
G001M095F10L2B00	9.5	10	2	2	0	Y
G002M095F10L2B10	9.5	10	2	2	10	Y
G007M095F10L3B00	9.5	10	3	2	0	N
G008M095F10L3B10	9.5	10	3	2	10	N
G009M095F10L3B30	9.5	10	3	2	30	N
G013M095F20L2B00	9.5	20	2	2	0	Y
G014M095F20L2B10	9.5	20	2	2	10	Y
G015M095F20L2B30	9.5	20	2	2	30	N
G019M095F20L3B00	9.5	20	3	2	0	N
G020M095F20L3B10	9.5	20	3	2	10	N
G021M095F20L3B30	9.5	20	3	2	30	N
G025M095F40L2B00	9.5	40	2	2	0	Y
G026M095F40L2B10	9.5	40	2	2	10	Y
G027M095F40L2B30	9.5	40	2	2	30	Y
G031M095F40L3B00	9.5	40	3	2	0	Y
G032M095F40L3B10	9.5	40	3	2	10	N
G033M095F40L3B30	9.5	40	3	2	30	N
G037M100F10L2B00	10	10	2	2	0	Y
G038M100F10L2B10	10	10	2	2	10	Y
G039M100F10L2B30	10	10	2	2	30	Y
G045M100F10L3B00	10	10	3	2	0	N
G046M100F10L3B10	10	10	3	2	10	N
G053M100F20L2B00	10	20	2	2	0	Y
G054M100F20L2B10	10	20	2	2	10	Y
G055M100F20L3B30	10	20	2	2	30	Y
G069M100F40L2B00	10	40	2	2	0	N
G070M100F40L2B10	10	40	2	2	10	Y
G105M105F10L3B00	10.5	10	3	2	0	Y
G106M105F10L3B10	10.5	10	3	2	10	Y
G137M105F20L3B00	10.5	20	3	2	0	Y
G138M105F20L3B10	10.5	20	3	2	10	Y
G161M110F10L5B00	11	10	5	2	0	Y
G162M110F10L5B10	11	10	5	2	10	N
G177M110F20L5B00	11	20	5	2	0	Y
G178M110F20L5B10	11	20	5	2	10	Y

Table 5.1: List of all models in the extended simulation set and the parameters used to set up their initial conditions. Columns from left to right are: name or label encapsulating those parameters, total stellar mass (M_* , here in \log_{10}), gas mass fraction F (in %), stellar scale length l_* (in kpc), scale length ratio l_g/l_* (gas over stellar scale lengths) and bulge mass fraction B (in %). The last column shows models developing a bar (Y) and never developing a bar (N) by the end of the run.

5.2.2 Gas surface density distribution

A systematic visual inspection of all simulations listed in Table 5.1 provides the first direct evidence for a change of regime: it is illustrated in Fig. 5.2 in the central gas structures observed before and after the bar forms. In this figure, we show the evolution of the face-on gas surface density as a function of the dimensionless parameter τ (i.e., absolute *time* normalised by the bar formation time t_{bar}) for four models, in two stellar-mass bins (i.e., $10^{9.5}$ and 10^{10} M_{\odot} - top and bottom rows, respectively, with two different gas fractions - left and right panels). $\tau = 1$ corresponds to the bar formation time set when A_2 reaches a threshold value of 0.2, with A_2 being the amplitude of the second Fourier term derived from the stellar density map (see Efstathiou et al., 1982b; Athanassoula, 2002; Athanassoula et al., 2013). The typical bar formation time is of the order of ~ 400 Myr and 800 Myr for models without and with an additional central ellipsoid (i.e. the bulge), respectively (see Verwilghen et al., 2024, for more details). Before the bar forms (i.e., $\tau = 0.5$), the gas distribution appears very clumpy and relatively unstructured, without any coherent large-scale gas structure. Once the stellar bar has formed, the gas distribution changes significantly, with the higher-density regions mostly clustered within the bar close to its major axis and along spiral-like structures outside the bar.

Around $\tau = 2$, the evolution starts to differ between the low and high stellar mass models. The higher-stellar mass models G037 and G053 (10^{10} M_{\odot} , with a gas fraction α of 10 and 20%, respectively) exhibit well-organised gas surface density distributions. We observe the emergence of a central gas concentration in both G037 and G053, leading to the formation of a well-defined central flattened overdensity at $\tau = 2$. At $\tau = 5$, that structure has grown into an inner gas disc connected with both ends of the bar via distinct lanes. This significantly contrasts with the structures observed in the lowest-stellar mass ($10^{9.5}$ M_{\odot}) models G013 and G025 (α of 20 and 40%, respectively): the central gas structure remains very clumpy even after the bar forms (see also Bland-Hawthorn et al., 2024), and there is no apparent significant change in the gas distribution with time until $\tau = 5$ and beyond.

At first glance, such a difference could be attributed to the higher gas fraction of models G013 and G025, which reflects the overall relative increased importance of gas in lower mass galaxies (see, e.g. Verwilghen et al., 2024). However, G013 and G053 are directly comparable: they are based on the same initial mass models for the stars, gas and dark matter, share the same gas fraction (20%), G013's total mass only being scaled down by a factor of about 3 (or $10^{0.5}$). At $\tau = 5$, the lower mass model G013 still exhibits a complex gas distribution made of rapidly evolving clumps and voids within the bar region with no well-defined centre, while the higher mass model G053 has a well-organised, nearly symmetric set of gas lanes fueling a central inner disc (the gas reservoir).

To provide a comparison of the evolution track between barred and unbarred models, we complementary provide in Fig B.1 the gas and new star density maps for four unbarred models (G015, G032, G045, and G069) at four different time steps: 500, 1000, 1500, and 2000 Myr. We see that simulated galaxies that do not form a bar form very few stars overall. We naturally do not observe the formation of a central gas reservoir in those

unbarred models. The case of model G069 is special because a bar forms around 315 Myr, but is later destroyed by a massive stellar cluster as shown in Fig. B.2 and is therefore considered as an unbarred model. In the rest of this work, the time corresponding to $\tau = 1$ is artificially assigned to unbarred models from the t_{bar} value of the barred model with similar initial conditions (e.g., model G007 has the same value of t_{bar} as G001, while G008 and G009 have the same value of t_{bar} as model G002).

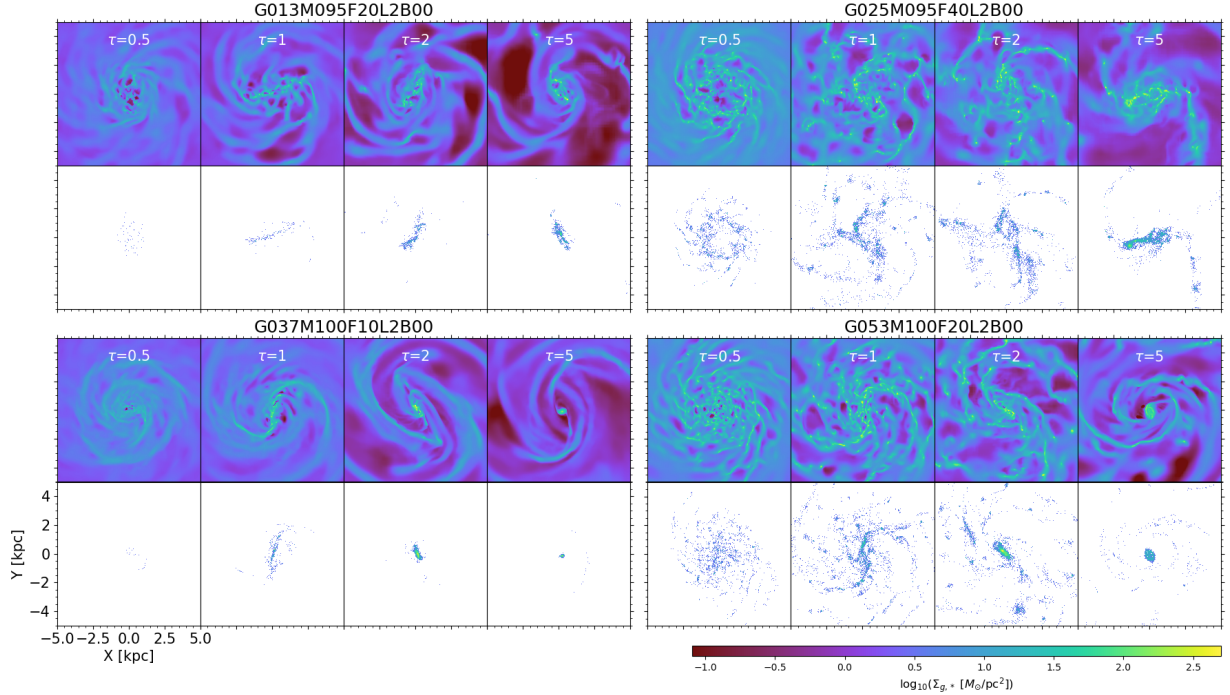


Figure 5.2: Surface density map of gas and newly-formed stars (≤ 100 Myr) of four models in two stellar mass bins (G013, G025, with an initial stellar mass of $10^{9.5} M_{\odot}$; G037, and G053 with an initial stellar mass of $10^{10} M_{\odot}$) from our set of simulations. Each panel shows one model at different values of the parameter τ , with $\tau = 1$ corresponding to the bar formation timescale. G013 and G053 have the same 20% gas mass fraction, while G025 and G037 have 40 and 10% gas mass fraction, respectively (the latter two following the averaged properties of star-forming main sequence galaxies at their respective stellar masses).

5.2.3 The radial gas density re-distribution

The presence or absence of an inner gas disc can be quantitatively illustrated by computing the radial gas density profiles from our simulations. Figure 5.3 shows the time evolution of the (azimuthally averaged) radial gas surface density profiles of the full set of models at $\tau = 0.5, 1$, and 2. To emphasise any potential time changes, we have normalised all density profiles by the initial radial gas (exponential) profile (at the start of the simulations, $t = 0$).

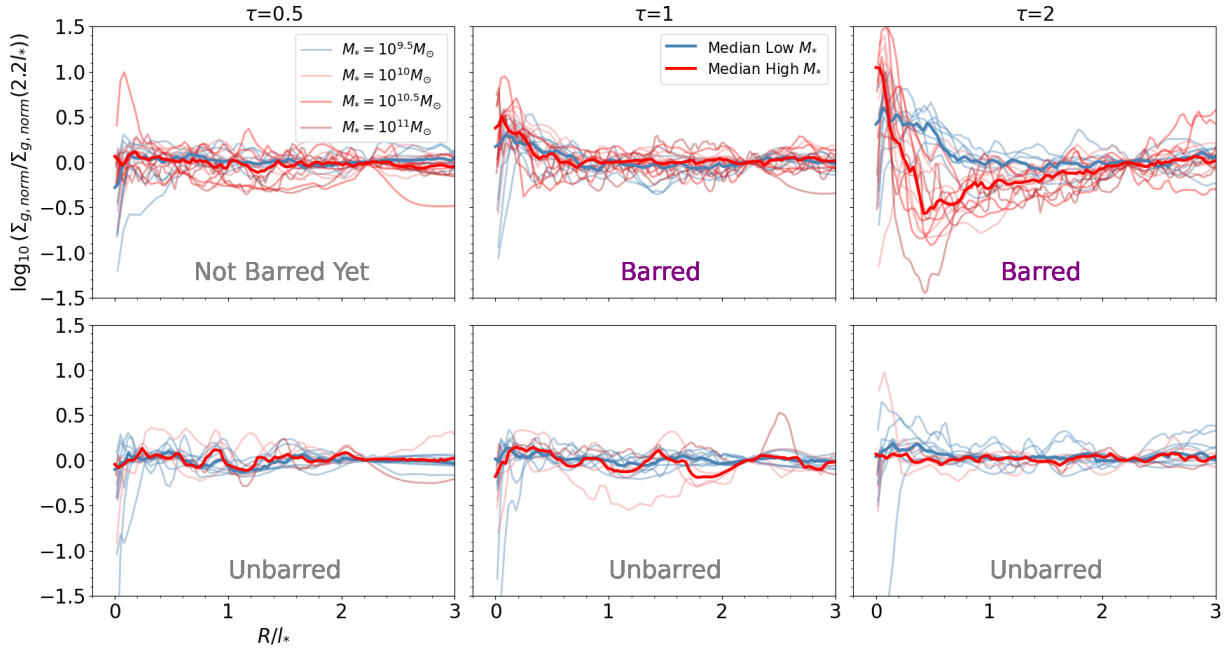


Figure 5.3: Normalised surface density profile of gas for our set of simulations at $\tau = 0.5$, 1, and 2 (see text). The faint blue curves represent low-stellar mass models ($< 10^{10} M_{\odot}$) and the faint red curves show higher-stellar mass models ($\geq 10^{10} M_{\odot}$). The strong blue and red lines are the median of the faint blue and red curves, respectively. The top panels show models that have formed a bar, sustained until the end of the simulation. The bottom panels illustrate the unbarred models.

The profiles are plotted as a function of the galactic radius (R/l_* , where l_* is the initial stellar disc scale length). To ease the inter-model comparison, all profiles are finally rescaled by their respective values at $2.2 l_*$ found in the literature and taken as a characteristic reference scaling for the underlying discs (in our models, the typical scale length of the gas disc (l_g) is twice the typical scale length of the stellar disc (l_*)). Figure 5.3 is split between barred galaxies (top panels) and unbarred ones (lower panels) using the classification at the end of the simulation ($t > 3$ Gyr).

The profiles of most unbarred galaxies consistently keep a rather flat profile (within ± 0.2 dex) at all times: the radial gas distribution does not seem to vary significantly over many 100s of Myr in the absence of a bar. Only one model departs significantly from this trend: G069. The bar in G069 forms around 315 Myr, but is subsequently ($t \sim 1500$ Myr) dissolved after interacting with an in-spiralling massive star cluster that has formed in the disk. Hence, this system is classified as unbarred by the end of the simulation, and its gas density profile becomes flat again after the bar has vanished, similar to other unbarred simulations.

This picture is radically different for barred galaxies as illustrated in the top panels of Fig. 5.3. For barred galaxies, we first witness a central increase of the density profiles for all models by the time the bar has formed ($\tau = 1$). At $\tau=2$, the lower and higher

mass models exhibit a significantly different radial profile within the central $\sim 2 l_*$. The higher-mass galaxies show a strong relative drop with a minimum at $\sim 0.4 l_*$ by a factor between 3 and 15, followed by a steep (factor of three of the initial ($t = 0$) density) increase towards the centre. This contrasts with the lower-mass systems that show a steady rise from $\sim 2 l_*$ inward. We note that the maximum (relative) central values for the density are similar for all models (both blue and red curves). The striking difference of evolution between the barred and unbarred systems emphasises the bar-driven re-organisation of the gas distribution. The observed peak within the central $\sim 0.4 l_*$ for the more massive models is a witness of the presence of an inner gas disc or "reservoir".

5.2.4 The redistribution of star formation across the disc

The change observed in the evolution of the gas distribution mentioned above can be associated with a redistribution of star-forming regions across the disc. In Fig. 5.2 we illustrate this via a few snapshots of the new stars (with ages less than 100 Myr) formed in four simulations distributed in two stellar mass bins (i.e., low-stellar mass models G013 and G025, and high-stellar mass models G037 and G053) for four different values of the parameter τ from 0.5 to 5. Low-stellar mass models (top panels) have their star-forming regions mainly located along the stellar bar for model G013 and spread over the disc for model G025, with no emergence of a well-defined central nuclear disc structure at any time in the simulation. The evolution of the high-stellar mass models (bottom panels) exhibits a clear transition in the distribution of star-forming regions, which is also observed in the highest-stellar mass bin models (i.e., $10^{10.5}$ and $10^{11} M_\odot$) developing a bar. At $\tau = 2$, the star-forming regions are located along the bar as in the low-stellar mass models. From $\tau = 2$ to $\tau = 5$, star-forming regions are mostly restricted to a central region with a typical size of a few hundred parsecs, associated with the formed central gas reservoirs (see Fig. 5.2).

5.3 Physical tracers

In the previous section, we emphasised the formation of a central gas reservoir and the associated central distribution of star-forming regions in high-stellar mass models ($\geq 10^{10} M_\odot$), and its absence in the lower-mass systems, by visually inspecting the gas and stellar surface densities. In this section, we turn to the physical properties of the gas to quantitatively follow the emergence of the central mass concentration, then examine the gas density probability distribution function (PDF), the virial parameter and the Mach number inside the central 1 kpc region as tracers of the physical state of the gas.

5.3.1 Emergence of the ILR

In Sect. 5.2.3, we showed that a change of regime is associated with the build-up of a central gas mass reservoir, that is accompanied by a corresponding central stellar overdensity made

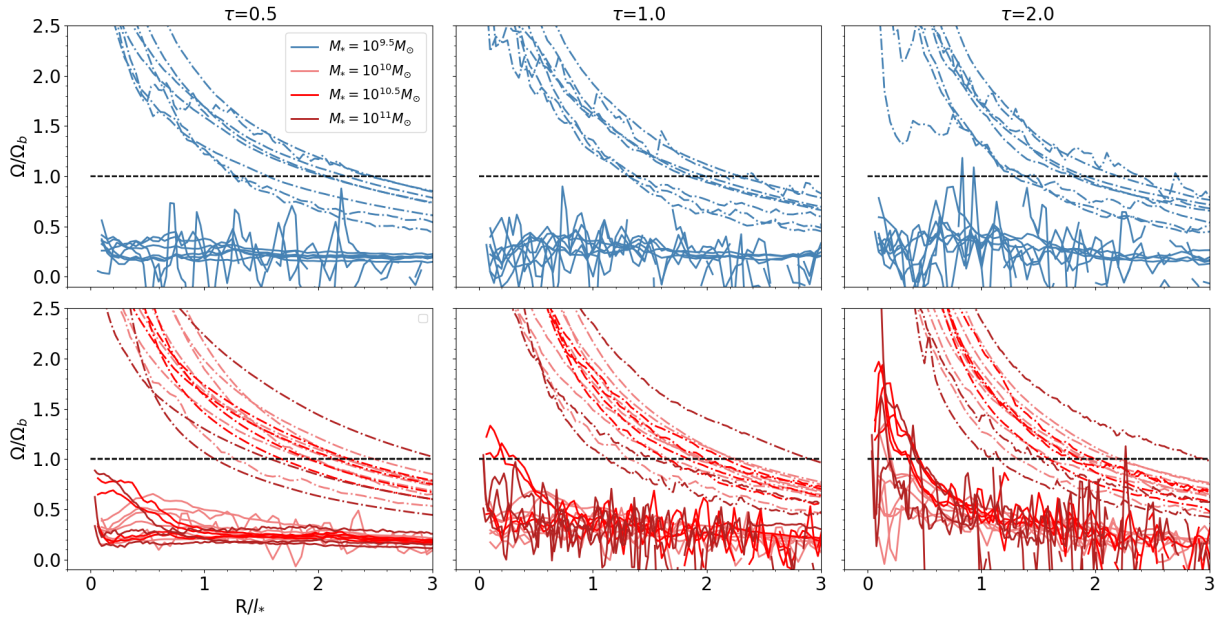


Figure 5.4: Evolution over time (from left to right, $\tau = 0.5, 1$ and 2) of the normalised angular frequency Ω and $\Omega - \kappa/2$ radial profiles of the barred low-stellar mass (blue curves, top row) and high-stellar mass (red curves, bottom row) models. The quantity we use in the normalisation is the bar pattern speed Ω_b . The black dashed curve represents $\Omega = \Omega_b$.

of newly formed stars. Such a change in the radial mass profile should be reflected in a steepening of the circular velocity and angular frequency (Ω) profiles. A bar rotating with a given pattern speed (Ω_b) implies the potential emergence of inner resonances, namely an inner Lindblad Resonance (ILR, REFS) when $\Omega_b = \Omega - \kappa/2$, where κ is the radial epicyclic frequency. In Fig. 5.4, we thus probe for all the barred models the time evolution of the angular frequency Ω (top dashed-dotted curves) and the quantity $(\Omega - \kappa/2)$ (bottom curves) normalised by the pattern speed of the bar Ω_b .

At $\tau = 0.5$, before the bar has formed, nearly all $\Omega - \kappa/2$ profiles are flat and all stay below the Ω_b value ($\Omega/\Omega_b = 1$; dashed lines). A few models exhibit a slight increase towards the centre and those are the systems with an initially added ellipsoid (flattened bulge): this is consistent with the bulge representing an extra mass concentration. At $\tau = 1$, a few high-mass systems exhibit central increases that cross the $\Omega/\Omega_b = 1$ line: an ILR is present. The models to first cross this threshold again have a bulge in their initial conditions, hence starting with a steeper central potential. At late times ($\tau = 5$) most of the higher-mass systems, including those that did not have an initial bulge, have a well-defined ILR. This result is consistent with the presence of a well-defined inner gas disc in the central region of those models. This dramatically contrasts with all of the lower-mass models being far from having the inner mass concentration that would lead to an ILR: the lower-mass systems were not able to form a central disc-like reservoir of gas.

5.3.2 The central PDF

To quantify further the state of the gas and the potential variation in clumpiness that appears in Fig. 5.2, we can rely on the gas density probability distribution function (PDF) that describes the relative importance of low and high-density regions. In Fig. 5.5, we show the evolution of the PDF inside a central cylindrical region of radius $1 l_*$ and height 2 kpc as a function of time for four values of τ (as in Fig. 5.2).

Overall, all models have gas densities from about 10^{-5} up to 10^3 cm^{-3} , initially with a rather flat distribution in the range $[10^{-2} - 10^2] \text{ cm}^{-3}$. At $\tau = 1$ (once the bar has formed) all four models exhibit a similar PDF, following small adjustments relative to the PDF. At $\tau = 0.5$, i.e., a slight increase (resp. decrease) of the high (resp. low) density tail, that corresponds to the steep increase in the star formation rate (see Verwilghen et al., 2024): this is qualitatively true for all four models. For lower-stellar mass models G013 and G025, the overall shape of the PDF does not change significantly with time beyond the formation of the bar (top panels of Fig. 5.5). This is consistent with the observed structure in the two-dimensional gas surface density map (Fig. 5.2): for those two models, the gas distribution tends to be more centrally concentrated within the bar region, but its morphology still appears very clumpy and disorganised. In other words, it is challenging to discern whether a bar has formed in such models just by examining the central PDF, even if we are limited by the maximum resolution (12 pc) of the simulations.

In contrast with such a steady state, the central PDF of the higher-stellar mass models G037 and G053 evolves at all scales after $\tau = 2$. After bar formation at $\tau=2$, the PDF develops a tail at high-density values reaching about $10^{3.5} \text{ cm}^{-3}$. This corresponds to the time when the bar-driven fuelling sets the seed of the central gas reservoir, a compact, dense and discy feature. Beyond $\tau = 2$, the shape of the PDF drastically changes. At $\tau=5$, the PDF is significantly skewed towards lower-density gas, with a bump in the gas density distribution at $\sim 10^{-4} \text{ cm}^{-3}$ and a negative slope up to $\sim 10^2 \text{ cm}^{-3}$ followed by an abrupt drop at $\sim 10^3 \text{ cm}^{-3}$. The low-density bump is a direct consequence of the re-organisation of the gas structuring within the bar. The gas fuelling towards the inner disc is associated with the denser bar lanes and those are surrounded by a depleted region between the bar ends and the inner gas disc. The abrupt cut at high densities certainly depends on resolution, but could also be associated with the emergence and radial growth of the inner gas disc (and the associated onset of the formation of the stellar disc) between $\tau=2$ and $\tau=5$. Most importantly, there is a relative decrease (factors of typically 3 to 5, and up to 10) of the PDF values in the full range between 10^{-3} and 10^2 cm^{-3} for both higher mass systems (Fig. 5.5).

5.3.3 Dynamical tracers

We next turn to dynamical tracers of the state of the gas in the bar region. Figure 5.6 illustrates the evolution over time of the distribution of the virial parameter (α_{vir}) and the Mach number \mathcal{M} . α_{vir} addresses the ratio between the local kinetic and gravitational energies and is proportional to the square of the velocity dispersion and the inverse of the

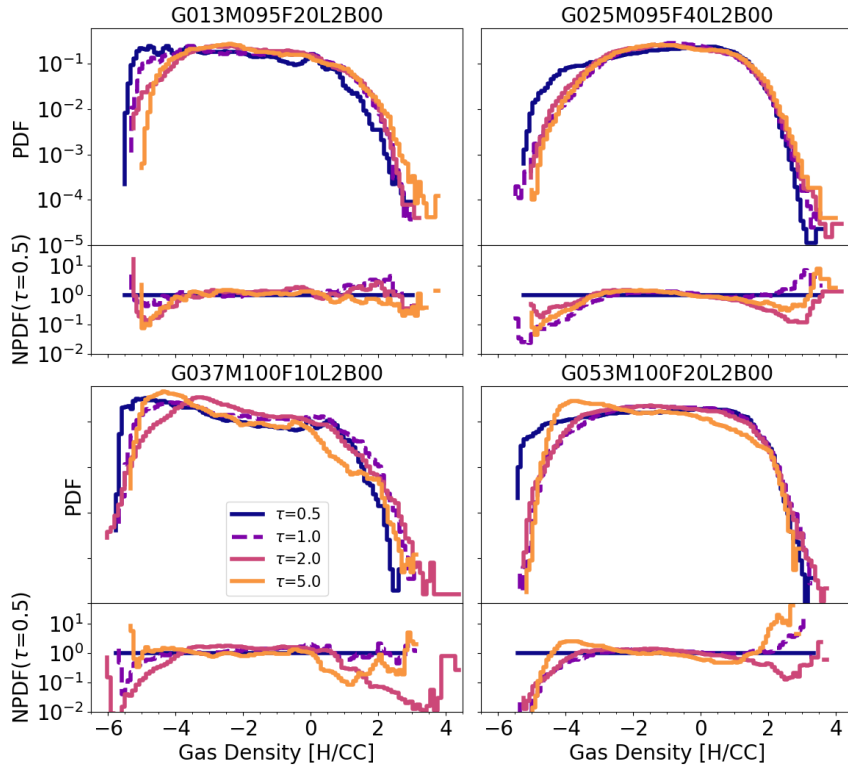


Figure 5.5: Evolution of the Gas density Probability Distribution Functions (PDF) of four of our simulated galaxies (i.e., models G013, G025, G037, and G053, see Fig. 5.2) as a function of τ (main panels). The normalised PDF by the PDF at $\tau = 0.5$ (NPDF) is shown at the bottom of each main panel.

compactness of the clouds. The Mach number is a quantity measuring the ratio between the velocity dispersion and the sound speed, that depends on the gas temperature. Those two quantities provide a quantitative description of the physical state of the star-forming gas and are often used as a relevant way to connect with observations (e.g. Sun et al., 2022). To compute those distributions, we have used a centred box with a side length of $2 l_*$ (4 kpc) and a height of 2 kpc (± 1 kpc) and averaged the 1D velocity dispersion (σ_{1D}), sound speed (v_s), potential energy (E_{grav}), virial parameter (α_{vir}), and the Mach number (\mathcal{M}) of the smallest star-forming gas cells (12 pc) contained inside volumes of 100 pc^3 . The typical number of events inside this volume varies between 5000 and 150000.

For this comparison, we focus on two models that best follow the observed properties of SFMS galaxies, namely G025 (low mass bin, with $10^{9.5} M_\odot$, and an initial gas fraction of 40%) and G053 (higher mass bin, with $10^{10} M_\odot$, and an initial gas fraction of 20%). The distribution of the virial parameter and Mach number for G025 exhibit no significant changes before and after the formation of the bar ($\tau = 1$, black dashed curve). A similar result was found in Bland-Hawthorn et al. (2024) for gaseous bars in LMC-mass ($< 10^{10} M_\odot$) objects (see their figure 15). This means that the dynamical and physical

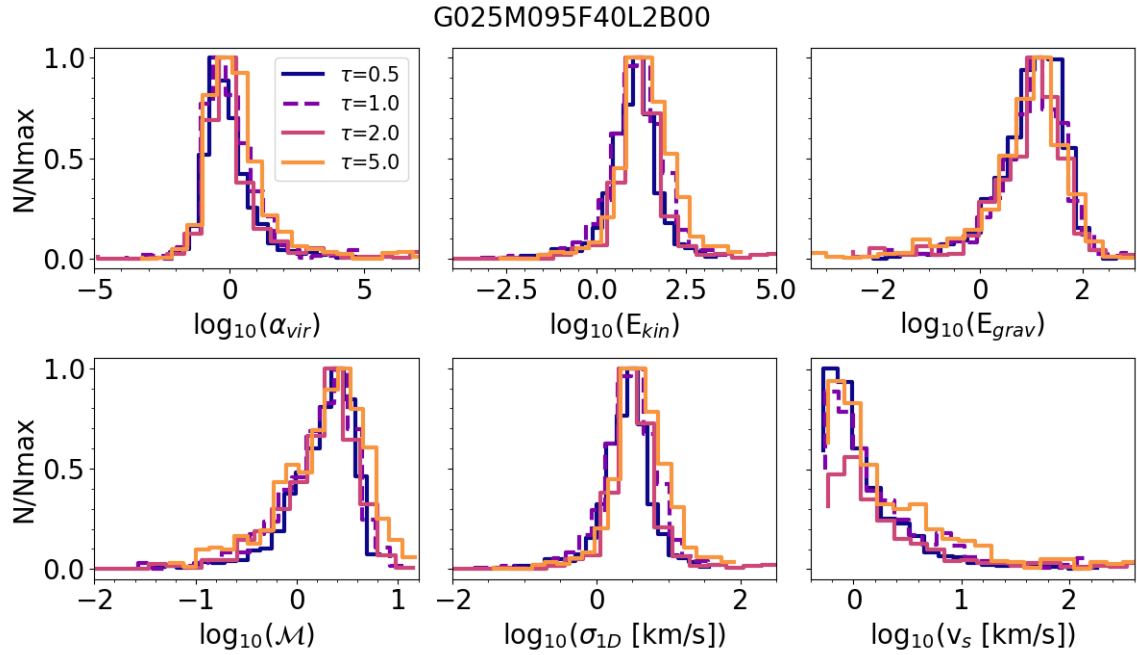


Figure 5.6: Normalised distribution of the virial parameter (top left) and Mach number (bottom left) and their components (i.e., kinetic energy E_{kin} and potential energy E_{grav} for the virial parameter and the one-dimensional velocity dispersion σ_{1D} and the sound speed v_s for the Mach number) as a function of time for the low-stellar mass model G025. The distributions are computed inside a box of $2 l_*$ in side length and a height of $1 l_*$ around the centre.

status of the central star-forming regions does not seem to be affected by the formation of the bar. This is quite a surprising result but already expected from the constancy of the global PDF illustrated in Fig. 5.3.

The high-stellar mass model G053 (Fig. 5.7) shows a radically different behaviour. Both α_{vir} and \mathcal{M} distributions develop a secondary peak after the formation of the bar at higher and lower values, respectively. In Fig. 5.6 and 5.7 we also provide the respective numerators and denominators for α_{vir} (resp. kinetic and gravitational energies) and \mathcal{M} (resp. velocity dispersion and sound speed). For G037, the sound speed distribution exhibits a secondary peak at higher values that is directly related to an increase in the gas temperature. That temperature increase is caused by more intense stellar feedback associated with the emergence of a central disc, which is then reflected in the subsonic peak at $\mathcal{M} \sim 0.25$.

As mentioned before, the drastic change in the evolution of such dynamical tracers could be related to the increase of the gas fraction in the low-mass systems. However, this does not seem to be the case, as a comparison between models G013 and G053 that share similar initial conditions (only with a mass scaling) and the same gas fraction of 20% shows consistent trends.

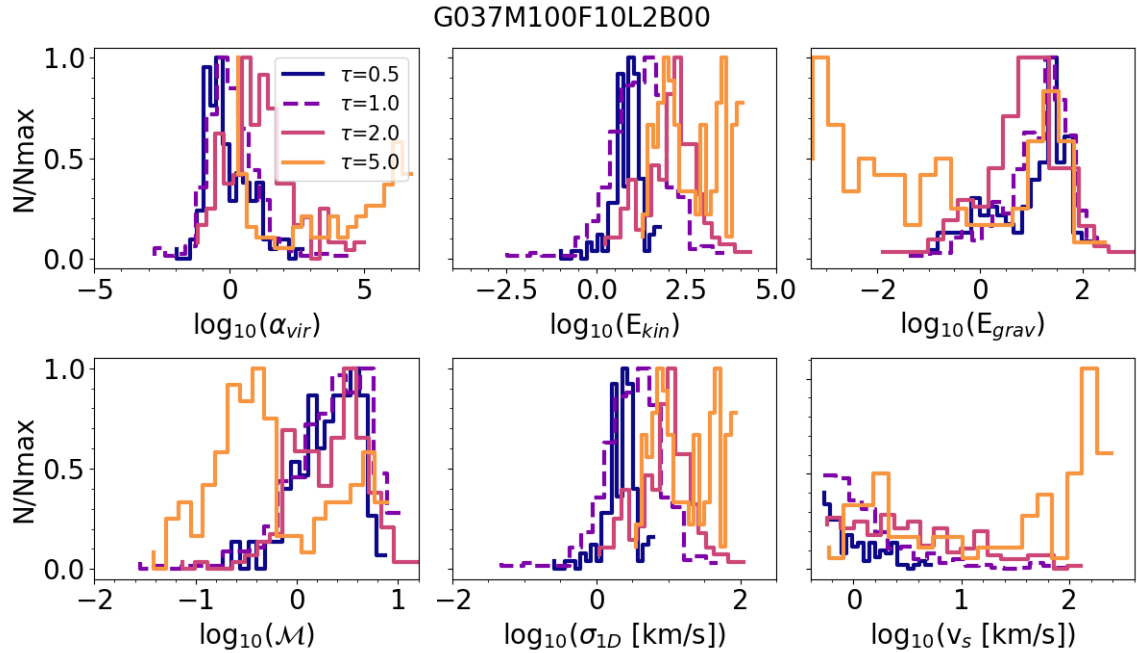


Figure 5.7: Same distributions as in Fig. 5.6 for the high-stellar mass model G037.

5.4 The balance between stellar feedback and gravity

In this section, we probe the physical origin of the observed change of regime traced via a variation of local values of \mathcal{M} and α_{vir} (Sect. 5.3) by studying the balance between stellar feedback and the gravitational potential, and the ratio between the ejected gas mass and the SFR (mass loading factor). Those two tracers allow us to understand the chaotic structures in our lower-mass models and the emergence of an inner gas disc in higher-stellar mass models.

5.4.1 Feedback versus gravity

Our simulations include stellar feedback in the form of supernovae and stellar winds. These processes inject energy and momentum into the surrounding ISM, leading to an increase of the local gas velocity dispersion σ (e.g. Mac Low & Klessen, 2004; Padoan et al., 2017; Agertz et al., 2009). When vigorous enough, feedback can drive galactic scale outflows and expel gas far beyond the stellar disc (for reviews, see e.g. Veilleux et al., 2005; Rupke, 2018), a process that is well studied in numerical simulations (e.g. Muratov et al., 2015; Nelson et al., 2019; Andersson et al., 2023). One direct tracer of the impact of feedback is the variation in the velocity dispersion, and more specifically its vertical component σ_z . Such outflowing gas is pulled back by the gravitational potential of the disc that may dominate (or not) the local energy budget, preventing the gas (or not) from escaping at large vertical distances.

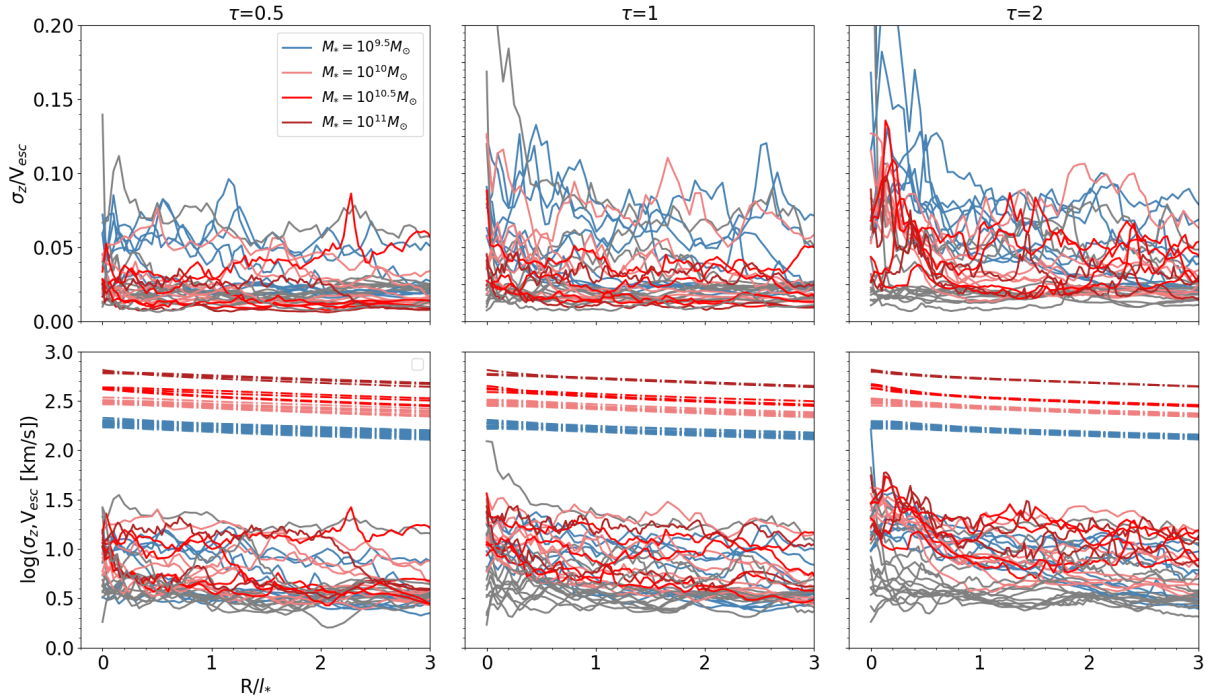


Figure 5.8: Evolution (from left to right) of the vertical velocity dispersion normalised by the local escape velocity (top row), the vertical velocity dispersion (solid curves), and the escape velocity (dot-dashed curves, bottom row) profiles as a function of τ . The blue curves represent low-stellar mass models and the red curve the higher-stellar mass models. The grey curves are models that do not display a bar at the end of the simulation.

To quantify the relative effect of feedback in our simulation, we measured the vertical velocity dispersion σ_{rel} normalised by the local escape velocity v_{esc} , the latter being directly connected with the depth of the local total gravitational potential for all simulations in our extended set. The evolution over time of this normalised dispersion is shown in Fig. 5.8.

We first note (bottom row of Fig. 5.8) that the escape velocity profiles do not significantly change with time, for any of these models. Hence most of the evolution observed in the normalised dispersion values can be linked back to an evolution in the dispersion itself. Remarkably, all unbarred systems show consistent and flat vertical velocity dispersion profiles with values around 3 km.s^{-1} , with an increase only in the central region ($R < 0.5 l_*$). The bar thus seems to have a prominent role in establishing a sustained higher value for the vertical velocity dispersion.

For all barred galaxies, we further see a clear trend that higher gas fraction systems have higher values of σ_z : this is expected considering that a higher gas fraction relates to a higher star formation rate, hence a relatively stronger role for stellar feedback, as predicted by [Ostriker et al. \(2010\)](#). The only exception seems to be model G069. As already noted (see Sect. 5.2) that model develops a bar which then gets dissolved and that is consistent with the fact that its velocity dispersion is first relatively high (as for other systems with

40% gas fractions) and settles back to a flat and lower value profile after the bar dissolution (see lowest red curve in the lower right panel at $\tau = 2$ in Fig. 5.8). By $\tau = 5$, all barred systems with at least 20% of gas exhibit σ_z values between 6 and 20 km.s⁻¹ with peaks up to 30 km.s⁻¹.

The normalised velocity dispersion profiles are presented in the top row of Fig. 5.8 with different colours depicting different stellar masses. What we mentioned in the previous paragraphs is now clearly emphasised:

- Higher gas fraction systems still tend to have higher normalised dispersion profiles *at fixed stellar mass* (i.e., fixed escape velocity).
- Lower stellar mass systems tend to have higher dispersion profiles with respect to their escape velocities (*at fixed gas fractions*).

5.4.2 The crucial role of supernovae in preventing the formation of an inner gas disc

As shown in the previous section and Fig. 5.8 both the formation of a bar and the depth of the gravitational potential have a clear impact on the physical status of the ISM in our simulations. It suggests that bars in lower-mass systems have a stronger impact due to both the shallower depth of the gravitational potential (as compared with higher stellar mass discs) and the observed higher gas fraction of main sequence star formation. We now show that stellar feedback, as implemented via subgrid recipes in our simulations, is the driver of such a trend with the bar in the lowest mass systems. We thus run a test case using model G001 (a low stellar mass model with a gas fraction of 10%) as a reference, where we turn off the feedback from supernovae (model named G001-NOSN). In that simulation, only the stellar feedback due to stellar winds is kept active.

Figure 5.9 illustrates the evolution of model G001 with (left panel) and without (right panel) supernovae feedback. We observe that the onset of a central disc is already visible in the model without feedback (G001-NOSN) at $\tau = 1$, and further develops into an extended central gas reservoir at $\tau = 5$. The impact of supernova feedback on the gas velocity dispersion is directly illustrated in Fig. 5.10 where we present the σ_z radial profile for both G001 models (with and without supernova feedback). As expected, model G001-NOSN has a low and rather constant vertical velocity dispersion ($\sigma_z \sim 3$ km.s⁻¹). Even though G001-NOSN develops a strong bar, its σ_z profile does not vary much with time and is consistent with those observed for all our unbarred models in Fig. 5.8.

The emergence of a central gas reservoir associated with a young stellar disc is further confirmed by the observed evolution of the frequency profiles, as shown in Fig. 5.11: in contrast with the G001 models, G001-NOSN exhibits a broad central increase of the $\Omega - \kappa/2$ at $\tau = 1$ and develops a clear ILR as observed in the profile at $\tau = 5$. Interestingly, by the end of the simulation ($\tau = 5$), model G001 that includes supernova feedback still exhibits a mild increase of its $\Omega - \kappa/2$ profile, suggesting that it may manage to build a bona fide central gas reservoir at a later time. Running test simulations such as G001-NOSN for

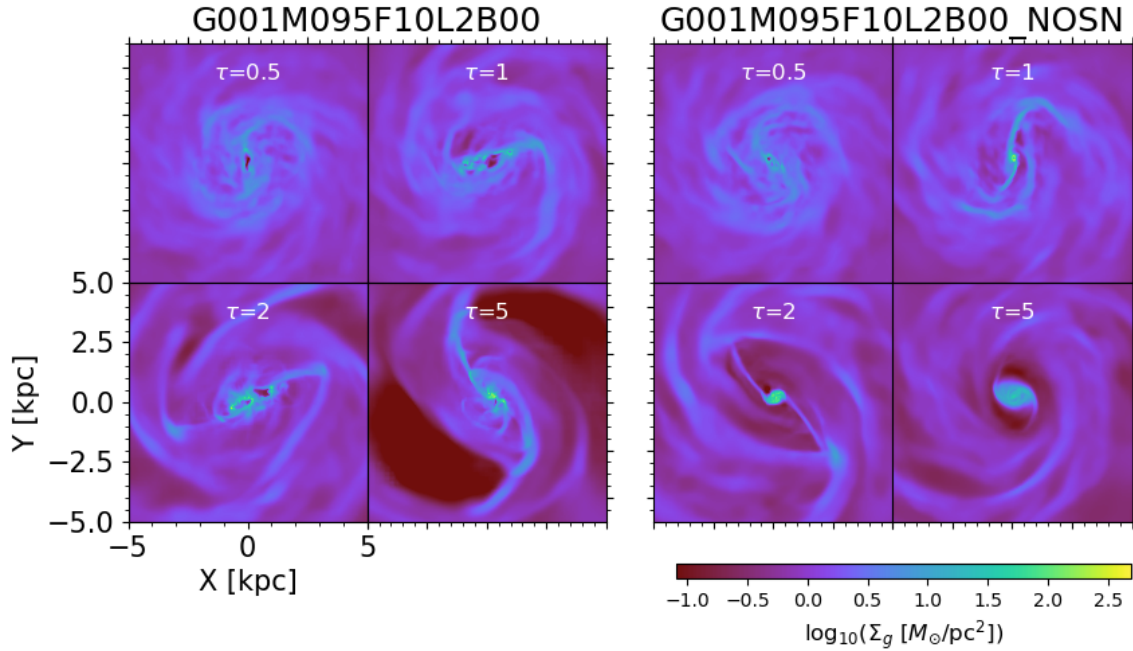


Figure 5.9: Surface density map of gas of model G001 (left panel) and G001-NOSN (right panel) at four characteristic times. The ‘NOSN’ stands for the run without feedback from supernovae and only includes feedback from stellar winds. Each subpanel shows one model at different values of the parameter τ .

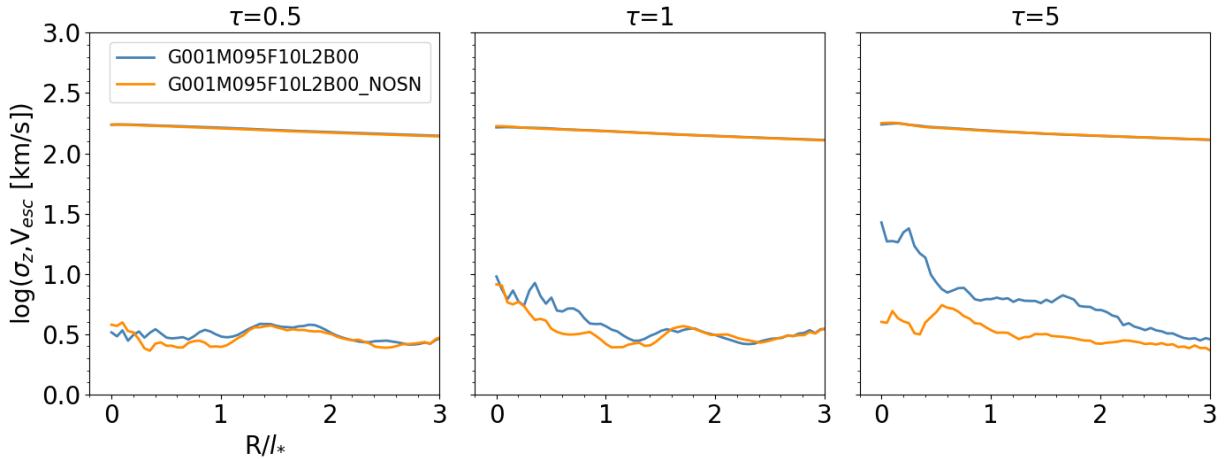


Figure 5.10: Same as bottom panels of Fig. 5.8 but for model G001 (blue curve) and G001-NOSN (orange curve).

all our simulations is beyond the scope of the present paper. Still, G001-NOSN provides strong evidence that stellar feedback, and more specifically supernovae feedback, is the main driver in our simulations for the change of regime between low and higher mass systems, and does prevent the emergence of a central gas reservoir in galaxies with shallow

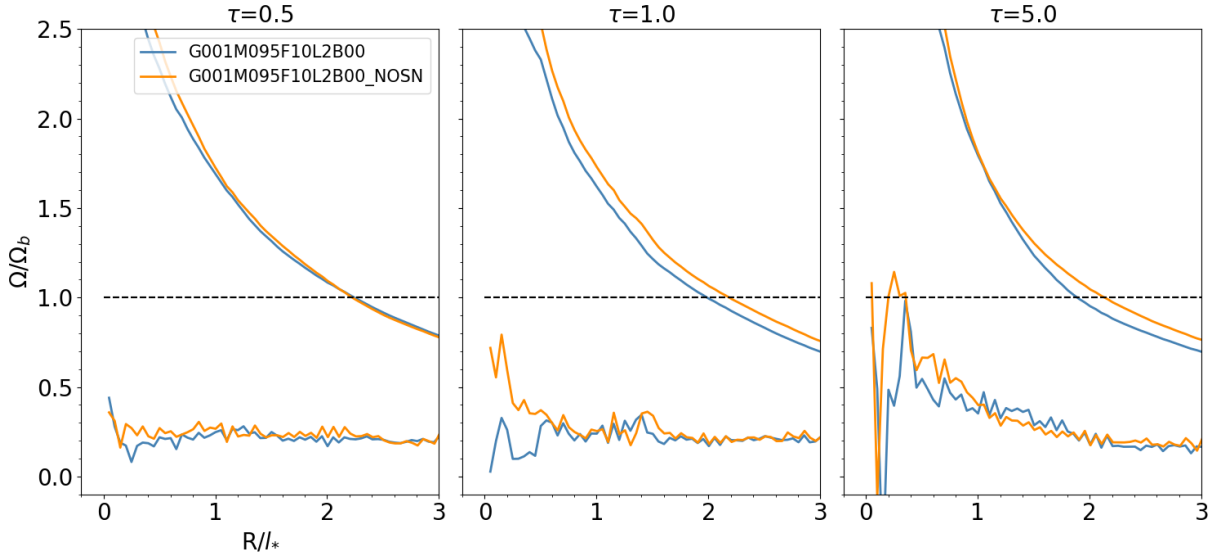


Figure 5.11: Same as in Fig. 5.4 but for model G001 (blue curve) and G001-NOSN (orange curve).

gravitational potentials.

5.5 Discussion and Conclusion

5.5.1 A gas reservoir chronicle

In the previous Sections, we have provided evidence that lower mass simulations of disc galaxies exhibit a different evolution in their gas redistribution driven by a stellar bar, and we have identified that stellar-driven feedback is a key factor in preventing a coherent structure from emerging. In higher mass systems, the gas reservoir is built while new stars have already started to accumulate within the central region of the bar (see e.g., Fig. 5.3).

The emergence of those structures is emphasised in Fig. 5.12 where we present a time sequence encapsulating the early formation of the gas reservoir for two reference simulated systems that lie on the SFMS, namely G025 ($10^{9.5} M_\odot$) and G053 ($10^{10} M_\odot$). Only the G053 higher mass run forms a well-structured gas flow and central gas disk structure in the first three Gyr (at a running time of about $t = 1400$ Myr). Over 600 Myr, the lower mass G025 run shows very little evolution in the total gas, molecular gas and stellar distribution. For G025, high gas density clumps are observed mostly travelling along the bar, significantly disturbed by continuous injection of feedback energy, and its associated one-dimensional gas density profile is flat. The case of G053 is radically different, with a very strong time evolution: while the averaged gas density profile along the bar axis resembles the G025 one in the first two panels, a clear peak forms after 1400 Myr (last two panels) surrounded by a region of depressed gas density. This is reminiscent of the observed signature from the

bar-driven organised gas flow seen in the profiles presented in Fig. 5.3. This is particularly visible in the molecular gas distribution and profile for G053 where the bar region is almost entirely devoid of gas except for the emerging central ~ 200 pc gas reservoir. It is also remarkable to follow how new stars preferentially accumulate in a growing and well-defined central exponential disk (with a scale length of about 100 pc when projected edge-on).

5.5.2 The importance of timescales

The emergence of a central gas reservoir appears to occur at early times for models with larger stellar masses only. This is illustrated in the formation of an ILR that is associated with a central (stellar and gas) mass concentration (Fig. 5.11). However, in Fig. 5.9, we observe a late onset of a more organised fueling flow for a lower-mass system (G001), which is also reflected in the slight central increase in the $\Omega - \kappa/2$ radial profile of Fig. 5.11. This suggests that the absence of a central gas reservoir at $\tau = 5$ in lower mass galaxies can be the consequence of a longer timescale needed by these smaller systems to acquire gas via a coherent, inward flow rather than of a stellar mass criterion alone.

To test this hypothesis, we have run an additional low stellar mass case using the same conditions as for the G001 model, but this time running up to 7 Gyr corresponding roughly to $\tau = 10$. Up to a time $t \sim 5.5$ Gyr, the gas distribution resembles other low mass simulations, with a rather disorganised, clumpy appearance. Around $t \sim 5.7$ Gyr the gas flow tends to a more ordered organisation, and by $t = 5.85$ Gyr (i.e., $\tau > 8$), the seed of a central gas disk appears. If we compare such a timescale with other larger-mass models at the same gas fraction, it is more than 4 times faster for model G037 (with an initial $10^{10} M_{\odot}$ stellar mass) to reach a similar state (both in absolute terms - Myr - and in terms of the corresponding τ). It is therefore likely that the observed transition between a stellar mass of $10^{9.5}$ and $10^{10} M_{\odot}$ also stems from a continuous varying timescale for the formation of a reservoir that depends in turn on the relative importance of feedback and gravity (see Sect. 5.4.1).

To probe such a transition further, we performed a simulation using an intermediate-stellar mass, namely $10^{9.75} M_{\odot}$ labelled G000M975F10L2B00. The resulting gas evolution is shown in Fig. 5.13 where we show the comparative evolution of our two reference models G001 (top panel; $10^{9.5} M_{\odot}$) and G037 (bottom panel; $10^{10} M_{\odot}$). We observe the formation of the gas reservoir and then the gas reservoir after $\tau = 4$ for the intermediate-mass models, while it forms at $\tau \sim 3$ and $\tau \sim 8$ for the higher-mass and lower-mass ones, respectively. The radial extent of the gas reservoir at $\tau = 6$ for this intermediate model is significantly larger than for the high-stellar mass model. This trend stands when using absolute times (formation time of the seed at about 5.9, 2.3 and 1.7 Gyr, respectively) or the time it takes after the formation of the bar (5.1, 1.8, and 1.2 Gyr, or 12, 5, and 5 bar rotations, respectively).

This suggests that the formation timescale of the gas reservoir depends on the galaxy's stellar mass. Following results of Section 5.4, this is expected since a change in stellar mass translates to a continuous change in the balance between stellar feedback and the depth of the gravitational potential. As stellar mass increases (at fixed gas mass fraction), the gas

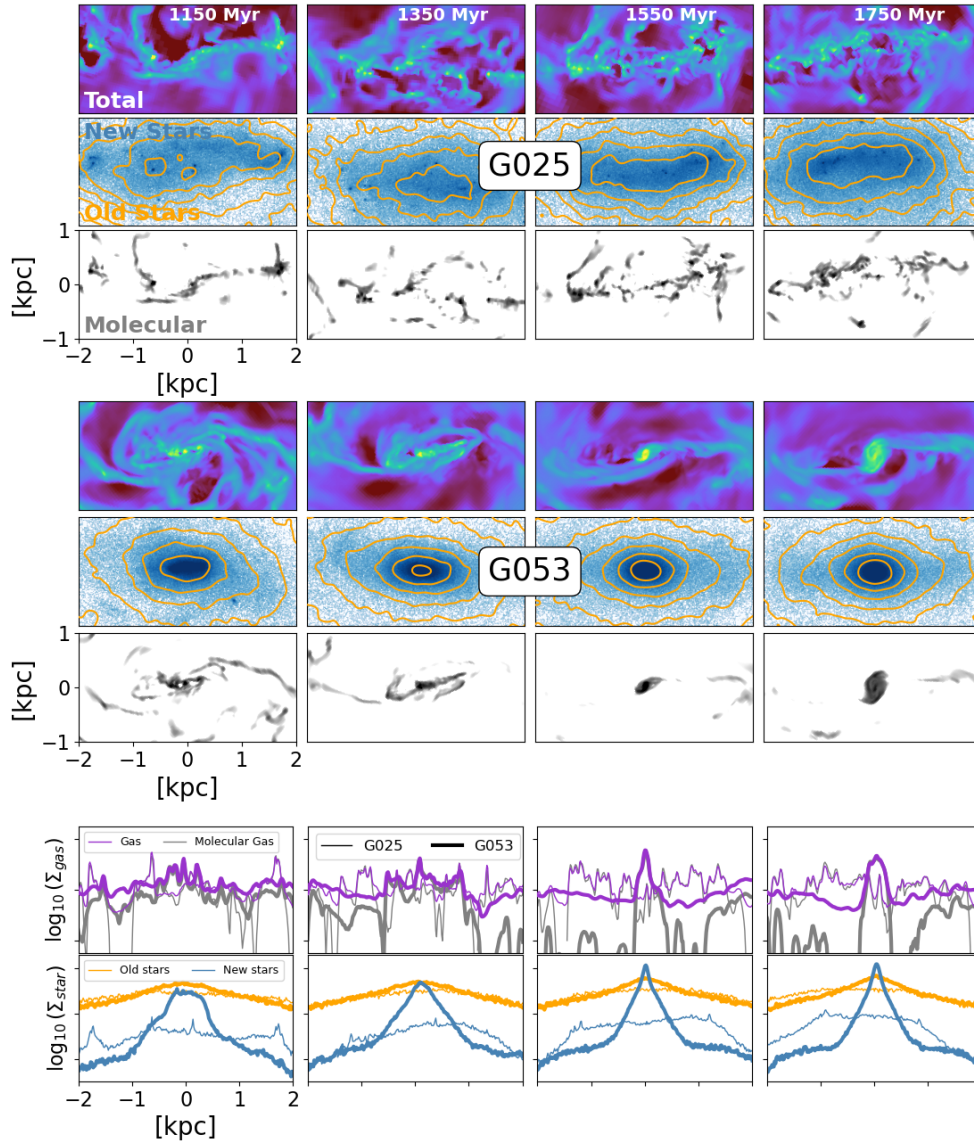


Figure 5.12: Time evolution of simulations G025 and G053, respectively a low and intermediate stellar mass system ($10^{9.5}$ and $10^{10} M_{\odot}$). Four running times are presented (from left to right, first six panels from top), with steps of 200 Myr, with a seed gas reservoir forming in G053 around $t = 1400$ Myr (in between the two middle panels). Maps with a field of view of $2 \text{ kpc} \times 1 \text{ kpc}$ of the total gas surface density, the mass of new stars (and old stars, as orange contours) and molecular gas density are shown as maps in the first to third rows for G025, and fourth to sixth row for G053. In all maps, the bar is aligned with the x-axis. The two bottom rows show the radial profiles, averaged over the y-axis ($\pm 1 \text{ kpc}$), first with the gas profiles (total and molecular), and then the stellar density profiles (bottom row; old and new stars).

being re-organised by the bar and fueled to the central region is less impacted by supernovae feedback and thus tends to be more prone to forming a central mass concentration.

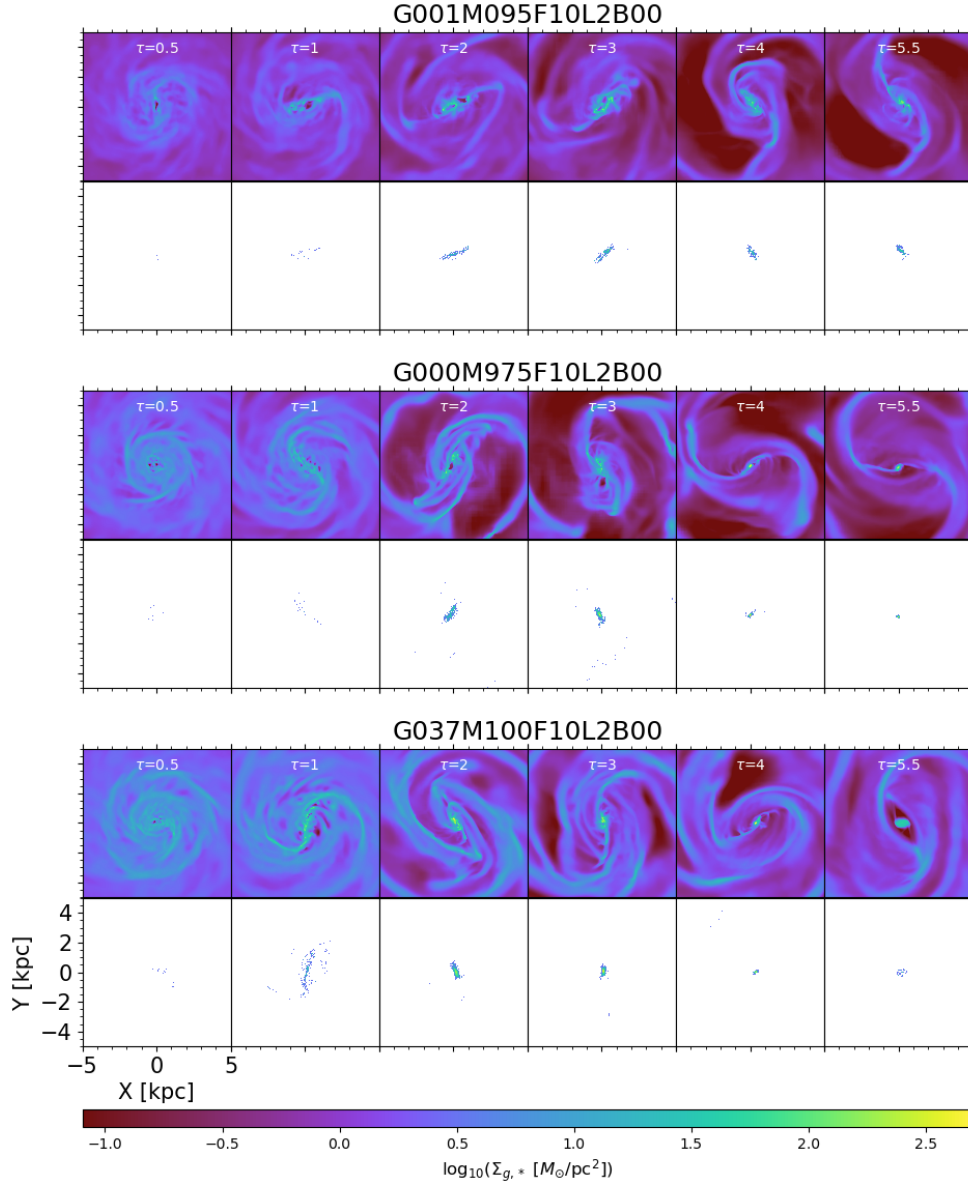


Figure 5.13: Illustration of the phase transition using models G001 (top panel), G000M975F10L2B00 (middle panel), and G037 (bottom panel), corresponding to a low-intermediate, and high-stellar mass model, respectively. In each panel, we show the evolution of the surface density map of gas at 6 different values of τ (0.5,1,2,4,5, and 5.5).

5.5.3 Summary

In this work, we have used our extended grid of simulations (35 models) based on 4 galactic parameters (i.e., stellar mass, gas fraction, scale length of the disc of stars, and the bulge mass fraction) coming from the PHANGS sample to investigate the main factors involved in the emergence of central gas reservoirs (central molecular discs or rings). We have noticed the presence of central gas reservoirs in our simulations and observed galaxies above a certain stellar-mass threshold corresponding approximately to $10^{10} M_{\odot}$, setting the low- and high-stellar mass regimes. Those gas reservoirs are observed in the surface density maps and in the specific distribution of SF across the disc. When a stellar bar has formed, we observe that the star-forming regions remain inside the bar in the low-stellar mass regime. In the high-stellar mass regime, we observe a redistribution of the star-forming regions into a central gas reservoir and near the bar ends.

The presence of a gas reservoir in high-stellar mass models creates a depletion of gas between the interior of the stellar bar and the gas reservoir. This gas depletion in the high-stellar mass models leads to a dip in the gas surface density profiles that we do not observe in the low-stellar mass models. In addition to this gas depletion, we have also studied the physical properties of the star-forming gas via the PDF, the distribution of the virial parameter, and the Mach number. We have shown that those physical properties remain unchanged over time in the low-stellar mass regime, but vary significantly as a function of time in the high-stellar mass regime. We highlight here that this gas depletion causes a dip in the gas surface density profiles, and the distribution of the mentioned physical parameters could be compared with real galaxy data in future work (Emsellem, in prep., Neumann, in prep.).

We computed the circular velocity coming from the gravitational potential, derived the angular frequency, and the bar pattern speed to check whether an inner Lindblad resonance (ILR) has formed in our barred models. We found that in the high-stellar mass regime, an ILR has emerged, which explains the formation of central gas reservoirs. However, we have not identified any ILR in the low-stellar mass regime.

We have investigated the role played by the stellar feedback and compared it with the gravitational potential of our different models. We have found that the variation of the kinetic energy we measure in the gas vertical velocity dispersion due to SN feedback has the same order of magnitude (15-30 km.s^{-1}) for all our barred models. The ratio between the vertical velocity dispersion and the escape velocity is higher (10-15%) in the low-stellar mass regime compared with the high-stellar mass one ($\sim 5\%$). This explains the fact that our low-stellar models do not form a central gas reservoir, which can be extended to observed galaxies.

The change of regime is not dictated by an abrupt stellar mass threshold around $10^{10} M_{\odot}$, but rather by a transition going with a continuous change of stellar mass between $10^{9.5}$ and $10^{10} M_{\odot}$. This transition occurs because of the varying balance between the SN feedback and the local gravitational potential, that allows, at higher stellar masses, the emergence of a seed, leading to the formation of an ILR, and the building of the gas reservoirs. This is further emphasised with a low stellar mass test model where a gas

reservoir forms when SN feedback is turned off. We have further probed this structure transition thanks to an intermediate-mass model with a stellar mass of $10^{9.75} M_{\odot}$ that exhibits the emergence of a late gaseous seed reservoir.

5.6 Mass loading factor and toy model

Note - This Section is not part of the submitted paper Verwilghen et al. (2025). We provide it as an extension for the discussion.

5.6.1 The mass loading factor

The balance between supernovae feedback and gravity was probed in the previous sections via a normalised velocity dispersion profile. It can be further quantified using the mass loading factor (MLF) as illustrated in Fig. 5.14. The mass loading factor is the ratio between the ejected mass (outflow) at a given radius (or altitude above the disc plane) and the SFR. This parameter plays an important role in galaxy formation models (Somerville et al., 2015). In this figure, we show the evolution over time of the ratio between the ejected mass and the SFR at a height of $1 l_*$ above the galactic plane as a function of the stellar mass for all barred models. The MLF decreases with the stellar mass at $\tau=1$ and 2. When the bar forms ($\tau = 1$) the MLF is also generally higher for larger gas fractions (thicker squares). While the trend looks much stronger at $\tau = 1$, close to the peak of the star formation rate, it is still present at $\tau = 5$. This result is consistent with the findings of observational (e.g. Chisholm et al., 2017) and theoretical work (e.g. Mitchell et al., 2020) that the mass loading factor in star-forming disc galaxies critically depends on stellar/halo mass and gas mass fractions (see also Hayward & Hopkins, 2017)

5.6.2 Toy model for the seed formation

To understand the conditions of the formation of a central seed and connect it with the stellar mass threshold, we propose a simple analytical model based on the balance between the energy of the SN feedback transmitted to the ISM and the fuelling of the gas due to the combination of the bar and the gravitational potential. The first ingredient we need is the kinetic energy transmitted by SN feedback to the ISM in a region of radius R surrounding the galaxy's centre. We can write this as an energy density (normalised by the available gas mass), as:

$$\Delta E_{\text{SN}} = \frac{\eta \text{SFR}(R)}{m_{\text{SN}}} \cdot \frac{\epsilon_{\text{SN}}}{M_{\text{gas}}(R)} \cdot \Delta t, \quad (5.1)$$

where $(\eta \text{SFR}(R)/m_{\text{SN}})$ corresponds to the rate of SNe production estimated from the star formation rate $\text{SFR}(R)$ within the considered region, a typical stellar mass for a supernova progenitor (m_{SN}) and a mass fraction η of the stellar population ending as SNe (fixed to 20% in our simulations), ϵ_{SN} is the total energy released by one supernova (assumed here

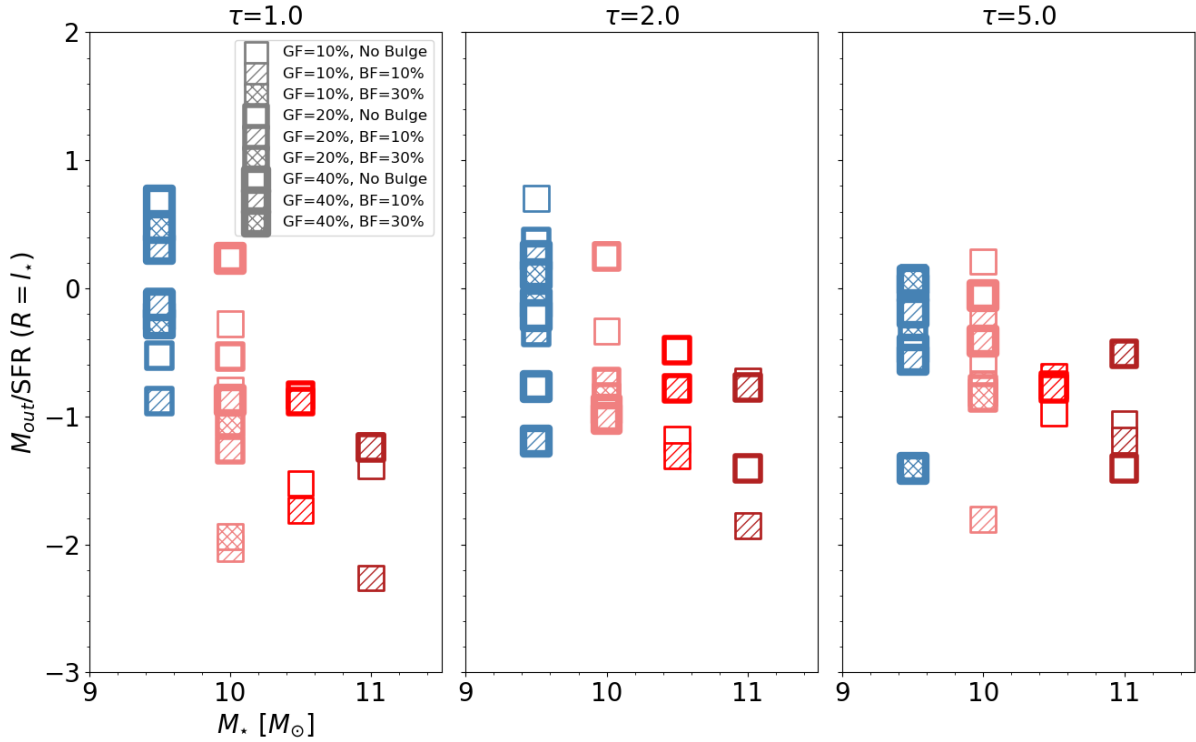


Figure 5.14: Evolution of the mass loading factor as a function of time for three values of the parameter τ (1, 2, 5) for all models. Each square has a pattern corresponding to its gas fraction, and a thickness that follows the stellar mass bin as indicated in the top corner of the first panel.

to be 10^{51} erg), $M_{\text{gas}}(R)$ is the mass of gas to which the SN energy is transferred inside the region of radius R and Δt is a typical timescale over which to integrate.

We can now compare such a transfer of energy ΔE_{SN} to an estimate of the energy of the gas (E_{gas}) meant to be fuelled to the centre, hence within the bar region ($R \geq R_{\text{bar}}$). Assuming gas is travelling from the end of the bar towards the centre with a maximum velocity proportional to the circular velocity (V_c) at R_{bar} , it is equivalent to the kinetic energy density:

$$E_{\text{gas}}^k = \frac{1}{2} V_c^2(R_{\text{bar}}). \quad (5.2)$$

In the following, we will assume that supernovae feedback can prevent the formation of a central mass concentration if it releases sufficient energy to perturb the coherence of the flow, i.e. when ΔE_{SN} integrated over a typical fuelling timescale is larger than E_{gas}^k . A relevant timescale is the orbital period for elongated orbits (*x1*; REF) along the bar, hence the period $2\pi/\Omega_b$ where Ω_b is the pattern speed of the bar. For gas to move from the bar

ends to the central region takes a fourth of that time, or about a crossing time given by:

$$\Delta t_c = \frac{R_{\text{bar}}}{V_c(R_{\text{bar}})} \approx \frac{R_{\text{bar}}^{3/2}}{\sqrt{GM(R_{\text{bar}})}} \quad (5.3)$$

where $M = M_* + M_{\text{gas}} = M_*/(1 - f_{\text{gas}})$ (assuming dark matter is negligible within the bar region, and with f_{gas} the gas mass fraction).

The condition to prevent a seed formation is then given by $\Delta E_{\text{SN}}(R) \geq \delta E_{\text{gas}}^k$ for radius $R = R_{\text{bar}}$ and a fraction of the time interval prescribed in Eq. 5.3: δ thus encompasses both the fraction of the SN energy that couples with the ISM (a few per cent) and the fraction of the crossing time needed to imprint such a perturbation. Using Eqs. 5.1 and 5.2, we can express that condition via the specific star formation rate (SSFR = SFR/ M_*) within the bar as:

$$\text{SSFR}(R_{\text{bar}}) \geq \frac{G^{3/2}}{2} \cdot \frac{\delta m_{\text{SN}}}{\eta \epsilon_{\text{SN}}} \cdot \left[\frac{f_{\text{gas}}}{(1 - f_{\text{gas}})^{5/2}} \cdot \frac{M_*^{3/2}}{R^{5/2}} \right]_{R_{\text{bar}}} = B(R_{\text{bar}}) \quad (5.4)$$

where f_{gas} is the gas mass fraction within the bar region.

For all of our simulations, both sides of Eq. 5.4 are evolving with time once the bar has formed. Assuming R_{bar} does vary slowly once the bar has formed, most of the time variation is encompassed within the star formation rate (on the left-hand side), and the gas mass fraction (on the right-hand side). For f_{gas} varying from 0 to 40%, the associated term varies from 0 to ~ 1.5 . The value of the parameter δ is estimated via the ratio SSFR/ B from our simulations as shown in Fig. 5.15. This figure shows the evolution of this ratio for models G013 (solid blue curve), G025 (blue dashed curve), G037 (solid red curve), and G053 (red dashed curve). We observe the formation of a gas reservoir in model G053 in the time interval corresponding to the green-shaded area, while we only start to see the structuring and building of a central gas concentration (seed) in model G037. This suggests that the value of δ should be between 10 and 20 when the seed forms and we thus fix its value to 15. Using observed radial profiles, we can then estimate those values for the PHANGS main sequence star-forming galaxies. Finally, we could try to estimate the local relation provided by Eq. 5.4 for samples like the MaNGA set of galaxies, using simple prescriptions to work from global SFR, gas and stellar mass values.

To understand where disc galaxies of the SFMS would lie in Fig. 5.16, we call the relation provided by (Leroy et al., 2019):

$$\log_{10}(\text{SFR}) = a \log_{10}(M_*) + b, \quad (5.5)$$

where $a = 0.68$ and $b = -6.97$.

The SFMS relation intersects the B function for a stellar mass of $10^{9.7} M_{\odot}$. Including uncertainties associated with the above-mentioned parameters, we see that the transition for the main sequence would occur at stellar masses between $10^{9.5}$ and $10^{10} M_{\odot}$, consistent with the observed change of regime in our simulations.

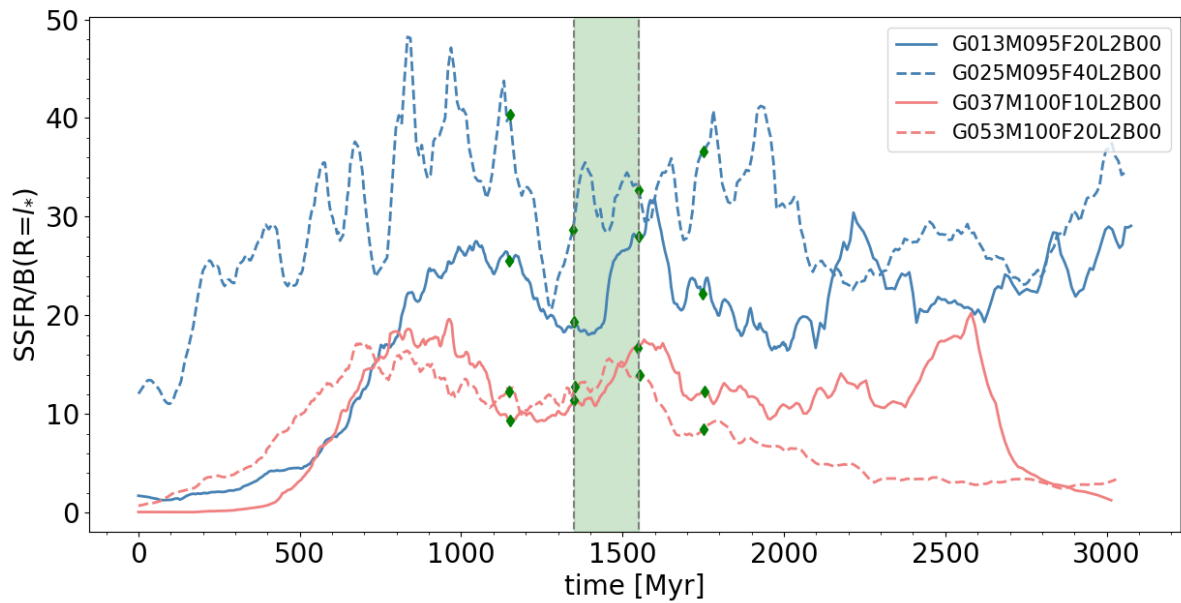


Figure 5.15: Evolution over time of the ratio $SSFR/B$ evaluated at $R=l_*$ for four of our models: G013 (solid blue curve), G025 (blue dashed curve), G037 (solid red curve), and G053 (red dashed curve). The green diamonds illustrate four reference times: 1150.0, 1350.0, 1550.0, and 1750.0 Myr. The green shaded area is the time interval for which we observe the formation of a gas reservoir in model G053.

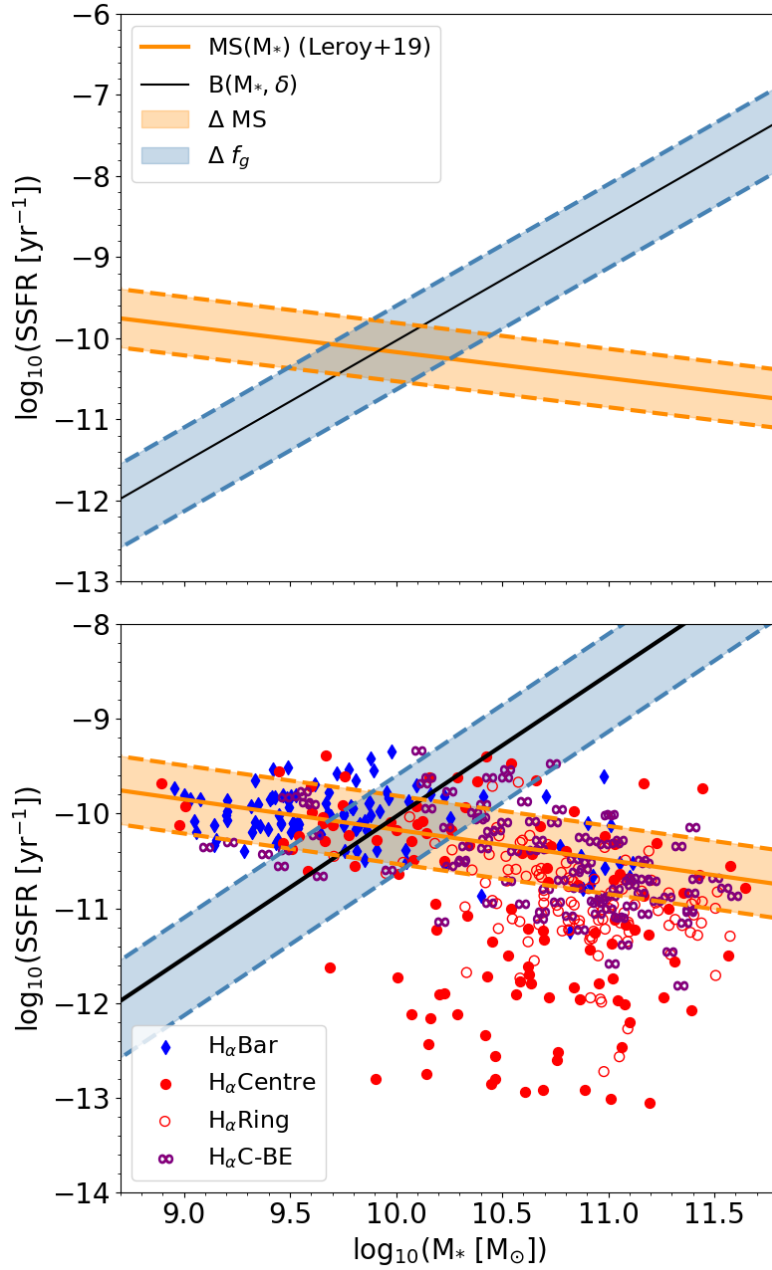


Figure 5.16: Comparison between our toy model and MaNGA data. The top panel shows the specific star formation rate (orange line) and the B function (black line) with their errors illustrated by the shaded areas. The bottom panel shows the same curves and the MaNGA data split into different morphological types as a function of the SF (H_{α}) distribution: along the bar (blue diamonds), centre (red dots), ring (red circles), and centre-bar ends (purple lemniscate (∞) symbols).

Chapter 6

Characterising the gas reservoir and
its connection with the black hole

6.1 The characteristics of the gas reservoir

- The analysis presented in this chapter is not part of the published papers as reported in the previous chapters.

This part of the thesis is a first step to characterise in more detail the building of the gas reservoir by probing its growth over time, its three-dimensional structure, and its orientation with respect to the bar. We also show the evolution of the position of the central SMBHs and the characteristics of their motion once the gas reservoir forms.

6.1.1 From the seed to the disc

The common scenario proposed to explain the formation and evolution of central gas reservoirs is the so-called ‘inside-out’ scenario. In this scenario, after the bar forms, it starts to fuel gas toward the central region, where it accumulates and reaches higher and higher densities, increasing the SFR. A central seed appears and gas fuelled by the bar arrives at the seed and makes it grow over time. In Chap. 5, we have shown that this seed appears because the gravitational potential is strong enough to counterbalance the impact of the SNe feedback, and keep a regulated and efficient fuelling pattern.

Results in Chap. 4 are in good agreement with the above scenario. In this chapter, we have seen that the gas density peaks around $\tau = 1.5$, followed by a starburst phase (from $\tau = 1.5$ to 2) with the formation of many stars inside the central 1 kpc region (i.e., SFR between 1 and 10 M_{\odot}/yr for $\sim 1 t_{\text{bar}}$). The last phase (from $\tau = 2$) is the long-term depletion phase during which the gas is fuelled to the centre and directly converted into stars. In our simulations forming a gas reservoir, we observe that it emerges during this depletion phase (i.e., after $\tau = 2$) as shown in Fig. 6.1. In this figure, we show the evolution of the size of the semi-major (blue curve) and semi-minor (orange curve) axes of the gas reservoir for three of our models. We also show the ellipticity ϵ illustrated by the grey curve. The two models in the top panels have a stellar mass of $10^{10} M_{\odot}$, while the two models in the bottom panels have a stellar mass of $10^{10.5} M_{\odot}$. We observe that the beginning of the growth (the seed) occurs earlier for the higher-mass models at around $\tau = 2$ and later for the lower-mass models around $\tau = 3 - 4$. We also see that the gas fraction plays a role since the 20% gas fraction models (G053 and G137) seem to form a seed earlier compared with the 10% gas fraction ones (G037 and G105). Once the seed is established, we observe a relatively linear growth of both the semi-minor and major axes in such a way that the ellipticity does not vary significantly over time. We also observe that the size of the reservoir depends on the stellar mass of the model, with the size increasing with the stellar mass. We note that the larger size of the gas reservoir of more massive models may be due to an earlier formation time.

The impact of a central bulge with a mass of 10% of the total stellar mass on the formation of the reservoir is shown in Fig. 6.2. This figure illustrates the growth of the central gas reservoir for the same models as above but with a central bulge added from the beginning of the simulation. We observe that the bulge helps to form a seed earlier than

in non-bulged models. This is explained by the fact that bulged models develop an ILR earlier. We see the same trend with stellar mass and the gas fraction. In the lower mass models (G038 and G054), we observe the formation of the seed around $\tau = 3$ for the 10% gas fraction model (G038) and around $\tau = 2$ for the 20% gas fraction model. In the case of the higher-stellar mass models, the seed appears even earlier around $\tau = 1.5$.

6.1.2 The 3D structure of the underlying stellar disc

We have briefly investigated the disc of newly-formed stars emerging with the formation of the gas reservoir. Figure 6.3 illustrates the time evolution of the central region of models G025 (top), G037 (middle), and G105 (bottom). In this figure, we see for each model the evolution of the face-on (x-y, five top panels) and edge-on (x-z, five bottom panels) view of their cumulated newly-formed stars for five different snapshots corresponding to 500, 1000, 1500, 2000, and 2500 Myr.

As we expected, model G025 does not show the formation of a central nuclear stellar disc because of its low-stellar mass (i.e., $10^{9.5} M_{\odot}$). We observe the emergence of a bar-like structure around 2000 Myr, but there is no central concentration of stars forming a disc-like structure. We see that the thickness of the disc grows over time, but the new stars continue to spread over most of the bar region. The evolution of model G037 shows the formation of a central nuclear stellar disc, which results from the formation of a central gas concentration. The face-on view illustrates its growth and we observe a clear disc-like structure emerging between 1500 and 2000 Myr. The edge-on view shows the emergence of a thinner stellar disc embedded in a larger ‘boxy-peanut’ bulge extending vertically to ~ 500 pc. This trend is even more visible in model G105, where we observe the emergence of a disc between 500 and 1000 Myr. The edge-on view reveals a more extended thinner disc surrounded by the ‘boxy-peanut’ bulge extending from 500 to ~ 500 pc. We have visually checked this trend for all our models forming a gas reservoir and we conclude that this ‘boxy-peanut’ bulge only forms when a central disc is established.

6.1.3 Orientation of the gas reservoir with the bar angle

We have computed the bar and gas reservoir angle to study their orientation with respect to each other in four of our models forming a gas reservoir. Figure 6.4 shows the evolution of the bar (red curve) and gas reservoir (blue curve) angle as a function of τ for four of our models G037, G053, G105, and G137. We see that the rotation of the bar becomes structured and periodical once the bar forms at $\tau = 1$. We observe the same trend for the gas reservoir angle with a clear oscillation pattern emerging once the gas reservoir forms. We have also computed the absolute difference (grey curve) between those two angles to probe the evolution of the orientation of the gas reservoir with respect to the bar semi-major axes. We note some oscillations of the curve which are artefacts uniquely due to abrupt periodical cuts in the bar and gas reservoir angle. In the case of models G037 and G137, we see that the algorithm we used does not show a good result for the angle of the gas reservoir, but is enough to observe a signal. We have computed the median and mean

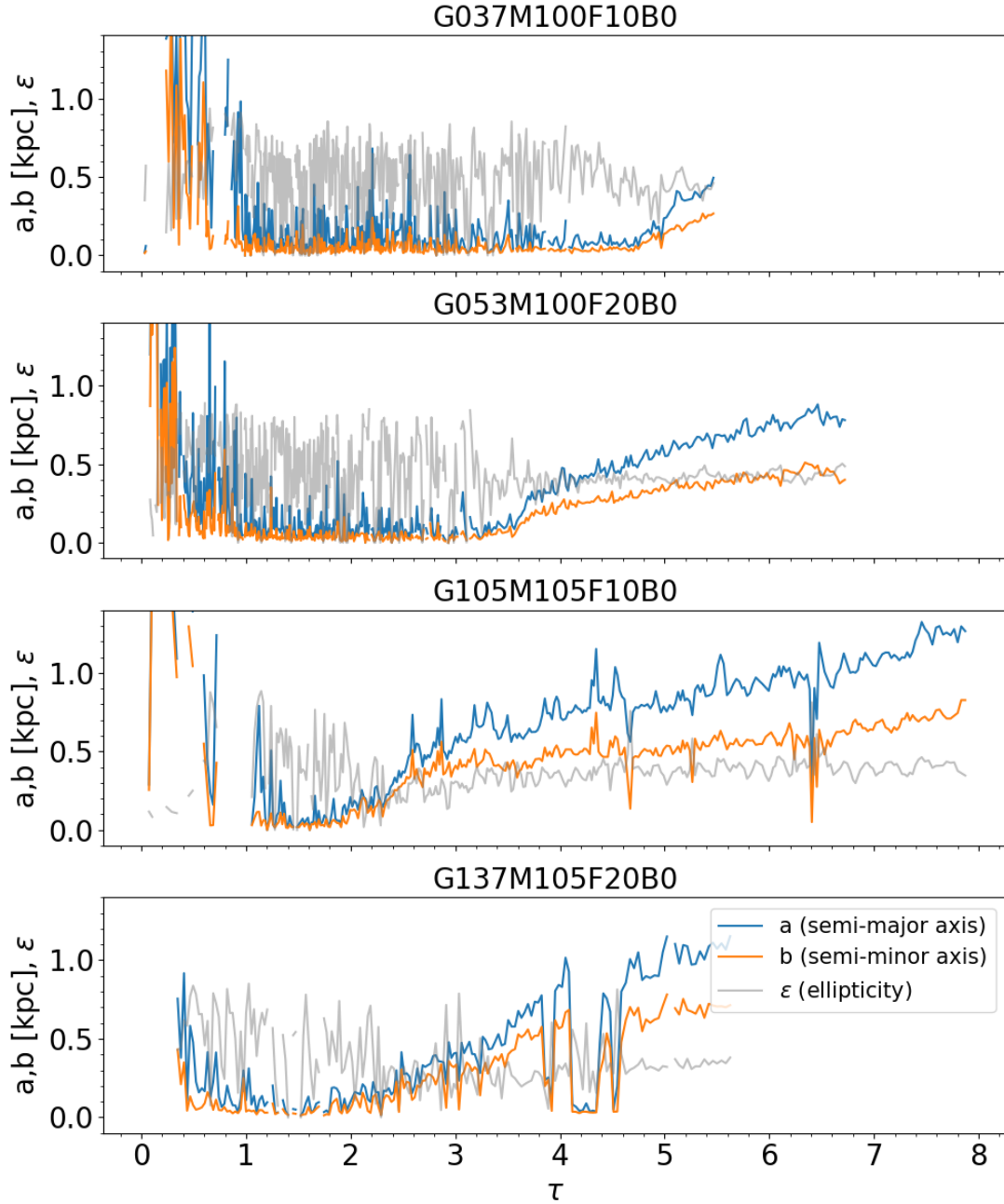


Figure 6.1: Evolution of the semi-major (blue curves) and semi-minor (orange curves) axes lengths of the gas reservoir for 4 of our non-bulged models. The two first top panels show models with a stellar mass of $10^{10} M_{\odot}$, and a gas fraction of 10 and 20% for G037 and G053, respectively. The two bottom panels show models with a stellar mass of $10^{10.5} M_{\odot}$, and a gas fraction of 10 and 20% for G105 and G137, respectively. The ellipticity is illustrated by the grey curve.

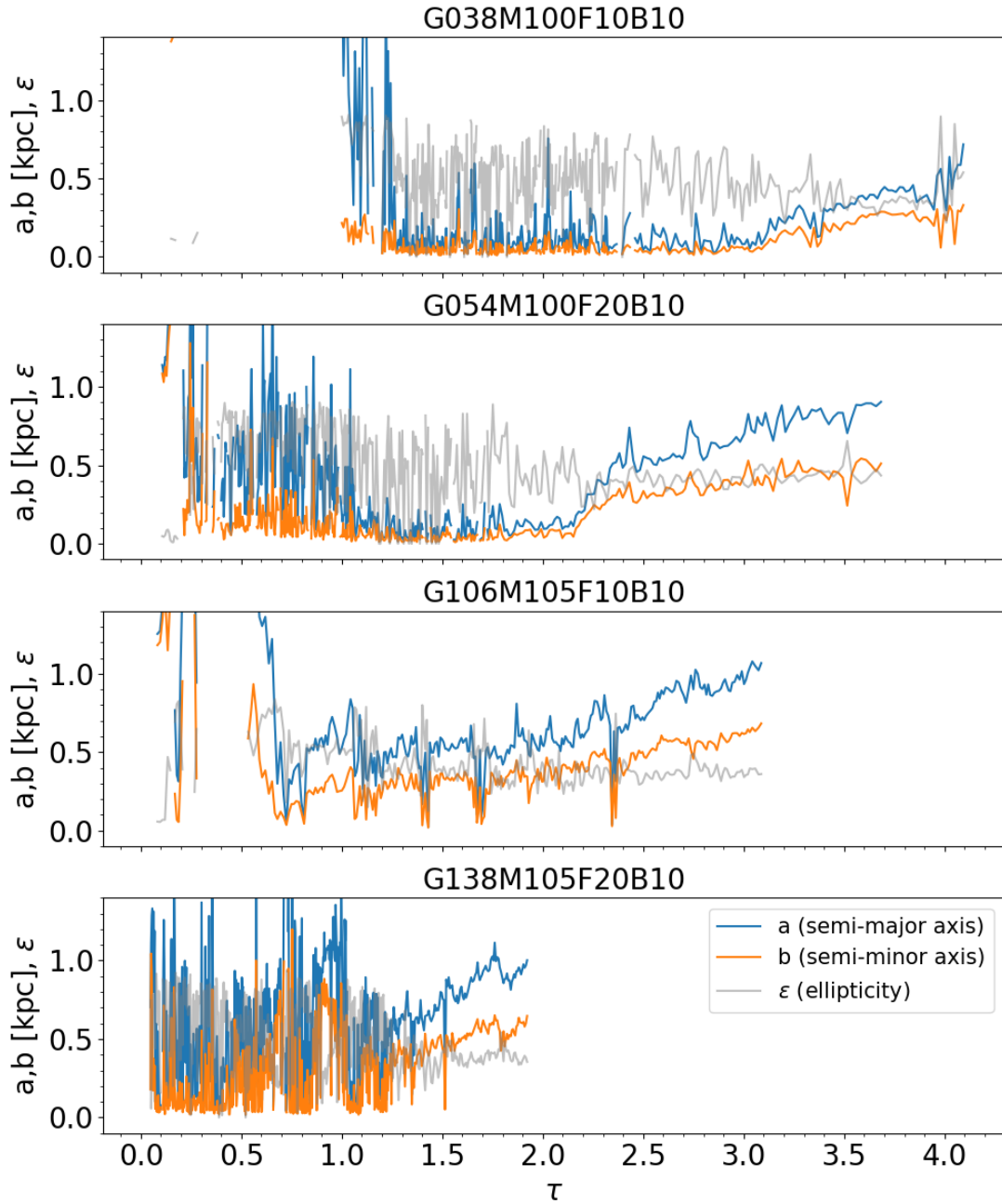


Figure 6.2: Same as in Fig. 6.1 but with the equivalent (in mass and gas fraction) bulged models.

values of the difference between those two angles and found a median value of 89, 89, 90, and 90 degrees for models G037, G053, G105, and G137, respectively. On average, we find the gas reservoir of all our models is almost perpendicular (± 1 degree from 90) to the bar. This result is coherent with previous works because the backbone family of orbits of

the bar (x1) and the gas reservoir (stellar disc, x2) are supposed to be perpendicular to each other. It is finally worth mentioning that we have not detected an oscillation of the gas reservoir with respect to the bar because the time resolution of our snapshots is not high enough to probe fast angle variations: a re-run of those models with a higher output frequency may be required to further examine this issue.

6.2 Motion of the central black hole

There is one aspect of the simulation we have not exploited yet. This aspect is the evolution of the position of the central BH we have initially placed at the centre of the box. We have only considered this central BH as a massive point particle and studying the evolution of its position over time could help constrain future experiments that probe the sub-pc fuelling processes. The main hurdle here is that the central gas and stellar disc structures move and do not stay at the centre of the box over time. It is then crucial to track the position of the centre of those structures and probe the BH position with respect to that centre. We chose to calculate this centre by using the newly formed stars and we show the evolution of the relative position of the BH with respect to that centre in Fig. 6.5, 6.6, and 6.7.

Figure 6.5 illustrates the evolution of the relative position of the BH for 4 low-mass models with a stellar mass of $10^{9.5} M_{\odot}$. We see that the trajectory of the BH is relatively chaotic and the amplitude of its motion increases with the gas fraction with 10, 20 and 40% for models G001, G013, and G025, respectively. In the four models, the normalised radius oscillates and we observe a decrease in its amplitude for models G001 and G013. The last model G026 is the same as G025 but with a stellar bulge since the beginning of the simulation. We observe that the motion of the BH is still chaotic. This emphasises that in such low-mass simulations, there is no well-defined ‘centre’ of mass within the bar region.

Figure 6.6 illustrates the evolution of the relative position of the BH for 4 high-mass models with a stellar mass of $10^{10} M_{\odot}$ for the two top panels and $10^{10.5} M_{\odot}$ for the two bottom panels. We observe a chaotic motion with amplitudes ranging from about 0.25 to 0.4 r/l_* for G037 and G053, and 0.15 to 0.25 for G105 and G137. This amplitude tends to decrease with increasing stellar mass and increase with the gas fraction. We witness a rapid and neat drop with an almost constant zero value of the normalised radius. It is worth mentioning that the drop we observe is correlated with the value of τ at which the seed emerges, as we can see in Fig. 6.1

The BH motion of the two test models G001-NOSN and G000M975 is shown in Fig. 6.7. We observe the same trend for the evolution of the normalised radius as in the higher-mass models. The model without supernovae does not show high amplitude oscillations of the position and the BH stays in the central $\sim 0.1 - 0.2$ kpc region inside the gas reservoir. This result is artificial for such a low-stellar mass model and suggests an impact of SNe feedback on the relative motion of the central BH. We measure that the SNe feedback tends to increase the amplitude of the oscillations of a factor from about 0.2 to 0.6 l_*

in model G001, while without feedback the maximum amplitude of the oscillations is limited to $\sim 0.02 l_*$. Concerning the intermediate-mass model G000M975, we observe some oscillations of the normalised radius before it drops and stays constant as in model G037. This is expected because this model also forms a gas reservoir and we think that its intermediate-stellar mass of $10^{9.75}$ places it at the border of the transition between the two regimes.

The evolution of the BH position we observe in the low- and high-stellar mass models may be a numerical artefact. We have chosen the same mass (i.e., $10,000 M_\odot$) for the old star particles in all of our models but the mass of the BH increases with the stellar mass of our models: $10^{5.5}$, 10^6 , $10^{6.5}$, and $10^7 M_\odot$ for models with a stellar mass of $10^{9.5}$, 10^{10} , $10^{10.5}$, and $10^{11} M_\odot$, respectively. The ratio between the individual mass of the star particles and the BH is, therefore, higher in the lower-stellar mass models and the BH will be easier to move from its initial position and will show higher amplitudes in the oscillations of its position.. We have not tested the impact of the initial position of the BH on the evolution of its position over time but this could also have an impact on the stellar and gas dynamics, perturbing the formation of the gas reservoir in our higher-stellar mass models.

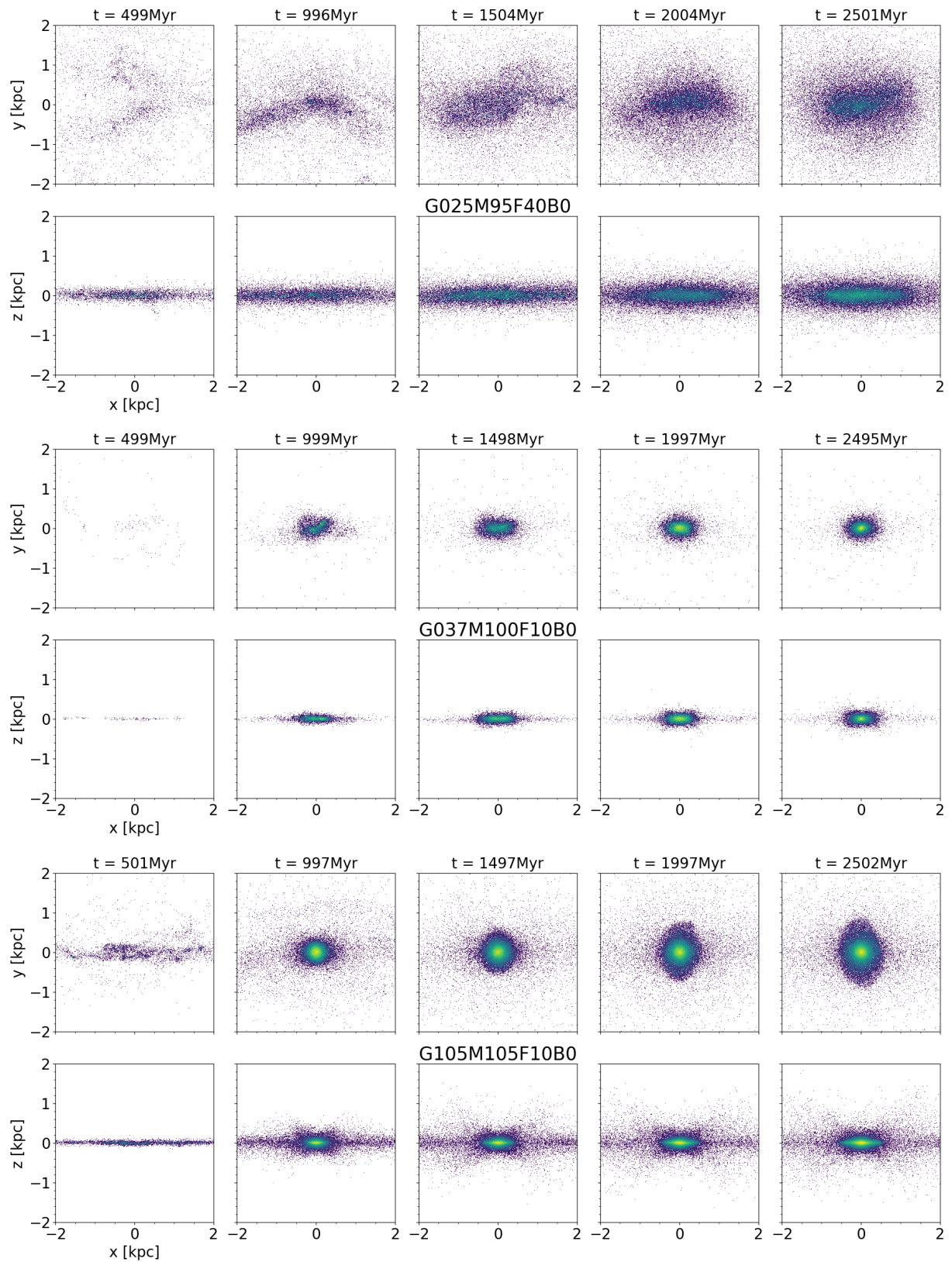


Figure 6.3: Formation and evolution of the disc of newly-formed stars for model G025, G037, and G105. For each model, the five top and bottom panels show the face-on (x-y) and edge-on (x-z) view of the disc, respectively.

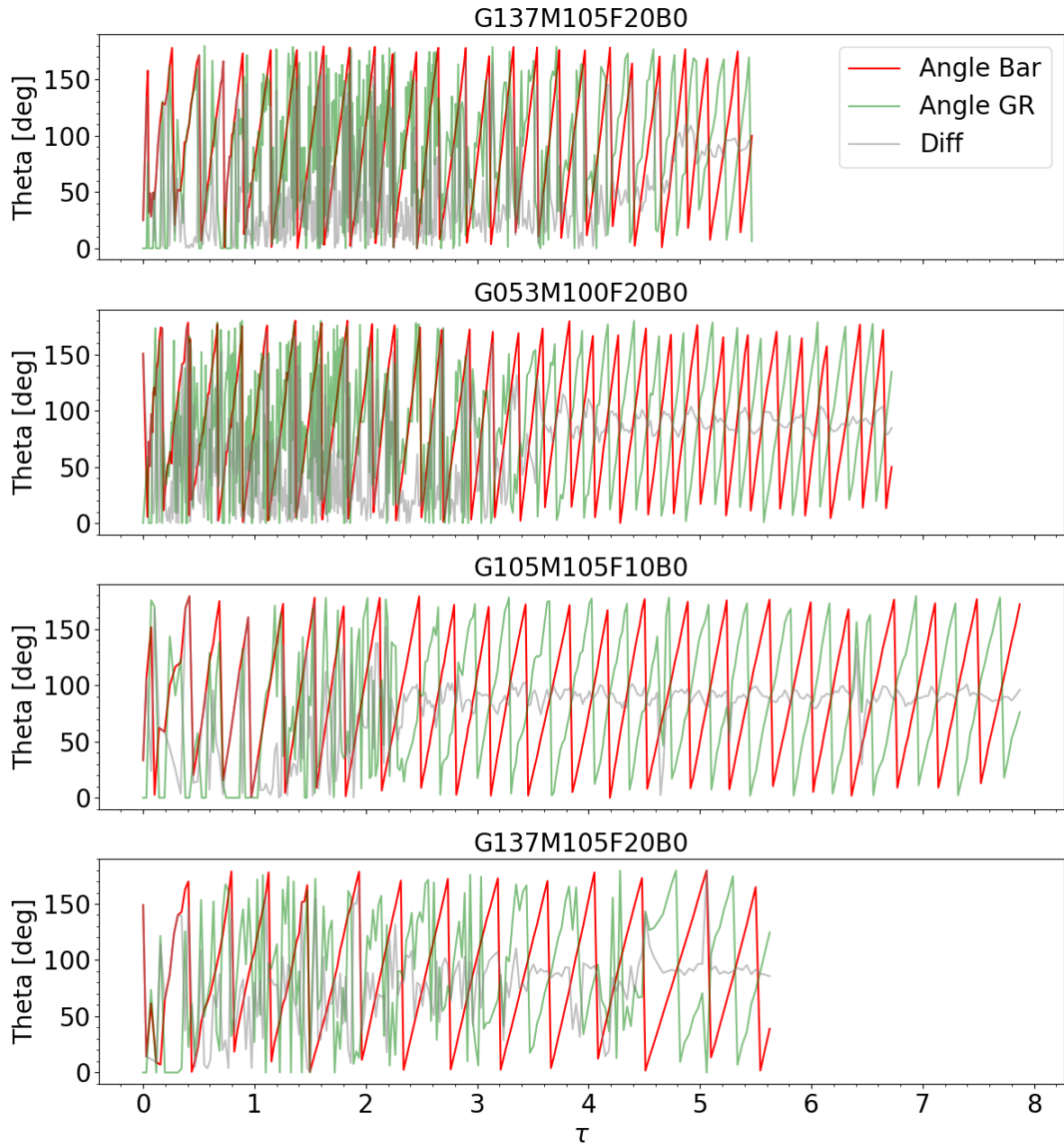


Figure 6.4: Evolution of the bar (red curve) and gas reservoir (green curve) angle as a function of the parameter τ for models G037, G053, G105, and G137. The grey curve illustrates the absolute difference between those two angles.

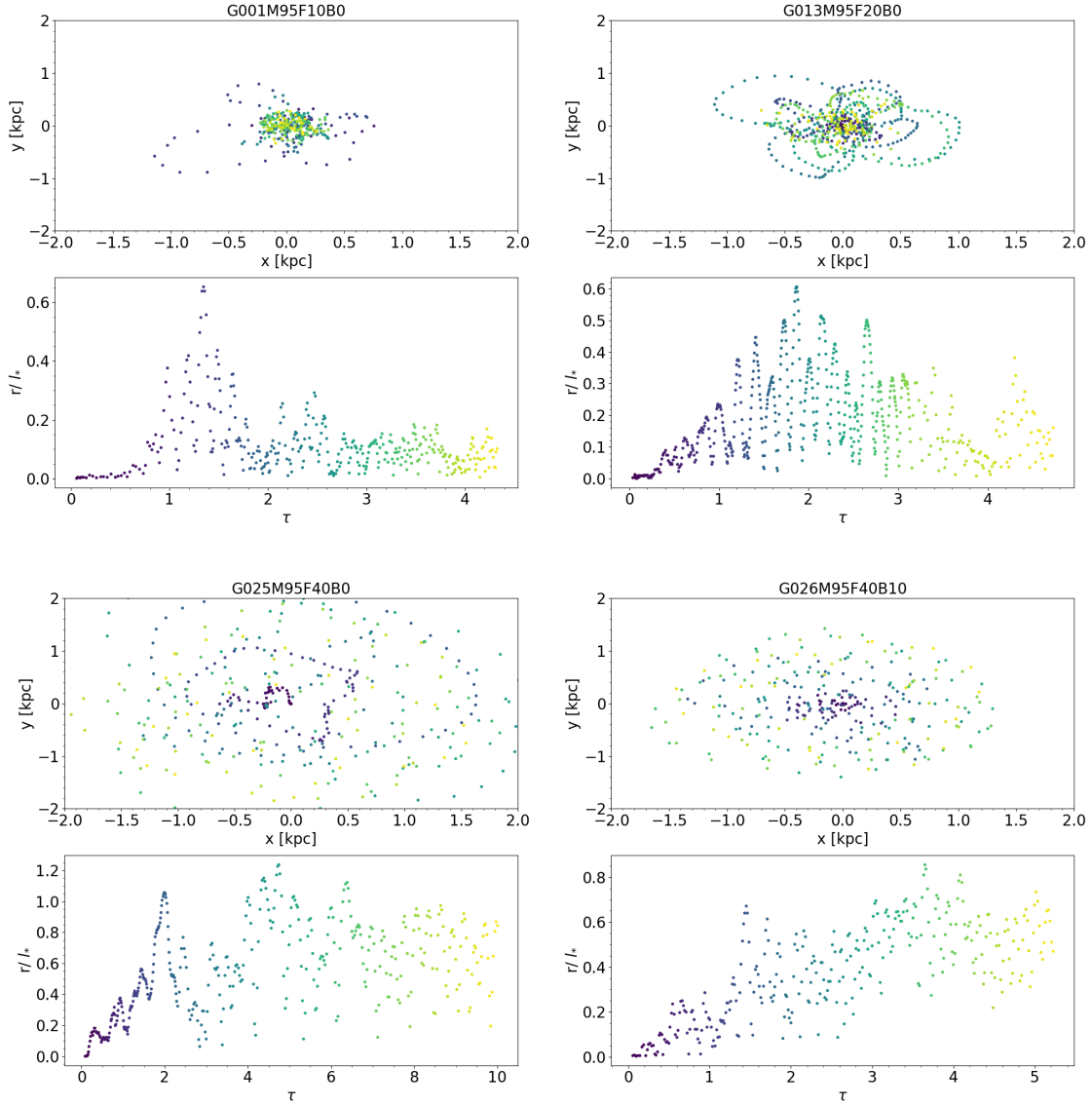


Figure 6.5: Evolution of the BH position over time for 4 low-mass models ($10^{9.5} M_{\odot}$). For each model, the top panel illustrates the relative position (X-Y in kpc) of the BH with respect to the centre of mass of the newly-formed stars. The bottom panel shows the evolution of the normalised radius (r/l_*) of the relative position observed in the top panel.

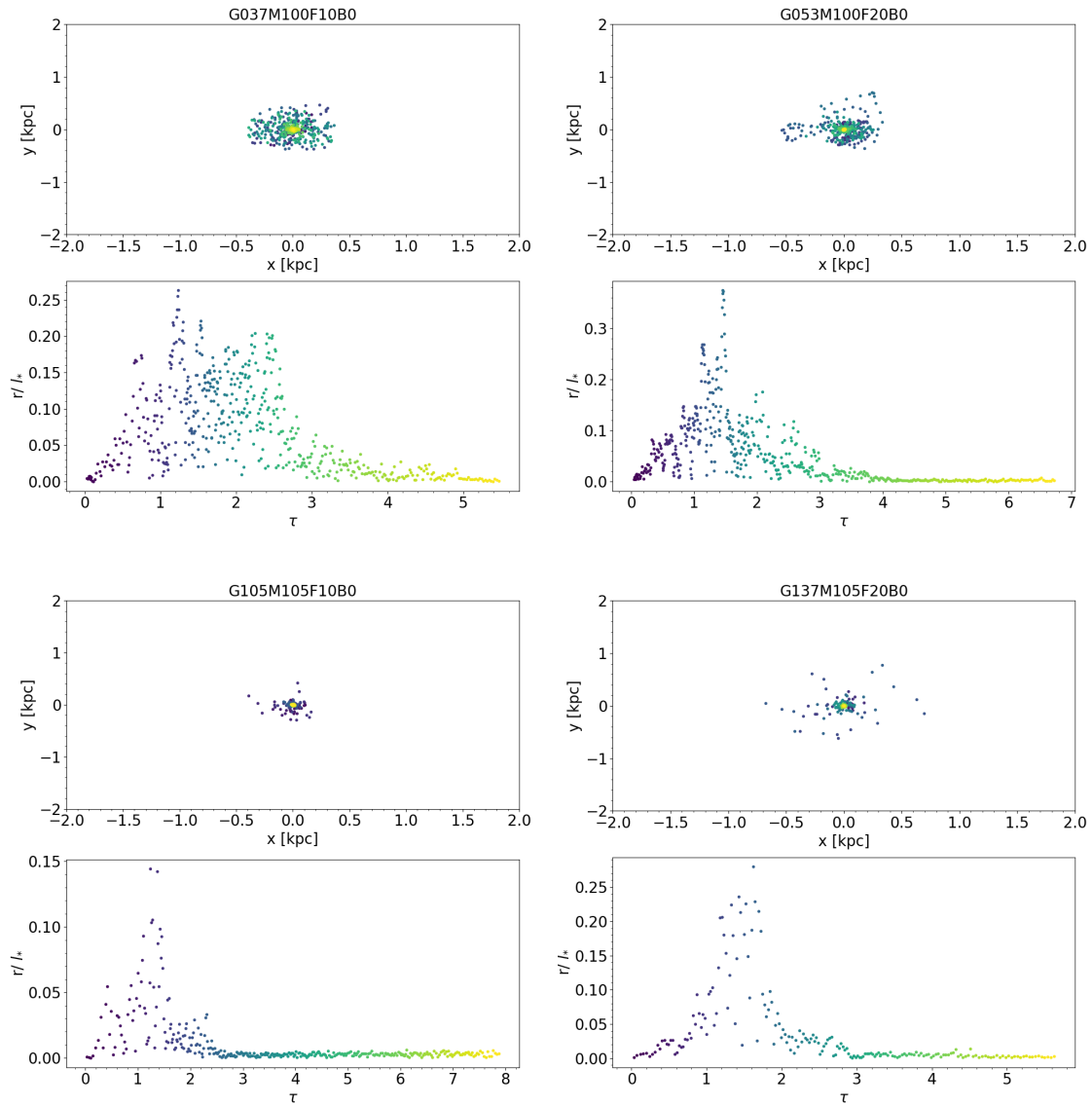


Figure 6.6: Same as in Fig. 6.5 but with two higher stellar-mass bins. The top panels show two models with a mass of $10^{10} M_{\odot}$, and the bottom panels show two models with a stellar mass of $10^{10.5} M_{\odot}$.

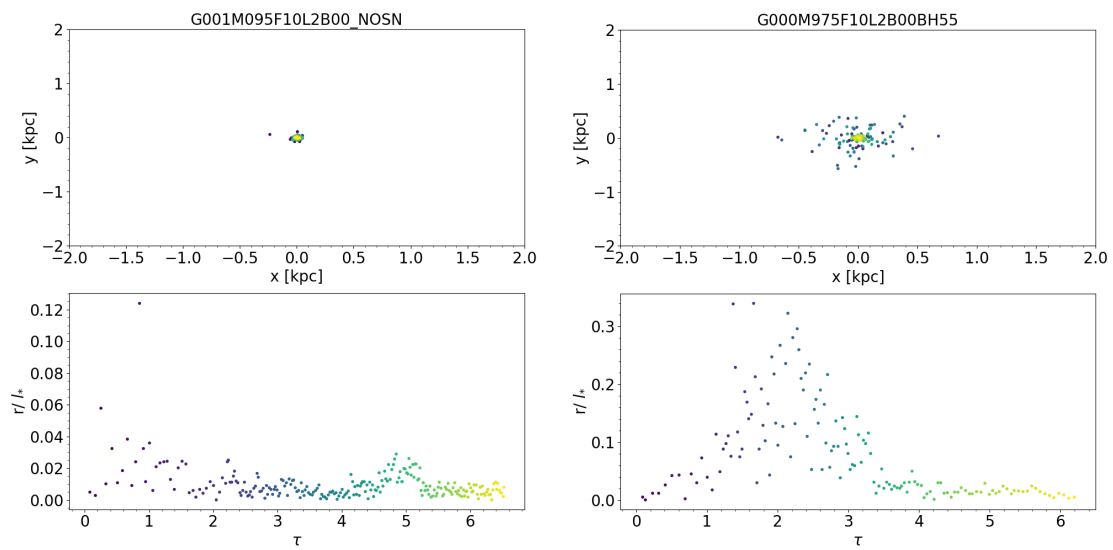


Figure 6.7: Same as in Fig. 6.5 but with the two test cases G001-NOSN and G000M975, having a stellar mass of $10^{9.5}$ and $10^{9.75}$, respectively.

Chapter 7

Conclusion and perspectives

7.1 Summary

7.1.1 The grid of models

In this project, we used hydro-dynamical N-body high-resolution simulations to study the building and evolution of central gas reservoirs in nearby barred star-forming disc galaxies. The main goal was to connect the formation and evolution of those gas reservoirs with the large kpc scale fuelling of the stellar bar, and their consumption with the star formation occurring inside the bar region. This work is a first step toward a comprehensive understanding of the central black hole fuelling, bridging the large kpc scale of the bar, the few hundred pc scale of the reservoir, and the sub-pc scale down to the vicinity of the SMBH. To this end, we have designed a grid of 54 galactic models based on the PHANGS-ALMA sample. Our models are composed of 4 control parameters out of 5 galactic parameters (i.e., the stellar mass, the gas fraction, the stellar scale length, the gas-to-stellar scale length ratio, and the bulge mass fraction). We have fixed the gas-to-stellar scale length ratio to 2 for the entire grid. The stellar mass is split into 4 bins (9.5, 10, 10.5, and 11 $\log_{10}(M_{\odot})$), the gas fraction, stellar scale length, and the bulge mass fraction depend on the stellar mass and their values have been selected by using the PHANGS galaxies.

We performed the simulations of the 54 models with the RAMSES code at a maximal spatial resolution of 12 pc. We have generated our initial conditions by using the Multi Gaussian Expansion (MGE) method, and the position and velocity of each particle (i.e., stars and DM) by solving the Jeans equations. Our initial conditions are axisymmetric about the z-axis and at dynamical equilibrium. The number of star particles increases with the stellar mass of the model, but we have fixed the mass resolution to $\sim 10^4 M_{\odot}$. The stellar component is composed of an exponential stellar disc and an ellipsoidal Sersic bulge is added for specific models. The DM halo follows an Einasto profile and the number of particles is always fixed to 10^6 for every model. The code treats the gas component on an AMR grid and generates an exponential gas disc twice as large as the stellar one. The gas component is self-gravitating, includes a cooling function, and can collapse and form new stars. The strategy we use for the adaptive refinement of the grid cells to the last level is based on the Jeans law and the density threshold we used for SF (i.e., 100 H/cc) is derived from the same law applied to the last level of refinement, corresponding to 12 pc.

7.1.2 The phases of the bar-driven fuelling

We have run a priority set of 16 simulations, focusing on the four stellar mass bins with a gas fraction of 10 and 20%, and a bulge mass fraction of 0 and 10% for each model. We have checked that our simulations are located on the star-forming main sequence and observed that the simulations of the lowest-stellar mass bins ($10^{9.5} M_{\odot}$) are below the main sequence. We explained the latter by their initial low gas mass fraction (10%) compared with observed galaxies with the same stellar mass ($\sim 40\%$). We have computed the evolution of the gas mass inside the central 1 kpc region and compared it with the evolution of the bar strength

(measured via the A_2 Fourier coefficient) and the SFR inside the same 1 kpc region. We have found a correlation between the evolution of the central 1 kpc gas mass and the growth of the bar and defined a dimensionless parameter τ , the normalisation of the time by the typical bar formation time t_{bar} . This typical bar formation time corresponds to the time at which the bar strength A_2 reaches the value of 0.2, commonly used in the literature. We compared our bar formation times with the Fuji relation and found some discrepancies between previous works and our models, that were not recovered even after performing a resolution study. The analysis of the evolution of the central 1 kpc gas mass as a function of τ has revealed four clear and distinct phases of the fuelling by the bar for all our models developing a bar:

1. $\tau \in [0, 1]$: formation of the bar,
2. $\tau \in [1, 1.5]$: increase of the gas mass in the central region,
3. $\tau \in [1.5, 2]$: peak in the gas mass triggering a starburst,
4. $\tau \in [2, \text{end}]$: long-term gas depletion.

We have analysed the gas and SF maps allowing us to highlight that the 4 low-stellar mass models did not form a gas reservoir. We also pointed out that those low-stellar mass models display uniform star-forming distribution along the bar compared with the higher-stellar mass models showing star-forming regions located inside the gas reservoir and at the bar ends. This last result was already reported in previous works and after a deeper analysis of the PHANGS-JWST galaxy imaging, we came to the same conclusion: low- and high-stellar mass galaxies have different regimes in the evolution of their gas structure.

7.1.3 The low- and high-mass regime

We have used an extended set of 35 models, including the discs with a gas fraction of 40% for the two lowest-stellar mass bins (i.e., 9.5 and 10) to probe and understand the physical origin behind this change of regime. We have found that once the bar forms, the gas structure in the low-stellar mass models remains turbulent and chaotic. This trend for the gas structure in the low-mass discs is more visible when we increase the gas fraction up to 40%, replacing those low-mass simulated galaxies on the SF main sequence that we missed with our first subset of 16 models. In the high-stellar mass models ($\leq 10^{10} M_{\odot}$), after the bar forms, we observe the formation of a central gas concentration (i.e., the seed) and have found the inside-out building of the gas reservoir. We have probed the SF distribution and confirmed our above-mentioned claim that low-stellar mass models have a spread distribution along the bar and high-stellar mass models have a concentrated central distribution. We have compared the evolution of the azimuthally-averaged gas mass profile with its initial exponential shape and found a clear difference for barred models. In both cases, the bar is responsible for steepening the profile within the $2 l_*$ region. In the low-mass models, the profile rises monotonically to the centre, while in the high-stellar mass discs, we observe a drop of the profile with a minimum value, followed by a steep

increase to the centre. The dip in the high-stellar mass models is associated with the emergence of a gas reservoir. We have computed the evolution of the distribution of the virial parameter and Mach number for the star-forming cells of two reference simulations. We have not found any significant change in those distributions for the low-stellar mass case but observed drastic changes with the formation of a subsonic peak in the high-mass model, tracing the gas reservoir. We have probed the presence of an ILR in the high-mass barred models, which supports the picture of a gas reservoir forming inside the resonance. We have measured the ratio between the vertical gas velocity dispersion and the escape velocity profile and used them as tracers of the supernova feedback and the gravitational potential, respectively. We found higher values of this ratio for the low-mass models, suggesting the role of supernovae in preventing the formation of gas reservoirs in low-mass discs. We have performed a low-mass test case model without supernovae feedback and exhibiting the formation of a gas reservoir, confirming our hypothesis about supernovae preventing the formation of gas reservoirs. To illustrate the balance between the energy released by supernovae in the ISM and the gravitational potential, we elaborated a simple toy model, allowing us to express the specific SFR as a function of the control parameters of our models. This potentially illustrates that the transition between the two regimes occurs at a stellar mass of around $10^{9.5} M_{\odot}$.

7.1.4 The growth and shape of the gas reservoir

In the last part of this work, we have briefly probed the physical properties of the gas reservoir and its configuration with respect to the central black hole. We have computed the evolution of its semi-major and minor axes over time and found that their growth rates start with an abrupt growth and then seem relatively linear with time. We have also noticed that their ellipticities seem constant over time, ranging from ~ 0.4 to 0.5 . We have observed the edge-on properties of the inner stellar disc and found a thinner disc embedded inside a larger ‘boxy-peanut’ bulge of new stars. We have briefly checked the orientation of the semi-major axes of the gas reservoir with respect to the bar angle and found a value of around 90 degrees. We have finally computed the location of the black hole with respect to the centre of mass of the inner stellar disc. We have found that the black hole wanders along the bar for the lower-stellar mass models, resulting in oscillations of its position with high amplitudes ($\sim 0.6 - 1.2 l_*$), increasing with the gas fraction, until the end of the simulation. In the higher-stellar mass models, we also observe oscillations with amplitudes increasing with the gas fraction and decreasing with the stellar mass. We notice an abrupt stop of those oscillations, corresponding to the formation and settlement of the gas reservoir, forcing the black hole to stay at the centre of the stellar disc. We mention that this last result could be mainly due to numerical effects and should be tested in different conditions (e.g., the mass resolution of the star and DM particles, the mass of the black hole, initial position of the black hole, black hole accretion). Therefore, this result must be taken with extreme caution.

7.2 Limitations of this work

We have carried out this work with a grid of models using galactic parameters based on a sample of observed galaxies. This sample does not offer a comprehensive view of all the characteristics of nearby disc galaxies but is meant to represent a first reference frame to answer the two questions that have motivated this work. There are still some limitations to this work that come from the grid of models, and the setup we have used for the simulations.

- **The discrepancy with the Fujii’s relation:** We have compared the typical bar formation time of our first subset of 16 models to the Fujii’s relation (see [Fujii et al., 2018](#)) and found they fall below the exponential curve derived by the work carried out by Fujii. We have not tested different dynamical initial conditions, by changing the model of the stellar and gas disc or DM halo that could impact the initial velocity curve. This may change the value of f_{disc} and help to recover the Fujii’s relation. In any case, this shows that Fujii’s relation is not an absolute reference and the bar formation time is a complex physical quantity which depends on more than one single parameter.
- **The numerical convergence:** The referee of our first publication has been required to perform a numerical study on the convergence of our typical bar formation times (t_{bar}). We have performed this resolution study on one case (i.e., model G037) by varying the number of particles and the maximum level of refinement. We have not concluded on a neat convergence of t_{bar} for this model, which leaves unknown uncertainties on the real bar formation time.

Moreover, a second grid of models run at a higher resolution (1 pc) was initially planned to check the convergence (i.e., bar formation time, formation of gas reservoirs, stellar feedback) of our first grid. Unfortunately, I did not manage to run those high-resolution models to include them in this work and could therefore not test them further.

- **The gas disc rejuvenation:** The four phases we have described in our first publication describe the bar-driven fuelling until about 2 to 4 times longer than the bar formation time. Then, we reach the long-term SF and depletion occurring inside the central kpc region until the emergence of the gas reservoir. We ignore how this scenario evolves once we consider a refuelling of the large 10 kpc scale gas disc. An interesting avenue would consist of generating an initial gas disc extending much farther than ours. It could then continuously supply gas to the galaxy, as we can see in NGC6946. The second method would initially generate additional massless particles in the gas disc, which would inject gas into the system during the run by turning on and off a simple button (an idea proposed by Florent Renaud and currently implemented by one of his students).

Throughout this work, we have used a simple view of our simulations, by mostly focusing on their central regions. Apart from the mass loading factor, we did not

consider the impact of potential outflows and fountains on the rejuvenation of the gas disc.

- **The connection with the observations:** This work aimed at building a grid of simulations with parameters spanning typical values of PHANGS. During this PhD, we did not manage to fully connect this suite of simulations with the PHANGS observations. It is worth mentioning that the property of the change of regime has emerged naturally from our models and we took this opportunity to compare it with the full set of PHANGS-JWST galaxies such as NGC1087 and NGC3507 illustrated in Chap. 5.

7.3 Outlook

- I **The exact value and conditions of the stellar mass threshold:** The attempt of the toy model to describe the physics of the change of regime is not enough. We would need to perform another set of simulations focusing on stellar masses from $10^{9.5}$ to $10^{10} M_{\odot}$ by step of 0.1 dex in stellar mass. This would allow us to better capture the mass threshold and the different physical conditions of the change of regime. The numerical recipes (e.g., stellar feedback, refinement strategy) we use can also impact the stellar-mass threshold and we would need to investigate their impact to be able to fully describe the physics of the change of regime.
- II **Improve the realism of our simulations:** We have already mentioned the subset of high-resolution (1 pc) simulations we plan to perform. At this resolution, in the central region, we could start to study the impact of the stellar feedback on the transport of gas inside the reservoir itself. In addition, we could also turn on the accretion of the central SMBH and the AGN feedback. This would allow us to study the impact of an AGN on our galactic systems, more particularly the connection of the AGN duty cycle with the gas reservoir and the impact on its secular evolution.
- III **The cosmological environment:** We have started this thesis by introducing the cosmological context, but we have never made the connection with our results in this work. An interesting perspective would be to perform the same grid of simulations by introducing an ‘external environment’ that may include, e.g., gas accretion, galaxy interactions, at different phases of the disc secular evolution.
- IV **Re-connection with PHANGS:** The PHANGS collaboration is an extremely active community and the launch of the JWST telescope has opened up new opportunities to explore the inner structures of the galaxy sample. A number of studies conducted in the course of the PHANGS project closely relate to my own research. In particular, the work of [Stuber et al. \(2023\)](#) on the morphological classification of CO maps and shapes of inner dust lanes is directly relevant to my line of work. A more direct comparison between our grid of simulations on one hand and the dust and molecular

gas distributions as witnessed by JWST and ALMA on the other hand could allow us to better constrain the conditions for and properties of the ongoing fuelling.

Final word

Throughout this manuscript, I mentioned a grid of simulations made of 54 models. We have run the full set of 54 models and, after a visual check, decided to use only some of them that are the most relevant for this work. All the models displaying a clear stellar bar after the end of the run (i.e., ~ 3 Gry) are already mentioned in Tab. 5.1.

Appendix A

Paper 1

A.1 Evolution of the models as a function of the parameter τ

As mentioned in Sect. 4.4.3, we have identified three distinct phases in the building and evolution of the gas reservoir by using the dimensionless parameter $\tau = t/t_{bar}$, where t_{bar} is the typical bar formation time. The following figures illustrate the time evolution of the system for the 16 simulations providing snapshots at four different values of τ (i.e. 1, 1.5, 2, and End, for the end of the simulation). For each simulation, we gather the four models belonging to the same initial stellar mass into one figure. Each panel corresponds to one labelled simulation: each include a zoom (box of 10 kpc on a side) and 4 row with the surface densities of (from top to bottom) the gas, of the (new) stars formed within 50 Myr of the corresponding snapshot time, of all old (initial) stars and of all (new) stars (formed since the beginning of the simulation). Fig. A.1, A.2, A.3, A.4 refer to the models with a stellar mass of 9.5, 10, 10.5 and 11 $\log_{10}(M_{\odot})$, respectively.

In the top rows of the most massive initial stellar mass bins (Fig. A.2, A.3, A.4) we witness the formation of a clearly marked inner gas structure (except for model G162M110F10L5B10, and for model G178M110F20L5B10), while simulations presented in Fig. A.1 do not exhibit such gas structures. We also observe a change in the distribution of new stars that tend to emerge along the bar structure for the lowest stellar mass models, and are more localised (inner region) for the higher stellar mass models from $\tau \geq 2$. There is an associated difference in the structure of the bar with the more massive galaxies presenting a more distinct and rounder stellar concentration (within the bars). This central concentration could be caused by the emergence of an ILR as discussed in Sect. 4.4.1, and 4.4.5.

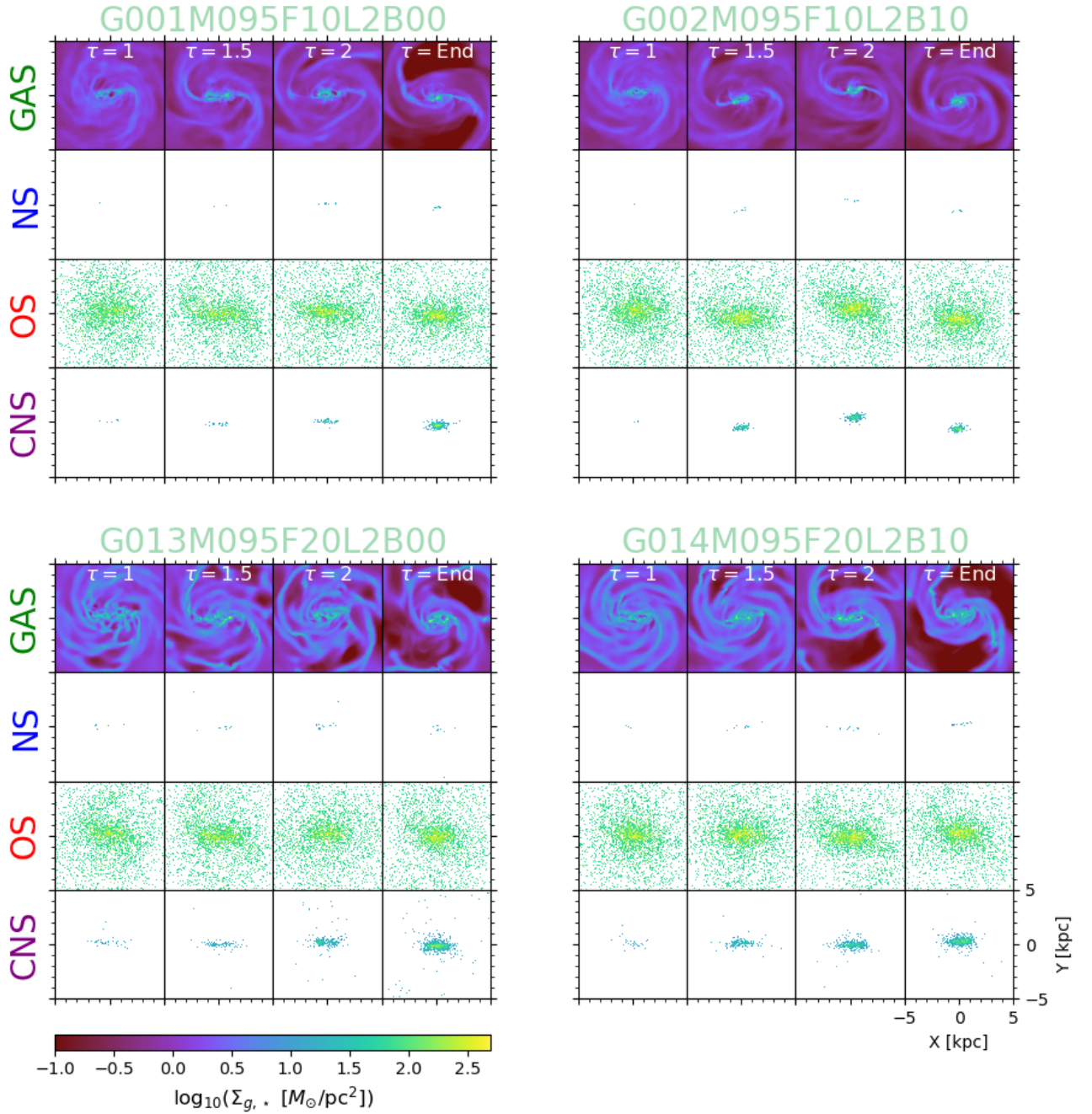


Figure A.1: Time evolution as a function of τ of the gas surface density (top row, **GAS**), formed stars' surface density (second row, **NS**), old stars' surface density (third row, **OS**), and cumulative formed stars' surface density (bottom row, **CNS**) of the four lowest stellar mass models ($10^{9.5} M_{\odot}$). Each panel shows a box with a side length of 10 kpc.

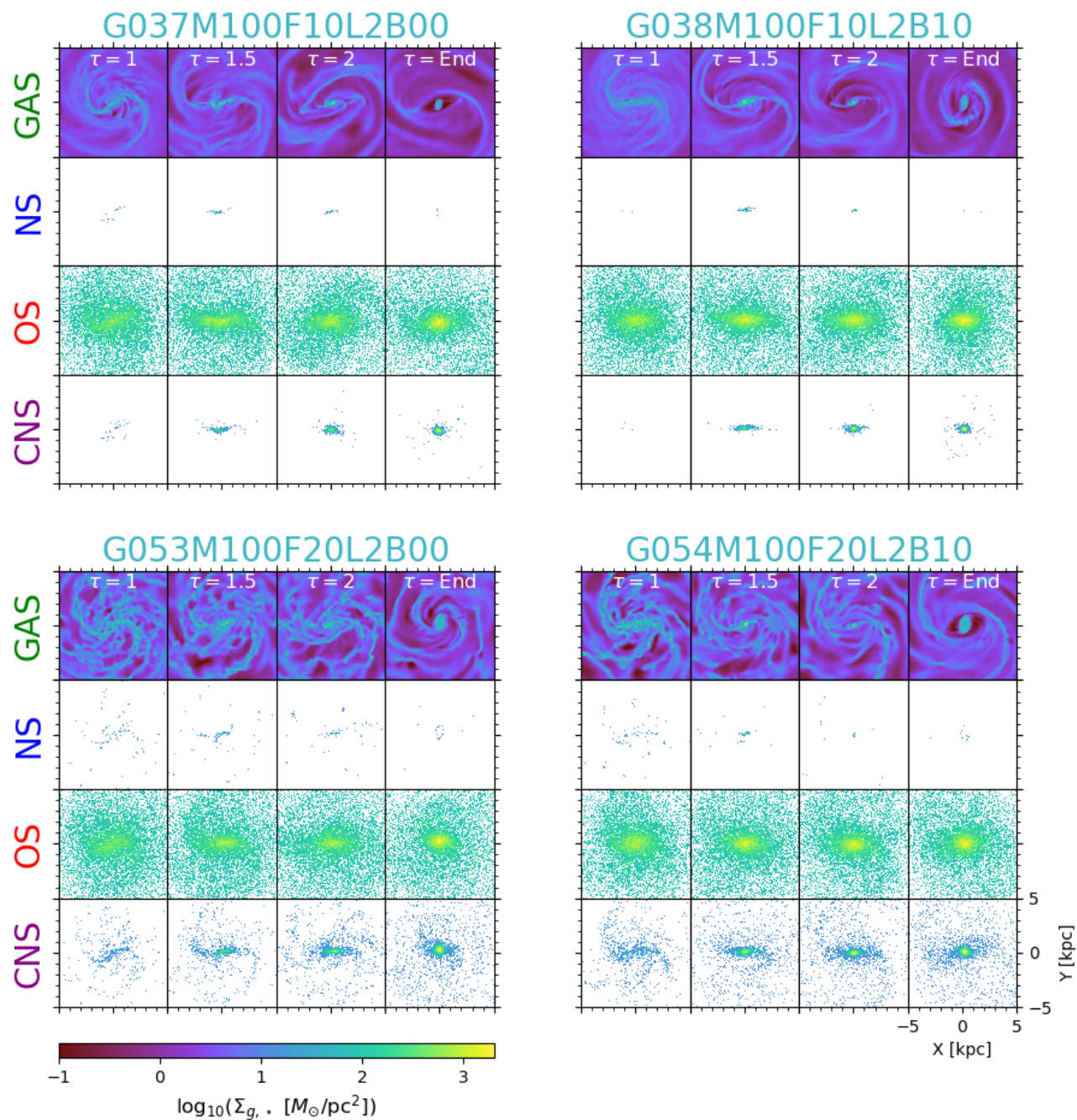


Figure A.2: Same as Fig. A.1 for the four $10^{10} M_{\odot}$ stellar mass models.

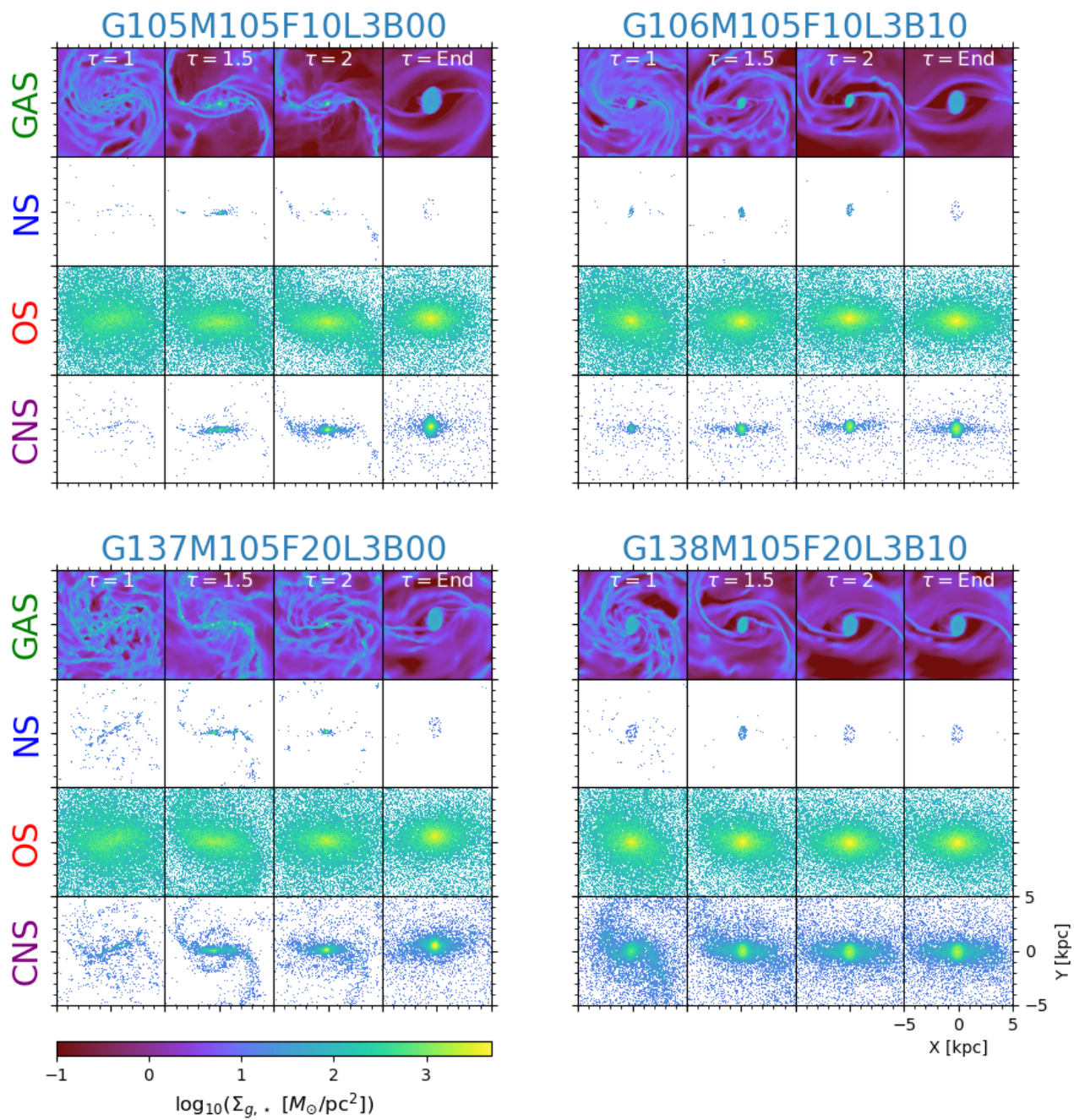


Figure A.3: Same as Fig. A.1 for the four $10^{10.5} M_{\odot}$ stellar mass models.

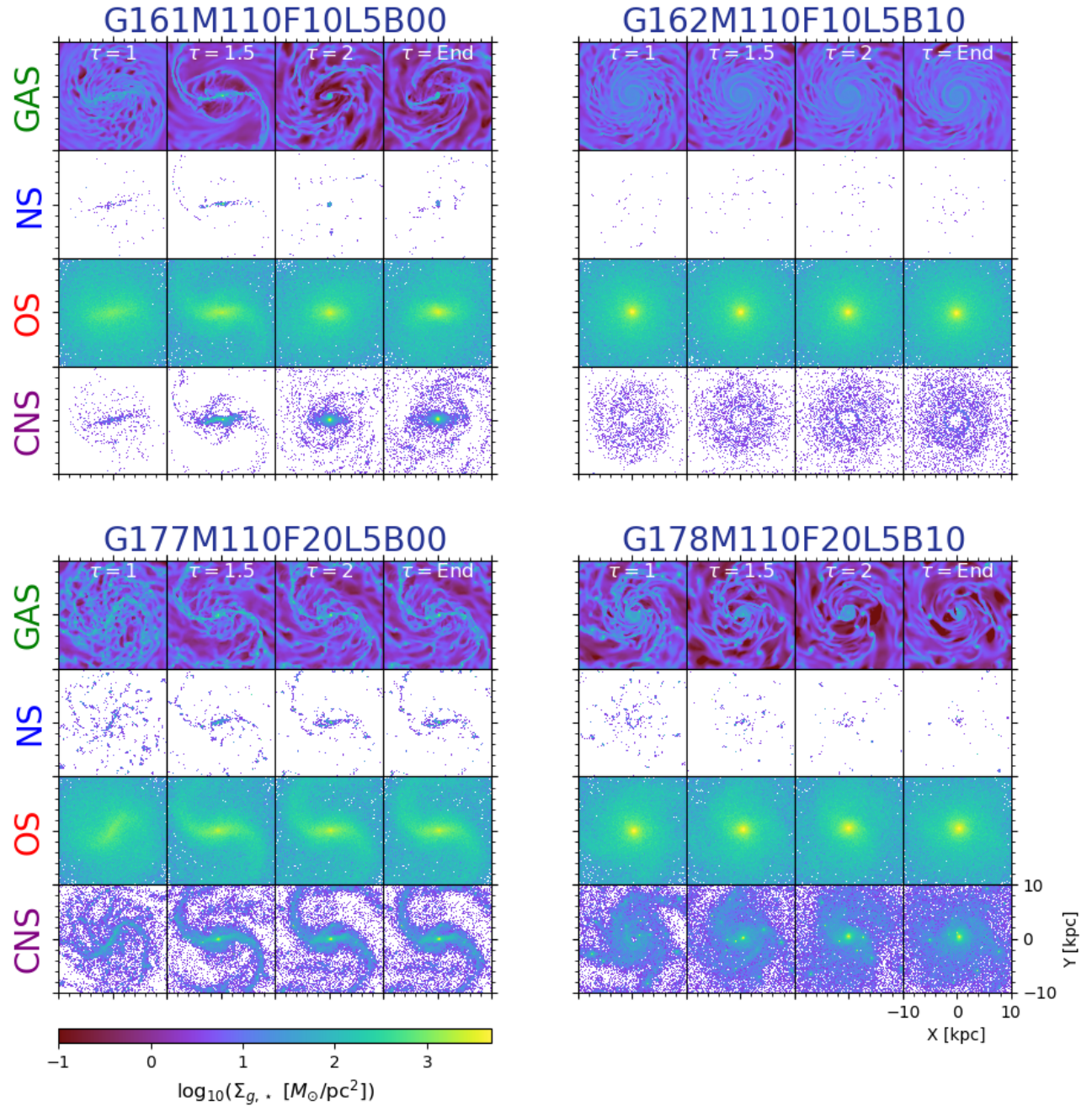


Figure A.4: Same as Fig. A.1 for the four $10^{11} M_{\odot}$ stellar mass models. The box size has been extended to 20 kpc for this most massive stellar bin.

Appendix B

Paper 2

B.1 The gas and star formation distribution in non-barred systems

The models we mainly use as illustrations in this work are the ones forming bars (Y, Tab. 5.1) because they highlight the two stellar-mass regimes. In this section, we show four models which never form a stellar bar (i.e., $A_2 \leq 0.2$) or do not keep it until the end of the run (~ 3000 Myr) to compare them with the four barred models in Fig. 5.2.

Figure B.1 illustrates the gas and newly-formed star density maps at four different time steps (i.e., 500, 1000, 2000, and 3000 Myr) of four of our models. In these figures, we show the two lower-stellar mass models G015 and G032 ($10^{9.5} M_\odot$, top panels) and two higher-stellar mass models G045 and G069 ($10^{10} M_\odot$, bottom panels). In the two top panels, the lower gas fraction model G015 (F=20%) displays a spiral structure that does not significantly evolve with time. The higher gas fraction model G032 (F=40%) also shows some spiral structures but the ISM is more turbulent because of the higher SFR due to a higher gas fraction. The two bottom panels show models with gas fractions of F=10 (G045) and 40% (G069). Model G045 also shows a spiral pattern but starts to develop a bar-like structure between 2 and 3 Gyr. We do not consider this structure as a bar because its A_2 Fourier coefficient stays below the value of 0.2. We observe in Fig. B.1 that the SFR of this model remains low until $t=2000$ Myr.

B.2 Interaction with a massive stellar cluster

The case of model G069 is more relevant for this work because of its high gas fraction and the fact that it forms a bar after ~ 315 Myr. The interesting part is that the bar is destroyed after ~ 1500 Myr by a massive stellar cluster ($\sim 10^7 M_\odot$) formed in situ during the run. In the bottom right panels of Fig. B.1, we observe that the bar has already formed after 500 Myr, with a higher gas density in the inner bar region, resulting in a high SFR. At $t=1000$ Myr, we see the formation of a central gas concentration, which marks the

beginning of the building of the gas reservoir. Between $t=1000$ and 2000 Myr, a massive stellar cluster is formed in the outer part of the disc and is transported by dynamical friction to the centre, where it interacts with the bar and destroys it completely, as shown in Fig. B.2. After the destruction of the bar, the SFR steadily decreases until the end of the simulation. Even though we did not classify model G069 as a barred model, its properties are very similar to the properties of higher-stellar mass barred models until the moment of the interaction with the massive stellar cluster.

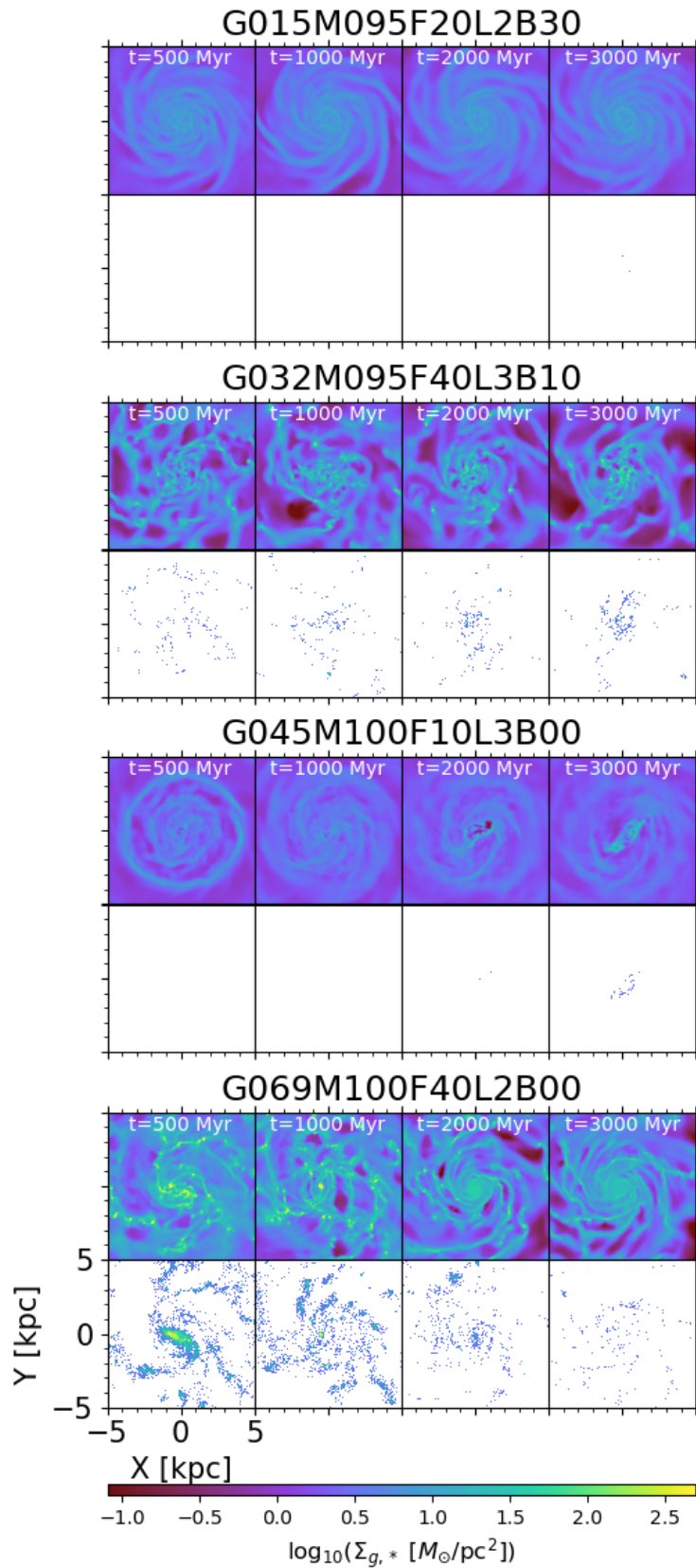


Figure B.1: Same as in Fig. 5.2 but for four non-barred models: G015, G032, G045, and G069.

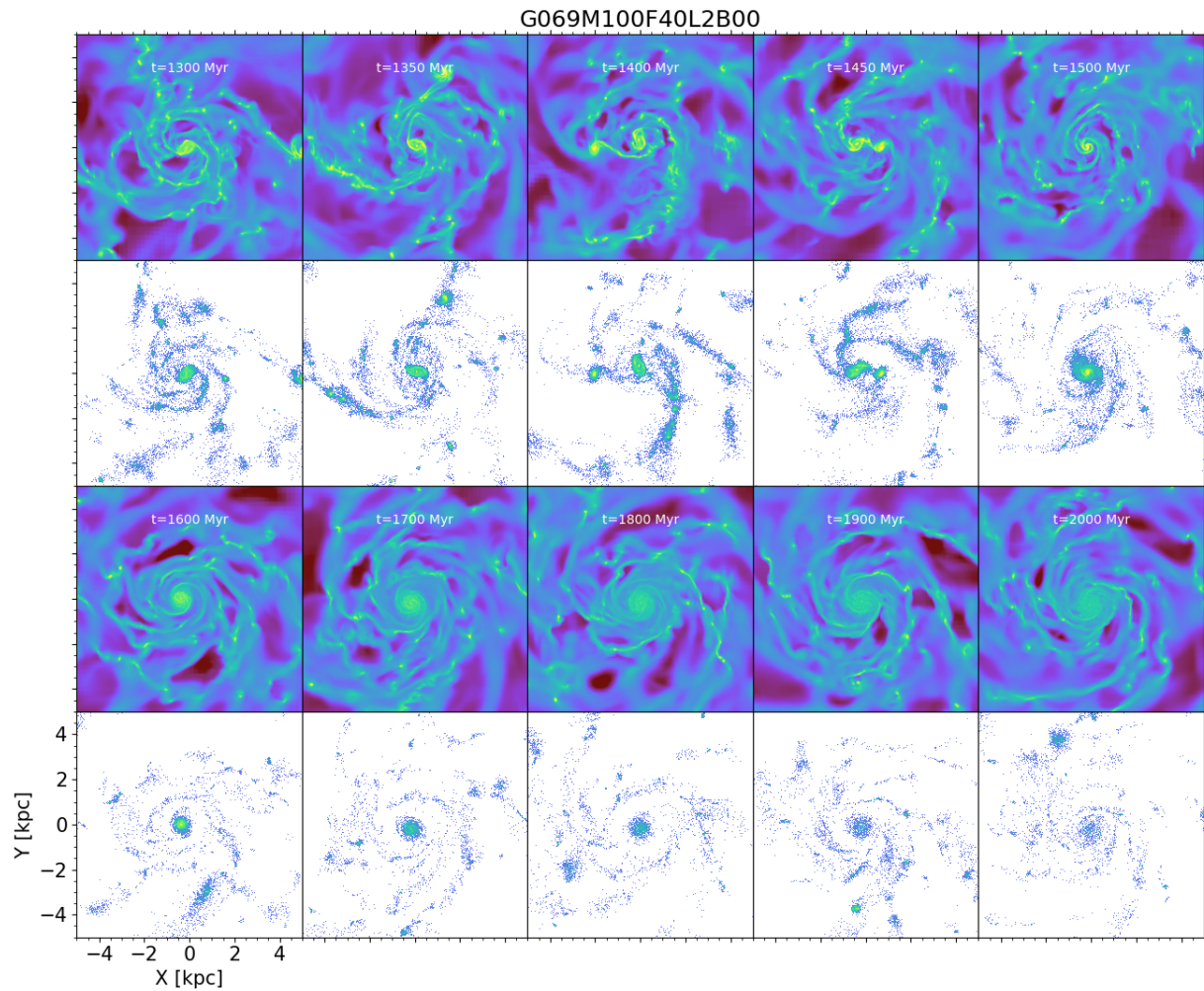


Figure B.2: Density map of the newly-formed stars of model G069 showing the interaction of the in situ formed stellar cluster and the bar region.

Bibliography

Aarseth S. J., 1999, [PASP](#), **111**, 1333

Abel T., Bryan G. L., Norman M. L., 2002, [Science](#), **295**, 93

Agertz O., Lake G., Teyssier R., Moore B., Mayer L., Romeo A. B., 2009, [MNRAS](#), **392**, 294

Agertz O., Kravtsov A. V., Leitner S. N., Gnedin N. Y., 2013, [ApJ](#), **770**, 25

Agertz O., et al., 2021a, [MNRAS](#), **503**, 5826

Agertz O., et al., 2021b, [MNRAS](#), **503**, 5826

Aguerri J. A. L., Méndez-Abreu J., Corsini E. M., 2009, [A&A](#), **495**, 491

Aird J., et al., 2010, [MNRAS](#), **401**, 2531

Andersson E. P., Agertz O., Renaud F., Teyssier R., 2023, [MNRAS](#), **521**, 2196

Anglés-Alcázar D., et al., 2021, [ApJ](#), **917**, 53

Ashtekar A., Rovelli C., Smolin L., 1991, [Phys. Rev. D](#), **44**, 1740

Athanassoula E., 1992a, [MNRAS](#), **259**, 328

Athanassoula E., 1992b, [MNRAS](#), **259**, 345

Athanassoula E., 2002, in Athanassoula E., Bosma A., Mujica R., eds, *Astronomical Society of the Pacific Conference Series Vol. 275, Disks of Galaxies: Kinematics, Dynamics and Perturbations*. pp 141–152 ([arXiv:astro-ph/0209438](#)), [doi:10.48550/arXiv.astro-ph/0209438](#)

Athanassoula E., 2003, [MNRAS](#), **341**, 1179

Athanassoula E., 2008, [MNRAS](#), **390**, L69

Athanassoula E., 2013, in Falcón-Barroso J., Knapen J. H., eds, *Secular Evolution of Galaxies*. p. 305

- Athanassoula E., Misiriotis A., 2002, [MNRAS](#), 330, 35
- Athanassoula E., Machado R. E. G., Rodionov S. A., 2013, [MNRAS](#), 429, 1949
- Baba J., 2015, [MNRAS](#), 454, 2954
- Bamford S. P., et al., 2009, [MNRAS](#), 393, 1324
- Barazza F. D., Jogee S., Marinova I., 2008, [ApJ](#), 675, 1194
- Barnes J., Hut P., 1986a, [Nature](#), 324, 446
- Barnes J., Hut P., 1986b, [Nature](#), 324, 446
- Barnes A. T., et al., 2022, [A&A](#), 662, L6
- Bilitewski T., Schönrich R., 2012, [MNRAS](#), 426, 2266
- Binney J., 2020, [MNRAS](#), 496, 767
- Binney J., Tremaine S., Freeman K., 2009, [Physics Today](#), 62, 56
- Bittner A., et al., 2020, [A&A](#), 643, A65
- Bland-Hawthorn J., Tepper-Garcia T., Agertz O., Freeman K., 2023, [ApJ](#), 947, 80
- Bland-Hawthorn J., Tepper-Garcia T., Agertz O., Federrath C., 2024, [ApJ](#), 968, 86
- Boone F., et al., 2007, [A&A](#), 471, 113
- Bouchet F. R., Hernquist L., 1988, [ApJS](#), 68, 521
- Bower R. G., Benson A. J., Crain R. A., 2012, [Monthly Notices of the Royal Astronomical Society](#), 422, 2816–2840
- Bryan G. L., et al., 2014, [ApJS](#), 211, 19
- Bundy K., et al., 2015, [ApJ](#), 798, 7
- Burkert A., 1995, [ApJ](#), 447, L25
- Buta R. J., et al., 2015, [ApJS](#), 217, 32
- Butcher Z., Schneider S., van Driel W., Lehnert M. D., Minchin R., 2016, [A&A](#), 596, A60
- Calvi R., Vulcani B., Poggianti B. M., Moretti A., Fritz J., Fasano G., 2018, [MNRAS](#), 481, 3456
- Carles C., Martel H., Ellison S. L., Kawata D., 2016, [MNRAS](#), 463, 1074
- Carniani S., et al., 2024, [Nature](#), 633, 318

- Catinella B., et al., 2012, *A&A*, 544, A65
- Chabrier G., 2003, *PASP*, 115, 763
- Cheung E., et al., 2015, *MNRAS*, 447, 506
- Chisholm J., Tremonti C. A., Leitherer C., Chen Y., 2017, *MNRAS*, 469, 4831
- Choi W., et al., 2023, *MNRAS*, 522, 4078
- Chown R., et al., 2024, *arXiv e-prints*, p. arXiv:2410.05397
- Collins M. L. M., Read J. I., 2022, *Nature Astronomy*, 6, 647
- Colombo D., et al., 2022, *A&A*, 658, A54
- Combes F., 2017, in Reylé C., Di Matteo P., Herpin F., Lagadec E., Lançon A., Meliani Z., Royer F., eds, SF2A-2017: Proceedings of the Annual meeting of the French Society of Astronomy and Astrophysics. p. Di (arXiv:1707.08733)
- Combes F., Sanders R. H., 1981, *A&A*, 96, 164
- Combes F., et al., 2004, *A&A*, 414, 857
- Comerón S., Knapen J. H., Beckman J. E., Laurikainen E., Salo H., Martínez-Valpuesta I., Buta R. J., 2010, *MNRAS*, 402, 2462
- Dale J. E., Ercolano B., Bonnell I. A., 2012, *MNRAS*, 424, 377
- Dehnen W., 2000, *ApJ*, 536, L39
- Delvecchio I., et al., 2014, *MNRAS*, 439, 2736
- Di Cintio A., Brook C. B., Dutton A. A., Macciò A. V., Stinson G. S., Knebe A., 2014, *MNRAS*, 441, 2986
- Díaz-García S., Salo H., Laurikainen E., 2016, *A&A*, 596, A84
- Díaz-García S., Moyano F. D., Comerón S., Knapen J. H., Salo H., Bouquin A. Y. K., 2020, *A&A*, 644, A38
- Dobbs C., Baba J., 2014, *PASA*, 31, e035
- Dubois Y., et al., 2014, *MNRAS*, 444, 1453
- Dubois Y., et al., 2021, *A&A*, 651, A109
- Dunn R. J. H., Fender R. P., Körding E. G., Belloni T., Cabanac C., 2010, *MNRAS*, 403, 61

- Efstathiou G., Lake G., Negroponte J., 1982a, [MNRAS](#), **199**, 1069
- Efstathiou G., Lake G., Negroponte J., 1982b, [MNRAS](#), **199**, 1069
- Einasto J., 1965, Trudy Astrofizicheskogo Instituta Alma-Ata, **5**, 87
- Einstein A., 1915, Sitzungsberichte der Königlich Preussischen Akademie der Wissenschaften, pp 844–847
- Emsellem E., Monnet G., Bacon R., 1994a, [A&A](#), **285**, 723
- Emsellem E., Monnet G., Bacon R., Nieto J. L., 1994b, [A&A](#), **285**, 739
- Emsellem E., Renaud F., Bournaud F., Elmegreen B., Combes F., Gabor J. M., 2015, [MNRAS](#), **446**, 2468
- Emsellem E., et al., 2022, [A&A](#), **659**, A191
- Eskridge P. B., et al., 2000, [AJ](#), **119**, 536
- Event Horizon Telescope Collaboration et al., 2019, [ApJ](#), **875**, L1
- Fabian A. C., 2012, [ARA&A](#), **50**, 455
- Ferland G. J., Korista K. T., Verner D. A., Ferguson J. W., Kingdon J. B., Verner E. M., 1998, [PASP](#), **110**, 761
- Ferrière K., Gillard W., Jean P., 2007, [A&A](#), **467**, 611
- Fontana A., et al., 2006, [A&A](#), **459**, 745
- Fragkoudi F., Di Matteo P., Haywood M., Gómez A., Combes F., Katz D., Semelin B., 2017, [A&A](#), **606**, A47
- Fraser-McKelvie A., et al., 2020, [MNRAS](#), **495**, 4158
- Freundlich J., et al., 2020, [MNRAS](#), **499**, 2912
- Friedmann A., 1922, [Zeitschrift für Physik](#), **10**, 377
- Fryxell B., et al., 2000, [ApJS](#), **131**, 273
- Fujii M. S., Bédorf J., Baba J., Portegies Zwart S., 2018, [MNRAS](#), **477**, 1451
- Fujii M. S., Bédorf J., Baba J., Portegies Zwart S., 2019, [MNRAS](#), **482**, 1983
- Fujii M. S., Wang L., Tanikawa A., Hirai Y., Saitoh T. R., 2024, [Science](#), **384**, 1488
- Fukuda H., Wada K., Habe A., 1998, [MNRAS](#), **295**, 463

- Gadotti D. A., 2008, in Bureau M., Athanassoula E., Barbuy B., eds, Vol. 245, Formation and Evolution of Galaxy Bulges. pp 117–120 ([arXiv:0708.2842](https://arxiv.org/abs/0708.2842)), [doi:10.1017/S1743921308017420](https://doi.org/10.1017/S1743921308017420)
- Gadotti D. A., et al., 2019, *MNRAS*, **482**, 506
- Gadotti D. A., et al., 2020, *A&A*, **643**, A14
- García-Burillo S., Combes F., Schinnerer E., Boone F., Hunt L. K., 2005, *A&A*, **441**, 1011
- Garma-Oehmichen L., et al., 2022, *MNRAS*, **517**, 5660
- Genel S., et al., 2014, *MNRAS*, **445**, 175
- Genel S., Fall S. M., Hernquist L., Vogelsberger M., Snyder G. F., Rodriguez-Gomez V., Sijacki D., Springel V., 2015, *ApJ*, **804**, L40
- Ghosh S., Di Matteo P., 2024, *A&A*, **683**, A100
- Giersz M., Leigh N., Hypki A., Lützgendorf N., Askar A., 2015, *MNRAS*, **454**, 3150
- Godunov S. K., 1959, *Sb. Math.*, 89
- Goz D., Monaco P., Murante G., Curir A., 2015, *MNRAS*, **447**, 1774
- Greene J. E., Strader J., Ho L. C., 2020, *ARA&A*, **58**, 257
- Groth F., Steinwandel U. P., Valentini M., Dolag K., 2023, *MNRAS*, **526**, 616
- Gruppioni C., et al., 2013, *MNRAS*, **432**, 23
- Guo R., Mao S., Athanassoula E., Li H., Ge J., Long R. J., Merrifield M., Masters K., 2019, *MNRAS*, **482**, 1733
- Guo M., Stone J. M., Kim C.-G., Quataert E., 2023, *ApJ*, **946**, 26
- Haardt F., Madau P., 1996, *ApJ*, **461**, 20
- Hayward C. C., Hopkins P. F., 2017, *MNRAS*, **465**, 1682
- Henshaw J. D., Barnes A. T., Battersby C., Ginsburg A., Sormani M. C., Walker D. L., 2023, in Inutsuka S., Aikawa Y., Muto T., Tomida K., Tamura M., eds, Astronomical Society of the Pacific Conference Series Vol. 534, Protostars and Planets VII. p. 83 ([arXiv:2203.11223](https://arxiv.org/abs/2203.11223)), [doi:10.48550/arXiv.2203.11223](https://doi.org/10.48550/arXiv.2203.11223)
- Hickox R. C., et al., 2012, *MNRAS*, **421**, 284
- Hilmi T., et al., 2020, *MNRAS*, **497**, 933
- Ho L. C., Filippenko A. V., Sargent W. L. W., 1997, *ApJ*, **487**, 591

- Hockney R. W., Eastwood J. W., 1988, Computer simulation using particles
- Hopkins P. F., Quataert E., 2010, [MNRAS](#), 407, 1529
- Hubble E., 1929, [Proceedings of the National Academy of Science](#), 15, 168
- Izumi T., et al., 2023, [arXiv e-prints](#), p. arXiv:2305.03993
- Joshi G. D., Pontzen A., Agertz O., Rey M. P., Read J., Renaud F., 2024, [MNRAS](#), 528, 2346
- Kataria S. K., Das M., 2018, [MNRAS](#), 475, 1653
- Kaufmann D. E., Contopoulos G., 1996, [A&A](#), 309, 381
- Kennicutt R. C., 2007, in Elmegreen B. G., Palous J., eds, Vol. 237, Triggered Star Formation in a Turbulent ISM. pp 311–316, [doi:10.1017/S1743921307001652](#)
- Kewley L. J., Groves B., Kauffmann G., Heckman T., 2006, [MNRAS](#), 372, 961
- Kim C.-G., Ostriker E. C., 2015, [ApJ](#), 802, 99
- Klessen R., 2019, in Latif M., Schleicher D., eds, , Formation of the First Black Holes. pp 67–97, [doi:10.1142/9789813227958_0004](#)
- Kormendy J., Ho L. C., 2013, [ARA&A](#), 51, 511
- Kormendy J., Kennicutt Robert C. J., 2004, [ARA&A](#), 42, 603
- Kraljic K., Bournaud F., Martig M., 2012, [ApJ](#), 757, 60
- Kravtsov A. V., Klypin A. A., Khokhlov A. M., 1997, [ApJS](#), 111, 73
- Krolik J. H., 1999, Active galactic nuclei : from the central black hole to the galactic environment
- Kruk S. J., et al., 2017, [MNRAS](#), 469, 3363
- Kun E., Keresztes Z., Simkó A., Szűcs G., Gergely L. Á., 2017, [A&A](#), 608, A42
- Lacey C. G., Fall S. M., 1985, [ApJ](#), 290, 154
- Lang P., et al., 2020, [ApJ](#), 897, 122
- Lapi A., Mancuso C., Bressan A., Danese L., 2017, [ApJ](#), 847, 13
- Lawrence A., 1987, [PASP](#), 99, 309
- Lee J. C., et al., 2022, [ApJS](#), 258, 10

- Lee J. C., et al., 2023, *ApJ*, 944, L17
- Leitherer C., et al., 1999, *ApJS*, 123, 3
- Lemaître G., 1931, *MNRAS*, 91, 483
- Leroy A. K., et al., 2019, *ApJS*, 244, 24
- Leroy A. K., et al., 2021, *ApJS*, 257, 43
- Lin C. C., Shu F. H., 1964, *ApJ*, 140, 646
- Lin L.-H., Yuan C., Buta R., 2008, *ApJ*, 684, 1048
- Longmore S. N., et al., 2013, *MNRAS*, 429, 987
- Lovell C. C., Vijayan A. P., Thomas P. A., Wilkins S. M., Barnes D. J., Irodotou D., Roper W., 2021, *MNRAS*, 500, 2127
- Ludlow A. D., Angulo R. E., 2017, *MNRAS*, 465, L84
- Mac Low M.-M., Klessen R. S., 2004, *Reviews of Modern Physics*, 76, 125
- Madau P., Dickinson M., 2014, *ARA&A*, 52, 415
- Magorrian J., et al., 1998, *AJ*, 115, 2285
- Marinacci F., et al., 2018, *MNRAS*, 480, 5113
- Marinova I., Joglee S., 2007, *ApJ*, 659, 1176
- Meidt S. E., et al., 2013, *ApJ*, 779, 45
- Michel-Dansac L., Wozniak H., 2006, *A&A*, 452, 97
- Mignone A., Bodo G., Massaglia S., Matsakos T., Tesileanu O., Zanni C., Ferrari A., 2007, *ApJS*, 170, 228
- Mitchell P. D., Schaye J., Bower R. G., Crain R. A., 2020, *MNRAS*, 494, 3971
- Monnet G., Bacon R., Emsellem E., 1992, *A&A*, 253, 366
- Moriondo G., Giovanardi C., Hunt L. K., 1998, *A&AS*, 130, 81
- Morris M., Serabyn E., 1996, *ARA&A*, 34, 645
- Mortlock A., et al., 2015, *MNRAS*, 447, 2
- Muratov A. L., Kereš D., Faucher-Giguère C.-A., Hopkins P. F., Quataert E., Murray N., 2015, *MNRAS*, 454, 2691

- Naiman J. P., et al., 2018, [MNRAS](#), 477, 1206
- Nair P. B., Abraham R. G., 2010, *The Astrophysical Journal Letters*, 714, L260
- Navarro J. F., Frenk C. S., White S. D. M., 1997, [ApJ](#), 490, 493
- Nelson D., et al., 2018, [MNRAS](#), 475, 624
- Nelson D., et al., 2019, [MNRAS](#), 490, 3234
- Neumann J., et al., 2019, [A&A](#), 627, A26
- O'Shea B. W., Norman M. L., 2007, [ApJ](#), 654, 66
- Ocvirk P., Pichon C., Teyssier R., 2008, [MNRAS](#), 390, 1326
- Ostriker E. C., Kim C.-G., 2022, [ApJ](#), 936, 137
- Ostriker E. C., McKee C. F., Leroy A. K., 2010, [ApJ](#), 721, 975
- Padoan P., Haugbølle T., Nordlund Å., Frimann S., 2017, [ApJ](#), 840, 48
- Padovani P., 2017, [Frontiers in Astronomy and Space Sciences](#), 4, 35
- Padovani P., et al., 2017, [A&A Rev.](#), 25, 2
- Penzias A. A., Wilson R. W., 1965, [ApJ](#), 142, 419
- Pezzulli G., Fraternali F., 2016, [Astronomische Nachrichten](#), 337, 913
- Pfenniger D., Saha K., Wu Y.-T., 2023, [A&A](#), 673, A36
- Pillepich A., et al., 2018, [MNRAS](#), 475, 648
- Porciani C., Dekel A., Hoffman Y., 2002, [MNRAS](#), 332, 325
- Portegies Zwart S. F., Baumgardt H., McMillan S. L. W., Makino J., Hut P., Ebisuzaki T., 2006, [ApJ](#), 641, 319
- Price D. J., et al., 2018, [PASA](#), 35, e031
- Puchwein E., Springel V., 2013, [MNRAS](#), 428, 2966
- Querejeta M., et al., 2021, [A&A](#), 656, A133
- Raiteri C. M., Villata M., Navarro J. F., 1996, [A&A](#), 315, 105
- Raskutti S., Ostriker E. C., Skinner M. A., 2016, [ApJ](#), 829, 130
- Read J. I., Agertz O., Collins M. L. M., 2016, [MNRAS](#), 459, 2573

- Reines A. E., Volonteri M., 2015, [ApJ](#), **813**, 82
- Reines A. E., Volonteri M., 2016, in American Astronomical Society Meeting Abstracts #227. p. 119.01
- Renaud F., et al., 2013a, [MNRAS](#), **436**, 1836
- Renaud F., et al., 2013b, [MNRAS](#), **436**, 1836
- Renaud F., Agertz O., Read J. I., Ryde N., Andersson E. P., Bensby T., Rey M. P., Feuillet D. K., 2021a, [MNRAS](#), **503**, 5846
- Renaud F., Agertz O., Andersson E. P., Read J. I., Ryde N., Bensby T., Rey M. P., Feuillet D. K., 2021b, [MNRAS](#), **503**, 5868
- Renaud F., Segovia Otero Á., Agertz O., 2022, [MNRAS](#), **516**, 4922
- Rey M. P., Pontzen A., Agertz O., Orkney M. D. A., Read J. I., Rosdahl J., 2020, [MNRAS](#), **497**, 1508
- Rey M. P., et al., 2023, [MNRAS](#), **521**, 995
- Romeo A. B., Agertz O., Renaud F., 2023, [MNRAS](#), **518**, 1002
- Rupke D. S. N., 2018, [Galaxies](#), **6**, 138
- Saha K., Naab T., 2013, [MNRAS](#), **434**, 1287
- Sanders R. H., 1977, [ApJ](#), **217**, 916
- Sanders D. B., Soifer B. T., Elias J. H., Neugebauer G., Matthews K., 1988, [ApJ](#), **328**, L35
- Sandstrom K. M., et al., 2023, [ApJ](#), **944**, L8
- Santini P., et al., 2022, [ApJ](#), **940**, 135
- Schaller M., et al., 2024, [MNRAS](#), **530**, 2378
- Schaye J., et al., 2015, [MNRAS](#), **446**, 521
- Schechter P., 1976, [ApJ](#), **203**, 297
- Schinnerer E., et al., 2023, [ApJ](#), **944**, L15
- Schmidt M., 1959, [ApJ](#), **129**, 243
- Schmidt T. M., Bigiel F., Klessen R. S., de Blok W. J. G., 2016, [MNRAS](#), **457**, 2642
- Schwarz J. H., 1982, [Phys. Rep.](#), **89**, 223

- Segovia Otero Á., Renaud F., Agertz O., 2022, *MNRAS*, 516, 2272
- Sellwood J. A., 2000, *Ap&SS*, 272, 31
- Sellwood J. A., Evans N. W., 2001, *ApJ*, 546, 176
- Sellwood J. A., Masters K. L., 2022, *ARA&A*, 60
- Seo W.-Y., Kim W.-T., Kwak S., Hsieh P.-Y., Han C., Hopkins P. F., 2019, *ApJ*, 872, 5
- Sérsic J. L., 1963, *Boletín de la Asociación Argentina de Astronomía La Plata Argentina*, 6, 41
- Shankar F., Weinberg D. H., Miralda-Escudé J., 2009, *ApJ*, 690, 20
- Shlosman I., Frank J., Begelman M. C., 1989, *Nature*, 338, 45
- Shlosman I., Begelman M. C., Frank J., 1990, *Nature*, 345, 679
- Somerville R. S., Popping G., Trager S. C., 2015, *MNRAS*, 453, 4337
- Sormani M. C., Barnes A. T., 2019, *MNRAS*, 484, 1213
- Sormani M. C., Binney J., Magorrian J., 2015, *MNRAS*, 451, 3437
- Sormani M. C., Tress R. G., Glover S. C. O., Klessen R. S., Battersby C. D., Clark P. C., Hatchfield H. P., Smith R. J., 2020, *MNRAS*, 497, 5024
- Sormani M. C., Sobacchi E., Sanders J. L., 2023a, *arXiv e-prints*, p. arXiv:2309.14093
- Sormani M. C., et al., 2023b, *MNRAS*, 523, 2918
- Sormani M. C., Sobacchi E., Sanders J. L., 2024, *MNRAS*, 528, 5742
- Sotnikova N. Y., Reshetnikov V. P., Mosenkov A. V., 2012, *Astronomical and Astrophysical Transactions*, 27, 325
- Springel V., et al., 2018, *MNRAS*, 475, 676
- Springel V., Pakmor R., Weinberger R., 2019, AREPO: Cosmological magnetohydrodynamical moving-mesh simulation code, *Astrophysics Source Code Library*, record ascl:1909.010
- Springel V., Pakmor R., Zier O., Reinecke M., 2022, GADGET-4: Parallel cosmological N-body and SPH code, *Astrophysics Source Code Library*, record ascl:2204.014
- Stark D. V., et al., 2018, *MNRAS*, 474, 2323
- Stewart K. R., Brooks A. M., Bullock J. S., Maller A. H., Diemand J., Wadsley J., Moustakas L. A., 2013, *ApJ*, 769, 74

- Stone J. M., Tomida K., White C. J., Felker K. G., 2020, *ApJS*, **249**, 4
- Stuber S. K., et al., 2023, *A&A*, **676**, A113
- Sun J., et al., 2022, *AJ*, **164**, 43
- Sutherland R. S., Dopita M. A., 1993, *ApJS*, **88**, 253
- Tauris T. M., van den Heuvel E. P. J., 2006, in Lewin W. H. G., van der Klis M., eds, , Vol. 39, Compact stellar X-ray sources. pp 623–665, doi:10.48550/arXiv.astro-ph/0303456
- Teyssier R., 2002a, *A&A*, **385**, 337
- Teyssier R., 2002b, *A&A*, **385**, 337
- Tinker J., Kravtsov A. V., Klypin A., Abazajian K., Warren M., Yepes G., Gottlöber S., Holz D. E., 2008, *ApJ*, **688**, 709
- Toomre A., 1964, *ApJ*, **139**, 1217
- Toomre A., 1981, in Fall S. M., Lynden-Bell D., eds, Structure and Evolution of Normal Galaxies. pp 111–136
- Toro E., 2009, Riemann Solvers and Numerical Methods for Fluid Dynamics: A Practical Introduction, doi:10.1007/b79761.
- Tremaine S., Weinberg M. D., 1984, *ApJ*, **282**, L5
- Turner J. A., et al., 2021, *MNRAS*, **502**, 1366
- Übler H., Naab T., Oser L., Aumer M., Sales L. V., White S. D. M., 2014, *MNRAS*, **443**, 2092
- Valencia-Enríquez D., Puerari I., Chaves-Velasquez L., 2017, *Rev. Mexicana Astron. Astrofis.*, **53**, 257
- Valentini M., Murante G., Borgani S., Monaco P., Bressan A., Beck A. M., 2017, *MNRAS*, **470**, 3167
- Veilleux S., Cecil G., Bland-Hawthorn J., 2005, *ARA&A*, **43**, 769
- Verley S., Combes F., Verdes-Montenegro L., Bergond G., Leon S., 2007, *A&A*, **474**, 43
- Verwilghen P., et al., 2024, *A&A*, **687**, A53
- Vogelsberger M., et al., 2014a, *MNRAS*, **444**, 1518
- Vogelsberger M., et al., 2014b, *Nature*, **509**, 177

Wada K., 1994, PASJ, [46](#), [165](#)

Weaver J. R., et al., 2023, [A&A](#), [677](#), [A184](#)

Weiss A., Abel T. G., Hill V., eds, 2000, The First Stars , [doi:10.1007/b75028](https://doi.org/10.1007/b75028)

Yu S.-Y., et al., 2022, [A&A](#), [666](#), [A175](#)

de Sá-Freitas C., et al., 2023, [A&A](#), [671](#), [A8](#)

van de Sande J., Fraser-McKelvie A., Fisher D. B., Martig M., Hayden M. R., Geckos Survey Collaboration 2024, in Tabatabaei F., Barbuy B., Ting Y.-S., eds, IAU Symposium Vol. 377, Early Disk-Galaxy Formation from JWST to the Milky Way. pp 27–33 ([arXiv:2306.00059](https://arxiv.org/abs/2306.00059)), [doi:10.1017/S1743921323001138](https://doi.org/10.1017/S1743921323001138)

Acknowledgements

Je tiens tout d'abord à remercier mon directeur de thèse, Eric, qui m'a permis de réaliser mes recherches avec une liberté totale, tout en sachant me guider lorsque cela a été nécessaire. Après trois ans, il m'est encore difficile d'imaginer la quantité de responsabilités qu'il doit endosser et qui, quelque part, vont avec le métier de chercheur. Je tiens aussi à souligner le calme et le sérieux dont il a su faire preuve lors de mes moments de doute, surtout lors de l'écriture des papiers et de ce manuscrit. Cela aura été une grande aventure et je suis heureux d'avoir pu la vivre en étant guidé par une personne aussi bienveillante.

Je remercie également Milena, qui s'est toujours montrée disponible et d'une grande aide lorsque j'ai eu besoin de ses conseils. Elle a su trouver les mots justes et me guider dans cette aventure, surtout durant les derniers mois de la thèse.

Je remercie aussi Florent pour m'avoir fait part de son expertise de RAMSES et de ses conseils avisés lors de nos échanges par mail et de ses visites à l'ESO.

I would like to thank Klaus, my official University supervisor, for allowing me to pursue this PhD at LMU and for his availability and advice when I needed to talk and be guided.

I would like to thank Louise and Amelia for being my fellow mentors. Thank you, Louise, for the support and all the chats we have had. Thank you, Amelia, for your support and the nice chats we had while walking around the campus.

I want to thank every person I have met during my stay at ESO, especially Nelma and Denisa who made my life much easier during my conference trips. I thank Benoit and Matthias for organising our board game nights and helping me to relax with good friends around a pizza once a week. I thank everyone: Stephen, Samuel, Ivanna, Josh, Alice, Tom, Tommy, Felipe, Rik, Marta, Chiara, Lara, Luca², Elena, Marco, Luigi, Julienne, Lennart, etc. for the memorable table football games we have played over the past 3 years. A special thank you to Samuel, Ivanna, Alice, Josh, Keegan, David, Tadeja, and Smaran for all the board game afternoons we have spent together.

Je tiens également à remercier Julien, Anthony, Kevin et Gregory, qui sont restés mes plus proches amis depuis la fin de nos études secondaires. Un merci tout particulier à mes amis de l'ULiège, Lionel et Victor, avec qui j'ai aussi partagé de bons moments lors de mes retours en Belgique. Je souhaiterais également mentionner, parmi mes amis physiciens de l'ULiège, Youri, qui est venu me rendre visite à Munich lors de l'une de ses conférences.

Et enfin, comment ne pas remercier ma famille qui m'a soutenu pendant ces 3 ans de thèse. Je remercie mon père et ma mère avec qui je n'ai (presque) jamais manqué un de nos e-déjeuners le samedi matin. Ils ont toujours été là pour m'écouter dans les moments

les plus difficiles de ce doctorat. J'ai traversé un bon nombre de moments de doute, mais une chose est sûre, je n'y serais jamais arrivé sans leur soutien! Je remercie également mon papy, ma mamy, mon parrain et ma marraine qui ont aussi su m'écouter et me soutenir dans les moments difficiles. Je terminerai par un dernier merci que j'adresse à mon cher frère et à ma tendre sœur qui, même avec la distance, m'ont toujours soutenu et avec qui j'ai continué à avoir des moments de complicité lorsque je rentrais en Belgique ou qu'ils venaient me visiter à Munich. Pour tout cela, je tiens à ce que vous sachiez que je vous suis infiniment reconnaissant.